MODELLING OF PHOTONIC CRYSTAL FIBRES

Lei Chen
A thesis submitted for the degree of Doctor of Philosophy
University of Bath
Department of Physics
October 2009

Contents

Acknowledgements

I first would like to show my sincere and deep gratitude to my supervisor, Professor David Bird. He recommended me for Overseas Research Studentship and offered me the chance in such an amazing domain under his direction. He took great effort and enthusiasm in teaching me the knowledge, guiding me in the research and assisting me in the thesis throughout the past four years.

I would also like to thank Professor Tim Birks and Dr Greg Pearce, who provided their pioneering work for me in the development of this research, and Professor John Roberts for providing the boundary element code.

I also thank Dr Matthew Mizielinski, who shared his experience in large-scale computations with me and helped me in solving many problems.

Thanks also go to the staff and students in the Department of Physics who provided me with a very efficient and comfortable research environment. Especially, the members in the theoretical group who gave me a lot of help.

Additionally, I would like to thank all my friends in UK and China, who inspired me to endlessly pursue my goal and gave me much pleasure in the years. Especially, my friend and schoolmate, Miss Lan Zhang, who gave me so much encouragement.

Finally, I am grateful to my parents. They tried the best they could to support me with any dream I believe.

Abstract

The work in this thesis is to understand, through theory and simulation, a guidance mechanism due to the weak interaction of modes in photonic crystal fibres (PCFs). Firstly, two common kinds of PCFs, that guide light by total internal reflection and by photonic bandgaps, are reviewed. Several typical PCF structures for which light propagation is governed by weak mode interaction are then discussed and particularly compared with bandgap-guiding PCFs.

Two independent methods are developed to model a set of related rectangular hollow-core PCF structures. The boundary element method is derived for a general PCF configuration and applied to our model structures. This method numerically provides some basic features about the guided modes, such as the propagation constant and field profile. The calculations show an ideal confinement in our model structure by considering a scalar wave equation and a high dielectric constant at the glass intersections. However, in realistic guidance, both confinement loss and the field of the guided modes indicate a raised leakage due to mode interactions.

The analytic methodology starts by solving the ideal case considered in boundary element calculations and leads to analytic solutions for the perfectly guided modes. A perturbation method corresponding to the realistic guidance is then applied to these analytic solutions. This method can provide insight into understanding the formation of leakage through an analysis of mode interactions. An approximate analytic method for obtaining the attenuation of guided modes from the perturbation interaction is demonstrated. Attenuations calculated in this way give good agreement with boundary element results in magnitude and trends in variation. The influences of frequency and fibre parameters on features of the attenuation are also investigated.

An overall interpretation of this guidance mechanism and suggestions for fibre optimisation are made in the final chapter, where further development of this work is also proposed.

Chapter 1

Introduction

1.1 Photonic crystals

Photonic crystals are a significant and promising domain in physics and material science. The definition of a 'photonic crystal' was brought out by Yablonovitch and John from publications in 1987 [1, 2]. An electromagnetic bandgap for the three dimensional periodic lattice was presented by both authors. The characteristics of inhibited spontaneous emission with respect to the photonic bandgap were also investigated.

Photonic crystals are materials constituted by periodic dielectric structures. The photonic bandgap, which is analogous to the electronic bandgap, therefore forms due to this regular alternation of high and low dielectric regions. Wave propagation will be allowed or forbidden in terms of the location of the photonic bandgap. The periodicity can be created in one, two or three dimensional structures. These different dimensions of photonic crystals offer great opportunities in application such as optical fibres, photonic crystal laser [3–5], light-emitting diodes [6–8], and photonic integrated circuits [9, 10].

1.2 Photonic bandgap

The formation of photonic bandgap can be understood through an analogy with the electronic bandgap, but the theoretical description is based on Maxwell's equations. The equation which describes wave propagation of magnetic fields in a three-dimensional photonic crystal can be expressed as [11]

$$\nabla \times \left(\frac{1}{\varepsilon(\mathbf{r})} \nabla \right) \times \mathbf{H} = \frac{\omega^2}{c^2} \mathbf{H}, \tag{1.1}$$

where $\varepsilon(\mathbf{r})$ and $\mathbf{H}$ are the dielectric function and magnetic field respectively and ω is the frequency. The dielectric constant in a photonic crystal is periodic and can therefore be written as $\varepsilon(\mathbf{r}) = \varepsilon(\mathbf{r} + \mathbf{R})$, where $\mathbf{R}$ is a set of lattice vectors. To describe wave propagation in such periodic structures, Bloch's theorem can be applied. For a photonic crystal this takes the form [11]

$$\mathbf{H}(\mathbf{r}) = e^{i\mathbf{k}\cdot\mathbf{r}} \mathbf{H}_{n,\mathbf{k}}(\mathbf{r}), \tag{1.2}$$

where $\mathbf{k}$ is the Bloch wavevector and $\mathbf{H}_{n,\mathbf{k}}$ is a periodic function. The labelled n represents the different bands or modes that exist for the Bloch wavevector $\mathbf{k}$. Based on Bloch's theorem, the modes at $\mathbf{k}$ and $\mathbf{k} + \mathbf{G}$ are identical, where $\mathbf{G}$ represents a reciprocal lattice vector and satisfies $\mathbf{G} \cdot \mathbf{R} = 2m\pi$. Thus by considering only the wavevectors $\mathbf{k}$ in the first Brillouin zone we can map out all of the frequencies that are solutions of Eq.(1.1).

The eigenvalues of Eq.(1.1) can be written as $\omega_n^2(\mathbf{k})$ and for all real values of $\mathbf{k}$ they determine the frequencies that can propagate within the photonic crystal. The photonic bandgap is defined as a range of frequencies for which no propagating solutions exist. However, when complex values of $\mathbf{k}$ are considered, then solutions for ω can be found within the bandgap. The imaginary part of $\mathbf{k}$ indicates that the wave has an exponentially growing or decaying amplitude. In such photonic bandgap materials, if a defect is fabricated, light can then be trapped or guided along the defect for frequencies within the bandgap of the surrounding material. The bandgap prevents propagation into the surroundings and the trapped mode has an exponentially decaying amplitude away from the defect.

1.3 Photonic crystal fibres

One of the most promising applications of photonic crystals is the photonic crystal fibre (PCF). These have a two-dimensional variation of the dielectric constant in the transverse plane perpendicular to the direction of light propagation. Photonic crystal fibres were first demonstrated in 1996 [12] (as shown by A(1) in Fig.1.1).

In this structure the solid central defect is surrounded by a periodic arrangement of air holes in the form of a triangular lattice. Light propagation is confined by total internal reflection (TIR) in the transverse plane but is free to propagate along the length of the fibre. The guidance mechanism in this case is the same as that for a conventional optical fibre.

The first bandgap-guiding PCF was reported in 1999 [13] (as shown by A(2) in Fig.1.1). This hollow-core fibre consisted of a central air hole (i.e. a 'defect'), surrounded by a periodic structure of air holes in glass. The central core has a low refractive index, and therefore the fibre must guide light by a different physical mechanism compared to conventional fibres and solid-core PCFs. Because of the periodic dielectric structure of the cladding, a photonic bandgap is created which prohibits light propagation into the cladding in the transverse plane. Light launched into the central defect is guided and travels along the fibre.

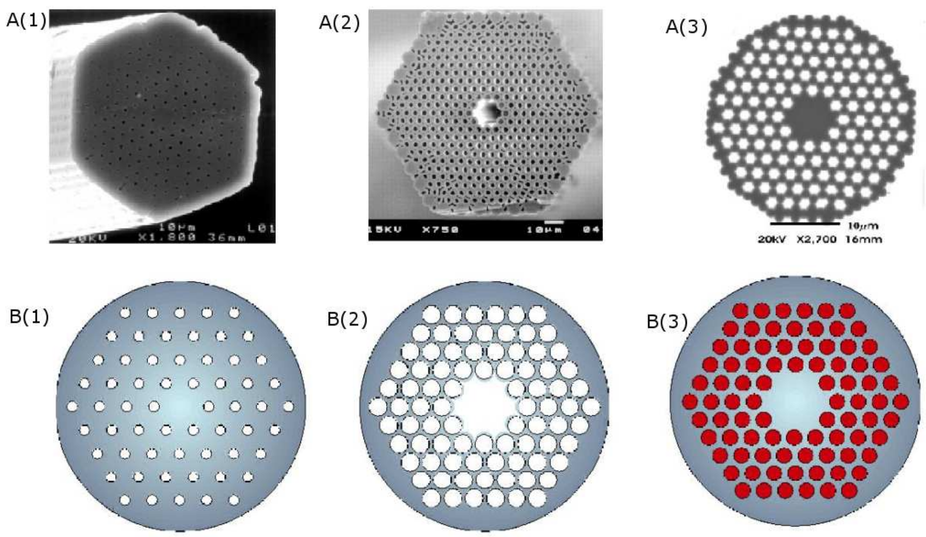

Figure 1.1: SEM micrographs A(1-3) and schematic diagrams B(1-3) of typical PCF structures in the cross-sectional plane. The left figures, A(1) and B(1), show an index-guiding PCF, which has a pure silica core surrounded by a lower-index cladding. The middle figures, A(2) and B(2), show a hollow-core PCF, in which the central defect is an air hole. The right figures, A(3) and B(3), shows an all-solid PCF, where the cladding has raised-index materials. In the schematic diagrams, the grey area represents silica glass (refractive index $n \approx 1.5$), the white area represents air (n=1.0), and the red area represents doped silica glass. Figures taken from those given in [12–15].

Compared with conventional fibres and PCFs with a solid central defect, hollow-core PCFs have several advantages. They can guide light with lower nonlinear effects [16, 17] and with a higher damage threshold [18, 19]. The optical nonlinearities are about 1,000 times lower than those in conventional fibres with solid cores [17]. Because the guidance mechanism depends on the photonic bandgap in the cladding rather than the refractive index of the core, they open the potential application to fill the central air hole with a gas or liquid. Hollow-core PCF filled with Xenon gas can support megawatt optical solitons due to the very small nonlinearity and the broad transmission band with anomalous dispersion [17]. On the other hand, the efficient laser-gas nonlinear interaction can also be achieved. For example, a stimulated Raman scattering in hydrogen-filled hollow-core PCFs was reported, and the threshold is two orders of magnitude lower than previous results [20].

Although the main focus of this thesis is on a novel guidance mechanism existing in hollow-core PCFs, it is useful to realise the significance of PCFs by introducing some typical index-guiding PCFs.

1.3.1 Endlessly single mode

Fibres which only allow the fundamental mode to travel for a given wavelength are called ‘single mode fibres’. The number of guided modes in conventional fibres is determined by the parameter [21]

$$V = (2\pi\rho/\lambda)(n_{co}^2 - n_{cl}^2)^{\frac{1}{2}}, \tag{1.3}$$

where ρ is the core radius, and n_{co} and n_{cl} are refractive indices of the core and cladding, respectively. For single-mode propagation in conventional fibres, V should be less than 2.405. Because of the inverse relationship between V and λ, single-mode conventional fibres will become multi-mode if the wavelength λ is small enough. Thus it is impossible for the conventional fibres to guide a single mode over a large range of wavelengths.

In contrast to conventional fibres, the equivalent parameter for index-guiding PCFs is [22]

$$V = (2\pi\Lambda/\lambda)(n_{co}^2 - n_{eff}^2)^{\frac{1}{2}}, \tag{1.4}$$

where Λ is the pitch between the nearest centres of the air-holes and n_{eff} represents the effective index for the cladding. The refractive index of the core is constant and same as that for conventional fibres, but the cladding effective index

n_{eff} is variable and is determined by the ratio d/Λ, where d is the diameter of the holes. A large n_{eff} value (i.e. small air-filling fraction) can reduce V for a short wavelength λ; this property allows for single mode propagation over a broad range of wavelengths, i.e. endlessly single mode fibres.

1.3.2 Large mode area

For conventional fibres, the number of guided modes is determined by the ratio of the core radius to wavelength, i.e. Eq.(1.3). If the core radius is increased, the number of modes increases and therefore single mode guidance and large mode area are incompatible. However, in single mode PCFs, the number of modes depends on the dimensionless ratio of the hole diameter to the distance between the centres of the neighbouring holes [22, 23]. This enables single mode PCFs to be fabricated with a large mode area.

Because the intensity of optical power is reduced by a large guidance area, this type of fibre therefore has a weaker nonlinear effect and a higher damage threshold. The PCF's combined properties of 'endlessly single mode' and 'large mode area' play an important role in the fabrication of high power fibre lasers and amplifiers. Single mode PCFs with a large mode area have been fabricated with a core diameter about $20\mu m$ [23, 24].

1.3.3 High numerical aperture

Numerical aperture is an important factor which determines the light capture for optical fibres. A fibre with a high numerical aperture can have many promising applications such as in high-power fibre lasers [25, 26]. The normal definition of numerical aperture (NA) is

$$NA = \sqrt{n_{co}^2 - n_{cl}^2}, \tag{1.5}$$

where n_{co} and n_{cl} are the refractive indices of the core and cladding respectively. Because of the large contrast between the core and the cladding, PCFs can provide very large numerical aperture. The numerical apertures in PCFs approaches about 0.9 [27], a much higher value than that for conventional fibres. The fibres with a high NA value can guide a larger number of modes and decrease the bend loss.

1.3.4 High birefringence

PCFs can be made into high modal birefringence fibres. The birefringence is defined by using polarisation beat length L_B and given as [28]

$$L_B = \frac{2\pi}{\beta_x - \beta_y} = \frac{\lambda}{n_x - n_y}, \tag{1.6}$$

where β_x and β_y are the propagation constants of two modes, n_x and n_y are the effective refractive indices for each mode, and λ is the wavelength. A small L_B value represents a large difference between the propagation constants, and therefore a high birefringence.

Compared with conventional fibres, PCFs can exhibit a strong birefringence. Both for index-guiding [28–30] and for bandgap-guiding [31] PCFs, a strong birefringence of the order $\Delta n = 10^{-3}$ can be achieved.

1.4 Thesis outline

The thesis is organised as follows. Chapter 2 describes the governing equations in PCFs. From Maxwell's equations, the vector wave equations for PCFs are derived. Particularly, the scalar approximation is also discussed. The importance of the scalar approximation is that it can serve as an important step in modelling and analysing the guidance of PCFs. In most current modelling of PCFs, a direct step is taken from the vector governing equations to the propagation constant and field solutions. The results are useful, but it is difficult to gain an understanding of the details of the guidance (such as the mode interactions). By employing both scalar and vector equations, the modelling can be divided into several parts, which are important in the analysis and design of PCFs. This point of view is developed here, and will be demonstrated in detail in the following chapters by using the boundary element method and perturbation methods. In the end of this chapter, we briefly review several of the most widely used theoretical methods.

Chapter 3 concerns the guidance mechanism in PCFs, which is fundamental in the modelling and analysis. The two guidance types in PCFs are explained and contrasted with the guidance for conventional fibres. Furthermore, the photonic band structure and density of states are introduced as a means to examine the type of guidance.

Chapter 4 focuses on the guidance mechanism operating in hollow-core PCFs. We first review the fibre structure and corresponding guidance properties in hollow-core bandgap-guiding PCFs. Two recently reported new types of PCFs are then compared with bandgap-guiding PCFs in terms of both structural and optical characteristics. The unique performance and novel guidance mechanism they display are discussed. Our model PCF structure is introduced; this will form the basis of the analysis in the thesis. The outline of the methods we use to understand and model this new type of guidance is also introduced.

Chapter 5 presents the derivation of the boundary element method for solving Maxwell's equations in PCFs. This method provides a powerful tool to support the modelling of our PCF structures. Both vector and scalar cases are discussed. Matrix expressions, from which the propagation constants and fields can be obtained, are presented.

Chapter 6 presents boundary element calculations for rectangular hollow-core PCFs based on the derivation in Chapter 5. The modelling methods are described and exemplified through a model calculation. The convergence and efficiency of the boundary element method are tested in solving for our PCF structures. Calculations are performed for a set of different model PCF structures, and we compare the difference between the ideal and realistic structures, and the dependence of the thickness of the cladding on the guidance.

In Chapter 7 we derive an analytic method to analyse guidance in an idealised rectangular hollow-core PCF structure. By employing the scalar governing equation and assuming the existence of high-index intersections of the glass strips, the transverse field is separated into two orthogonal directions. A transfer matrix method is described to solve for the modes of the perfect cladding, a structure with a defect and a supercell geometry. Within the supercell geometry, a method is presented to construct a full set of modes, which are used in a perturbation analysis in later chapters.

Chapter 8 presents results based on the analytic method derived in Chapter 7. The guidance mechanism for rectangular hollow-core PCFs is discussed by investigating the distribution of photonic bandgaps and the occurrence of guided modes. For a given frequency, both air-guided and glass-guided modes are found within a supercell geometry. The characteristics of the fields are analysed and discussed.

In Chapter 9 we extend the analysis of Chapters 7 and 8 by including the elements of real PCF structures that are neglected in the analytic calculations. A perturbation approach is described and matrix expressions for the vector governing equations in the realistic structure are obtained. Expressions for the imaginary part of the propagation constant of the fundamental guided mode are derived by introducing the photonic density of states and Green's functions.

Chapter 10 gives the results of the perturbation calculation for the modes of the supercell geometry derived in Chapter 8, based on the theory developed in Chapter 9. The general interaction of the modes is discussed by analysing the perturbation matrix. The perturbed modes are investigated with respect to the propagation constant and field profile. We also demonstrate how to calculate the attenuation through perturbation methods.

In Chapter 11 we investigate the dependence of attenuation on the frequency and fibre parameters in rectangular hollow-core PCFs by using the perturbation calculation developed in Chapter 10. The results are compared with the boundary element calculations developed in Chapters 5 and 6 and experimental results.

Chapter 12 is the conclusion of this thesis. The guidance mechanism due to the weak interaction of guided modes in PCFs is explained. Suggestions for fibre optimisation and the further development of our work are also discussed.

Chapter 2

The governing equations

In this chapter we discuss the equations which govern the propagation of light in PCFs. A variety of methods have been developed in recent years to solve these equations. These methods are also briefly reviewed.

2.1 Maxwell's equations

Maxwell's equations provide the fundamental description of electromagnetism, which includes the propagation of light in PCFs. The differential formulation is given by [21]

$$\nabla \cdot \mathbf{B} = 0 \tag{2.1}$$

$$\nabla \cdot \mathbf{D} = \rho \tag{2.2}$$

$$\nabla \times \mathbf{E} = -\frac{\partial \mathbf{B}}{\partial t} \tag{2.3}$$

$$\nabla \times \mathbf{H} = \mathbf{J} + \frac{\partial \mathbf{D}}{\partial t}, \tag{2.4}$$

where $\mathbf{E}$ and $\mathbf{H}$ are electric and magnetic fields, $\mathbf{D}$ and $\mathbf{B}$ are the electric displacement field and the magnetic flux density, and ρ and $\mathbf{J}$ are the electric charge density and the electric current density. PCFs are source-free regions for light propagation, thus we have $\rho = 0$ and $\mathbf{J} = 0$.

For a linear, isotropic medium, the relationship between **D** and **E** is

$$\mathbf{D} = \varepsilon_r \varepsilon_0 \mathbf{E}, \tag{2.5}$$

where ε_0 is the permittivity of free space and ε_r is the dielectric constant, which is related to the refractive index n by $\varepsilon_r = n^2$ at optical frequencies. The relationship between **B** and **H** for a non-magnetic material is given by

$$\mathbf{B} = \mu_0 \mathbf{H}. \tag{2.6}$$

The time dependence of the electric and magnetic fields can be expressed as

$$\mathbf{E}(\mathbf{r}, t) = \mathbf{E}(\mathbf{r})e^{-i\omega t} \tag{2.7}$$

$$\mathbf{H}(\mathbf{r}, t) = \mathbf{H}(\mathbf{r})e^{-i\omega t}. \tag{2.8}$$

In Cartesian coordinates, we assume that the light is guided along the fibre in the z direction. The fibre is assumed to be uniform in this direction, and so the dielectric constant varies only in the transverse (x, y) plane. The fields in Eqs.(2.7) and (2.8) can be written in a separable form

$$\mathbf{E}(\mathbf{r}) = \mathbf{E}(x, y, z) = \mathbf{e}(x, y)e^{i\beta z} \tag{2.9}$$

$$\mathbf{H}(\mathbf{r}) = \mathbf{H}(x, y, z) = \mathbf{h}(x, y)e^{i\beta z}, \tag{2.10}$$

where β is defined as the propagation constant.

The field expressions in Eqs.(2.9) and (2.10) are now substituted into Maxwell's equations, Eqs.(2.1) to (2.4), to give following expressions

$$(\nabla_t^2 + n^2 k_0^2 - \beta^2)\mathbf{e} = -(\nabla_t + i\beta\hat{\mathbf{z}})\mathbf{e} \cdot \nabla_t \ln n^2 \tag{2.11}$$

$$(\nabla_t^2 + n^2 k_0^2 - \beta^2)\mathbf{h} = [(\nabla_t + i\beta\hat{\mathbf{z}}) \times \mathbf{h}] \times \nabla_t \ln n^2, \tag{2.12}$$

where $k_0 = 2\pi/\lambda$ and λ is the vacuum wavevector, ∇_t represents the transverse components of ∇, so ∇_t^2 has the form $\partial^2/\partial x^2 + \partial^2/\partial y^2$. The logarithmic derivative of the dielectric function, $\nabla_t \ln n^2$, arises from $\nabla_t(\varepsilon_r^{-1})$, which is produced by the combination of the time-independent expressions of Eqs.(2.3) and (2.4). If the refractive index consists of piecewise constant terms, for example, glass and air regions, then this term acts only at the boundaries. The transverse part of

Eqs.(2.11) and (2.12) in the (x, y) plane then can be written as

$$(\nabla_t^2 + n^2 k_0^2 - \beta^2)\mathbf{e}_t = -\nabla_t(\mathbf{e}_t \cdot \nabla_t \ln n^2) \tag{2.13}$$

$$(\nabla_t^2 + n^2 k_0^2 - \beta^2)\mathbf{h}_t = (\nabla_t \times \mathbf{h}_t) \times \nabla_t \ln n^2. \tag{2.14}$$

Eqs.(2.13) and (2.14) are the wave equations for the transverse electric and magnetic fields in PCFs. It is conventional to solve Eq.(2.14) rather than Eq.(2.13). The reason is that, in the transverse plane, the magnetic fields match directly at the boundaries of regions with different refractive indices, whereas the electric field is discontinuous. We therefore treat Eq.(2.14) as being the fundamental equation for light propagation in PCFs.

Once $\mathbf{h}_t$ has been calculated, all the other field components can be obtained from the following relations [21]

$$h_z = \frac{i}{\beta}\nabla_t \cdot \mathbf{h}_t \tag{2.15}$$

$$e_z = i\left(\frac{\mu_0}{\varepsilon_0}\right)^{\frac{1}{2}} \frac{1}{k_0 n^2}\hat{\mathbf{z}} \cdot \nabla_t \times \mathbf{h}_t \tag{2.16}$$

$$\mathbf{e}_t = -\left(\frac{\mu_0}{\varepsilon_0}\right)^{\frac{1}{2}} \frac{1}{k_0 n^2}\hat{\mathbf{z}} \times \{\beta \mathbf{h}_t + i\nabla_t h_z\}. \tag{2.17}$$

2.2 Scalar approximation

The scalar approximation simplifies the vector governing equations Eqs.(2.13) and (2.14) into Helmholtz equations

$$(\nabla_t^2 + n^2 k_0^2 - \beta^2)\mathbf{e}_t = 0 \tag{2.18}$$

$$(\nabla_t^2 + n^2 k_0^2 - \beta^2)\mathbf{h}_t = 0. \tag{2.19}$$

When applied to low-index cladding PCFs (i.e. the refractive index of the core is larger than the average of the cladding), this method can be used to introduce an effective index of the cladding with respect to the value of the refractive indices and their fractional areas [22]. After this treatment, the cladding can be viewed as a uniform medium. The effective cladding index can be defined by [22]

$$n_{eff} = \beta_{FSM}/k_0, \tag{2.20}$$

where β_{FSM} is the maximum propagation constant in the cladding (FSM refers to the fundamental space filling mode). These cladding modes can be found by the boundary condition that the normal derivative at the boundary of the unit cell is zero, where a 'unit cell' is the smallest unit repeating at regular intervals in the formation of the cladding structure [22, 32]. This method for analysing index-guiding PCFs is called the 'effective index approach' in some reviews [32, 33]. The scalar approximation is also useful for the analysis of bandgap-guiding PCFs because it makes analysis easier and improves the efficiency of calculations. It is accurate when the index contrast is low, but it also shows the correct qualitative behaviour for a wide range of PCF structures [34].

This point will be developed in greater depth later in this thesis. In our analysis of rectangular hollow-core PCFs we will show that the scalar approximation allows for an analytic solution that shows for certain PCF structures localised guided modes can exist without the need for a bandgap in the cladding. The vector terms presented in Eq.(2.14) can then be treated as a perturbation on the scalar solutions. As we will show, this can provide an insight into the guidance mechanism that could not be provided just with numerical solutions of Eq.(2.14).

2.3 Modelling of PCFs

In the previous section, the governing equations for PCFs have been described. In this section, we introduce a number of methods used in PCF simulations. PCF modelling plays a critical role in the analysis and design of fibres. Modelling work is economical and efficient in contrast to experimental work in finding optimised structures for guidance. It can provide important information on the properties of PCFs (such as the location of photonic bandgaps), which can lead to an improved understanding of the guidance mechanism. Another important point is that, without the restriction of experimentally realistic conditions, novel guidance structures can be designed and these can drive the development of fabrication in new directions. This point will be discussed future in our analysis of Kagome PCFs in Chapter 4.

2.3.1 Plane wave method

The plane wave method provides an accurate method to calculate the properties of PCF structures. In this application, the dielectric constant and field are expanded as sums of plane waves [35]

$$n^2(\mathbf{r}) = \sum_{\mathbf{G}} n^2_{\mathbf{G}} e^{i\mathbf{G}\cdot\mathbf{r}} \tag{2.21}$$

$$h^i(\mathbf{r}) = \sum_{\mathbf{G}} h^i_{\mathbf{k},\mathbf{G}} e^{i(\mathbf{k}+\mathbf{G})\cdot\mathbf{r}}, \tag{2.22}$$

where $\mathbf{k}$ and $\mathbf{G}$ are the Bloch wavevector and reciprocal lattice vector in the transverse plane respectively, and i represents x and y field labels. These forms contain plane waves $e^{(i\mathbf{G}\cdot\mathbf{r})}$, where $\mathbf{G}$ is a set of reciprocal lattice vectors. By using these expressions, the vector governing equation Eq.(2.14) can be formulated as a matrix eigenvalue problem.

In order to solve this eigenvalue problem, the matrix can be diagonalised, but this is time consuming because of the large number of elements in the matrix expression. Iterative methods are more effective than diagonalisation in the calculation of the eigenvalues, which correspond to the required guided modes in the analysis of PCFs [35–37]. These iterative methods can be used both for a fixed-frequency [35, 36] and for a fixed-wavevector [37].

Plane wave methods require that the dielectric function should be periodic. This is a good approximation for the cladding of a PCF, but real fibres have a central defect. To deal with this, a supercell structure is constructed in the cross-sectional plane. Each supercell contains a central defect together with the cladding. These supercells are repeated in the transverse plane to form the periodic structure required in the application of the plane wave method. Although the supercell method is efficient in calculations of guided modes, it does not allow for the calculation of confinement loss.

2.3.2 Localised function method

Guided modes in PCFs are localised in the vicinity of the core. Based on this property, the fields can be expanded in terms of a set of orthogonal Hermite-

Gaussian functions, which have the form [38, 39]

$$\phi_{m,n}(x, y) = exp[-(x^2 + y^2)/2\Lambda^2]H_m(x/\Lambda)H_n(y/\Lambda), \tag{2.23}$$

where m, n are the orders, Λ is the pitch of the cladding lattice, and $H_{m/n}$ is the Hermite polynomial. The governing equation for the magnetic field Eq.(2.14) can be expressed as [38, 39]

$$\sum_{k,l} L_{k,l}^{m,n}\mathbf{h}_t^{k,l} = \beta^2\mathbf{h}_t^{m,n}, \tag{2.24}$$

where $\mathbf{h}_t^{m,n}$ is the transverse field in the Hermite-Gaussian expansion, and $L_{k,l}^{m,n}$ is the matrix element corresponding to the terms in Eq.(2.14). Expressions for the matrix elements can be found analytically by expanding the refractive index into Fourier series [39], and further reduced by considering the the parity property of the field symmetry [40]. Finally, by solving this eigenvalue system, the propagation constant and corresponding field profiles can be found for the scalar [38, 40] and vector cases [39, 41].

In the application of localised function methods, the selection and number of the basis functions, and the geometry of the transverse structure are important points that affect the final results. In general, these methods are not efficient or as widely applicable as the plane wave method.

2.3.3 Multipole method

The multipole method can be applied only to PCF geometries based on cylindrical structures, but for these structures they are highly efficient. The electromagnetic field at each circular scatterer is written in terms of cylindrical harmonic functions [42–45]. The longitudinal electric field component e_z for the neighborhood of each scatterer has the form of a Fourier Bessel series [42, 43]

$$e_z = \sum_{m=-\infty}^{\infty}\left[A_m^l J_m(k_t^e r_l) + B_m^l H_m^{(1)}(k_t^e r_l)\right]exp(im\phi_l), \tag{2.25}$$

where A_m and B_m are coefficients, (r_l, θ_l) is a pair of local polar coordinates for the l^{th} cylinder, J_m and $H_m^{(1)}$ are Bessel and Hankel functions of m^{th} order respectively, and $k_t^e = \sqrt{k_0^2 n_e^2 - \beta^2}$ represents the transverse wave vector in a region of refractive index n_e. Inside the scatterer, Eq.(2.25) reduces to

$$e_z = \sum_{m=-\infty}^{\infty} \Big[C_m^l J_m(k_t^s r_l) \Big] exp(im\phi_l), \tag{2.26}$$

where $k_t^s = \sqrt{k_0^2 n_s^2 - \beta^2}$ and n_s is the refractive index for the scatterer. The magnetic field h_z can also be written using similar expressions.

Boundary conditions for the electric and magnetic fields at the edge of the scatterers and the calculation domain are then used to relate the coefficients A_m, B_m and C_m in Eqs.(2.25) and (2.26). These coefficients are determined by the fact that, in the vicinity of the cylinder l, the incident part (i.e. J_m) of the field must be due to the outgoing parts (i.e. $H_m^{(1)}$) from all the other cylinders [46]. A limited number of orders m makes the calculation well converged [44], so that the propagation constant can be obtained by solving a matrix with a relative small number of elements.

2.3.4 Finite Element method

The finite element method is a numerical tool widely used in the analysis of electromagnetic fields and has been applied to a variety of PCF structures [47]. The cross-sectional plane of a PCF is divided into elementary elements (such as triangles or quadrilaterals) and a simple form for the fields is assumed in each element. The division into elements, especially near to the centre of the fibres, should be fine enough for an accurate simulation [48, 49].

The magnetic governing equation, Eq.(2.12) is expressed in a matrix form [50]

$$\big([A] - n_{eff}^2 [B]\big)\{h\} = 0, \tag{2.27}$$

where the eigenvalue $n_{eff} = \beta/k_0$ and eigenvector $\{h\}$ represent the effective index and the magnetic field at the vertices of the element. $[A]$ and $[B]$ are sparse finite element matrices and are expressed in terms of the derivatives of the properties of the edges and nodes of the elements. The propagation constant and the corresponding fields are calculated by solving Eq.(2.27) and taking into account the relevant boundary conditions.

2.3.5 Boundary Element method

The boundary element method can be applied to PCFs that consist of a finite number of regions with different refractive indices [51–54]. In the first step, the Helmholtz equations in each region and their Green's functions are combined to give expressions for the fields. Secondly, Green's second identity is employed to describe the fields using only expressions on the boundaries between regions. In the third step, the boundaries are divided into a number of elements, and the fields are matched at each boundary element, leading to a matrix equation for β. Finally, the propagation constants can be obtained by searching for zero values of the determinant of the matrix. The corresponding magnetic and electric fields can then be found for each value of the propagation constant.

The boundary element method can be applied to a wide variety of PCF structures both for the scalar and vector wave equations. As for the multipole method and finite element method, the domain of the calculation is bounded, so confinement losses can be calculated. Unlike the multipole method, there is no restriction on the shapes of the scatterers. A detailed derivation and application of the boundary element method will be introduced in Chapters 5 and 6 of this thesis.

2.4 Summary

The vector governing equations accurately describe the propagation of light in PCFs, but the complicated format makes it difficult to obtain analytic solutions. The approximate scalar equation can make calculations efficient, but it is not suitable to obtain the high precision. The comparison of vector and scalar methods will be useful in understanding the guidance of PCFs.

The PCF equations can be solved by several methods. The multipole method is straightforward and efficient, but it requires a particular geometry of the fibre. The plane wave method is efficient and accurate, but it only deals with the supercell boundary condition. The finite element method is versatile, but many elements are required to proved an accurate representation of the two-dimensional space occupied by the PCF structures. By comparison, the boundary element method gives the complex propagation constant by calculating only with elements on the boundaries between the materials; it can be widely used for arbitrary fibre configurations.

Chapter 3

Light guidance in PCFs

To guide light along the PCFs' axis, light must be confined within the central defect. This light confinement can be understood by two different physical mechanisms: index guidance and photonic bandgap guidance. These two guidance principles will be discussed in this chapter. A comparison between the guidance of conventional fibres and PCFs is also described.

3.1 Index guidance

The typical index-guiding PCF structure consists of a silica core surrounded by air holes (as shown by B(1) in Fig.1.1), which form a periodic array in the transverse plane. Because the diameter of the air holes is much smaller than the transverse wavelength of light, the air holes in the silica background can be viewed as a homogeneous medium by introducing the effective refractive index. If the refractive index in the core is higher than the effective refractive index of the cladding, light can be guided by the principle of total internal reflection; this is very similar to the guidance mechanism of conventional fibres.

This fundamental mechanism of light reflection and refraction at the interface of two optical materials is shown in Fig.3.1. Light propagation from one medium to another is governed by Snell's law

$$n_1 \sin\theta_1 = n_2 \sin\theta_2, \tag{3.1}$$

where n_1 and n_2 represent the refractive indices of the two materials.

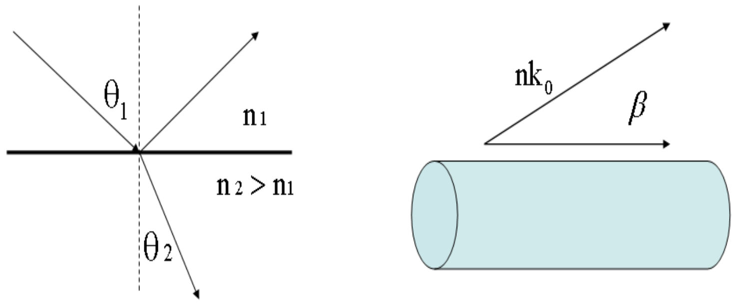

Figure 3.1: Propagation of light in a conventional optical fibre. The left figure shows the reflection and refraction at the interface, the right gives the definition of β in the fibre. n is the refractive index for the corresponding material, and k_0 is the free-space wavevector.

The quantity $\beta = nk_0 \sin\theta$ is conserved within both of the media, where $k_0 = 2\pi/\lambda$ is the free-space wavevector. This conserved quantity is defined as the 'propagation constant'; it is the component of the total wavevector parallel to the direction of propagation. The propagation constant can be used as the criterion for the wave propagation in the materials. The maximum value allowed in a medium with refractive index n is $\beta = nk_0$, and for a given β light can propagate in media where $n > \beta/k_0$.

In order to provide a comprehensive analysis for guidance in a fibre, the media both inside and outside the fibre are included. A comparison of the guidance characteristics of conventional fibres and PCFs is shown in Fig.3.2. For the conventional fibre (the upper part of Fig.3.2), there are four regions corresponding to the ratio of normalised frequency $k_0\Lambda$ (i.e. $\omega\Lambda/c$ in Fig.3.2) and normalised propagation constant $\beta\Lambda$. For an optical material with refractive index n, light can propagate when $n > \beta/k_0$. In region 1 ($\beta/k_0 < 1.0$), light can propagate in air ($n = 1.0$), pure silica ($n = 1.45$) and germanium-doped silica ($n = 1.47$). This case indicates that light can escape outside the fibre. In region 2 ($1.0 < \beta/k_0 < 1.45$), light will propagate in both pure silica and germanium-doped silica. This case has light confined within the fibre, but extending through the core and cladding. In region 3 ($1.45 < \beta/k_0 < 1.47$), the only allowed propagation is in germanium-doped silica. Thus for this region light is confined within the core of the fibre. The point R in region 3 indicates an example of propagation in a real

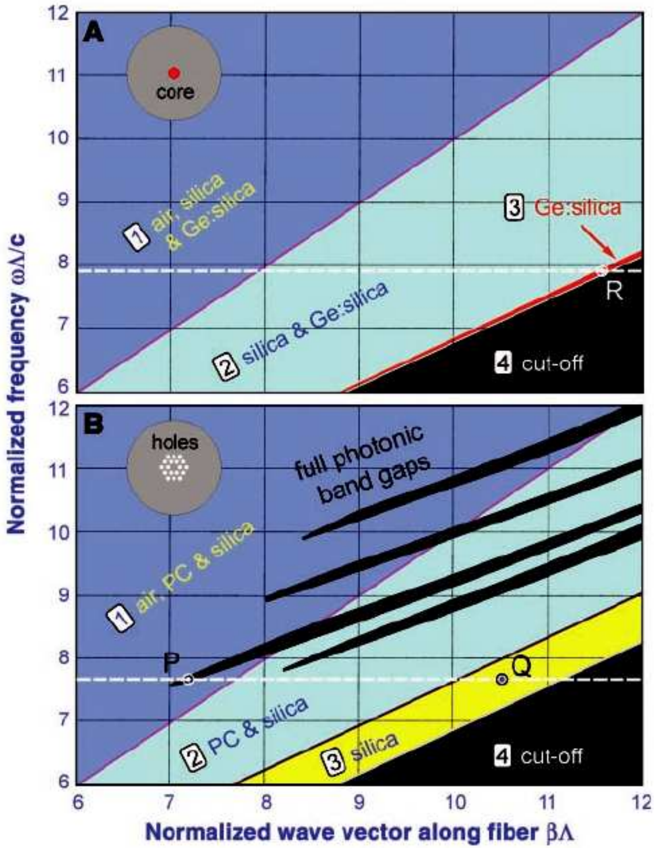

Figure 3.2: Light propagation in a conventional optical fibre (upper figure) and PCFs (lower figure), where the scales are normalised with the pitch Λ. In conventional fibres, the core and cladding are made from germanium-doped silica and pure silica, and their refractive indices are about 1.47 and 1.45 respectively. In the example PCF, the core and cladding are pure silica and there is a triangular array of air holes in the cladding (with 45% air-filling proportion). Points R, Q, P are located at the guidance regions for conventional fibres, index-guiding PCFs and bandgap-guiding PCFs respectively. The different colours in both figures represent the allowed light propagation regions for the optical materials. Figure taken from that given in [55].

application of a conventional fibre. In region 4 ($\beta/k_0 > 1.47$), light propagation is forbidden in all of the materials.

Light propagation in PCFs is presented in the lower part of Fig.3.2. It contains separate regions for the allowed light propagation, which are similar to the diagram for conventional fibres. However, there are two apparent differences between them. The first is that the shape of region 3 in the two figures are different. The second are the 'fingers' that appear and extend to region 1; these are the bandgaps caused by the periodic array of air holes in the PCF cladding, where light propagation is not allowed.

Neglecting for the moment the 'fingers', the analysis of index-guiding PCFs is similar to that of conventional fibres. In region 1 ($\beta/k_0 < 1.0$), light propagates inside and outside of the fibres. In region 2 ($1.0 < \beta/k_0 < n_{eff}$), where n_{eff} has been defined in Eq.(2.20) and represents an effective index for the cladding, light is confined in the fibre but propagates both in the core and in the cladding. In region 3 ($n_{eff} < \beta/k_0 < 1.45$), light can propagate in the silica core but is forbidden in the cladding because the average effective index of cladding is less than 1.45. The point Q in this region denotes a typical propagation constant for index-guiding PCFs. In region 4, no propagation is allowed for any of the materials.

For the index-guiding PCFs, the common feature is a 'low-index cladding', which means that the refractive index in the core is larger than that in the cladding. In contrast to the conventional fibres, index-guiding PCFs have a dependence of the effective refractive index on the diameter and spacing of the air holes. This enables index-guiding PCFs to have different properties than conventional fibres, such as endless single mode behaviour and a large mode area, as discussed in Chapter 1.

3.2 Bandgap guidance

In contrast to index-guiding PCFs, bandgap-guiding PCFs have a low-index core. The central defect can be made from different optical materials. One type are hollow-core PCFs (as shown by B(2) in Fig.1.1), where the cladding is a regular array of air holes separated by thin silica struts, and the central defect is formed by a large air hole. Another type are bandgap-guiding all-solid PCFs (as shown by B(3) in Fig.1.1), where the cladding consists of an array of raised-index rods and the central defect is made from relatively low-index materials [14, 56].

The key feature in understanding bandgap guidance is the 'finger' zones (i.e. photonic bandgaps) shown in the lower part of Fig.3.2. The appearance of a photonic bandgap forbids light at certain values of β to propagate into the cladding region. If the central defect is a large air hole, then for a specific wavevector (as shown by point P), the launched light will be confined in the core but is free to propagate along the fibre axis. This is the bandgap guidance mechanism.

In order to illustrate this confinement in the transverse plane, we simplify the governing equation into a scalar, one-dimensional case, which is governed by

$$[\frac{\partial^2}{\partial x^2} + n^2(x)k_0^2]h(x) = \beta^2 h(x). \tag{3.2}$$

The variation of the dielectric constant $n^2(x)$ and field profile $h(x)$ are illustrated in the schematic diagram shown in Fig.3.3. Based on this figure, we can explain the effect of the fibre structure on the fields and propagation constant. From Bloch's theorem (as discussed in Chapter 1) the solution of Eq.(3.2) has the form

$$h(x + l) = e^{ikl}h(x), \tag{3.3}$$

where l is one-dimensional lattice vector. In the case where there is bandgap guidance, the wavevector k is a complex number in the cladding and can be expressed as $k = k_R + ik_I$. Placing this expression into Eq.(3.3), we have

$$h(x + l) = e^{ik_R l}e^{-k_I l}h(x). \tag{3.4}$$

In an infinitely periodic structure, the complex wave vector does not exist because the wave function will also approach infinity (i.e. $e^{-k_I l} \to +\infty$). However, the existence of the central defect means that these exponentially decaying solutions can exist when there is a photonic bandgap. For some frequencies, there are guided modes with a real β that are localised in the central defect and which decay exponentially when entering the periodic structure of the cladding. This exponential dependence shows that the fields do exist in the cladding, but they are small.

The cross section (including both the central defect and the cladding) of PCFs is also limited in practice, the guided modes will leak outside the boundaries of the PCF. This confinement loss gives rise to a small imaginary part of β in the real fibres [57, 58].

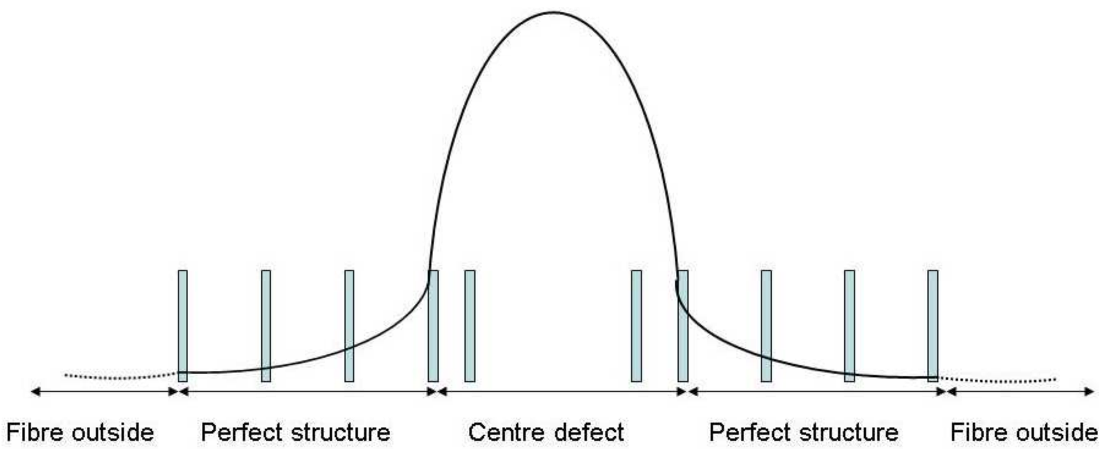

Figure 3.3: Schematic of the wave function in a one-dimensional fibre structure. The continuous line is the wave inside the fibre. The dotted line represents the confinement loss, which results in an imaginary part of β.

Figs.3.2 and 3.3 give a schematic picture of how bandgap-guiding PCF works. However to analysis a specific PCF structure it is important to go beyond a schematic diagram to determine exactly where bandgaps arise and how the design of the central defect affects the guidance of light. The photonic band structure and photonic density of states (PDOS) are important quantities for understanding the details of guidance in particular PCF structures. They are properties of the periodic cladding structure of the PCF, and they provide the means to describe features such as the existence of bandgaps, and their depth and width. Both are based on Bloch's theorem and depend on the solutions $\beta_n(\mathbf{k})$ of Eq.(2.14) as a function of the Bloch wavevector $\mathbf{k}$.

In band structure plots, the β calculation is performed for a given frequency of light along a specific line around the irreducible wedge of the first Brillouin zone. The bandwidth is shown by the range between the maximum and minimum of β along the line, and a bandgap will exist if no wavevector $\mathbf{k}$ can be found to give a particular β value. The photonic density of states is a way to represent the bandstructure for a range of frequencies. To calculate the PDOS for a particular cladding structure, a set of Bloch wavevectors $\mathbf{k}$ is produced by evenly dividing the irreducible zone of the first Brillouin zone into a fine grid. For a given frequency, the β values are calculated for all of these $\mathbf{k}$. The PDOS is defined as the number of states within a small variation of β and can be expressed as [59]

$$\rho(k_0\Lambda, \beta\Lambda) = \sum_{\mathbf{k}} w_{\mathbf{k}} \sum_{i} \delta(\beta\Lambda - \beta_{i\mathbf{k}}\Lambda), \tag{3.5}$$

where i labels the different β values for the wavevector $\mathbf{k}$, $w_{\mathbf{k}}$ is the normalisation weight satisfying $\sum_{\mathbf{k}} w_{\mathbf{k}} = 1$, and δ is the Dirac delta function. If ρ is plotted for a range of β and k_0, the existence of bandgaps becomes very clear; examples are given in references [59–62]. Both band structure [63, 64] and PDOS are widely investigated in PCF research.

3.3 Summary

In this chapter the two guidance mechanisms in PCFs, index guidance and bandgap guidance, have been presented. The comparison of the average refractive indices of the core and cladding plays an important role to differentiate the type of guidance. To characterise bandgap-guiding PCFs, it is useful to examine the photonic band structure or density of states. Guided modes can exist within the bandgap zone, where the photonic density of states is zero.

Chapter 4

Weak interaction guidance

As discussed in the previous chapter, the properties of index-guiding and bandgap-guiding PCFs are now well understood. Recently, a new type of PCF structure, called 'Kagome fibre', has been reported [65, 66]. This exhibits remarkable and distinct optical properties compared to previous PCFs. The Kagome PCF (named after its cladding structure) has a low-index core. Experimentally, they are found to guide light well over a wide range of frequencies, but neither index guidance nor bandgap guidance can explain the mechanism. A novel physical mechanism, which is called 'weak interaction guidance' in this thesis, is required to explain the observed guidance properties. In the remainder of this chapter, hollow-core bandgap-guiding PCFs will be discussed in terms of the exact fibre structures and guidance characteristics. Then two members belonging to the 'weak interaction guidance' family, Kagome and square-lattice hollow-core PCFs, are introduced and their particular structures and guidance properties are discussed. Our model structures, rectangular hollow-core PCFs, are also presented; their fibre structures are formed in a more ideal way compared to reported square-lattice hollow-core PCFs.

4.1 Hollow-core bandgap-guiding PCFs

The basic principle for hollow-core bandgap-guiding PCFs is that the photonic bandgap of the periodic structure of the cladding is used to trap light within the central air defect. But the particular fibre structure significantly affects the guidance properties. In this section, the fibre configurations and corresponding guidance characteristics will be discussed in detail, so that they can be compared with Kagome PCFs later in the chapter.

4.1.1 Fibre structure

For hollow-core bandgap-guiding PCFs, there are several important properties of the fibre structure that affect the guidance performance, such as core radius, thickness of the core wall, cladding geometry, and thickness of the cladding struts. These parameters can be scaled with respect to the wavelength, therefore they can generally describe the guidance of PCFs for different frequencies [67]. A combination of these quantities leads to the ratio between the air and high-index areas in the cladding, which is called the 'air-filling factor' or 'air-filling fraction'. For example, if the cladding structure consists of a triangular lattice of circular holes of diameter D, the air-filling fraction is $(\sqrt{3}\pi/6)(D/\Lambda)^2$ [68], where Λ is the pitch. For circular air holes in a high-index background, the maximum of the air-filling fraction is 0.907, where the hole diameter is same as the pitch. But such an ideal design is impossible to fabricate because the thickness of the glass struts goes to zero. To achieve a higher air-filling fraction, the cladding can be made from rounded hexagons so that the air holes cover the larger area of the unit cell than a circle [68–70].

The central defect of a hollow-core PCF is created by removing a number of unit cell areas, as shown in Fig.4.1. It should be noted that the number of removed cells is not the only criterion to determine the core diameter, and a refined core wall can also vary the core size. The configuration of the core together with the thickness of the core wall is an important factor that affects the guidance of PCFs, as discussed below.

4.1.2 Guidance properties

The photonic bandgap provides the fundamental mechanism in the guidance and is determined by the pattern of the cladding structure. The dependence of the photonic bandgap on the parameters of the cladding structure has been widely investigated [59, 68–71]. For air-silica structures it has been found that the photonic bandgap becomes wider with an increase of the air-filling factor [68, 69].

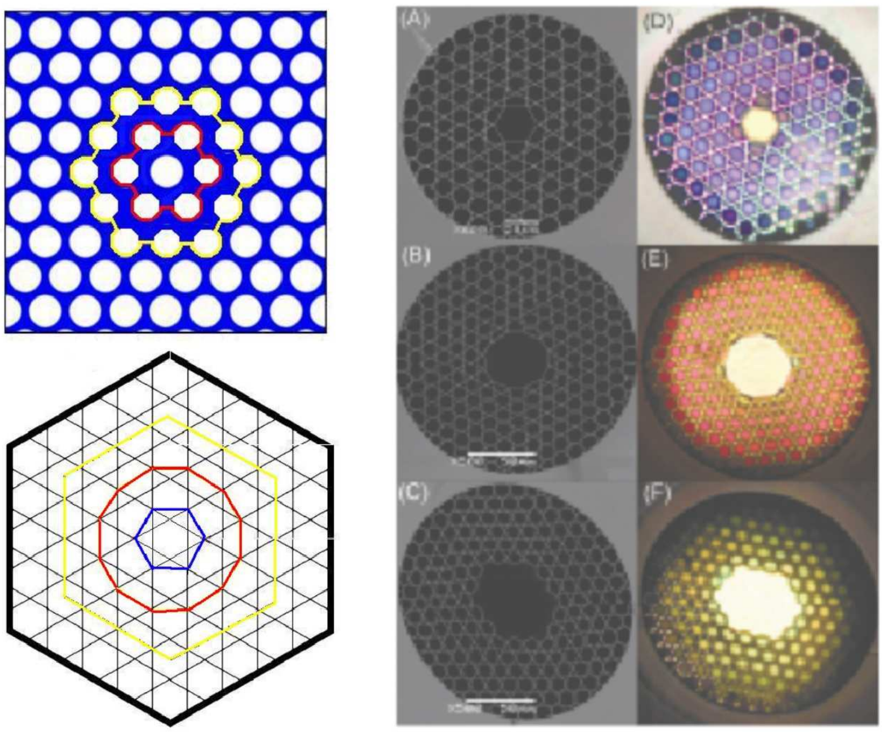

Figure 4.1: The transverse planes of bandgap-guiding hollow-core and Kagome PCFs. The left figures are schematics of the central defect for hollow-core (upper left) and Kagome (lower left) PCFs. The areas enclosed by blue, red and yellow lines show 1-cell, 7-cell and 19-cell central defects. The right figures are a series of Kagome PCFs with different sizes of the central air hole. Figures (A) to (C) are SEM images of 1-cell, 7-cell and 19-cell Kagome PCFs. Figures (D) to (F) are their corresponding light transmission images. The right figures are taken from Ref. [66].

For higher refractive index glasses with $n > 2.0$, Pottage *et al.* found that a new bandgap develops for structures with an air-filling fraction of about 0.6 [59]. However, in this work we will be interested only in structures made from silica glass.

An effect of the air core on the guidance comes from the surface modes that reside near the boundary between the air core and the cladding [72]. These surface modes are bounded modes and are located in the photonic bandgap. They have their intensity localised in the glass struts and decay exponentially both into the core area and the cladding structure [73]. The propagation constant for surface modes can closely approach that of the fundamental air-guided mode and therefore a strong coupling can exist between the two for a narrow range of frequencies [74]. This is referred to as a surface crossing. The attenuation of the surface modes is quite high because of their high energy density in the air-dielectric boundary [75]. These two facts lead to a considerable loss for the fundamental air-guided modes when surface crossings occur.

Based on these considerations, the properties of bandgap-guiding PCFs can be varied by selecting the core radius [73–76], or by designing what is referred to as an antiresonant core surrounding. The thickness of the glass layer closest to the central defect is adjusted to minimise the amplitude of the fundamental guided mode at the air-glass boundary [77–82]. Moreover, for the strength of the bandgap, the optimum hollow-core bandgap-guiding PCF has a high air-filling fraction (usually larger than 0.90) and a thin core wall. For example, recent progress shows a hollow-core PCF with a 7-cell central defect, a pitch of $\Lambda = 6.7\mu m$, and an air-filling fraction of 0.96, which can guide light within a bandgap of approximately $350 - 400nm$ at central wavelength of $1550nm$ and with a low attenuation of about $10dB/km$ [83].

4.2 Kagome PCFs

4.2.1 Kagome PCF structure

The Kagome PCF has a low index air hole in a periodic cladding structure and can be identified as a hollow-core PCF. The cladding is formed from silica struts in an air medium. These interlaced struts run parallel along three different directions at 120° degrees to each other, and each crossing point has four points in close vicinity (as shown in Fig.4.1). Although the struts can be reduced to $290nm$ [65], the occurrence of small air-hole subspaces makes the air-filling fraction of Kagome PCFs a little lower than most hollow-core bandgap-guiding PCFs. The cladding typically has a large pitch of about $12\mu m$ [66] but also can be made with a small pitch of about $6-7\mu m$ [20]. By comparison, the pitch for typical hollow-core bandgap-guiding PCFs varies between $4\mu m$ and $7\mu m$. The central defect in Kagome PCFs is an air hole, which can be fabricated at different sizes. Couny *et al*. report 1-cell, 7-cell and 19-cell Kagome fibres, where the pitch is $11.8\mu m$, $11.5\mu m$ and $10.9\mu m$ respectively and the air-filling fractions are 0.82, 0.83 and 0.85 [66].

4.2.2 Guidance of Kagome PCFs

As a hollow-core PCF, it is obvious that the guidance in Kagome PCF is not dependent on TIR. The investigation of the PDOS therefore becomes crucial to check whether or not it guides light in a photonic bandgap. Fig.4.2 shows a comparison of the PDOS for a representative bandgap-guiding hollow-core PCF (the upper part of Fig.4.2) and a Kagome PCF (the lower part of Fig.4.2).

The plot of the PDOS for a typical hollow-core PCF shows the existence of a photonic bandgap and therefore a guided mode appears within the restricted frequency range of the bandgap zone. However for the Kagome PCF, there is no bandgap over a broad range of normalised frequency. Nevertheless, both experiment and computer simulations show that light can be trapped in the central defect of the Kagome PCF even when there is no photonic bandgap; the bandgap guidance mechanism can not be applied to explain this type of PCF.

By looking at the guidance properties of Kagome PCFs, it has been found that the attenuation characteristics are different from those of bandgap-guiding PCFs. For a 19-cell defect (upper right in Fig.4.3) the two high transmission regions extend about $250nm$ and $700nm$, and two similar regions also appear for the one-cell defect case (lower right in Fig.4.3) [66]. By comparison, the high transmission region for a typical low-loss hollow-core PCF is less than $400nm$. The low loss area is also located at a higher normalised frequency than that for standard bandgap-guiding hollow-core PCFs. The key characteristic of Kagome PCFs is that they can guide over a broader transmission band than other types of PCFs. The

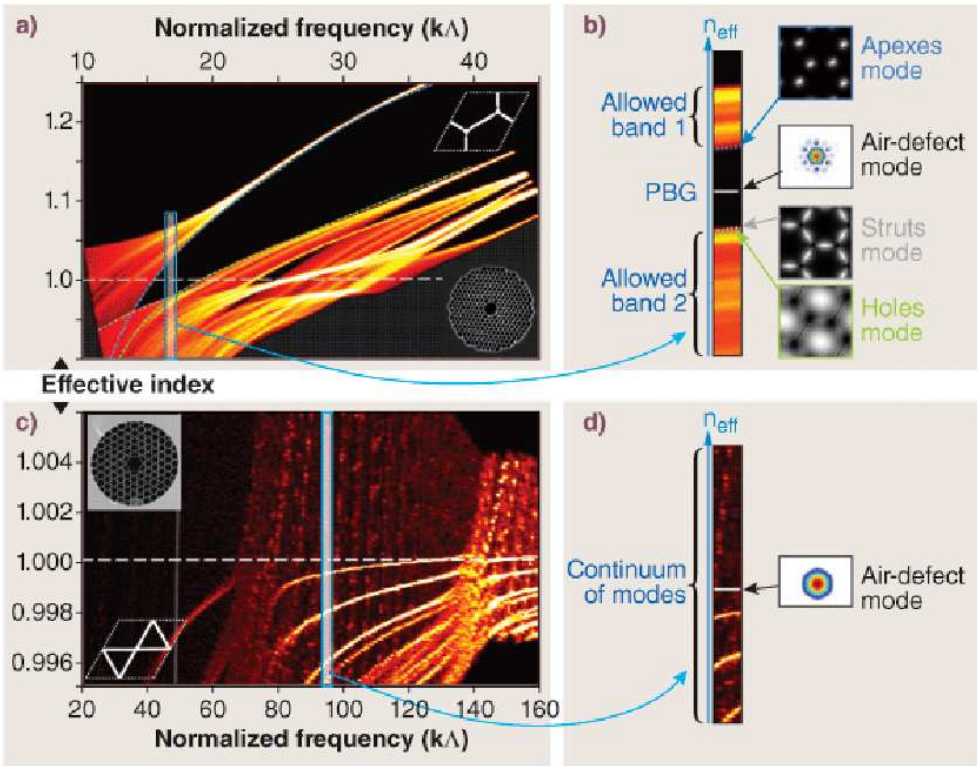

Figure 4.2: Comparison of the PDOS and mode locations between bandgap-guiding (a) and Kagome (c) PCFs together with their transverse structures (inset figures of (a) and (c)). The axes are effective index β/k_0 and normalised frequency $k_0\Lambda$. For a given normalised frequency, all the allowed propagation constants for the central defect and cladding are shown by a light colour (intensity from red (low) to white (high)). The black area represents photonic bandgaps with zero PDOS for the cladding. Figures (a) and (c) show that a photonic bandgap exists in hollow-core PCFs, but there is no photonic bandgap for Kagome PCFs over a large range of frequency. Selected normalised frequencies for hollow-core and Kagome PCFs are shown in (b) and (d) respectively, where modes near to the air-line and their field profiles are plotted. For the hollow-core PCF (b), guided modes exist within the photonic bandgap (i.e. the black area), while cladding modes are located at the edges of the bandgap. For the Kagome PCF (d), the guided modes are located within the photonic bands but they still are well confined within the central air core. Figure taken from Ref. [84].

bandgap in standard hollow-core PCF is centred at about $k_0\Lambda = 20$ (see Fig.4.2), while the guidance in Kagome PCFs can extend to $k_0\Lambda \approx 100$. Although the average attenuation of Kagome PCFs is relatively higher than for current hollow-core bandgap-guiding PCFs, the bandwidth of guidance is several times larger. This unique characteristic makes Kagome PCFs excellent candidates for advances in nonlinear optical effects in gases.

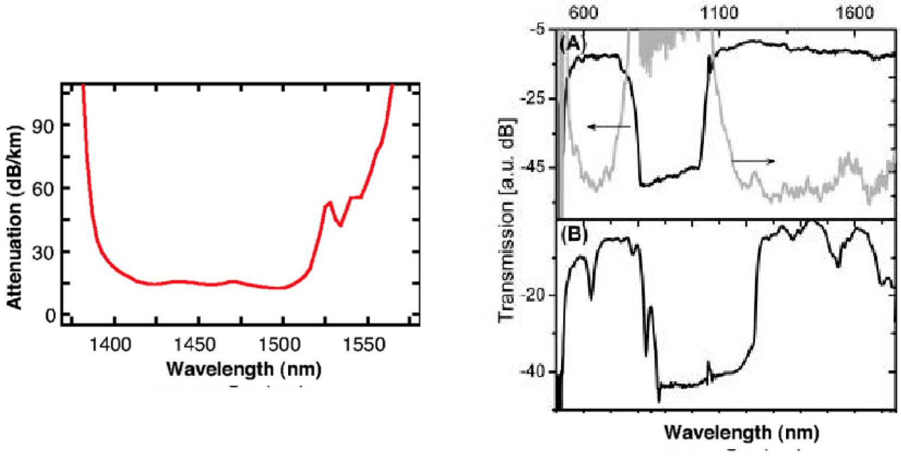

Figure 4.3: Comparison of the experimentally measured attenuation in typical hollow-core and Kagome PCFs. The left figure shows the attenuation in a hollow-core bandgap-guiding PCF [17], for which the diameter of the cental defect and the pitch of nearest air holes are 12.7μm and 4.7μm respectively. The right two figures are the transmission (black line) and attenuation (grey line) for Kagome PCFs [66]. The upper right is for a 19-cell Kagome PCF, and the lower right is for a 1-cell Kagome PCF.

4.2.3 Nonlinear optics in gases

Raman scattering is an inelastic scattering phenomenon of photons by matter. Vibrational energy is transferred to or from a primary pump laser via an intermediate state, which is dipole coupled to the initial and final states [85]. The photons emitted at a higher or lower frequency compared to the pump are called anti-Stokes or Stokes respectively [85]. Spontaneous Raman scattering is a weak process, but stimulated Raman scattering (SRS) is much stronger, and it is possible to transfer 10% or more of the pump energy to the Stokes frequency [86]. By using stimulated Raman scattering (SRS), broadband Raman amplifiers and tunable Raman lasers can be fabricated based on optical fibres [87].

By filling the core of a hollow-core PCF with a gas, the interaction between the guided light and the gas can be substantially enhanced. This leads to a large reduction in the laser power required to observe SRS. Both bandgap-guiding and Kagome hollow-core PCFs have been used in SRS experiments on hydrogen [65,88]. The advantage of the enhanced bandwidth of Kagome PCFs can be seen in the 45 Stokes and anti-Stokes lines observed in Ref. [65], with wavelengths spanning from $325nm$ to $2300nm$. It is believed that all these lines are coherent, which allows the possibility of ultrashort pulse generation.

4.2.4 Weak interaction mechanism

The novel guidance mechanism existing in Kagome PCFs is described as the 'weak interaction mechanism' because of the weak coupling between the fundamental guided mode and the cladding modes [65]. The fast phase oscillation of the cladding modes and the slow spatial variation of the fundamental mode suppresses the interaction between them in the transverse plane and therefore leads to the confinement of light in the centre of the fibres [65].

In Ref. [89], Argyros *et al.* discuss this effect in terms of the mismatch of the propagation constants $\triangle\beta$ between the fundamental guided modes and cladding modes, the PDOS for the cladding modes, and the overlap of the fundamental guided modes and the cladding modes, by comparing these with typical hollow-core bandgap-guiding PCFs. From numerical simulations and comparisons with the previous results, they found that the main contribution to the leakage in Kagome PCFs comes from strut modes due to their β values being close to the fundamental mode. Although the $\triangle\beta$ value for hollow-core bandgap-guiding PCFs is several times larger than that for Kagome PCFs, the overlap of the wavefunctions between the fundamental modes and strut modes in Kagome PCFs is about one magnitude lower than in typical hollow-core bandgap-guiding PCFs [89]. This low level of overlap causes a small perturbation for the guided modes and makes light mainly confined in the central defect [89].

The relationship between the guidance properties and the fibre structure has also been discussed in Ref. [90], where real Kagome PCFs are compared with a simplified model consisting of concentric hexagonal annuli and rings of silica in air. It was found that a uniform strut thickness can make the resonance narrow and minimise the propagation loss [90]. The calculation also indicates that the confinement loss for the real Kagome PCFs are similar when the thickness of the cladding is varied, but for the concentric hexagons and rings the loss is reduced with an increase of the cladding [90]. The reason is that no photonic bandgap exists in Kagome PCFs to reduce the leakage of light within the cladding structure [90].

However, a problem still exists in that these works are largely descriptive and qualitative. They do not really explain why well localised modes can exist in the absence of a bandgap and they do not give a quantitative description for the loss.

4.3 Square-lattice hollow-core PCFs

In recent months, a new type of PCF has been reported [91]. The cladding structure has a square lattice, as shown in left figures in Fig.4.4. The central defect is a large polygon (Fig.4.4 (a)) or an approximate square (Fig.4.4 (b)); these are formed by removing some glass strips or pressurizing the central air hole [91]. The air-filling fraction in these fibres varies from 0.94 to 0.96, which is larger than that for Kagome PCFs (typically 0.82 to 0.85). The calculated PDOS for the square cladding lattice shows similar features to the Kagome structure, indicating that the photonic bands cover a broad range of frequency. The difference from Kagome PCFs is that, the average value of the PDOS is relatively lower [91]. In these fibres, the guided fundamental mode is found to coexist with the cladding modes and the low attenuation of less than $4dB/m$ extends over a wide range of wavelengths, larger than $800nm$. These features indicate that square-lattice hollow-core PCFs guide light with the same mechanism as Kagome PCFs, that is, weak interaction guidance.

In order to understand the guidance in square-lattice hollow-core PCFs, some theoretical work has been performed by either using a finite element solver [91], or employing a simple resonance model in terms of the glass strips [92]. However, as for Kagome PCFs, these provide little insight into why the attenuation has the observed behavior. The main aim of this thesis is an attempt to provide a more quantitative theory of weak interaction guidance. To do this, a model structure different from, but related to, the Kagome and square-lattice PCFs is analysed in the remainder of the thesis. The reason for this is that the model structure allows for an analytic theory and this can provide a greater insight into weak interaction guidance.

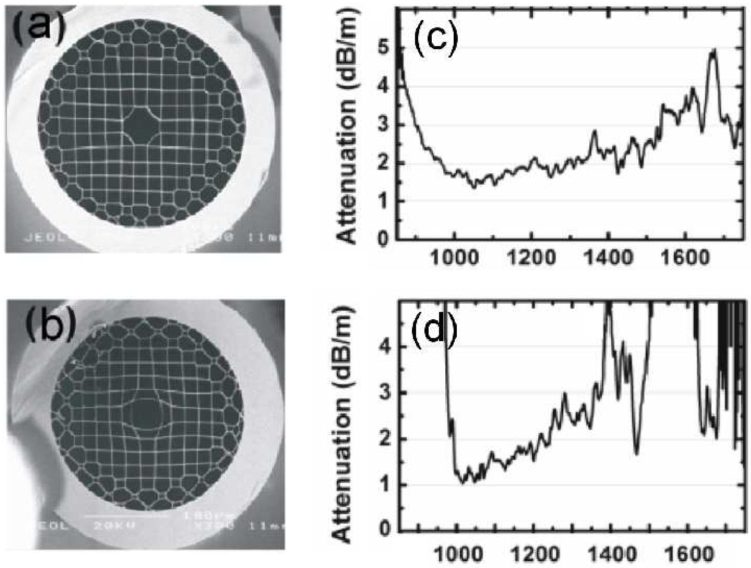

Figure 4.4: Fibre structures and guidance properties of square-lattice hollow-core PCFs. Fibres (a) and (b) have the same structure in the cladding but different configurations of the central defects. Figures (c) and (d) are the plots of the attenuation for fibre (a) (where the max/min of core diameter is $46/39\mu m$, the pitch is $17\mu m$ and the cladding thickness is $310\mu m$) and (b) (where the max/min of core diameter is $42/36\mu m$, the pitch is $17\mu m$ and the cladding thickness is $400\mu m$), respectively. Figures taken from Ref. [91].

4.4 Rectangular model PCFs

In Kagome PCFs, the air subspaces are enclosed by three groups of parallel glass strips. This geometry prevents the governing equations, even in the scalar case, from being separable. We therefore propose a rectangular PCF structure, as shown in Fig.4.5. The cladding structure in our model is the same as the square-lattice hollow-core PCFs reported previously, but the defect is created in a different way. As we shall see, this structure allows for separable solutions and therefore provides the basis for a more quantitative theory of weak interaction guidance.

We consider two slightly different structures in terms of the refractive indices. In both of them the cladding is formed by square regions of air surrounded by thin glass strips. In order to form guided modes in the centre of these structures, we enlarge the size of the central square by moving the four strips which enclose it, by the same and small distance. The positions of the other glass strips are not changed. This movement forms a central defect where modes can be created and guided. The model PCFs have a low-index core and can be viewed as hollow-core

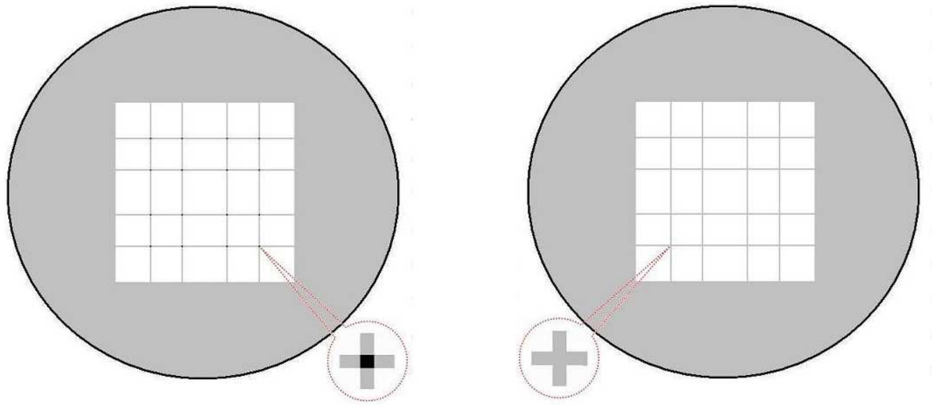

Figure 4.5: Cross-sectional view of the model PCF structures with high-index intersections (left) and without high-index intersections (right). The different colours represent the different refractive indices for the intersections (black), straight strips (gray), and the squares (white). There is a central defect to guide the modes, formed by moving the four glass strips closest to the centre. The left and right pictures are called the 'ideal' and 'real' structures, respectively.

PCFs.

The difference between the two model structures lies in the intersections of the glass strips, as shown in Fig.4.5. In the 'ideal' model structure (left of Fig.4.5), the intersections have a higher refractive index of $\sqrt{2n_g^2 - n_a^2}$ (where n_g and n_a are the indices of the glass strips and air holes, respectively) than the glass strips. The reason for this, as will be discussed in more detail in Chapter 7, is that the scalar governing equation becomes separable. This allows for analytic solutions for the scalar equation and the use of perturbation theory to analyse more realistic structures. The refractive index of the intersections in the 'real' structure (right of Fig.4.5) is equal to that of the strips. This represents a structure that could in principle be fabricated. The perturbation theory we develop in Chapter 9 will start from analytic, scalar solutions of the ideal structure and include the vector terms and the realistic intersections of the real structures.

In all realistic PCF configurations, the cladding is limited in the transverse plane. In our designs, the outside of the cladding area is treated differently based on the different modelling methods. In the boundary element calculations in Chapters 5 and 6, this region is assumed to be made of the same glass as the strips and extends to infinity. In Chapter 7 and 8, an analytic method will be used, based on either an infinite cladding, or a supercell geometry.

4.5 Summary

In this chapter, the structure and guidance characteristics of hollow-core PCFs have been discussed. In contrast to bandgap-guiding PCFs, hollow-core Kagome and square-lattice PCFs exhibit many striking characteristics, including the transverse fibre structure, guidance properties, and nonlinear effects. These phenomena can not be explained by analogy to hollow-core bandgap-guiding PCFs because there is no photonic bandgap in these PCFs. In order to obtain a deeper understanding of the guidance mechanism of this novel PCF family, model structures with a standard shape of the central defect in a rectangular lattice have been proposed. As will be discussed in Chapter 8, this PCF can exhibit photonic bandgaps, but guided modes exist both in the bandgaps and in the bands. Hence, the analysis of model PCF structures will provide an understanding of the guidance mechanism for this new PCF family.

In the following chapters, both numerical and analytic methods are developed and used to solve the ideal (using scalar governing equations) and real (using vector governing equations) model structures. Chapter 5 gives a derivation of the boundary element method for an arbitrary PCF transverse structure. In Chapter 6, this is applied to the model structures, and the guidance characteristics (such as the propagation constant and field profile) are discussed in detail. In Chapters 7 and 8, the scalar approximation is used to model the ideal structure analytically, and the propagation constant, field profiles and PDOS are calculated. In Chapters 9, 10 and 11, a perturbation method is then applied to analyse the properties of the real model structure.

Chapter 5

Boundary element method for PCFs

Boundary element methods are powerful numerical methods for solving systems governed by partial differential equations. They can be applied, for example, to Laplace and Helmholtz equations, where Green's function methods can be applied. In contrast to other numerical methods (e.g. finite element method) the boundary element method has a number of advantages [93, 94]:

1. The problem is solved by employing only the boundary, rather than the whole area. It can be more efficient in computation by using less memory and spending a shorter CPU time.

2. The input data has a reduced dimension, for example, for a two-dimensional system, the boundary is a curve.

3. It is effective when applied in complicated structures with bounded interior domains and an unbounded exterior domain.

The derivation of the boundary element method for PCF structures in this chapter is based on a set of notes written by Professor P. J. Roberts at the Danish Technical University that accompanied a basic set of boundary element codes he had written. Here we give full details of the derivation, which correct some errors in the expressions for the transverse fields and for the high-order derivatives of the Green's functions. The derivation is for a general PCF configuration, where, in the transverse plane perpendicular to the direction of light propagation, the scatterers in the surrounding medium are arbitrarily shaped and have different refractive indices. The PCF governing equations then can be divided into two parts. First, we consider solutions of the Helmholtz equation, for which Green's functions are applied to express the fields. Second we apply boundary conditions to the scatterers. By combining these two parts, the propagation constant and field profiles can be obtained.

The sections in this chapter are organised as follows: In section 5.1, the Green's function and its solution for PCFs are presented. Section 5.2 and 5.3 concern derivations of expressions for the transverse magnetic field far away and near to the boundary, respectively. In section 5.4, we form matrix expressions for the field close to the boundary, which, in section 5.5 are matched according to the electromagnetic boundary conditions. Full expressions for the fields are deduced in section 5.6. In section 5.7, we show simplified expressions for the case of the scalar governing equation. Section 5.8 is the summary of this chapter.

5.1 Green's function for Helmholtz equation

We consider propagation in a PCF structure, which has been discussed in Section 1.3, that is translationally invariant along its length, which is taken to be the z-axis. The transverse plane of PCF is assumed to consist of a set of N scatterers (as shown in Fig.5.1). The refractive indices for the scatterers and surrounding medium are n_j ($j \in [1, N]$) and n_h respectively. A_j (A_h) and C_j (C_h) represent the areas and boundaries for the scatterers (surrounding medium).

The magnetic and electric fields are determined by Maxwell's equations. Based on the previous discussion in Section 2.1, we know that the wave dependence takes the form $e^{i(\beta z-\omega t)}$ along the fibre, in which case Maxwell's equations in each region of the fibre can be reduced to the Helmholtz equation with a complex propagation constant β. In the cross-sectional plane perpendicular to the direction of propagation, the governing equations for the magnetic and electric fields in each region of constant refractive index are same as in the scalar approximation, Eqs.(2.18) and (2.19), and can be written as

$$[\nabla_t^2 + (k_0^2 n^2 - \beta^2)]H_a = 0 \tag{5.1}$$

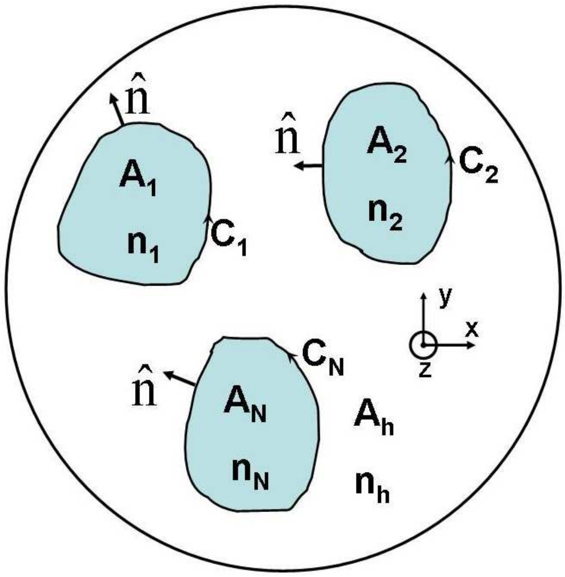

Figure 5.1: Schematic of the scatterers (the dark areas) and surrounding medium (the white area) in the cross-sectional plane. n, A, and C denote the refractive index, area and boundary. The subscripts from 1 to N represent the scatterers, and h represents the surrounding medium.

$$[\nabla_t^2 + (k_0^2 n^2 - \beta^2)]E_a = 0, \tag{5.2}$$

where k_0 is the vacuum wavevector of the light, n^2 is the dielectric constant, β is the propagation constant for the modes of the fibre, a is x or y for the two different components, and $\nabla_t^2 = \partial^2/\partial x^2 + \partial^2/\partial y^2$.

We start by considering the H_x component for region j in Eq. (5.1), which can be written as

$$[\nabla_t^2 + K_j^2]H_x(\mathbf{r}) = 0, \tag{5.3}$$

where $K_j = \sqrt{k_0^2 n_j^2 - \beta^2}$. We now introduce the Green's function $G(\mathbf{r}, \mathbf{r}_0; K_j)$, where $\mathbf{r}_0$ indicates the position of a point source and $\mathbf{r}$ is the variable with respect to which the differentiation is carried out. For each $\mathbf{r}_0$ in the plane, $G(\mathbf{r}, \mathbf{r}_0; K_j)$ satisfies the Helmholtz equation [95, 96]

$$[\nabla_t^2 + K_j^2]G(\mathbf{r}, \mathbf{r}_0; K_j) = \delta(\mathbf{r} - \mathbf{r}_0), \tag{5.4}$$

where $\delta(\mathbf{r} - \mathbf{r}_0)$ is the Dirac delta function. The solution of Eq.(5.4) can be written in terms of Hankel functions as

$$G(\mathbf{r}, \mathbf{r}_0; K_j) = \frac{1}{4i} H_0^{(1)}(K_j|\mathbf{r} - \mathbf{r}_0|), \tag{5.5}$$

where $H_0^{(1)}$ is a Hankel function of zero order and can be written as $H_0^{(1)} = J_0 + iY_0$, where J_0 and Y_0 are Bessel functions.

5.2 Magnetic fields away from the boundary

We can now combine Eqs.(5.3) and (5.4) to express the magnetic fields. Eq.(5.3) is multiplied by $G(\mathbf{r}, \mathbf{r}_0; K_j)$ to give

$$G(\mathbf{r}, \mathbf{r}_0; K_j) \cdot \nabla_t^2 H_x(\mathbf{r}) + G(\mathbf{r}, \mathbf{r}_0; K_j) \cdot K_j^2 H_x(\mathbf{r}) = 0, \tag{5.6}$$

and Equation (5.4) is multiplied by $H_x(\mathbf{r})$ to give

$$\begin{aligned} H_x(\mathbf{r}) \cdot \nabla_t^2 G(\mathbf{r}, \mathbf{r}_0; K_j) + H_x(\mathbf{r}) \cdot K_j^2 G(\mathbf{r}, \mathbf{r}_0; K_j) \\ = H_x(\mathbf{r}) \delta(\mathbf{r} - \mathbf{r}_0). \end{aligned} \tag{5.7}$$

These equations are combined to give

$$\begin{aligned} H_x(\mathbf{r}) \delta(\mathbf{r} - \mathbf{r}_0) = H_x(\mathbf{r}) \cdot \nabla_t^2 G(\mathbf{r}, \mathbf{r}_0; K_j) \\ - G(\mathbf{r}, \mathbf{r}_0; K_j) \cdot \nabla_t^2 H_x(\mathbf{r}). \end{aligned} \tag{5.8}$$

Eq.(5.8) is then integrated over all $\mathbf{r}$ in the j^{th} scatterer to give the magnetic field as

$$\begin{aligned} H_x(\mathbf{r}_0) = \int\int_{A_j} [H_x(\mathbf{r}) \cdot \nabla_t^2 G(\mathbf{r}, \mathbf{r}_0; K_j) \\ - G(\mathbf{r}, \mathbf{r}_0; K_j) \cdot \nabla_t^2 H_x(\mathbf{r})] d\mathbf{r}, \end{aligned} \tag{5.9}$$

where the integral area A_j denotes the j^{th} scatterer or the surrounding medium, as shown in Fig.5.1.

Eq.(5.9) gives the magnetic field as an area integral. In the following steps, we transform it into a line integral along the boundary using Green's second identity. Green's second identity in the two-dimensional region R is expressed as [97]

$$\int\int_R (\varphi \nabla^2 \phi - \phi \nabla^2 \varphi) dx dy = \oint_{\partial R} (\varphi \nabla \phi - \phi \nabla \varphi) \cdot \hat{\mathbf{n}} ds, \tag{5.10}$$

where φ and ϕ are arbitrary functions and the integration on the left is performed over a region R bounded by a closed surface ∂R. The integral on the right is then a surface integral over ∂R, and $\hat{\mathbf{n}}$ is the outward normal to ∂R. In our case

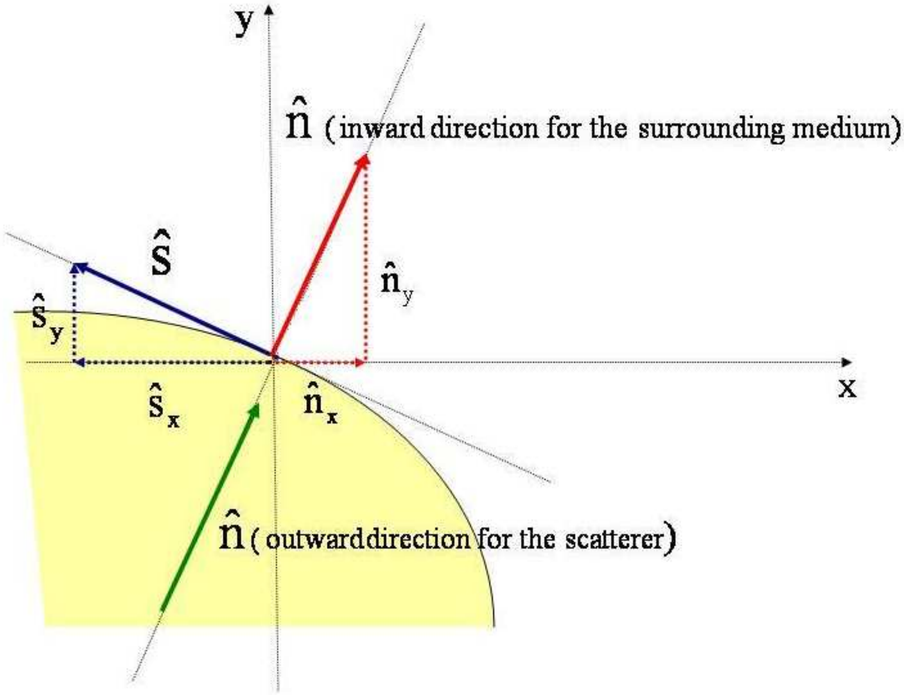

Figure 5.2: The directions of tangent and normal unit vectors for the scatterers (the yellow area) and surrounding medium (the light area). The tangent unit vector $\hat{\mathbf{s}}$ for the scatterers and surrounding medium are same (blue arrow). The normal unit vector $\hat{\mathbf{n}}$ is outward (green arrow) and inward (red arrow) for the scatterer and surrounding medium, respectively.

Green's second identity can be used to give expressions for the scatterers and the surrounding medium respectively:

$$\int\int(\varphi\nabla^2\phi - \phi\nabla^2\varphi)dxdy = \oint(\varphi\frac{\partial\phi}{\partial n} - \phi\frac{\partial\varphi}{\partial n})ds \tag{5.11}$$

$$\int\int(\varphi\nabla^2\phi - \phi\nabla^2\varphi)dxdy = -\oint(\varphi\frac{\partial\phi}{\partial n} - \phi\frac{\partial\varphi}{\partial n})ds. \tag{5.12}$$

where $\partial/\partial n$ represent normal derivatives. The difference between Eq.(5.11) and (5.12) comes from the normal unit vectors $\hat{\mathbf{n}}$, which is outward for the scatterer (shown by a green arrow in Fig.5.2) and inward for the surrounding medium (shown by a red arrow in Fig.5.2).

By using Eqs.(5.11) and (5.12) in Eq.(5.9) we find expressions for the magnetic fields in the j^{th} scatterer and the surrounding medium:

$$\begin{aligned} H_x^{in}(\mathbf{r}_0) = \int_{C_j} & [H_x(\mathbf{r}) \cdot \frac{\partial G(\mathbf{r}, \mathbf{r}_0; K_j)}{\partial n} \\ & - G(\mathbf{r}, \mathbf{r}_0; K_j) \cdot \frac{\partial H_x(\mathbf{r})}{\partial n}] ds \end{aligned} \tag{5.13}$$

$$\begin{aligned} H_x^{out}(\mathbf{r}_0) = -\sum_{k=1}^{N} \int_{C_k} & [H_x(\mathbf{r}) \cdot \frac{\partial G(\mathbf{r}, \mathbf{r}_0; K_h)}{\partial n} \\ & - G(\mathbf{r}, \mathbf{r}_0; K_h) \cdot \frac{\partial H_x(\mathbf{r})}{\partial n}] ds, \end{aligned} \tag{5.14}$$

where N boundaries are included in the calculation of the magnetic field for the surrounding medium. We also note that the argument K_h in the Green's functions in Eq.(5.14) refers to the refractive index of the surrounding medium. Eqs.(5.13) and (5.14) use the solutions on the boundary to express $H_x(\mathbf{r}_0)$ away from the boundary by calculating integrals of the field and Green's function along the interfaces. In the next section, we derive expressions for the field near the boundary, where the influence of $\mathbf{r}_0$ on the derivatives and integrals should be included.

5.3 Magnetic fields near the boundary

In order to match the fields in different regions, we need to express the 'inside' and 'outside' fields very close to the boundary of the scatterers. In this case, the derivation in the previous section is still valid but it needs to be modified by considering the effect as $\mathbf{r}_0$ approaches a boundary.

In Eq.(5.13), when the variable $\mathbf{r}$ approaches $\mathbf{r}_0$, which is located near the boundary C_j, the term involving G behaves smoothly, but the term $\partial G/\partial n$ will produce a singular contribution of $\frac{1}{2}H_x(\mathbf{r}_0)$. This arises from the Plemelj formula, where the integral is performed along a part of the circumference of a circle centred at the point $\mathbf{r}_0$ with an extremely small radius approaching zero. Details are given in references [51] and [98]. Eq.(5.13) then becomes, for $\mathbf{r}_0$ on the boundary of the

j^{th} scatterer,

$$\frac{1}{2}H_x^{in}(\mathbf{r}_0) = P\int_{C_j}[H_x(\mathbf{r})\cdot\frac{\partial G(\mathbf{r},\mathbf{r}_0;K_j)}{\partial n} \\ -G(\mathbf{r},\mathbf{r}_0;K_j)\cdot\frac{\partial H_x(\mathbf{r})}{\partial n}]ds, \tag{5.15}$$

where P denotes that the principal value of integrals is taken [52, 99]. Similarly, for the case of the outer region, the term $\partial G/\partial n$ will produce a contribution of $-\frac{1}{2}H_x(\mathbf{r}_0)$. Eq.(5.14) can then be expressed as

$$\frac{1}{2}H_x^{out}(\mathbf{r}_0) = -\sum_{k=1}^{N}P\int_{C_k}[H_x(\mathbf{r})\cdot\frac{\partial G(\mathbf{r},\mathbf{r}_0;K_h)}{\partial n} \\ -G(\mathbf{r},\mathbf{r}_0;K_h)\cdot\frac{\partial H_x(\mathbf{r})}{\partial n}]ds. \tag{5.16}$$

We now change variables to write our expressions for the fields in a more convenient way. We rewrite $\mathbf{r}_0$ as $\mathbf{r}$ and $\mathbf{r}$ as $\mathbf{r}'$, so Eqs.(5.15) and (5.16) become

$$\frac{1}{2}H_x^{in}(\mathbf{r}) = P\int_{C_j}[H_x(\mathbf{r}')\cdot\frac{\partial G(\mathbf{r}',\mathbf{r};K_j)}{\partial n'} \\ -G(\mathbf{r}',\mathbf{r};K_j)\cdot\frac{\partial H_x(\mathbf{r}')}{\partial n'}]ds' \tag{5.17}$$

$$\frac{1}{2}H_x^{out}(\mathbf{r}) = -\sum_{k=1}^{N}P\int_{C_k}[H_x(\mathbf{r}')\cdot\frac{\partial G(\mathbf{r}',\mathbf{r};K_h)}{\partial n'} \\ -G(\mathbf{r}',\mathbf{r};K_h)\cdot\frac{\partial H_x(\mathbf{r}')}{\partial n'}]ds', \tag{5.18}$$

where $\partial n'$ and ds' correspond to $\mathbf{r}'$. By considering the expression for the Green's function in Eq.(5.5), we can establish the symmetry of the Green's function under the interchange of the field and source variables [100]

$$G(\mathbf{r}_1,\mathbf{r}_2;K_j) = G(\mathbf{r}_2,\mathbf{r}_1;K_j). \tag{5.19}$$

This allows us to write Eqs.(5.17) and (5.18) as

$$\frac{1}{2}H_x^-(\mathbf{r}_p^j) = P\int_{C_j}[H_x(\mathbf{r}')\cdot\frac{\partial G(\mathbf{r}_p^j,\mathbf{r}';K_j)}{\partial n'}$$
$$-G(\mathbf{r}_p^j,\mathbf{r}';K_j)\cdot\frac{\partial H_x(\mathbf{r}')}{\partial n'}]ds' \tag{5.20}$$

$$\frac{1}{2}H_x^+(\mathbf{r}_p^j) = -\sum_{k=1}^{N}P\int_{C_k}[H_x(\mathbf{r}')\cdot\frac{\partial G(\mathbf{r}_p^j,\mathbf{r}';K_h)}{\partial n'}$$
$$-G(\mathbf{r}_p^j,\mathbf{r}';K_h)\cdot\frac{\partial H_x(\mathbf{r}')}{\partial n'}]ds', \tag{5.21}$$

where $H_x^-(\mathbf{r}_p^j)$ and $H_x^+(\mathbf{r}_p^j)$ are used to represent $H_x^{in}(\mathbf{r})$ and $H_x^{out}(\mathbf{r})$, the magnetic field close to the inner and outer boundaries at the point $\mathbf{r}_p$ on the j^{th} scatterer.

The next step is to match the fields inside and outside the boundaries. Before doing this, we transform Eqs.(5.20) and (5.21) into matrix expressions, which are used in practical calculations for the boundary fields.

5.4 Matrix expressions for the boundary fields

In the application of the boundary element method, the interface C_j of the j^{th} scatterer is divided into Q_j elements, which can be expressed as

$$\sum_{q=1}^{Q_j} C_{j,q} = C_j, \tag{5.22}$$

where j is the label of the scatterer and q is the index of the element in the boundary of the scatterer. The key assumption made in the boundary element method is that the magnetic field and its normal derivative do not vary over each boundary element. In practice, this requires that we test that sufficient boundary elements are used to obtain converged results, as will be discussed in Chapter 6. Eq.(5.20) can then be rewritten as

$$\frac{1}{2}H_x^-(\mathbf{r}_p^j) = -\sum_{q=1}^{Q_j}\Big\{\frac{\partial H_x^-(\mathbf{r}_q^j)}{\partial n'}P\int_{C_{j,q}}ds'G\big(\mathbf{r}_p^j,\mathbf{r}';K_j\big)$$
$$-H_x^-(\mathbf{r}_q^j)P\int_{C_{j,q}}ds'\frac{\partial G\big(\mathbf{r}_p^j,\mathbf{r}';K_j\big)}{\partial n'}\Big\}, \tag{5.23}$$

where $\mathbf{r}_p^j$ and $\mathbf{r}_q^j$ are the position vectors for the p^{th} and q^{th} boundary elements in the j^{th} scatterer. Eq.(5.23) can be written in a vector notation as

$$\frac{1}{2}\underline{H}_x^- = -\left[\underline{\underline{G}}_D\frac{\partial \underline{H}_x^-}{\partial n'} - \frac{\partial \underline{\underline{G}}_D}{\partial n'}\underline{H}_x^-\right], \tag{5.24}$$

where the elements of the vectors and matrices are defined as

$$[\underline{H}_x^-]_{jp} = H_x^-(\mathbf{r}_p^j) \tag{5.25}$$

$$\left[\frac{\partial \underline{H}_x^-}{\partial n'}\right]_{jq} = \frac{\partial H_x^-(\mathbf{r}_q^j)}{\partial n'} \tag{5.26}$$

$$\left[\underline{\underline{G}}_D\right]_{jp,kq} = \delta_{j,k}P\int_{C_{k,q}} ds' G(\mathbf{r}_p^j, \mathbf{r}'; K_j) \tag{5.27}$$

$$\left[\frac{\partial \underline{\underline{G}}_D}{\partial n'}\right]_{jp,kq} = \delta_{j,k}P\int_{C_{k,q}} ds'\frac{\partial G(\mathbf{r}_p^j, \mathbf{r}'; K_j)}{\partial n'}. \tag{5.28}$$

The subscript D is used to show that the matrix elements of the Green's function are diagonal in the label of the scatterer. For the surrounding medium, Eq.(5.21) can be expressed in terms of the boundary elements as

$$\begin{aligned}\frac{1}{2}H_x^+(\mathbf{r}_p^j) = \sum_{k=1}^{N}\sum_{q=1}^{Q_k}\Bigg\{&\frac{\partial H_x^+(\mathbf{r}_q^k)}{\partial n'}P\int_{C_{k,q}} ds' G\big(\mathbf{r}_p^j, \mathbf{r}'; K_h\big)\\ &-H_x^+(\mathbf{r}_q^k)P\int_{C_{k,q}} ds'\frac{\partial G\big(\mathbf{r}_p^j, \mathbf{r}'; K_h\big)}{\partial n'}\Bigg\}.\end{aligned} \tag{5.29}$$

Eq.(5.29) can also be expressed in vector form as

$$\frac{1}{2}\underline{H}_x^+ = \left[\underline{\underline{G}}\frac{\partial \underline{H}_x^+}{\partial n'} - \frac{\partial \underline{\underline{G}}}{\partial n'}\underline{H}_x^+\right], \tag{5.30}$$

where

$$[\underline{H}_x^+]_{jp} = H_x^+(\mathbf{r}_p^j) \tag{5.31}$$

$$\left[\frac{\partial \underline{H}_x^+}{\partial n'}\right]_{kq} = \frac{\partial H_x^+(\mathbf{r}_q^k)}{\partial n'} \tag{5.32}$$

$$\left[\underline{\underline{G}}\right]_{jp,kq} = P\int_{C_{k,q}} ds' G(\mathbf{r}_p^j, \mathbf{r}'; K_h) \tag{5.33}$$

$$\left[\frac{\partial \underline{\underline{G}}}{\partial n'}\right]_{jp,kq} = P\int_{C_{k,q}} ds'\frac{\partial G(\mathbf{r}_p^j, \mathbf{r}'; K_h)}{\partial n'}. \tag{5.34}$$

We note that the Green's functions $\underline{\underline{G}}_D$ and $\underline{\underline{G}}$ and their normal derivatives in Eqs.(5.24) and (5.30) can be calculated for any structure by calculating the relevant Green's functions and performing the integrals along the boundaries.

Eqs.(5.24) and (5.30) can be simplified by multiplying by $\underline{\underline{G}}_D^{-1}$ and $\underline{\underline{G}}^{-1}$ respectively to give expressions for the derivative of the magnetic field

$$\frac{\partial \underline{H}_x^-}{\partial n'} = \underline{\underline{G}}_D^{-1}\left[-\frac{1}{2}\underline{\underline{1}} + \frac{\partial \underline{\underline{G}}_D}{\partial n'}\right]\underline{H}_x^- \tag{5.35}$$

$$\frac{\partial \underline{H}_x^+}{\partial n'} = \underline{\underline{G}}^{-1}\left[\frac{1}{2}\underline{\underline{1}} + \frac{\partial \underline{\underline{G}}}{\partial n'}\right]\underline{H}_x^+, \tag{5.36}$$

where $\underline{\underline{1}}$ is the identity matrix. We note that similar equations can be derived for any component of the $\underline{E}$ and $\underline{H}$ fields in the transverse plane.

5.5 Application of the boundary conditions

In the previous section, concise matrix expressions relating the fields and their derivatives have been given in Eqs.(5.35) and (5.36). In this section, the boundary conditions for the vector wave equation will be established and used to derive equations for the field variables.

In the vector governing equations, there are four independent boundary conditions: H_x, H_y, H_z and E_z must all be continuous at every interface. For the magnetic fields H_x and H_y the continuity equations are

$$H_x^+(\mathbf{r}_p^j) = H_x^-(\mathbf{r}_p^j) \tag{5.37}$$

$$H_y^+(\mathbf{r}_p^j) = H_y^-(\mathbf{r}_p^j). \tag{5.38}$$

It is convenient to express the continuity conditions for H_z and E_z in terms of H_x and H_y. H_z has been given in Eq.(2.15) in Section 2.1 and can be written in form

$$H_z = \frac{i}{\beta}\nabla_t \cdot \mathbf{H}_t(\mathbf{r}), \tag{5.39}$$

where t represents the transverse component. The boundary condition for H_z is therefore given by

$$\hat{\mathbf{n}}_p^j \cdot \frac{\partial \mathbf{H}^-(\mathbf{r}_p^j)}{\partial n} + \hat{\mathbf{s}}_p^j \cdot \frac{\partial \mathbf{H}^-(\mathbf{r}_p^j)}{\partial s} = \hat{\mathbf{n}}_p^j \cdot \frac{\partial \mathbf{H}^+(\mathbf{r}_p^j)}{\partial n} + \hat{\mathbf{s}}_p^j \cdot \frac{\partial \mathbf{H}^+(\mathbf{r}_p^j)}{\partial s}, \tag{5.40}$$

where $\partial/\partial s$ represents a derivative along the boundary element, and $\hat{\mathbf{n}}_p^j$ and $\hat{\mathbf{s}}_p^j$, which are shown as $\hat{\mathbf{n}}$ and $\hat{\mathbf{s}}$ in Fig.5.2, are unit vectors normal and tangential to the boundary respectively at point $\mathbf{r}_p$ on the j^{th} scatterer. Because the $\mathbf{H}$ fields match across the boundary, the derivatives along the boundary must be the same in the inner and outer areas. Thus we can reduce Eq.(5.40) to

$$\hat{\mathbf{n}}_p^j \cdot \frac{\partial \mathbf{H}^-(\mathbf{r}_p^j)}{\partial n} = \hat{\mathbf{n}}_p^j \cdot \frac{\partial \mathbf{H}^+(\mathbf{r}_p^j)}{\partial n}. \tag{5.41}$$

The expression for E_z shown in Eq.(2.16) in Section 2.1 is rewritten as

$$E_z(\mathbf{r}) = i(\frac{\mu_0}{\varepsilon_0})^{\frac{1}{2}} \frac{1}{k_0 n^2} \hat{\mathbf{z}} \cdot \nabla_t \times \mathbf{H}_t(\mathbf{r}), \tag{5.42}$$

and, by using

$$\nabla_t \times \mathbf{H}_t = (\frac{\partial H_y}{\partial x} - \frac{\partial H_x}{\partial y})\hat{\mathbf{z}}, \tag{5.43}$$

the matching condition becomes

$$\begin{aligned} &\frac{1}{n_j^2}\left[\hat{\mathbf{s}}_p^j \cdot \frac{\partial \mathbf{H}^-(\mathbf{r}_p^j)}{\partial n} - \hat{\mathbf{n}}_p^j \cdot \frac{\partial \mathbf{H}^-(\mathbf{r}_p^j)}{\partial s}\right] = \\ &\frac{1}{n_h^2}\left[\hat{\mathbf{s}}_p^j \cdot \frac{\partial \mathbf{H}^+(\mathbf{r}_p^j)}{\partial n} - \hat{\mathbf{n}}_p^j \cdot \frac{\partial \mathbf{H}^+(\mathbf{r}_p^j)}{\partial s}\right], \end{aligned} \tag{5.44}$$

where we note n_h and n_j are the refractive indices for the surrounding medium and j^{th} scatterer, respectively.

The boundary conditions Eqs.(5.41) and (5.44) can be written in matrix form as

$$\begin{bmatrix} \underline{\underline{\hat{n}}}_x & \underline{\underline{\hat{n}}}_y \end{bmatrix} \begin{bmatrix} \frac{\partial \underline{H}_x^-}{\partial n'} \\ \frac{\partial \underline{H}_y^-}{\partial n'} \end{bmatrix} = \begin{bmatrix} \underline{\underline{\hat{n}}}_x & \underline{\underline{\hat{n}}}_y \end{bmatrix} \begin{bmatrix} \frac{\partial \underline{H}_x^+}{\partial n'} \\ \frac{\partial \underline{H}_y^+}{\partial n'} \end{bmatrix} \tag{5.45}$$

$$\begin{aligned} &\begin{bmatrix} \underline{\underline{\varepsilon}}^{-1}\underline{\underline{\hat{s}}}_x & \underline{\underline{\varepsilon}}^{-1}\underline{\underline{\hat{s}}}_y \end{bmatrix} \begin{bmatrix} \frac{\partial \underline{H}_x^-}{\partial n'} \\ \frac{\partial \underline{H}_y^-}{\partial n'} \end{bmatrix} - \begin{bmatrix} \underline{\underline{\varepsilon}}^{-1}\underline{\underline{\hat{n}}}_x & \underline{\underline{\varepsilon}}^{-1}\underline{\underline{\hat{n}}}_y \end{bmatrix} \begin{bmatrix} \frac{\partial \underline{H}_x^-}{\partial s'} \\ \frac{\partial \underline{H}_y^-}{\partial s'} \end{bmatrix} \\ = &\begin{bmatrix} \varepsilon_h^{-1}\underline{\underline{\hat{s}}}_x & \varepsilon_h^{-1}\underline{\underline{\hat{s}}}_y \end{bmatrix} \begin{bmatrix} \frac{\partial \underline{H}_x^+}{\partial n'} \\ \frac{\partial \underline{H}_y^+}{\partial n'} \end{bmatrix} - \begin{bmatrix} \varepsilon_h^{-1}\underline{\underline{\hat{n}}}_x & \varepsilon_h^{-1}\underline{\underline{\hat{n}}}_y \end{bmatrix} \begin{bmatrix} \frac{\partial \underline{H}_x^+}{\partial s'} \\ \frac{\partial \underline{H}_y^+}{\partial s'} \end{bmatrix}, \end{aligned} \tag{5.46}$$

where

$$[\underline{\underline{\varepsilon}}^{-1}]_{jp,kq} = n_j^{-2}\delta_{j,k}\delta_{p,q} \tag{5.47}$$

$$\varepsilon_h^{-1} = n_h^{-2} \tag{5.48}$$

$$[\underline{\underline{\hat{n}}}_{x,y}]_{jp,kq} = [\hat{\mathbf{n}}_p^j]_{x,y}\delta_{j,k}\delta_{p,q} \tag{5.49}$$

$$[\underline{\underline{\hat{s}}}_{x,y}]_{jp,kq} = [\hat{\mathbf{s}}_p^j]_{x,y}\delta_{j,k}\delta_{p,q}. \tag{5.50}$$

where $[\hat{\mathbf{n}}_p^j]_{x,y}$ and $[\hat{\mathbf{s}}_p^j]_{x,y}$ are projected values of the unit vectors $\hat{\mathbf{n}}$ and $\hat{\mathbf{s}}$ along the x and y directions at point $\mathbf{r}_p$ on the j^{th} scatterer, as shown in Fig.5.2.

We can now combine Eqs.(5.45) and (5.46) to give a matrix expression for the boundary conditions

$$\begin{bmatrix} \underline{\underline{\hat{n}}}_x & \underline{\underline{\hat{n}}}_y \\ \underline{\underline{\varepsilon}}^{-1}\underline{\underline{\hat{s}}}_x & \underline{\underline{\varepsilon}}^{-1}\underline{\underline{\hat{s}}}_y \end{bmatrix} \begin{bmatrix} \frac{\partial \underline{H}_x^-}{\partial n'} \\ \frac{\partial \underline{H}_y^-}{\partial n'} \end{bmatrix} - \begin{bmatrix} \underline{\underline{0}} & \underline{\underline{0}} \\ \underline{\underline{\varepsilon}}^{-1}\underline{\underline{\hat{n}}}_x & \underline{\underline{\varepsilon}}^{-1}\underline{\underline{\hat{n}}}_y \end{bmatrix} \begin{bmatrix} \frac{\partial \underline{H}_x^-}{\partial s'} \\ \frac{\partial \underline{H}_y^-}{\partial s'} \end{bmatrix} = \begin{bmatrix} \underline{\underline{\hat{n}}}_x & \underline{\underline{\hat{n}}}_y \\ \varepsilon_h^{-1}\underline{\underline{\hat{s}}}_x & \varepsilon_h^{-1}\underline{\underline{\hat{s}}}_y \end{bmatrix} \begin{bmatrix} \frac{\partial \underline{H}_x^+}{\partial n'} \\ \frac{\partial \underline{H}_y^+}{\partial n'} \end{bmatrix} - \begin{bmatrix} \underline{\underline{0}} & \underline{\underline{0}} \\ \varepsilon_h^{-1}\underline{\underline{\hat{n}}}_x & \varepsilon_h^{-1}\underline{\underline{\hat{n}}}_y \end{bmatrix} \begin{bmatrix} \frac{\partial \underline{H}_x^+}{\partial s'} \\ \frac{\partial \underline{H}_y^+}{\partial s'} \end{bmatrix}. \tag{5.51}$$

In the following steps, we aim to replace $\partial\underline{H}^{\pm}/\partial n'$ and $\partial\underline{H}^{\pm}/\partial s'$ by $\underline{H}^{\pm}$. This will allow us to express the continuity equations at the boundary in a matrix form that depends only on $\underline{H}$. For the two different directions, the expressions for the magnetic field, Eqs.(5.35) and (5.36), can be written as

$$\begin{bmatrix} \underline{\underline{G}}_D^{-1}[-\frac{1}{2}\underline{\underline{1}} + \frac{\partial \underline{\underline{G}}_D}{\partial n'}] & \underline{\underline{0}} \\ \underline{\underline{0}} & \underline{\underline{G}}_D^{-1}[-\frac{1}{2}\underline{\underline{1}} + \frac{\partial \underline{\underline{G}}_D}{\partial n'}] \end{bmatrix} \begin{bmatrix} \underline{H}_x^- \\ \underline{H}_y^- \end{bmatrix} = \begin{bmatrix} \frac{\partial \underline{H}_x^-}{\partial n'} \\ \frac{\partial \underline{H}_y^-}{\partial n'} \end{bmatrix} \tag{5.52}$$

$$\begin{bmatrix} \underline{\underline{G}}^{-1}[\frac{1}{2}\underline{\underline{1}} + \frac{\partial \underline{\underline{G}}}{\partial n'}] & \underline{\underline{0}} \\ \underline{\underline{0}} & \underline{\underline{G}}^{-1}[\frac{1}{2}\underline{\underline{1}} + \frac{\partial \underline{\underline{G}}}{\partial n'}] \end{bmatrix} \begin{bmatrix} \underline{H}_x^+ \\ \underline{H}_y^+ \end{bmatrix} = \begin{bmatrix} \frac{\partial \underline{H}_x^+}{\partial n'} \\ \frac{\partial \underline{H}_y^+}{\partial n'} \end{bmatrix}. \tag{5.53}$$

Eqs.(5.52) and (5.53) are used to replace $\partial \underline{H}/\partial n'$ by $\underline{H}$ in Eq.(5.51) to give

$$\begin{bmatrix} \underline{\underline{\hat{n}}}_x & \underline{\underline{\hat{n}}}_y \\ \underline{\underline{\varepsilon}}^{-1}\underline{\underline{\hat{s}}}_x & \underline{\underline{\varepsilon}}^{-1}\underline{\underline{\hat{s}}}_y \end{bmatrix} \begin{bmatrix} \underline{\underline{G}}_D^{-1}[-\frac{1}{2}\underline{\underline{1}} + \frac{\partial \underline{\underline{G}}_D}{\partial n'}] & \underline{\underline{0}} \\ \underline{\underline{0}} & \underline{\underline{G}}_D^{-1}[-\frac{1}{2}\underline{\underline{1}} + \frac{\partial \underline{\underline{G}}_D}{\partial n'}] \end{bmatrix} \begin{bmatrix} \underline{H}_x^- \\ \underline{H}_y^- \end{bmatrix}$$
$$- \begin{bmatrix} \underline{\underline{0}} & \underline{\underline{0}} \\ \underline{\underline{\varepsilon}}^{-1}\underline{\underline{\hat{n}}}_x & \underline{\underline{\varepsilon}}^{-1}\underline{\underline{\hat{n}}}_y \end{bmatrix} \begin{bmatrix} \frac{\partial \underline{H}_x^-}{\partial s'} \\ \frac{\partial \underline{H}_y^-}{\partial s'} \end{bmatrix} =$$
$$\begin{bmatrix} \underline{\underline{\hat{n}}}_x & \underline{\underline{\hat{n}}}_y \\ \varepsilon_h^{-1}\underline{\underline{\hat{s}}}_x & \varepsilon_h^{-1}\underline{\underline{\hat{s}}}_y \end{bmatrix} \begin{bmatrix} \underline{\underline{G}}^{-1}[\frac{1}{2}\underline{\underline{1}} + \frac{\partial \underline{\underline{G}}}{\partial n'}] & \underline{\underline{0}} \\ \underline{\underline{0}} & \underline{\underline{G}}^{-1}[\frac{1}{2}\underline{\underline{1}} + \frac{\partial \underline{\underline{G}}}{\partial n'}] \end{bmatrix} \begin{bmatrix} \underline{H}_x^+ \\ \underline{H}_y^+ \end{bmatrix}$$
$$- \begin{bmatrix} \underline{\underline{0}} & \underline{\underline{0}} \\ \varepsilon_h^{-1}\underline{\underline{\hat{n}}}_x & \varepsilon_h^{-1}\underline{\underline{\hat{n}}}_y \end{bmatrix} \begin{bmatrix} \frac{\partial \underline{H}_x^+}{\partial s'} \\ \frac{\partial \underline{H}_y^+}{\partial s'} \end{bmatrix}. \tag{5.54}$$

The derivatives of $\mathbf{H}$ in the s-direction can also be expressed in terms of $\mathbf{H}$ provided the boundary elements are small enough. The derivative is approximated as a finite difference:

$$\frac{\partial \mathbf{H}^{\pm}(\mathbf{r}_p^j)}{\partial s} \approx \left\{ \frac{\mathbf{H}^{\pm}(\mathbf{r}_{p+1}^j) - \mathbf{H}^{\pm}(\mathbf{r}_p^j)}{|\mathbf{r}_{p+1}^j - \mathbf{r}_p^j|} + \frac{\mathbf{H}^{\pm}(\mathbf{r}_p^j) - \mathbf{H}^{\pm}(\mathbf{r}_{p-1}^j)}{|\mathbf{r}_p^j - \mathbf{r}_{p-1}^j|} \right\} /2, \tag{5.55}$$

where the two neighbouring elements located on either side of $\mathbf{r}_p^j$ are considered and the average value is taken. Eq.(5.55) can also be expressed in matrix form:

$$\frac{\partial \underline{H}_{x,y}^{\pm}}{\partial s'} = \underline{\underline{D}}\,\underline{H}_{x,y}^{\pm}, \tag{5.56}$$

where

$$[\underline{\underline{D}}]_{jp,kq} = \left\{ \frac{\delta_{j,k}(\delta_{q,p+1} - \delta_{q,p})}{|\mathbf{r}_{p+1}^j - \mathbf{r}_p^j|} + \frac{\delta_{j,k}(\delta_{q,p} - \delta_{q,p-1})}{|\mathbf{r}_p^j - \mathbf{r}_{p-1}^j|} \right\} /2 \tag{5.57}$$

with

$$p+1 = \begin{cases} p+1, & \text{if } 1 \le p < Q_j \\ 1, & \text{if } p = Q_j \end{cases} \tag{5.58}$$

$$p-1 = \begin{cases} p-1, & \text{if } 1 < p \le Q_j \\ Q_j, & \text{if } p = 1 \end{cases}. \tag{5.59}$$

We note that each boundary is a closed curve, so that if $p = Q_j$, then $p+1 \equiv 1$, and if $p = 1$, then $p-1 \equiv Q_j$.

Eq.(5.56) is now substituted into Eq.(5.54) to give

$$\begin{aligned}
&\begin{bmatrix} \underline{\underline{\hat{n}}}_x & \underline{\underline{\hat{n}}}_y \\ \underline{\underline{\varepsilon}}^{-1}\underline{\underline{\hat{s}}}_x & \underline{\underline{\varepsilon}}^{-1}\underline{\underline{\hat{s}}}_y \end{bmatrix} \begin{bmatrix} \underline{\underline{G}}_D^{-1}[-\frac{1}{2}\underline{\underline{1}} + \frac{\partial \underline{\underline{G}}_D}{\partial n'}] & \underline{\underline{0}} \\ \underline{\underline{0}} & \underline{\underline{G}}_D^{-1}[-\frac{1}{2}\underline{\underline{1}} + \frac{\partial \underline{\underline{G}}_D}{\partial n'}] \end{bmatrix} \begin{bmatrix} \underline{H}_x^- \\ \underline{H}_y^- \end{bmatrix} \\
&\qquad - \begin{bmatrix} \underline{\underline{0}} & \underline{\underline{0}} \\ \underline{\underline{\varepsilon}}^{-1}\underline{\underline{\hat{n}}}_x\underline{\underline{D}} & \underline{\underline{\varepsilon}}^{-1}\underline{\underline{\hat{n}}}_y\underline{\underline{D}} \end{bmatrix} \begin{bmatrix} \underline{H}_x^- \\ \underline{H}_y^- \end{bmatrix} = \\
&\begin{bmatrix} \underline{\underline{\hat{n}}}_x & \underline{\underline{\hat{n}}}_y \\ \varepsilon_h^{-1}\underline{\underline{\hat{s}}}_x & \varepsilon_h^{-1}\underline{\underline{\hat{s}}}_y \end{bmatrix} \begin{bmatrix} \underline{\underline{G}}^{-1}[\frac{1}{2}\underline{\underline{1}} + \frac{\partial \underline{\underline{G}}}{\partial n'}] & \underline{\underline{0}} \\ \underline{\underline{0}} & \underline{\underline{G}}^{-1}[\frac{1}{2}\underline{\underline{1}} + \frac{\partial \underline{\underline{G}}}{\partial n'}] \end{bmatrix} \begin{bmatrix} \underline{H}_x^+ \\ \underline{H}_y^+ \end{bmatrix} \\
&\qquad - \begin{bmatrix} \underline{\underline{0}} & \underline{\underline{0}} \\ \varepsilon_h^{-1}\underline{\underline{\hat{n}}}_x\underline{\underline{D}} & \varepsilon_h^{-1}\underline{\underline{\hat{n}}}_y\underline{\underline{D}} \end{bmatrix} \begin{bmatrix} \underline{H}_x^+ \\ \underline{H}_y^+ \end{bmatrix}. \qquad (5.60)
\end{aligned}$$

Eq.(5.60) is a matrix equation expressed in terms only of $\underline{H}$ at the boundary. By considering the continuity of the transverse magnetic fields, Eq.(5.60) can be simplified to the following expression (the details of the derivation are shown in Appendix A)

$$\begin{aligned}
&\Bigg\{ -\left[\frac{1}{2}\underline{\underline{1}} + \frac{\partial \underline{\underline{G}}}{\partial n'}\right] \otimes \mathbf{1}_2 + \left[\underline{\underline{G}}\,\underline{\underline{G}}_D^{-1}[-\frac{1}{2}\underline{\underline{1}} + \frac{\partial \underline{\underline{G}}_D}{\partial n'}]\right] \otimes \mathbf{1}_2 + \\
&+ \Big\{ [\underline{\underline{G}}(\underline{\underline{1}} - \varepsilon_h \underline{\underline{\varepsilon}}^{-1})] \otimes \mathbf{1}_2 \Big\} \underline{\underline{P}} \cdot \\
&\left\{ \left[\underline{\underline{G}}_D^{-1}[-\frac{1}{2}\underline{\underline{1}} + \frac{\partial \underline{\underline{G}}_D}{\partial n'}]\right] \otimes \mathbf{1}_2 + \begin{bmatrix} \underline{\underline{0}} & \underline{\underline{D}} \\ -\underline{\underline{D}} & \underline{\underline{0}} \end{bmatrix} \right\} \Bigg\} \begin{bmatrix} \underline{H}_x \\ \underline{H}_y \end{bmatrix} = 0, \qquad (5.61)
\end{aligned}$$

where for an arbitrary matrix $\underline{\underline{A}}$, the combination with tensor product term $\otimes \mathbf{1}_2$ takes the form:

$$\underline{\underline{A}} \otimes \mathbf{1}_2 = \begin{bmatrix} \underline{\underline{A}} & \underline{\underline{0}} \\ \underline{\underline{0}} & \underline{\underline{A}} \end{bmatrix}, \qquad (5.62)$$

and $\underline{\underline{P}}$ is defined by

$$\underline{\underline{P}} = \begin{bmatrix} -\underline{\underline{\hat{n}}}_y^2 & \underline{\underline{\hat{n}}}_x\underline{\underline{\hat{n}}}_y \\ \underline{\underline{\hat{n}}}_x\underline{\underline{\hat{n}}}_y & -\underline{\underline{\hat{n}}}_x^2 \end{bmatrix}. \qquad (5.63)$$

It is important to note that $\underline{\underline{G}}^{-1}$ does not appear in Eq.(5.61), meaning that we do not have to invert this dense and large matrix. The block diagonal matrix $\underline{\underline{G}}_D$ is easy to invert.

Eq.(5.61) is our final expression for the boundary element method. It has the form of a matrix equation $\underline{\underline{A}} \cdot \underline{H} = 0$, where the matrix $\underline{\underline{A}}$ can be calculated for any structure and for any value of the propagation constant β. If there are Q_j boundary elements for each scatterer, then the size of the matrix $\underline{\underline{A}}$ is $(2\sum_j Q_j) \times (2\sum_j Q_j)$. An equation of the form $\underline{\underline{A}} \cdot \underline{H} = 0$ has non-trivial solutions only if the determinant of $\underline{\underline{A}}$ goes to zero. By searching for a zero determinant, we can therefore find the allowed value of β corresponding to the fundamental modes. We note that Eq.(5.61) can also be written as the form $\underline{\underline{A}} \cdot \underline{H} = \lambda \underline{H}$, where for an allowed value of β the eigenvalue λ is zero. In this eigenvalue equation, both the determinant and the set of eigenvalues can be calculated. The required propagation constant β can therefore be obtained by looking either at the determinant of the matrix or the eigenvalue of the fundamental modes. These two search methods will be detailed in the next chapter.

5.6 Full field expressions

In this section, expressions for the electric and magnetic fields are derived based on the β value determined by Eq.(5.61). In Section 5.4, we derived expressions for the magnetic fields, Eqs.(5.23) and (5.29), for the scatterers and the surrounding medium in the $x - y$ plane, where the Plemelj formula and Principal value P are used because the field is required at the boundary. For a point away from the boundary, the magnetic fields can be expressed in a similar way, but without the effects of the Plemelj formula and the Principal value P:

$$\begin{aligned} H_{x,y}^{in}(\mathbf{r}) = -\sum_{q=1}^{Q_j} \Bigg\{ & \frac{\partial H_{x,y}^{-}(\mathbf{r}_q^j)}{\partial n'} \int_{C_{j,q}} ds' G\big(\mathbf{r}, \mathbf{r}'; K_j\big) \\ & - H_{x,y}^{-}(\mathbf{r}_q^j) \int_{C_{j,q}} ds' \frac{\partial G\big(\mathbf{r}, \mathbf{r}'; K_j\big)}{\partial n'} \Bigg\} \end{aligned} \tag{5.64}$$

$$\begin{aligned} H_{x,y}^{out}(\mathbf{r}) = \sum_{k=1}^{N} \sum_{q=1}^{Q_k} \Bigg\{ & \frac{\partial H_{x,y}^{+}(\mathbf{r}_q^k)}{\partial n'} \int_{C_{k,q}} ds' G\big(\mathbf{r}, \mathbf{r}'; K_h\big) \\ & - H_{x,y}^{+}(\mathbf{r}_q^k) \int_{C_{k,q}} ds' \frac{\partial G\big(\mathbf{r}, \mathbf{r}'; K_h\big)}{\partial n'} \Bigg\}. \end{aligned} \tag{5.65}$$

The expression for H_z given in Section 2.1 is again used to give

$$H_z(\mathbf{r}) = -\frac{1}{i\beta}\nabla_t \cdot \mathbf{H}_t(\mathbf{r}). \tag{5.66}$$

We place Eqs.(5.64) and (5.65) into (5.66) respectively to give H_z expressions for the scatterers and the surrounding medium:

$$\begin{aligned} H_z^{in}(\mathbf{r}) = \frac{1}{i\beta}\sum_{q=1}^{Q_j}\sum_{a=1}^{2}\Bigg\{ & \frac{\partial H_a^-(\mathbf{r}_q^j)}{\partial n'}\int_{C_{j,q}} ds' \frac{\partial G\big(\mathbf{r},\mathbf{r}';K_j\big)}{\partial r_a} \\ & - H_a^-(\mathbf{r}_q^j)\int_{C_{j,q}} ds' \frac{\partial^2 G\big(\mathbf{r},\mathbf{r}';K_j\big)}{\partial n'\partial r_a}\Bigg\} \end{aligned} \tag{5.67}$$

$$\begin{aligned} H_z^{out}(\mathbf{r}) = -\frac{1}{i\beta}\sum_{k=1}^{N}\sum_{q=1}^{Q_k}\sum_{a=1}^{2}\Bigg\{ & \frac{\partial H_a^+(\mathbf{r}_q^k)}{\partial n'}\int_{C_{k,q}} ds' \frac{\partial G\big(\mathbf{r},\mathbf{r}';K_h\big)}{\partial r_a} \\ & - H_a^+(\mathbf{r}_q^k)\int_{C_{k,q}} ds' \frac{\partial^2 G\big(\mathbf{r},\mathbf{r}';K_h\big)}{\partial n'\partial r_a}\Bigg\}, \end{aligned} \tag{5.68}$$

where $a = 1, 2$ is introduced to express the x and y directions.

The electric fields can be derived from the magnetic fields as shown in Section 2.1. We use

$$E_z(\mathbf{r}) = i\left(\frac{\mu_0}{\varepsilon_0}\right)^{\frac{1}{2}} \frac{1}{k_0 n^2(\mathbf{r})}\hat{\mathbf{z}} \cdot \nabla_t \times \mathbf{H}_t(\mathbf{r}) \tag{5.69}$$

$$\mathbf{E}_t(\mathbf{r}) = -\left(\frac{\mu_0}{\varepsilon_0}\right)^{\frac{1}{2}} \frac{1}{k_0 n^2(\mathbf{r})}\hat{\mathbf{z}} \times \{\beta\mathbf{H}_t + i\nabla_t H_z\}, \tag{5.70}$$

where the fields and the dielectric constant n^2 have the same argument $\mathbf{r}$, which indicates the location where we aim to calculate the electric fields. Eq.(5.69) can be written as

$$E_z(\mathbf{r}) = i\left(\frac{\mu_0}{\varepsilon_0}\right)^{\frac{1}{2}} \frac{1}{k_0 n^2(\mathbf{r})}\left\{\frac{\partial H_y(\mathbf{r})}{\partial r_x} - \frac{\partial H_x(\mathbf{r})}{\partial r_y}\right\}. \tag{5.71}$$

By substituting the magnetic field expressions Eqs.(5.64) and (5.65) into Eq.(5.71), the electric field in the z-direction in the scatterers is given by

$$
\begin{aligned}
E_z^{in}(\mathbf{r}) = -i\left(\frac{\mu_0}{\varepsilon_0}\right)^{\frac{1}{2}} \frac{1}{k_0 n^2(\mathbf{r})} \sum_{q=1}^{Q_j} \Bigg\{ \\
\left[\frac{\partial H_y^-(\mathbf{r}_q^j)}{\partial n'} \int_{C_{j,q}} ds' \frac{\partial G\big(\mathbf{r},\mathbf{r}';K_j\big)}{\partial r_x} - H_y^-(\mathbf{r}_q^j) \int_{C_{j,q}} ds' \frac{\partial^2 G\big(\mathbf{r},\mathbf{r}';K_j\big)}{\partial n' \partial r_x}\right] \\
-\left[\frac{\partial H_x^-(\mathbf{r}_q^j)}{\partial n'} \int_{C_{j,q}} ds' \frac{\partial G\big(\mathbf{r},\mathbf{r}';K_j\big)}{\partial r_y} - H_x^-(\mathbf{r}_q^j) \int_{C_{j,q}} ds' \frac{\partial^2 G\big(\mathbf{r},\mathbf{r}';K_j\big)}{\partial n' \partial r_y}\right] \Bigg\}. \quad (5.72)
\end{aligned}
$$

We now introduce the Levi-Civita symbol

$$
\varepsilon_{ijk} = \begin{cases} +1 & \text{if } (\ i,\ j,\ k\ ) \text{ is } (\ 1,\ 2,\ 3\ ),\ (\ 2,\ 3,\ 1\ ) \text{ or } (\ 3,\ 1,\ 2\ ) \\ -1 & \text{if } (\ i,\ j,\ k\ ) \text{ is } (\ 3,\ 2,\ 1\ ),\ (\ 1,\ 3,\ 2\ ) \text{ or } (\ 2,\ 1,\ 3\ ) \\ \ \ 0 & \text{otherwise: if } i = j,\ j = k \text{ or } k = i \end{cases} \quad (5.73)
$$

to simplify Eq.(5.72):

$$
\begin{aligned}
E_z^{in}(\mathbf{r}) = -i\left(\frac{\mu_0}{\varepsilon_0}\right)^{\frac{1}{2}} \frac{1}{k_0 n^2(\mathbf{r})} \sum_{q=1}^{Q_j} \sum_{a,b=1}^{2} \varepsilon_{ab3} \Bigg\{ \frac{\partial H_b^-(\mathbf{r}_q^j)}{\partial n'} \int_{C_{j,q}} ds' \frac{\partial G\big(\mathbf{r},\mathbf{r}';K_j\big)}{\partial r_a} \\
-H_b^-(\mathbf{r}_q^j) \int_{C_{j,q}} ds' \frac{\partial^2 G\big(\mathbf{r},\mathbf{r}';K_j\big)}{\partial n' \partial r_a} \Bigg\}, \quad (5.74)
\end{aligned}
$$

where $H_{1,2,3}$ is used to express $H_{x,y,z}$. Similarly, the z-direction electric field in the surrounding medium is given by

$$
\begin{aligned}
E_z^{out}(\mathbf{r}) = i\left(\frac{\mu_0}{\varepsilon_0}\right)^{\frac{1}{2}} \frac{1}{k_0 n^2(\mathbf{r})} \sum_{k=1}^{N} \sum_{q=1}^{Q_k} \sum_{a,b=1}^{2} \varepsilon_{ab3} \Bigg\{ \frac{\partial H_b^+(\mathbf{r}_q^k)}{\partial n'} \int_{C_{k,q}} ds' \frac{\partial G\big(\mathbf{r},\mathbf{r}';K_h\big)}{\partial r_a} \\
-H_b^+(\mathbf{r}_q^k) \int_{C_{k,q}} ds' \frac{\partial^2 G\big(\mathbf{r},\mathbf{r}';K_h\big)}{\partial n' \partial r_a} \Bigg\}. \quad (5.75)
\end{aligned}
$$

We now derive the electric field in the x and y directions. Eq.(5.70) can be expressed as

$$
\mathbf{E}_t(\mathbf{r}) = -\left(\frac{\mu_0}{\varepsilon_0}\right)^{\frac{1}{2}} \frac{1}{k_0 n^2(\mathbf{r})} \hat{\mathbf{z}} \times \left\{ \beta H_x \hat{\mathbf{x}} + \beta H_y \hat{\mathbf{y}} + i \frac{\partial H_z}{\partial r_x} \hat{\mathbf{x}} + i \frac{\partial H_z}{\partial r_y} \hat{\mathbf{y}} \right\}, \quad (5.76)
$$

which can be simplified as

$$\mathbf{E}_t(\mathbf{r}) = \left(\frac{\mu_0}{\varepsilon_0}\right)^{\frac{1}{2}} \frac{1}{k_0 n^2(\mathbf{r})} \Big\{ -\beta H_x \hat{\mathbf{y}} + \beta H_y \hat{\mathbf{x}} - i\frac{\partial H_z}{\partial r_x}\hat{\mathbf{y}} + i\frac{\partial H_z}{\partial r_y}\hat{\mathbf{x}} \Big\}. \tag{5.77}$$

Eq.(5.77) is then divided into the two different directions

$$E_x = \frac{1}{i}\left(\frac{\mu_0}{\varepsilon_0}\right)^{\frac{1}{2}} \frac{1}{k_0 n^2(\mathbf{r})} \Big\{ i\beta H_y - \frac{\partial H_z}{\partial r_y} \Big\} \tag{5.78}$$

$$E_y = \frac{1}{i}\left(\frac{\mu_0}{\varepsilon_0}\right)^{\frac{1}{2}} \frac{1}{k_0 n^2(\mathbf{r})} \Big\{ -i\beta H_x + \frac{\partial H_z}{\partial r_x} \Big\}. \tag{5.79}$$

The magnetic field expressions Eqs.(5.64), (5.65), (5.67) and (5.68) are placed into Eq.(5.78) to give expressions for E_x:

$$\begin{aligned} E_x^{in} &= \frac{1}{i}\left(\frac{\mu_0}{\varepsilon_0}\right)^{\frac{1}{2}} \frac{1}{k_0 n^2(\mathbf{r})} \Bigg\{ i\beta H_y^{in} \\ &- \frac{1}{i\beta}\sum_{q=1}^{Q_j} \Bigg\{ \Bigg[\frac{\partial H_x^-(\mathbf{r}_q^j)}{\partial n'} \int_{C_{j,q}} ds' \frac{\partial^2 G(\mathbf{r},\mathbf{r}';K_j)}{\partial r_x \partial r_y} - H_x^-(\mathbf{r}_q^j) \int_{C_{j,q}} ds' \frac{\partial^3 G(\mathbf{r},\mathbf{r}';K_j)}{\partial n' \partial r_x \partial r_y} \Bigg] \\ &+ \Bigg[\frac{\partial H_y^-(\mathbf{r}_q^j)}{\partial n'} \int_{C_{j,q}} ds' \frac{\partial^2 G(\mathbf{r},\mathbf{r}';K_j)}{\partial^2 r_y} - H_y^-(\mathbf{r}_q^j) \int_{C_{j,q}} ds' \frac{\partial^3 G(\mathbf{r},\mathbf{r}';K_j)}{\partial n' \partial^2 r_y} \Bigg] \Bigg\} \Bigg\} \end{aligned} \tag{5.80}$$

$$\begin{aligned} E_x^{out} &= \frac{1}{i}\left(\frac{\mu_0}{\varepsilon_0}\right)^{\frac{1}{2}} \frac{1}{k_0 n^2(\mathbf{r})} \Bigg\{ i\beta H_y^{out} \\ &+ \frac{1}{i\beta}\sum_{k=1}^{N}\sum_{q=1}^{Q_k} \Bigg\{ \Bigg[\frac{\partial H_x^+(\mathbf{r}_q^k)}{\partial n'} \int_{C_{k,q}} ds' \frac{\partial^2 G(\mathbf{r},\mathbf{r}';K_h)}{\partial r_x \partial r_y} - H_x^+(\mathbf{r}_q^k) \int_{C_{k,q}} ds' \frac{\partial^3 G(\mathbf{r},\mathbf{r}';K_h)}{\partial n' \partial r_x \partial r_y} \Bigg] \\ &+ \Bigg[\frac{\partial H_y^+(\mathbf{r}_q^k)}{\partial n'} \int_{C_{k,q}} ds' \frac{\partial^2 G(\mathbf{r},\mathbf{r}';K_h)}{\partial^2 r_y} - H_y^+(\mathbf{r}_q^k) \int_{C_{k,q}} ds' \frac{\partial^3 G(\mathbf{r},\mathbf{r}';K_h)}{\partial n' \partial^2 r_y} \Bigg] \Bigg\} \Bigg\}. \end{aligned} \tag{5.81}$$

Similarly, the expressions for the electric field in the y-direction are given by:

$$\begin{aligned} E_y^{in} &= -\frac{1}{i}\left(\frac{\mu_0}{\varepsilon_0}\right)^{\frac{1}{2}} \frac{1}{k_0 n^2(\mathbf{r})} \Bigg\{ i\beta H_x^{in} \\ &- \frac{1}{i\beta}\sum_{q=1}^{Q_j} \Bigg\{ \Bigg[\frac{\partial H_x^-(\mathbf{r}_q^j)}{\partial n'} \int_{C_{j,q}} ds' \frac{\partial^2 G(\mathbf{r},\mathbf{r}';K_j)}{\partial^2 r_x} - H_x^-(\mathbf{r}_q^j) \int_{C_{j,q}} ds' \frac{\partial^3 G(\mathbf{r},\mathbf{r}';K_j)}{\partial n' \partial^2 r_x} \Bigg] \\ &+ \Bigg[\frac{\partial H_y^-(\mathbf{r}_q^j)}{\partial n'} \int_{C_{j,q}} ds' \frac{\partial^2 G(\mathbf{r},\mathbf{r}';K_j)}{\partial r_y \partial r_x} - H_y^-(\mathbf{r}_q^j) \int_{C_{j,q}} ds' \frac{\partial^3 G(\mathbf{r},\mathbf{r}';K_j)}{\partial n' \partial r_y \partial r_x} \Bigg] \Bigg\} \Bigg\} \end{aligned} \tag{5.82}$$

$$
\begin{aligned}
E_y^{out} &= -\frac{1}{i}\left(\frac{\mu_0}{\varepsilon_0}\right)^{\frac{1}{2}} \frac{1}{k_0 n^2(\mathbf{r})}\Bigg\{ i\beta H_x^{out} \\
&+\frac{1}{i\beta}\sum_{k=1}^{N}\sum_{q=1}^{Q_k}\Bigg\{\left[\frac{\partial H_x^{+}(\mathbf{r}_q^k)}{\partial n'}\int_{C_{k,q}} ds' \frac{\partial^2 G\big(\mathbf{r},\mathbf{r}';K_h\big)}{\partial^2 r_x} - H_x^{+}(\mathbf{r}_q^k)\int_{C_{k,q}} ds' \frac{\partial^3 G\big(\mathbf{r},\mathbf{r}';K_h\big)}{\partial n' \partial^2 r_x}\right] \\
&+\left[\frac{\partial H_y^{+}(\mathbf{r}_q^k)}{\partial n'}\int_{C_{k,q}} ds' \frac{\partial^2 G\big(\mathbf{r},\mathbf{r}';K_h\big)}{\partial r_y \partial r_x} - H_y^{+}(\mathbf{r}_q^k)\int_{C_{k,q}} ds' \frac{\partial^3 G\big(\mathbf{r},\mathbf{r}';K_h\big)}{\partial n' \partial r_y \partial r_x}\right]\Bigg\}\Bigg\}. \qquad (5.83)
\end{aligned}
$$

The Levi-Civita symbol is again used to simplify Eqs.(5.80) and (5.82) as

$$
\begin{aligned}
E_a^{in} = \frac{1}{i}\left(\frac{\mu_0}{\varepsilon_0}\right)^{\frac{1}{2}} \frac{1}{k_0 n^2(\mathbf{r})}\sum_{b=1}^{2}\varepsilon_{ab3}\Bigg\{ & i\beta H_b^{in} \\
&-\frac{1}{i\beta}\sum_{q=1}^{Q_j}\sum_{c=1}^{2}\left[\frac{\partial H_c^{-}(\mathbf{r}_q^j)}{\partial n'}\int_{C_{j,q}} ds' \frac{\partial^2 G\big(\mathbf{r},\mathbf{r}';K_j\big)}{\partial r_b \partial r_c}\right. \\
&\left. -H_c^{-}(\mathbf{r}_q^j)\int_{C_{j,q}} ds' \frac{\partial^3 G\big(\mathbf{r},\mathbf{r}';K_j\big)}{\partial n' \partial r_b \partial r_c}\right]\Bigg\}, \qquad (5.84)
\end{aligned}
$$

and Eqs.(5.81) and (5.83) as

$$
\begin{aligned}
E_a^{out} = \frac{1}{i}\left(\frac{\mu_0}{\varepsilon_0}\right)^{\frac{1}{2}} \frac{1}{k_0 n^2(\mathbf{r})}\sum_{b=1}^{2}\varepsilon_{ab3}\Bigg\{ & i\beta H_b^{out} \\
&+\frac{1}{i\beta}\sum_{k=1}^{N}\sum_{q=1}^{Q_k}\sum_{c=1}^{2}\left[\frac{\partial H_c^{+}(\mathbf{r}_q^k)}{\partial n'}\int_{C_{k,q}} ds' \frac{\partial^2 G\big(\mathbf{r},\mathbf{r}';K_h\big)}{\partial r_b \partial r_c}\right. \\
&\left. -H_c^{+}(\mathbf{r}_q^k)\int_{C_{k,q}} ds' \frac{\partial^3 G\big(\mathbf{r},\mathbf{r}';K_h\big)}{\partial n' \partial r_b \partial r_c}\right]\Bigg\}. \qquad (5.85)
\end{aligned}
$$

For any PCF configuration, a complete description of the electromagnetic fields is now obtained: Eqs.(5.64), (5.67), (5.74) and (5.84) are for the scatterers; Eqs.(5.65), (5.68), (5.75) and (5.85) are for the surrounding medium.

To evaluate these expressions for the magnetic and electric fields at an arbitrary point, the magnetic fields $H_{x,y}$, their derivatives and the derivatives of Green's function close to the boundary must be calculated. The boundary values for H_x and H_y come directly from the solution of the defining equation Eq.(5.61).

Eqs.(5.35) and (5.36) are then rewritten as

$$\frac{\partial \underline{H}^{-}_{x,y}}{\partial n'} = \underline{\underline{G}}_D^{-1}\Big[-\frac{1}{2}\underline{\underline{1}} + \frac{\partial \underline{\underline{G}}_D}{\partial n'}\Big]\underline{H}^{-}_{x,y} \tag{5.86}$$

$$\frac{\partial \underline{H}^{+}_{x,y}}{\partial n'} = \underline{\underline{G}}^{-1}\Big[\frac{1}{2}\underline{\underline{1}} + \frac{\partial \underline{\underline{G}}}{\partial n'}\Big]\underline{H}^{+}_{x,y}, \tag{5.87}$$

which enables us to find the boundary values of $\partial H_{x,y}/\partial n'$. In Eq.(5.87) $\underline{\underline{G}}^{-1}$ is unwanted because the $\underline{\underline{G}}$ matrix is large and not sparse. In the earlier derivation to obtain β values in Section 5.5, a matrix transformation has been used to replace $\underline{\underline{G}}^{-1}$ (as shown in Appendix A). A similar treatment also can be used in Eq.(5.87) by multiplying by $\underline{\underline{G}}$ on both sides. $\partial H_{x,y}/\partial n'$ for the surrounding medium can then be found by solving the resulting linear equation. The required deductions and expressions for the derivatives of the Green's function are shown in Appendix B.

5.7 Scalar boundary element method

For the scalar case, the governing equations of the magnetic fields are same as Eq.(5.1). Based on our previous derivations from Section 5.1 to Section 5.4, the matrix expressions for the magnetic field are

$$\begin{bmatrix} \underline{\underline{G}}_D^{-1}[-\frac{1}{2}\underline{\underline{1}} + \frac{\partial \underline{\underline{G}}_D}{\partial n'}] & \underline{\underline{0}} \\ \underline{\underline{0}} & \underline{\underline{G}}_D^{-1}[-\frac{1}{2}\underline{\underline{1}} + \frac{\partial \underline{\underline{G}}_D}{\partial n'}] \end{bmatrix} \begin{bmatrix} \underline{H}_x^- \\ \underline{H}_y^- \end{bmatrix} = \begin{bmatrix} \frac{\partial \underline{H}_x^-}{\partial n'} \\ \frac{\partial \underline{H}_y^-}{\partial n'} \end{bmatrix} \tag{5.88}$$

$$\begin{bmatrix} \underline{\underline{G}}^{-1}[\frac{1}{2}\underline{\underline{1}} + \frac{\partial \underline{\underline{G}}}{\partial n'}] & \underline{\underline{0}} \\ \underline{\underline{0}} & \underline{\underline{G}}^{-1}[\frac{1}{2}\underline{\underline{1}} + \frac{\partial \underline{\underline{G}}}{\partial n'}] \end{bmatrix} \begin{bmatrix} \underline{H}_x^+ \\ \underline{H}_y^+ \end{bmatrix} = \begin{bmatrix} \frac{\partial \underline{H}_x^+}{\partial n'} \\ \frac{\partial \underline{H}_y^+}{\partial n'} \end{bmatrix}, \tag{5.89}$$

which are the same as the vector boundary element method expressions of Eqs.(5.52) and (5.53).

In the scalar case, the magnetic fields and their derivatives are continuous at the interface. We then have

$$\begin{bmatrix} \hat{\underline{\underline{n}}}_x & \hat{\underline{\underline{n}}}_y \end{bmatrix} \begin{bmatrix} \frac{\partial \underline{H}_x^-}{\partial n'} \\ \frac{\partial \underline{H}_y^-}{\partial n'} \end{bmatrix} = \begin{bmatrix} \hat{\underline{\underline{n}}}_x & \hat{\underline{\underline{n}}}_y \end{bmatrix} \begin{bmatrix} \frac{\partial \underline{H}_x^+}{\partial n'} \\ \frac{\partial \underline{H}_y^+}{\partial n'} \end{bmatrix} \tag{5.90}$$

$$\begin{bmatrix} \underline{H}_x^- \\ \underline{H}_y^- \end{bmatrix} = \begin{bmatrix} \underline{H}_x^+ \\ \underline{H}_y^+ \end{bmatrix} = \begin{bmatrix} \underline{H}_x \\ \underline{H}_y \end{bmatrix}. \tag{5.91}$$

Eqs.(5.88) and (5.89) are substituted into (5.90) to give

$$\begin{aligned} &\begin{bmatrix} \underline{\underline{G}}_D^{-1}[-\frac{1}{2}\underline{\underline{1}} + \frac{\partial \underline{\underline{G}}_D}{\partial n'}] & \underline{\underline{0}} \\ \underline{\underline{0}} & \underline{\underline{G}}_D^{-1}[-\frac{1}{2}\underline{\underline{1}} + \frac{\partial \underline{\underline{G}}_D}{\partial n'}] \end{bmatrix} \begin{bmatrix} \underline{H}_x^- \\ \underline{H}_y^- \end{bmatrix} \\ &= \begin{bmatrix} \underline{\underline{G}}^{-1}[\frac{1}{2}\underline{\underline{1}} + \frac{\partial \underline{\underline{G}}}{\partial n'}] & \underline{\underline{0}} \\ \underline{\underline{0}} & \underline{\underline{G}}^{-1}[\frac{1}{2}\underline{\underline{1}} + \frac{\partial \underline{\underline{G}}}{\partial n'}] \end{bmatrix} \begin{bmatrix} \underline{H}_x^+ \\ \underline{H}_y^+ \end{bmatrix} \end{aligned} \tag{5.92}$$

and Eqs.(5.91) and (5.92) can be combined to give

$$\begin{aligned} &\begin{bmatrix} \underline{\underline{G}}_D^{-1}[-\frac{1}{2}\underline{\underline{1}} + \frac{\partial \underline{\underline{G}}_D}{\partial n'}] & \underline{\underline{0}} \\ \underline{\underline{0}} & \underline{\underline{G}}_D^{-1}[-\frac{1}{2}\underline{\underline{1}} + \frac{\partial \underline{\underline{G}}_D}{\partial n'}] \end{bmatrix} \begin{bmatrix} \underline{H}_x \\ \underline{H}_y \end{bmatrix} \\ &= \begin{bmatrix} \underline{\underline{G}}^{-1}[\frac{1}{2}\underline{\underline{1}} + \frac{\partial \underline{\underline{G}}}{\partial n'}] & \underline{\underline{0}} \\ \underline{\underline{0}} & \underline{\underline{G}}^{-1}[\frac{1}{2}\underline{\underline{1}} + \frac{\partial \underline{\underline{G}}}{\partial n'}] \end{bmatrix} \begin{bmatrix} \underline{H}_x \\ \underline{H}_y \end{bmatrix}, \end{aligned} \tag{5.93}$$

which is the equivalent of Eq.(5.61) for the scalar case. We bring all the terms of Eq.(5.93) into the left hand side, and multiply by $\underline{\underline{G}}$ to give

$$\begin{aligned} &\left\{ \begin{bmatrix} \underline{\underline{G}}\,\underline{\underline{G}}_D^{-1}[-\frac{1}{2}\underline{\underline{1}} + \frac{\partial \underline{\underline{G}}_D}{\partial n'}] & \underline{\underline{0}} \\ \underline{\underline{0}} & \underline{\underline{G}}\,\underline{\underline{G}}_D^{-1}[-\frac{1}{2}\underline{\underline{1}} + \frac{\partial \underline{\underline{G}}_D}{\partial n'}] \end{bmatrix} \right. \\ &\left. - \begin{bmatrix} [\frac{1}{2}\underline{\underline{1}} + \frac{\partial \underline{\underline{G}}}{\partial n'}] & \underline{\underline{0}} \\ \underline{\underline{0}} & [\frac{1}{2}\underline{\underline{1}} + \frac{\partial \underline{\underline{G}}}{\partial n'}] \end{bmatrix} \right\} \begin{bmatrix} \underline{H}_x \\ \underline{H}_y \end{bmatrix} = 0. \end{aligned} \tag{5.94}$$

From Eq.(5.94), we can find the β value corresponding to a vacuum wavevector k_0 for the scalar governing equation.

5.8 Summary

In this chapter, we have derived the boundary element method for any PCF structure. Both vector and scalar calculations have been presented. Moreover, the formulae have been translated into matrix expressions, where the matrix elements correspond to the elements in the boundary of each scatterer. In this form it is possible to compute all the expressions for the propagation constant and the fields.

Appendix A: Simplification of matrix field expressions

In this appendix we show how to derive Eq.(5.61) form Eq.(5.60). The purpose of doing this is to remove the dependence of $\underline{\underline{G}}^{-1}$. We start with Eq.(5.60) by using an equivalent form with the tensor product:

$$\begin{aligned}
&\begin{bmatrix} \hat{\underline{\underline{n}}}_x & \hat{\underline{\underline{n}}}_y \\ \underline{\underline{\varepsilon}}^{-1}\hat{\underline{\underline{s}}}_x & \underline{\underline{\varepsilon}}^{-1}\hat{\underline{\underline{s}}}_y \end{bmatrix} \left\{ \left[\underline{\underline{G}}_D^{-1}[-\frac{1}{2}\underline{\underline{1}} + \frac{\partial \underline{\underline{G}}_D}{\partial n'}] \right] \otimes \mathbf{1}_2 \right\} \begin{bmatrix} \underline{H}_x^- \\ \underline{H}_y^- \end{bmatrix} \\
&\qquad - \begin{bmatrix} \underline{\underline{0}} & \underline{\underline{0}} \\ \underline{\underline{\varepsilon}}^{-1}\hat{\underline{\underline{n}}}_x \underline{\underline{D}} & \underline{\underline{\varepsilon}}^{-1}\hat{\underline{\underline{n}}}_y \underline{\underline{D}} \end{bmatrix} \begin{bmatrix} \underline{H}_x^- \\ \underline{H}_y^- \end{bmatrix} = \\
&\begin{bmatrix} \hat{\underline{\underline{n}}}_x & \hat{\underline{\underline{n}}}_y \\ \varepsilon_h^{-1}\hat{\underline{\underline{s}}}_x & \varepsilon_h^{-1}\hat{\underline{\underline{s}}}_y \end{bmatrix} \left\{ \left[\underline{\underline{G}}^{-1}[\frac{1}{2}\underline{\underline{1}} + \frac{\partial \underline{\underline{G}}}{\partial n'}] \right] \otimes \mathbf{1}_2 \right\} \begin{bmatrix} \underline{H}_x^+ \\ \underline{H}_y^+ \end{bmatrix} \\
&\qquad - \begin{bmatrix} \underline{\underline{0}} & \underline{\underline{0}} \\ \varepsilon_h^{-1}\hat{\underline{\underline{n}}}_x \underline{\underline{D}} & \varepsilon_h^{-1}\hat{\underline{\underline{n}}}_y \underline{\underline{D}} \end{bmatrix} \begin{bmatrix} \underline{H}_x^+ \\ \underline{H}_y^+ \end{bmatrix},
\end{aligned} \tag{5.95}$$

where we indicate again that for a sample matrix $\underline{\underline{A}}$, the form of $\begin{bmatrix} \underline{\underline{A}} & \underline{\underline{0}} \\ \underline{\underline{0}} & \underline{\underline{A}} \end{bmatrix}$ can be simplified as $\underline{\underline{A}} \otimes \mathbf{1}_2$.

We first note that at each boundary element the unit directions $\hat{\underline{\underline{n}}}$ and $\hat{\underline{\underline{s}}}$ are related by (as shown in Fig.5.2)

$$\hat{\underline{\underline{s}}}_x = -\hat{\underline{\underline{n}}}_y; \qquad \hat{\underline{\underline{s}}}_y = \hat{\underline{\underline{n}}}_x. \tag{5.96}$$

By using Eq.(5.96) and $\hat{\underline{\underline{n}}}_x^2 + \hat{\underline{\underline{n}}}_y^2 = \underline{\underline{1}}$ we find the following equations

$$\begin{bmatrix} \hat{\underline{\underline{n}}}_x & \hat{\underline{\underline{n}}}_y \\ \varepsilon_h^{-1}\hat{\underline{\underline{s}}}_x & \varepsilon_h^{-1}\hat{\underline{\underline{s}}}_y \end{bmatrix}^{-1} = \begin{bmatrix} \hat{\underline{\underline{n}}}_x & \hat{\underline{\underline{n}}}_y \\ -\varepsilon_h^{-1}\hat{\underline{\underline{n}}}_y & \varepsilon_h^{-1}\hat{\underline{\underline{n}}}_x \end{bmatrix}^{-1} = \begin{bmatrix} \hat{\underline{\underline{n}}}_x & -\varepsilon_h\hat{\underline{\underline{n}}}_y \\ \hat{\underline{\underline{n}}}_y & \varepsilon_h\hat{\underline{\underline{n}}}_x \end{bmatrix} \tag{5.97}$$

$$
\begin{aligned}
&\begin{bmatrix} \underline{\underline{\hat{n}}}_x & -\varepsilon_h \underline{\underline{\hat{n}}}_y \\ \underline{\underline{\hat{n}}}_y & \varepsilon_h \underline{\underline{\hat{n}}}_x \end{bmatrix}
\begin{bmatrix} \underline{\underline{\hat{n}}}_x & \underline{\underline{\hat{n}}}_y \\ -\underline{\underline{\varepsilon}}^{-1} \underline{\underline{\hat{n}}}_y & \underline{\underline{\varepsilon}}^{-1} \underline{\underline{\hat{n}}}_x \end{bmatrix} \\
&= \begin{bmatrix} \underline{\underline{\hat{n}}}_x^2 + \varepsilon_h \underline{\underline{\varepsilon}}^{-1} \underline{\underline{\hat{n}}}_y^2 & \underline{\underline{\hat{n}}}_x \underline{\underline{\hat{n}}}_y - \varepsilon_h \underline{\underline{\varepsilon}}^{-1} \underline{\underline{\hat{n}}}_y \underline{\underline{\hat{n}}}_x \\ \underline{\underline{\hat{n}}}_x \underline{\underline{\hat{n}}}_y - \varepsilon_h \underline{\underline{\varepsilon}}^{-1} \underline{\underline{\hat{n}}}_y \underline{\underline{\hat{n}}}_x & \underline{\underline{\hat{n}}}_y^2 + \varepsilon_h \underline{\underline{\varepsilon}}^{-1} \underline{\underline{\hat{n}}}_x^2 \end{bmatrix} \\
&= \begin{bmatrix} (\underline{\underline{\hat{n}}}_x^2 + \underline{\underline{\hat{n}}}_y^2) - \underline{\underline{\hat{n}}}_y^2 (1 - \varepsilon_h \underline{\underline{\varepsilon}}^{-1}) & \underline{\underline{\hat{n}}}_x \underline{\underline{\hat{n}}}_y (1 - \varepsilon_h \underline{\underline{\varepsilon}}^{-1}) \\ \underline{\underline{\hat{n}}}_x \underline{\underline{\hat{n}}}_y (1 - \varepsilon_h \underline{\underline{\varepsilon}}^{-1}) & (\underline{\underline{\hat{n}}}_x^2 + \underline{\underline{\hat{n}}}_y^2) - \underline{\underline{\hat{n}}}_x^2 (1 - \varepsilon_h \underline{\underline{\varepsilon}}^{-1}) \end{bmatrix} \\
&= \begin{bmatrix} \underline{\underline{1}} & \underline{\underline{0}} \\ \underline{\underline{0}} & \underline{\underline{1}} \end{bmatrix} + \begin{bmatrix} -\underline{\underline{\hat{n}}}_y^2 (1 - \varepsilon_h \underline{\underline{\varepsilon}}^{-1}) & \underline{\underline{\hat{n}}}_x \underline{\underline{\hat{n}}}_y (1 - \varepsilon_h \underline{\underline{\varepsilon}}^{-1}) \\ \underline{\underline{\hat{n}}}_x \underline{\underline{\hat{n}}}_y (1 - \varepsilon_h \underline{\underline{\varepsilon}}^{-1}) & -\underline{\underline{\hat{n}}}_x^2 (1 - \varepsilon_h \underline{\underline{\varepsilon}}^{-1}) \end{bmatrix} \\
&= \begin{bmatrix} \underline{\underline{1}} & \underline{\underline{0}} \\ \underline{\underline{0}} & \underline{\underline{1}} \end{bmatrix} + \begin{bmatrix} \underline{\underline{1}} - \varepsilon_h \underline{\underline{\varepsilon}}^{-1} & \underline{\underline{0}} \\ \underline{\underline{0}} & \underline{\underline{1}} - \varepsilon_h \underline{\underline{\varepsilon}}^{-1} \end{bmatrix} \begin{bmatrix} -\underline{\underline{\hat{n}}}_y^2 & \underline{\underline{\hat{n}}}_x \underline{\underline{\hat{n}}}_y \\ \underline{\underline{\hat{n}}}_x \underline{\underline{\hat{n}}}_y & -\underline{\underline{\hat{n}}}_x^2 \end{bmatrix}
\end{aligned} \tag{5.98}
$$

$$
\begin{aligned}
&\begin{bmatrix} \underline{\underline{\hat{n}}}_x & -\varepsilon_h \underline{\underline{\hat{n}}}_y \\ \underline{\underline{\hat{n}}}_y & \varepsilon_h \underline{\underline{\hat{n}}}_x \end{bmatrix}
\begin{bmatrix} \underline{\underline{0}} & \underline{\underline{0}} \\ \underline{\underline{\hat{n}}}_x & \underline{\underline{\hat{n}}}_y \end{bmatrix} = \varepsilon_h \begin{bmatrix} -\underline{\underline{\hat{n}}}_x \underline{\underline{\hat{n}}}_y & -\underline{\underline{\hat{n}}}_y^2 \\ \underline{\underline{\hat{n}}}_x^2 & \underline{\underline{\hat{n}}}_x \underline{\underline{\hat{n}}}_y \end{bmatrix} \\
&= \varepsilon_h \begin{bmatrix} -\underline{\underline{\hat{n}}}_y^2 & \underline{\underline{\hat{n}}}_x \underline{\underline{\hat{n}}}_y \\ \underline{\underline{\hat{n}}}_x \underline{\underline{\hat{n}}}_y & -\underline{\underline{\hat{n}}}_x^2 \end{bmatrix} \begin{bmatrix} \underline{\underline{0}} & \underline{\underline{1}} \\ -\underline{\underline{1}} & \underline{\underline{0}} \end{bmatrix}.
\end{aligned} \tag{5.99}
$$

We note that Eqs.(5.98) and (5.99) contain the same matrix $\begin{bmatrix} -\underline{\underline{\hat{n}}}_y^2 & \underline{\underline{\hat{n}}}_x \underline{\underline{\hat{n}}}_y \\ \underline{\underline{\hat{n}}}_x \underline{\underline{\hat{n}}}_y & -\underline{\underline{\hat{n}}}_x^2 \end{bmatrix}$.

Eq.(5.95) is then simplified by multiplying by $\begin{bmatrix} \underline{\underline{\hat{n}}}_x & \underline{\underline{\hat{n}}}_y \\ \varepsilon_h^{-1} \underline{\underline{\hat{s}}}_x & \varepsilon_h^{-1} \underline{\underline{\hat{s}}}_y \end{bmatrix}^{-1}$ to give

$$
\begin{aligned}
&\begin{bmatrix} \underline{\underline{\hat{n}}}_x & -\varepsilon_h \underline{\underline{\hat{n}}}_y \\ \underline{\underline{\hat{n}}}_y & \varepsilon_h \underline{\underline{\hat{n}}}_x \end{bmatrix}
\begin{bmatrix} \underline{\underline{\hat{n}}}_x & \underline{\underline{\hat{n}}}_y \\ \underline{\underline{\varepsilon}}^{-1} \underline{\underline{\hat{s}}}_x & \underline{\underline{\varepsilon}}^{-1} \underline{\underline{\hat{s}}}_y \end{bmatrix}
\left\{ \left[\underline{\underline{G}}_D^{-1} [-\frac{1}{2} \underline{\underline{1}} + \frac{\partial \underline{\underline{G}}_D}{\partial n'}] \right] \otimes \mathbf{1}_2 \right\}
\begin{bmatrix} \underline{H}_x^- \\ \underline{H}_y^- \end{bmatrix} \\
&\quad - \begin{bmatrix} \underline{\underline{\hat{n}}}_x & -\varepsilon_h \underline{\underline{\hat{n}}}_y \\ \underline{\underline{\hat{n}}}_y & \varepsilon_h \underline{\underline{\hat{n}}}_x \end{bmatrix}
\begin{bmatrix} \underline{\underline{0}} & \underline{\underline{0}} \\ \underline{\underline{\varepsilon}}^{-1} \underline{\underline{\hat{n}}}_x \underline{\underline{D}} & \underline{\underline{\varepsilon}}^{-1} \underline{\underline{\hat{n}}}_y \underline{\underline{D}} \end{bmatrix}
\begin{bmatrix} \underline{H}_x^- \\ \underline{H}_y^- \end{bmatrix} \\
&\quad = \left\{ \left[\underline{\underline{G}}^{-1} [\frac{1}{2} \underline{\underline{1}} + \frac{\partial \underline{\underline{G}}}{\partial n'}] \right] \otimes \mathbf{1}_2 \right\}
\begin{bmatrix} \underline{H}_x^+ \\ \underline{H}_y^+ \end{bmatrix} \\
&\quad - \begin{bmatrix} \underline{\underline{\hat{n}}}_x & -\varepsilon_h \underline{\underline{\hat{n}}}_y \\ \underline{\underline{\hat{n}}}_y & \varepsilon_h \underline{\underline{\hat{n}}}_x \end{bmatrix}
\begin{bmatrix} \underline{\underline{0}} & \underline{\underline{0}} \\ \varepsilon_h^{-1} \underline{\underline{\hat{n}}}_x \underline{\underline{D}} & \varepsilon_h^{-1} \underline{\underline{\hat{n}}}_y \underline{\underline{D}} \end{bmatrix}
\begin{bmatrix} \underline{H}_x^+ \\ \underline{H}_y^+ \end{bmatrix},
\end{aligned} \tag{5.100}
$$

where Eq.(5.97) has been used. Eq.(5.100) is then multiplied by $\underline{\underline{G}} \otimes \mathbf{1}_2$ to remove the $\underline{\underline{G}}^{-1}$ terms:

$$
\begin{aligned}
&[\underline{\underline{G}} \otimes \mathbf{1}_2] \begin{bmatrix} \hat{\underline{\underline{n}}}_x & -\varepsilon_h \hat{\underline{\underline{n}}}_y \\ \hat{\underline{\underline{n}}}_y & \varepsilon_h \hat{\underline{\underline{n}}}_x \end{bmatrix} \begin{bmatrix} \hat{\underline{\underline{n}}}_x & \hat{\underline{\underline{n}}}_y \\ \underline{\underline{\varepsilon}}^{-1} \hat{\underline{\underline{s}}}_x & \underline{\underline{\varepsilon}}^{-1} \hat{\underline{\underline{s}}}_y \end{bmatrix} \left\{ \left[\underline{\underline{G}}_D^{-1} [-\frac{1}{2}\underline{\underline{1}} + \frac{\partial \underline{\underline{G}}_D}{\partial n'}] \right] \otimes \mathbf{1}_2 \right\} \begin{bmatrix} \underline{H}_x^- \\ \underline{H}_y^- \end{bmatrix} \\
&- [\underline{\underline{G}} \otimes \mathbf{1}_2] \begin{bmatrix} \hat{\underline{\underline{n}}}_x & -\varepsilon_h \hat{\underline{\underline{n}}}_y \\ \hat{\underline{\underline{n}}}_y & \varepsilon_h \hat{\underline{\underline{n}}}_x \end{bmatrix} \begin{bmatrix} \underline{\underline{0}} & \underline{\underline{0}} \\ \underline{\underline{\varepsilon}}^{-1} \hat{\underline{\underline{n}}}_x \underline{\underline{D}} & \underline{\underline{\varepsilon}}^{-1} \hat{\underline{\underline{n}}}_y \underline{\underline{D}} \end{bmatrix} \begin{bmatrix} \underline{H}_x^- \\ \underline{H}_y^- \end{bmatrix} \\
&= \left\{ \left[\frac{1}{2}\underline{\underline{1}} + \frac{\partial \underline{\underline{G}}}{\partial n'} \right] \otimes \mathbf{1}_2 \right\} \begin{bmatrix} \underline{H}_x^+ \\ \underline{H}_y^+ \end{bmatrix} \\
&- [\underline{\underline{G}} \otimes \mathbf{1}_2] \begin{bmatrix} \hat{\underline{\underline{n}}}_x & -\varepsilon_h \hat{\underline{\underline{n}}}_y \\ \hat{\underline{\underline{n}}}_y & \varepsilon_h \hat{\underline{\underline{n}}}_x \end{bmatrix} \begin{bmatrix} \underline{\underline{0}} & \underline{\underline{0}} \\ \varepsilon_h^{-1} \hat{\underline{\underline{n}}}_x \underline{\underline{D}} & \varepsilon_h^{-1} \hat{\underline{\underline{n}}}_y \underline{\underline{D}} \end{bmatrix} \begin{bmatrix} \underline{H}_x^+ \\ \underline{H}_y^+ \end{bmatrix}. \qquad (5.101)
\end{aligned}
$$

Eq.(5.96) is then used to replace $\hat{\underline{\underline{s}}}$ by $\hat{\underline{\underline{n}}}$ to give

$$
\begin{aligned}
&[\underline{\underline{G}} \otimes \mathbf{1}_2] \begin{bmatrix} \hat{\underline{\underline{n}}}_x & -\varepsilon_h \hat{\underline{\underline{n}}}_y \\ \hat{\underline{\underline{n}}}_y & \varepsilon_h \hat{\underline{\underline{n}}}_x \end{bmatrix} \begin{bmatrix} \hat{\underline{\underline{n}}}_x & \hat{\underline{\underline{n}}}_y \\ -\underline{\underline{\varepsilon}}^{-1} \hat{\underline{\underline{n}}}_y & \underline{\underline{\varepsilon}}^{-1} \hat{\underline{\underline{n}}}_x \end{bmatrix} \left\{ \left[\underline{\underline{G}}_D^{-1} [-\frac{1}{2}\underline{\underline{1}} + \frac{\partial \underline{\underline{G}}_D}{\partial n'}] \right] \otimes \mathbf{1}_2 \right\} \begin{bmatrix} \underline{H}_x^- \\ \underline{H}_y^- \end{bmatrix} \\
&- [\underline{\underline{G}} \otimes \mathbf{1}_2] \begin{bmatrix} \hat{\underline{\underline{n}}}_x & -\varepsilon_h \hat{\underline{\underline{n}}}_y \\ \hat{\underline{\underline{n}}}_y & \varepsilon_h \hat{\underline{\underline{n}}}_x \end{bmatrix} \begin{bmatrix} \underline{\underline{0}} & \underline{\underline{0}} \\ \underline{\underline{\varepsilon}}^{-1} \hat{\underline{\underline{n}}}_x \underline{\underline{D}} & \underline{\underline{\varepsilon}}^{-1} \hat{\underline{\underline{n}}}_y \underline{\underline{D}} \end{bmatrix} \begin{bmatrix} \underline{H}_x^- \\ \underline{H}_y^- \end{bmatrix} \\
&= \left\{ \left[\frac{1}{2}\underline{\underline{1}} + \frac{\partial \underline{\underline{G}}}{\partial n'} \right] \otimes \mathbf{1}_2 \right\} \begin{bmatrix} \underline{H}_x^+ \\ \underline{H}_y^+ \end{bmatrix} \\
&- [\underline{\underline{G}} \otimes \mathbf{1}_2] \begin{bmatrix} \hat{\underline{\underline{n}}}_x & -\varepsilon_h \hat{\underline{\underline{n}}}_y \\ \hat{\underline{\underline{n}}}_y & \varepsilon_h \hat{\underline{\underline{n}}}_x \end{bmatrix} \begin{bmatrix} \underline{\underline{0}} & \underline{\underline{0}} \\ \varepsilon_h^{-1} \hat{\underline{\underline{n}}}_x \underline{\underline{D}} & \varepsilon_h^{-1} \hat{\underline{\underline{n}}}_y \underline{\underline{D}} \end{bmatrix} \begin{bmatrix} \underline{H}_x^+ \\ \underline{H}_y^+ \end{bmatrix}. \qquad (5.102)
\end{aligned}
$$

All the terms of Eq.(5.102) are brought to the left hand side to give

$$
\begin{aligned}
&\Bigg\{ - \left[\frac{1}{2}\underline{\underline{1}} + \frac{\partial \underline{\underline{G}}}{\partial n'} \right] \otimes \mathbf{1}_2 \\
&+ [\underline{\underline{G}} \otimes \mathbf{1}_2] \begin{bmatrix} \hat{\underline{\underline{n}}}_x & -\varepsilon_h \hat{\underline{\underline{n}}}_y \\ \hat{\underline{\underline{n}}}_y & \varepsilon_h \hat{\underline{\underline{n}}}_x \end{bmatrix} \begin{bmatrix} \hat{\underline{\underline{n}}}_x & \hat{\underline{\underline{n}}}_y \\ -\underline{\underline{\varepsilon}}^{-1} \hat{\underline{\underline{n}}}_y & \underline{\underline{\varepsilon}}^{-1} \hat{\underline{\underline{n}}}_x \end{bmatrix} \left\{ \left[\underline{\underline{G}}_D^{-1} [-\frac{1}{2}\underline{\underline{1}} + \frac{\partial \underline{\underline{G}}_D}{\partial n'}] \right] \otimes \mathbf{1}_2 \right\} \\
&+ [\underline{\underline{G}} \otimes \mathbf{1}_2] \begin{bmatrix} \hat{\underline{\underline{n}}}_x & -\varepsilon_h \hat{\underline{\underline{n}}}_y \\ \hat{\underline{\underline{n}}}_y & \varepsilon_h \hat{\underline{\underline{n}}}_x \end{bmatrix} \begin{bmatrix} \underline{\underline{0}} & \underline{\underline{0}} \\ \hat{\underline{\underline{n}}}_x & \hat{\underline{\underline{n}}}_y \end{bmatrix} \left\{ \left[\varepsilon_h^{-1} \underline{\underline{D}} - \underline{\underline{\varepsilon}}^{-1} \underline{\underline{D}} \right] \otimes \mathbf{1}_2 \right\} \Bigg\} \begin{bmatrix} \underline{H}_x \\ \underline{H}_y \end{bmatrix} = 0, \quad (5.103)
\end{aligned}
$$

where we have used (5.37) and (5.38) to equate $\underline{H}^+$ and $\underline{H}^-$. Eqs.(5.98) and

(5.99) are now substituted into Eq.(5.103) to give

$$\left\{ -\left[\frac{1}{2}\underline{\underline{1}} + \frac{\partial \underline{\underline{G}}}{\partial n'}\right] \otimes \mathbf{1}_2 \right.$$
$$+ \left[\underline{\underline{G}} \otimes \mathbf{1}_2\right] \left\{ \begin{bmatrix} \underline{\underline{1}} & \underline{\underline{0}} \\ \underline{\underline{0}} & \underline{\underline{1}} \end{bmatrix} + \left\{ \left[\underline{\underline{1}} - \varepsilon_h \underline{\underline{\varepsilon}}^{-1}\right] \otimes \mathbf{1}_2 \right\} \underline{\underline{P}} \right\} \left\{ \left[\underline{\underline{G}}_D^{-1}[-\frac{1}{2}\underline{\underline{1}} + \frac{\partial \underline{\underline{G}}_D}{\partial n'}]\right] \otimes \mathbf{1}_2 \right\}$$
$$\left. + \left[\underline{\underline{G}} \otimes \mathbf{1}_2\right] \varepsilon_h \underline{\underline{P}} \begin{bmatrix} \underline{\underline{0}} & \underline{\underline{1}} \\ -\underline{\underline{1}} & \underline{\underline{0}} \end{bmatrix} \left\{ \left[\varepsilon_h^{-1} \underline{\underline{D}} - \underline{\underline{\varepsilon}}^{-1} \underline{\underline{D}}\right] \otimes \mathbf{1}_2 \right\} \right\} \begin{bmatrix} \underline{H}_x \\ \underline{H}_y \end{bmatrix} = 0, \tag{5.104}$$

where $\underline{\underline{P}}$ is defined by

$$\underline{\underline{P}} = \begin{bmatrix} -\underline{\underline{\hat{n}}}_y^2 & \underline{\underline{\hat{n}}}_x \underline{\underline{\hat{n}}}_y \\ \underline{\underline{\hat{n}}}_x \underline{\underline{\hat{n}}}_y & -\underline{\underline{\hat{n}}}_x^2 \end{bmatrix}. \tag{5.105}$$

Eq.(5.104) can be simplified further as

$$\left\{ -\left[\frac{1}{2}\underline{\underline{1}} + \frac{\partial \underline{\underline{G}}}{\partial n'}\right] \otimes \mathbf{1}_2 + \left[\underline{\underline{G}}\,\underline{\underline{G}}_D^{-1}[-\frac{1}{2}\underline{\underline{1}} + \frac{\partial \underline{\underline{G}}_D}{\partial n'}]\right] \otimes \mathbf{1}_2 \right.$$
$$+ \left[\underline{\underline{G}} \otimes \mathbf{1}_2\right] \left\{ \left[\underline{\underline{1}} - \varepsilon_h \underline{\underline{\varepsilon}}^{-1}\right] \otimes \mathbf{1}_2 \right\} \underline{\underline{P}} \left\{ \left[\underline{\underline{G}}_D^{-1}[-\frac{1}{2}\underline{\underline{1}} + \frac{\partial \underline{\underline{G}}_D}{\partial n'}]\right] \otimes \mathbf{1}_2 \right\}$$
$$\left. + \left[\underline{\underline{G}} \otimes \mathbf{1}_2\right] \underline{\underline{P}} \begin{bmatrix} \underline{\underline{0}} & \underline{\underline{D}} \\ -\underline{\underline{D}} & \underline{\underline{0}} \end{bmatrix} \left\{ \left[\underline{\underline{1}} - \varepsilon_h \underline{\underline{\varepsilon}}^{-1}\right] \otimes \mathbf{1}_2 \right\} \right\} \begin{bmatrix} \underline{H}_x \\ \underline{H}_y \end{bmatrix} = 0. \tag{5.106}$$

By combining the third and fourth terms in the left hand side of Eq.(5.106), we obtain

$$\left\{ -\left[\frac{1}{2}\underline{\underline{1}} + \frac{\partial \underline{\underline{G}}}{\partial n'}\right] \otimes \mathbf{1}_2 + \left[\underline{\underline{G}}\,\underline{\underline{G}}_D^{-1}[-\frac{1}{2}\underline{\underline{1}} + \frac{\partial \underline{\underline{G}}_D}{\partial n'}]\right] \otimes \mathbf{1}_2 \right.$$
$$+ \left\{ \left[\underline{\underline{G}}(\underline{\underline{1}} - \varepsilon_h \underline{\underline{\varepsilon}}^{-1})\right] \otimes \mathbf{1}_2 \right\} \underline{\underline{P}} \cdot$$
$$\left. \left\{ \left[\underline{\underline{G}}_D^{-1}[-\frac{1}{2}\underline{\underline{1}} + \frac{\partial \underline{\underline{G}}_D}{\partial n'}]\right] \otimes \mathbf{1}_2 + \begin{bmatrix} \underline{\underline{0}} & \underline{\underline{D}} \\ -\underline{\underline{D}} & \underline{\underline{0}} \end{bmatrix} \right\} \right\} \begin{bmatrix} \underline{H}_x \\ \underline{H}_y \end{bmatrix} = 0. \tag{5.107}$$

Eq.(5.107) is the final matrix expression used in determining the propagation constant.

Appendix B: Derivatives of the Green's function

In this appendix we calculate the required derivatives of the Green's function in the field expressions in Section 5.6. As mentioned earlier in Section 5.1, the Green's function for Helmholtz equation is defined by (see Eq.(5.5) in Section 5.1)

$$G(\mathbf{r}, \mathbf{r}'; K) = \frac{1}{4i} H_0^{(1)}(K r_d), \tag{5.108}$$

where $r_d = |\mathbf{r} - \mathbf{r}'|$, and K represents K_j and K_h for the scatterers and surrounding medium respectively. We require expressions for two first-order derivatives ($\partial G/\partial n'$, $\partial G/\partial r_a$), two second-order derivatives ($\partial^2 G/\partial n' \partial r_a$, $\partial^2 G/\partial r_a \partial r_b$), and one third-order derivative ($\partial^3 G/\partial n' \partial r_a \partial r_b$), where r_a and r_b can be either x or y. These derivatives with respect to r_a and n' correspond to the different variables in the Green's function: $\mathbf{r}$ and $\mathbf{r}'$ respectively.

To begin, it is useful to find expressions for $\partial r_d/\partial r_a$ and $\partial r_d/\partial n'$. For the former we find (where sums over repeated indices are implied)

$$\begin{aligned}
\frac{\partial r_d}{\partial r_a} &= \frac{\partial |\mathbf{r} - \mathbf{r}'|}{\partial r_a} = \frac{\partial \left[(\mathbf{r} - \mathbf{r}') \cdot (\mathbf{r} - \mathbf{r}')\right]^{\frac{1}{2}}}{\partial r_a} \\
&= \frac{\partial \left[r_i r_i - 2 r_i r_i' + r_i' r_i'\right]^{\frac{1}{2}}}{\partial r_a} = \frac{1}{2 r_d}(2 r_i \delta_{ia} - 2 r_i' \delta_{ia}) \\
&= \frac{(\mathbf{r} - \mathbf{r}')_a}{r_d} = \hat{\mathbf{r}}_a \cdot \hat{\mathbf{r}}_d,
\end{aligned} \tag{5.109}$$

where $\mathbf{r}_d = \mathbf{r} - \mathbf{r}'$ and $\hat{\mathbf{r}}_a$ is the unit vector in the a-direction. The subscript i represents the component in the x or y direction throughout this appendix. For the latter we find

$$\frac{\partial r_d}{\partial n'} = \hat{\mathbf{n}}' \cdot \nabla_{r'} r_d = \hat{n}_i' \frac{\partial r_d}{\partial r_i'} = -\hat{n}_i' (\hat{r}_d)_i = -\hat{\mathbf{n}}' \cdot \hat{\mathbf{r}}_d. \tag{5.110}$$

The two required first-order derivatives then become

$$\frac{\partial G(\mathbf{r}, \mathbf{r}'; K)}{\partial r_a} = \frac{1}{4i} \frac{\partial H_0^{(1)}(K r_d)}{\partial (K r_d)} \cdot \frac{\partial (K r_d)}{\partial r_a} = -\frac{K}{4i} H_1^{(1)}(K r_d) \hat{\mathbf{r}}_a \cdot \hat{\mathbf{r}}_d \tag{5.111}$$

$$\frac{\partial G(\mathbf{r}, \mathbf{r}'; K)}{\partial n'} = \frac{1}{4i} \frac{\partial H_0^{(1)}(K r_d)}{\partial (K r_d)} \cdot \frac{\partial (K r_d)}{\partial n'} = \frac{K}{4i} H_1^{(1)}(K r_d) \hat{\mathbf{n}}' \cdot \hat{\mathbf{r}}_d, \tag{5.112}$$

where the following relationship is used [21]

$$\frac{dH_0^{(1)}(z)}{dz} = -H_1^{(1)}(z). \tag{5.113}$$

Before calculating the second- and third-order derivatives we first evaluate $\partial\hat{\mathbf{r}}_d/\partial r_a$ and $\partial\hat{\mathbf{r}}_d/\partial n'$. The first of these can be expressed as (using Eq.(5.109))

$$\begin{aligned}\left(\frac{\partial\hat{\mathbf{r}}_d}{\partial r_a}\right)_i &= \frac{\partial}{\partial r_a}\left(\frac{(r_d)_i}{r_d}\right) = (r_d)_i\frac{\partial}{\partial r_a}\left(\frac{1}{r_d}\right) + \frac{1}{r_d}\frac{\partial(r_d)_i}{\partial r_a} \\ &= -\frac{(r_d)_i}{r_d^2}\frac{\partial r_d}{\partial r_a} + \frac{1}{r_d}\delta_{ia} = -\frac{(r_d)_i}{r_d^2}\hat{\mathbf{r}}_a\cdot\hat{\mathbf{r}}_d + \frac{1}{r_d}\delta_{ia},\end{aligned} \tag{5.114}$$

Eq.(5.114) can be written as

$$\frac{\partial\hat{\mathbf{r}}_d}{\partial r_a} = -\frac{(\hat{\mathbf{r}}_a\cdot\hat{\mathbf{r}}_d)}{r_d}\hat{\mathbf{r}}_d + \frac{1}{r_d}\hat{\mathbf{r}}_a. \tag{5.115}$$

The second becomes

$$\left(\frac{\partial\hat{\mathbf{r}}_d}{\partial n'}\right)_i \equiv \frac{\partial}{\partial n'}\left(\frac{(r_d)_i}{r_d}\right) = \hat{n}'_j\frac{\partial}{\partial r'_j}\left(\frac{(r_d)_i}{r_d}\right). \tag{5.116}$$

The derivative required here is the same as in Eq.(5.114), but with r replaced by r'. This leads to

$$\frac{\partial\hat{\mathbf{r}}_d}{\partial n'} = \hat{n}'_j\frac{(r_d)_i}{r_d^2}(\hat{r}_d)_j - \hat{n}'_j\frac{1}{r_d}\delta_{ij} = \frac{(\hat{\mathbf{n}}'\cdot\hat{\mathbf{r}}_d)}{r_d}\hat{\mathbf{r}}_d - \frac{1}{r_d}\hat{\mathbf{n}}'. \tag{5.117}$$

The first of the required second-order derivatives becomes (from Eq.(5.112))

$$\begin{aligned}&\frac{\partial^2 G(\mathbf{r},\mathbf{r}';K)}{\partial r_a\partial n'} = \frac{K}{4i}\frac{\partial[H_1^{(1)}(Kr_d)(\hat{\mathbf{n}}'\cdot\hat{\mathbf{r}}_d)]}{\partial r_a} \\ &= \frac{K}{4i}\left[(\hat{\mathbf{n}}'\cdot\hat{\mathbf{r}}_d)\left(\frac{\partial H_1^{(1)}(Kr_d)}{\partial(Kr_d)}\frac{\partial(Kr_d)}{\partial r_a}\right) + H_1^{(1)}(Kr_d)\hat{\mathbf{n}}'\cdot\frac{\partial\hat{\mathbf{r}}_d}{\partial r_a}\right].\end{aligned} \tag{5.118}$$

By using Eqs.(5.109), (5.115) and the standard formula [21]

$$z\frac{dH_\mu^{(1)}(z)}{dz} = zH_{\mu-1}^{(1)}(z) - \mu H_\mu^{(1)}(z), \tag{5.119}$$

this becomes

$$
\begin{aligned}
&\frac{\partial^2 G(\mathbf{r},\mathbf{r}';K)}{\partial r_a \partial n'} \\
&\quad= \frac{K}{4i}\Big[(\hat{\mathbf{n}}'\cdot\hat{\mathbf{r}}_d)\Big(H_0^{(1)}(Kr_d)-\frac{H_1^{(1)}(Kr_d)}{Kr_d}\Big)K(\hat{\mathbf{r}}_a\cdot\hat{\mathbf{r}}_d) \\
&\qquad\qquad +H_1^{(1)}(Kr_d)\Big(\frac{\hat{\mathbf{n}}'\cdot\hat{\mathbf{r}}_a}{r_d}-\frac{(\hat{\mathbf{r}}_a\cdot\hat{\mathbf{r}}_d)(\hat{\mathbf{n}}'\cdot\hat{\mathbf{r}}_d)}{r_d}\Big)\Big] \\
&\quad= \frac{K}{4i}\Big[K(\hat{\mathbf{n}}'\cdot\hat{\mathbf{r}}_d)(\hat{\mathbf{r}}_a\cdot\hat{\mathbf{r}}_d)H_0^{(1)}(Kr_d) \\
&\qquad\qquad +\Big(\frac{\hat{\mathbf{n}}'\cdot\hat{\mathbf{r}}_a}{r_d}-\frac{2(\hat{\mathbf{r}}_a\cdot\hat{\mathbf{r}}_d)(\hat{\mathbf{n}}'\cdot\hat{\mathbf{r}}_d)}{r_d}\Big)H_1^{(1)}(Kr_d)\Big].
\end{aligned}
\tag{5.120}
$$

The other second-order derivative is obtained in a similar way by differentiation of Eq.(5.111)

$$
\begin{aligned}
&\frac{\partial^2 G(\mathbf{r},\mathbf{r}';K)}{\partial r_a \partial r_b} \\
&\quad= -\frac{K}{4i}\frac{\partial[H_1^{(1)}(Kr_d)(\hat{\mathbf{r}}_a\cdot\hat{\mathbf{r}}_d)]}{\partial r_b} \\
&\quad= -\frac{K}{4i}\Big[(\hat{\mathbf{r}}_a\cdot\hat{\mathbf{r}}_d)\Big(\frac{\partial H_1^{(1)}(Kr_d)}{\partial(Kr_d)}\frac{\partial(Kr_d)}{\partial r_b}\Big)+H_1^{(1)}(Kr_d)\hat{\mathbf{r}}_a\cdot\frac{\partial\hat{\mathbf{r}}_d}{\partial r_b}\Big] \\
&\quad= -\frac{K}{4i}\Big[(\hat{\mathbf{r}}_a\cdot\hat{\mathbf{r}}_d)\Big(H_0^{(1)}(Kr_d)-\frac{H_1^{(1)}(Kr_d)}{Kr_d}\Big)K(\hat{\mathbf{r}}_b\cdot\hat{\mathbf{r}}_d) \\
&\qquad\qquad +H_1^{(1)}(Kr_d)\Big(\frac{\delta_{ab}}{r_d}-\frac{(\hat{\mathbf{r}}_a\cdot\hat{\mathbf{r}}_d)(\hat{\mathbf{r}}_b\cdot\hat{\mathbf{r}}_d)}{r_d}\Big)\Big] \\
&\quad= -\frac{K}{4i}\Big[K(\hat{\mathbf{r}}_a\cdot\hat{\mathbf{r}}_d)(\hat{\mathbf{r}}_b\cdot\hat{\mathbf{r}}_d)H_0^{(1)}(Kr_d) \\
&\qquad\qquad +\Big(\frac{\delta_{ab}}{r_d}-\frac{2(\hat{\mathbf{r}}_a\cdot\hat{\mathbf{r}}_d)(\hat{\mathbf{r}}_b\cdot\hat{\mathbf{r}}_d)}{r_d}\Big)H_1^{(1)}(Kr_d)\Big].
\end{aligned}
\tag{5.121}
$$

Finally, we turn to the third derivative, which is obtained by differentiation of Eq.(5.121) with respect to n'. By making use of Eqs.(5.110), (5.113), (5.117) and

(5.119) we find

$$
\begin{aligned}
&\frac{\partial^3 G(\mathbf{r},\mathbf{r}';K)}{\partial r_a \partial r_b \partial n'} \\
&= -\frac{K}{4i}\Bigg\{ K(\hat{\mathbf{r}}_a\cdot\hat{\mathbf{r}}_d)(\hat{\mathbf{r}}_b\cdot\hat{\mathbf{r}}_d)\frac{\partial H_0^{(1)}(Kr_d)}{\partial(Kr_d)}\frac{\partial(Kr_d)}{\partial n'} \\
&+K(\hat{\mathbf{r}}_a\cdot\hat{\mathbf{r}}_d)(\hat{\mathbf{r}}_b\cdot\frac{\partial\hat{\mathbf{r}}_d}{\partial n'})H_0^{(1)}(Kr_d)+K(\hat{\mathbf{r}}_a\cdot\frac{\partial\hat{\mathbf{r}}_d}{\partial n'})(\hat{\mathbf{r}}_b\cdot\hat{\mathbf{r}}_d)H_0^{(1)}(Kr_d) \\
&+\delta_{ab}K\Big[\frac{\partial}{\partial(Kr_d)}\Big(\frac{H_1^{(1)}(Kr_d)}{(Kr_d)}\Big)\Big]\frac{\partial(Kr_d)}{\partial n'} \\
&-2K(\hat{\mathbf{r}}_a\cdot\hat{\mathbf{r}}_d)(\hat{\mathbf{r}}_b\cdot\hat{\mathbf{r}}_d)\Big[\frac{\partial}{\partial(Kr_d)}\Big(\frac{H_1^{(1)}(Kr_d)}{(Kr_d)}\Big)\Big]\frac{\partial(Kr_d)}{\partial n'} \\
&-2\frac{(\hat{\mathbf{r}}_a\cdot\hat{\mathbf{r}}_d)}{r_d}\Big(\hat{\mathbf{r}}_b\cdot\frac{\partial\hat{\mathbf{r}}_d}{\partial n'}\Big)H_1^{(1)}(Kr_d)-2\Big(\hat{\mathbf{r}}_a\cdot\frac{\partial\hat{\mathbf{r}}_d}{\partial n'}\Big)\frac{(\hat{\mathbf{r}}_b\cdot\hat{\mathbf{r}}_d)}{r_d}H_1^{(1)}(Kr_d)\Bigg\}. \quad (5.122)
\end{aligned}
$$

To simplify this we note that

$$
\frac{d}{dz}\Big(\frac{H_1^{(1)}(z)}{z}\Big)=\frac{zH_1^{(1)\prime}(z)-H_1^{(1)}(z)}{z^2}=\frac{zH_0^{(1)}(z)-2H_1^{(1)}(z)}{z^2}. \quad (5.123)
$$

Eq.(5.122) then becomes

$$
\begin{aligned}
&\frac{\partial^3 G(\mathbf{r},\mathbf{r}';K)}{\partial r_a \partial r_b \partial n'} \\
&= -\frac{K}{4i}\Bigg\{K^2(\hat{\mathbf{r}}_a\cdot\hat{\mathbf{r}}_d)(\hat{\mathbf{r}}_b\cdot\hat{\mathbf{r}}_d)(\hat{\mathbf{n}}'\cdot\hat{\mathbf{r}}_d)H_1^{(1)}(Kr_d) \\
&+K\frac{(\hat{\mathbf{r}}_a\cdot\hat{\mathbf{r}}_d)(\hat{\mathbf{n}}'\cdot\hat{\mathbf{r}}_d)(\hat{\mathbf{r}}_b\cdot\hat{\mathbf{r}}_d)}{r_d}H_0^{(1)}(Kr_d)-K\frac{(\hat{\mathbf{r}}_a\cdot\hat{\mathbf{r}}_d)(\hat{\mathbf{r}}_b\cdot\hat{\mathbf{n}}')}{r_d}H_0^{(1)}(Kr_d) \\
&+K\frac{(\hat{\mathbf{r}}_a\cdot\hat{\mathbf{r}}_d)(\hat{\mathbf{n}}'\cdot\hat{\mathbf{r}}_d)(\hat{\mathbf{r}}_b\cdot\hat{\mathbf{r}}_d)}{r_d}H_0^{(1)}(Kr_d)-K\frac{(\hat{\mathbf{r}}_a\cdot\hat{\mathbf{n}}')(\hat{\mathbf{r}}_b\cdot\hat{\mathbf{r}}_d)}{r_d}H_0^{(1)}(Kr_d) \\
&-\delta_{ab}K^2(\hat{\mathbf{n}}'\cdot\hat{\mathbf{r}}_d)\frac{H_0^{(1)}(Kr_d)}{Kr_d}+\delta_{ab}2K^2(\hat{\mathbf{n}}'\cdot\hat{\mathbf{r}}_d)\frac{H_1^{(1)}(Kr_d)}{K^2r_d^2} \\
&+2K^2(\hat{\mathbf{r}}_a\cdot\hat{\mathbf{r}}_d)(\hat{\mathbf{r}}_b\cdot\hat{\mathbf{r}}_d)(\hat{\mathbf{n}}'\cdot\hat{\mathbf{r}}_d)\frac{H_0^{(1)}(Kr_d)}{Kr_d}-4K^2(\hat{\mathbf{r}}_a\cdot\hat{\mathbf{r}}_d)(\hat{\mathbf{r}}_b\cdot\hat{\mathbf{r}}_d)(\hat{\mathbf{n}}'\cdot\hat{\mathbf{r}}_d)\frac{H_1^{(1)}(Kr_d)}{K^2r_d^2} \\
&-\frac{2(\hat{\mathbf{r}}_a\cdot\hat{\mathbf{r}}_d)(\hat{\mathbf{r}}_b\cdot\hat{\mathbf{r}}_d)(\hat{\mathbf{n}}'\cdot\hat{\mathbf{r}}_d)}{r_d^2}H_1^{(1)}(Kr_d)+\frac{2(\hat{\mathbf{r}}_a\cdot\hat{\mathbf{r}}_d)(\hat{\mathbf{r}}_b\cdot\hat{\mathbf{n}}')}{r_d^2}H_1^{(1)}(Kr_d) \\
&-\frac{2(\hat{\mathbf{r}}_a\cdot\hat{\mathbf{r}}_d)(\hat{\mathbf{n}}'\cdot\hat{\mathbf{r}}_d)(\hat{\mathbf{r}}_b\cdot\hat{\mathbf{r}}_d)}{r_d^2}H_1^{(1)}(Kr_d)+\frac{2(\hat{\mathbf{r}}_a\cdot\hat{\mathbf{n}}')(\hat{\mathbf{r}}_b\cdot\hat{\mathbf{r}}_d)}{r_d^2}H_1^{(1)}(Kr_d)\Bigg\}. \quad (5.124)
\end{aligned}
$$

By collecting similar terms we can simplify this to give:

$$
\begin{aligned}
&\frac{\partial^3 G(\mathbf{r}, \mathbf{r}'; K)}{\partial r_a \partial r_b \partial n'} \\
&= -\frac{K}{4i}\Bigg\{K^2(\hat{\mathbf{r}}_a \cdot \hat{\mathbf{r}}_d)(\hat{\mathbf{r}}_b \cdot \hat{\mathbf{r}}_d)(\hat{\mathbf{n}}' \cdot \hat{\mathbf{r}}_d)H_1^{(1)}(Kr_d) \\
&+K^2\Big[4(\hat{\mathbf{r}}_a \cdot \hat{\mathbf{r}}_d)(\hat{\mathbf{r}}_b \cdot \hat{\mathbf{r}}_d)(\hat{\mathbf{n}}' \cdot \hat{\mathbf{r}}_d) - (\hat{\mathbf{r}}_a \cdot \hat{\mathbf{r}}_d)(\hat{\mathbf{r}}_b \cdot \hat{\mathbf{n}}') \\
&-(\hat{\mathbf{r}}_a \cdot \hat{\mathbf{n}}')(\hat{\mathbf{r}}_b \cdot \hat{\mathbf{r}}_d) - \delta_{ab}(\hat{\mathbf{n}}' \cdot \hat{\mathbf{r}}_d)\Big]\frac{H_0^{(1)}(Kr_d)}{(Kr_d)} \\
&-K^2\Big[8(\hat{\mathbf{r}}_a \cdot \hat{\mathbf{r}}_d)(\hat{\mathbf{r}}_b \cdot \hat{\mathbf{r}}_d)(\hat{\mathbf{n}}' \cdot \hat{\mathbf{r}}_d) - 2(\hat{\mathbf{r}}_a \cdot \hat{\mathbf{r}}_d)(\hat{\mathbf{r}}_b \cdot \hat{\mathbf{n}}') \\
&-2(\hat{\mathbf{r}}_a \cdot \hat{\mathbf{n}}')(\hat{\mathbf{r}}_b \cdot \hat{\mathbf{r}}_d) - 2\delta_{ab}(\hat{\mathbf{n}}' \cdot \hat{\mathbf{r}}_d)\Big]\frac{H_0^{(1)}(Kr_d)}{K^2 r_d^2}\Big]\Bigg\}.
\end{aligned}
\tag{5.125}
$$

The full set of derivatives for the Green's function are given by Eqs.(5.111) and (5.112) for the first-order, Eqs.(5.120) and (5.121) for the second-order, and Eq.(5.125) for the third-order. All of those expressions are straightforward to compute.

Chapter 6

Application of Boundary Element Method in Rectangular PCFs

The previous chapter contained a derivation of the boundary element method for an arbitrary PCF transverse structure. In this chapter, the boundary element method will be applied to calculate the guidance properties of our model structures, rectangular hollow-core PCFs. The ideal structure with high-index intersections is calculated using scalar governing equations. As we will see in Chapters 7 and 8, this ideal structure combined with scalar governing equations has analytic solutions, thus the boundary element calculations are different from this analytic solution only due to the finite cladding structure. The real structure governed by vector wave equations is also investigated. This calculation corresponds to a more realistic guidance characteristic.

In Section 6.1 we present the parameters of our model structures. The modelling processes are described in Section 6.2, which involve the input files, program structure, and the root finding process. In Section 6.3, a simple example is used to check the accuracy of the boundary element method by comparing with an analytic solution. Sections 6.4 and 6.5 describe the convergence testing and discuss the efficiency of the method in terms of the required memory and CPU time. Section 6.6 presents the results for rectangular hollow-core PCFs, where both propagation constant and field profiles are obtained and discussed. The conclusion is given in Section 6.7.

6.1 Structural details

The model PCF structures have been presented in Section 4.4: square air holes are enclosed by orthogonal glass strips in the cladding, which has a limited area. Here it is useful to emphasise again the difference of the fibre structure between the two types of rectangular PCFs in our modelling: the ideal structure has a high-index interaction of glass strips (refractive index is $\sqrt{2n_g^2 - n_a^2}$, where n_g and n_a are refractive indices of the glass and air); the refractive index of the intersections in the real structure is same as the glass (i.e. n_g). In our simulations, the ideal and real model structures are solved by using scalar and vector governing equations, respectively.

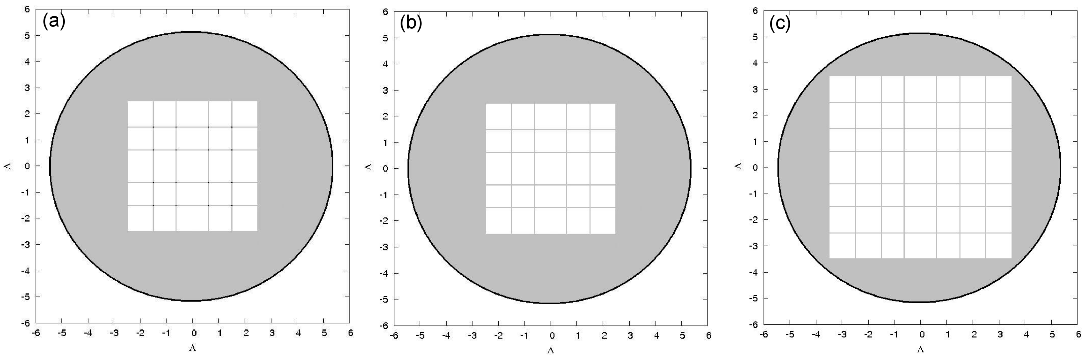

Figure 6.1: The transverse planes of our model rectangular PCFs. The left and middle figures are the 5×5 ideal and 5×5 real structures, which contains 25 air holes, and the right figure is the 7×7 real structure. The different colours display different values of the refractive indices: white is air, gray is glass, and black is high-index intersections.

Fig.6.1 shows three models of rectangular PCFs, which have an odd number of air holes in each direction in the cross-sectional plane and the central defect is in the middle of the whole structure. Figures (a) and (b) are ideal and real structures. They are identical except for the different value of the refractive index in the intersections of the strips. There are 25 air holes in each case, therefore we call them '5×5 ideal' and '5×5 real' structures for simplification. In order to analyse the effect of the cladding on the guidance properties, a larger cladding structure, which is called the '7×7 real' structure, is also presented in Fig.6.1 (c). In all the structures, the central defect is formed in the way as discussed in Section 4.4; the four strips enclosing the central air hole are moved outwards by the same distance.

The structural parameters are defined as follows. The refractive indices for the air holes n_a and glass strips n_g are 1.0 and 1.5 respectively. The ratio of the thickness of the glass strips to the pitch d/Λ is 0.05, where Λ is the original periodicity of the structure. The central defect is created by moving four strips by a distance of 0.125Λ. The air-filling fraction of our model structures is 0.9025, which lies between those reported for Kagome and square-lattice weak interaction guidance PCFs.

In the application of the boundary element method, the cross-sectional plane of PCFs is treated as a set of scatterers surrounded by a medium. This requires that, in our modelling, the scatterers are selected as the 'air holes' and 'high-index intersections' for the ideal model structure, and 'air holes' for the real model. The surrounding medium consists of the glass strips and the region outside the periodic cladding, which is formed from the same material as the strips.

6.2 Modelling processes

6.2.1 Input setting

The boundary element calculation begins from reading an input file, which contains the parameters of the structure (e.g. Rectangular, Circular) and the output settings. For rectangular hollow-core PCFs, the input information consists of the position of the scatterers, their sizes, the number of elements on each side of the rectangular scatterers, and the refractive indices of each region. The output settings are the search region for the propagation constant; field plots for selected modes can also be chosen.

6.2.2 Program structure

The program operates in two main parts: constructing the matrix given by Eq.(5.61) or (5.94) and solving the matrix. Construction of the matrix is performed by 'private' and 'public' subroutines. The 'private' subroutine is written based on the particular structure, and produces information about the location and length of each boundary element and the x and y components of their normal and tangent unit vectors. The 'public' subroutines are the general programs to apply the boundary element method, which are based on the whole derivation in

Chapter 5. After obtaining a set of eigenvalues, the corresponding magnetic and electric fields can be plotted.

6.2.3 Root finding process

Two different methods are used to determine the β values that satisfy Eq.(5.61) or (5.94). One is to find the lowest absolute value of the determinant of the matrix. Both the fundamental guided mode and cladding modes correspond to zero eigenvalues, which make the determinant also approach zero, as discussed in Section 5.5. The other method is to trace the absolute value of the eigenvalue of a particular mode until it approaches zero. To differentiate the types of modes, we can look at plots of the fields. For example, for the fundamental guided mode, the key characteristic is that the magnetic field is localised in the central defect. This mode can therefore be identified by finding the largest value of H_x or H_y in the centre of the whole structure. This enables us to trace the variation of the eigenvalues of the selected guided modes, and to efficiently find their exact β values.

Our calculation proceeds by first searching the real β value based on an estimated imaginary β value. The selected real β value corresponds to the smallest absolute value of the eigenvalue for the selected modes. We then search the imaginary part of β using the real part from the first step to find a lower absolute value for the eigenvalue. This search is repeated with the alternation of the real and imaginary parts of β until the absolute value of the eigenvalue is very close to zero. In each step of searching for β we calculate the eigenvalues at a set of β values (typically about 30) and use interpolation to obtain successively more accurate values.

6.3 Circular fibre example

To check our codes we can perform calculations on simple structures for which analytic solutions exist. Here we choose to analyse a circular fibre [21]. For this single isolated rod in a surrounding medium, the wavefunctions can be expressed in terms of Bessel functions J and K together with an angular part. The propagation constants can be determined from the equations [21]

$$\frac{J_1(U)}{UJ_0(U)} + \frac{K_1(W)}{WK_0(W)} = 0 \tag{6.1}$$

$$n_{co}^2 \frac{J_1(U)}{UJ_0(U)} + n_{cl}^2 \frac{K_1(W)}{WK_0(W)} = 0 \tag{6.2}$$

$$\left\{ \frac{J_\nu'(U)}{UJ_\nu(U)} + \frac{K_\nu'(W)}{WK_\nu(W)} \right\} \left\{ \frac{J_\nu'(U)}{UJ_\nu(U)} + \frac{n_{cl}^2}{n_{co}^2} \frac{K_\nu'(W)}{WK_\nu(W)} \right\} = \left(\frac{\nu\beta}{k_0 n_{co}} \right)^2 \left(\frac{V}{UW} \right)^4, \tag{6.3}$$

where n_{co} and n_{cl} are the refractive indices of the rod and the surrounding medium, J_ν and K_ν are ν^{th} order Bessel functions, and U, W and V are defined as

$$U = \left[(k_0\rho)^2 n_{co}^2 - (\beta\rho)^2\right]^{1/2} \tag{6.4}$$

$$W = \left[(\beta\rho)^2 - (k_0\rho)^2 n_{cl}^2\right]^{1/2} \tag{6.5}$$

$$V = (k_0\rho)\left(n_{co}^2 - n_{cl}^2\right)^{1/2}, \tag{6.6}$$

where ρ is the radius of the rod, $k_0\rho$ and $\beta\rho$ are the normalised wavevector and propagation constant. Eqs.(6.1), (6.2) and (6.3) correspond to TE, TM and HE (EH) modes. Their magnetic and electric fields can be calculated by using the $\beta\rho$ values determined from Eq.(6.1) to Eq.(6.3). For example, the azimuthal component of the magnetic field for the TM mode is given by

$$h_\phi = \begin{cases} \left(\frac{\varepsilon_0}{\mu_0}\right)^{1/2} \frac{k_0 n_{co}^2}{\beta} \frac{J_1(UR)}{J_1(U)} & \text{for the core} \quad (R \leq 1) \\ \left(\frac{\varepsilon_0}{\mu_0}\right)^{1/2} \frac{k_0 n_{co}^2}{\beta} \frac{K_1(WR)}{K_1(W)} & \text{for the cladding} \quad (R > 1), \end{cases} \tag{6.7}$$

where the dimensionless variable $R = r/\rho$ and r is the distance between a selected point and the origin.

In the vector boundary element calculation we put $n_{co} = 1.45$, $n_{cl} = 1.0$, $k_0\rho = 3.242934$. The boundary of the rod is evenly divided into 128 elements, and the search region for $\beta\rho$ varies from 3.4 to 4.4. The logarithm of the determinant is shown by green curve in Fig.6.2. There are four values of $\beta\rho$ for which the determinant approaches zero. These solutions for $\beta\rho$ in the boundary element method have been checked against the analytic result by using Eqs.(6.1) to (6.3) (as shown by the red arrows in Fig.6.2).

Based on the calculated values of $\beta\rho$, we have compared the transverse magnetic fields along a chosen angle of $\phi = \pi/3$. For the TM mode with $\beta\rho = 3.5927$, H_x and H_y are shown in Fig.6.3. Both in the central defect and cladding areas, the boundary element results (as shown by red dots in Fig.6.3) perfectly match with the analytic solutions (as shown by green lines in Fig.6.3). The whole field plots

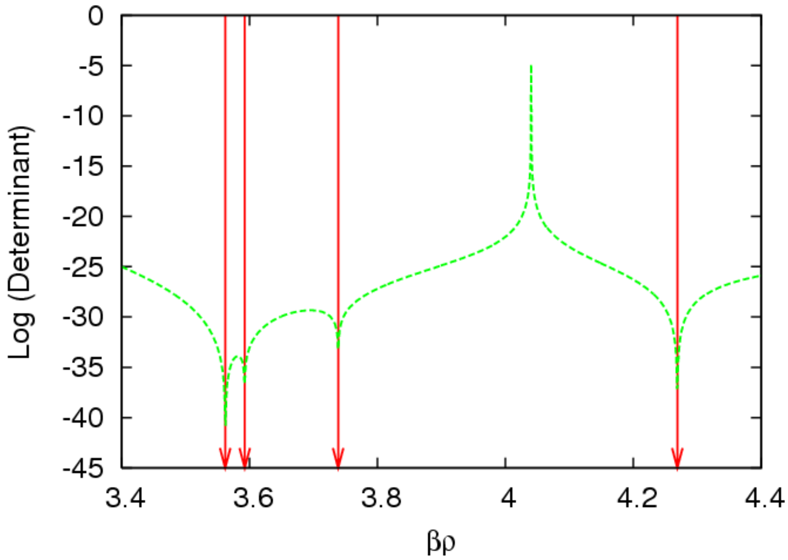

Figure 6.2: Comparison of the analytic and boundary element method. The solutions for $\beta\rho$ are 3.5621 (HE/EH mode), 3.5927 (TM mode), 3.7388 (TE mode) and 4.2691 (HE/EH mode), which are calculated by finding the minimum of the determinant in the boundary element method (the green curve) and confirmed by analytic calculation (the red straight lines).

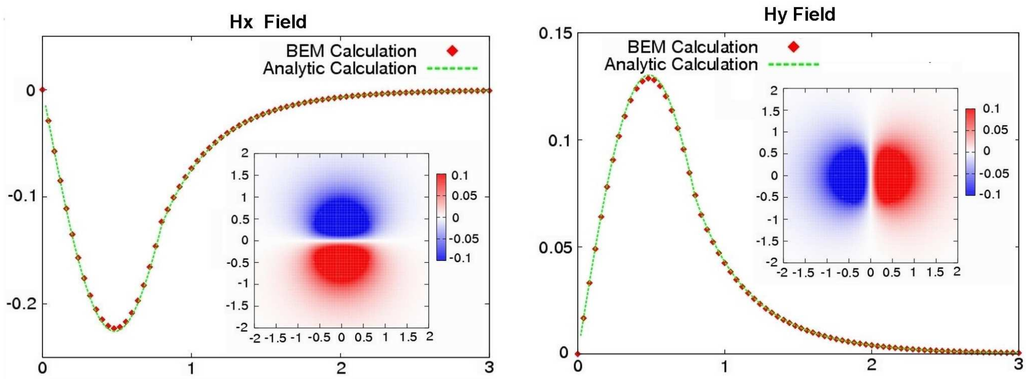

Figure 6.3: Transverse magnetic fields for $\beta = 3.5927$ (TM mode) in the circular fibre. The left and right figures are magnetic fields H_x and H_y along a line with the angle of $\phi = \pi/3$. The analytic results (the lines) are consistent with the boundary element method calculation (the dots). The whole field profiles are shown in the inner figures.

given by these two methods are the same and are shown in the inner figures in Fig.6.3 .

6.4 Convergence tests

In the application of the boundary element method, the issues involved in the accuracy of calculations are the precision of the integrals and the number of the elements used for each scatterer. The precision contains two parts: one is the principal value of integrals P in Eqs.(5.15) and (5.16), where we have to choose a finite distance to avoid infinities in the integrand; the other is the numerical accuracy of the integrals of the Green's functions and their derivatives in Eqs.(5.27), (5.28), (5.33), and (5.34). The tolerances should be small enough to enable us to obtain accurate values, especially for the small imaginary part of β. A choice of less than 10^{-8} for the limit of the principal value integrals and 10^{-6} for the tolerance of the integrals of the Green's functions have been found to be satisfactory for most calculations. In order to ensure the high precision results, 10^{-12} and 10^{-10} are used as the tolerances in the following calculations.

The number of elements in the boundary of each scatterer should be large enough to ensure that both the real and imaginary parts of β are well converged. We performed calculations for the 5×5 real structure using the vector governing equations and with 80, 100, 120 and 140 elements for each scatterer, where each of the four sides of each air hole has the same number of elements. The real and imaginary parts of β/k_0 for the fundamental air-guided mode are plotted over a range of $k_0\Lambda$ from 20 to 40 in Figs.6.4 and 6.5, respectively.

In Fig.6.4, our simulation shows that the real part of β/k_0 is converged well from 80 to 140 elements for each scatterer. For example, the values for 80 and 100 elements are the same as for 140 elements to 4 decimal places; those for 120 elements are the same as 140 elements to 5 decimal places. The convergence of imaginary part of β/k_0 is shown in Fig.6.5. The value of $\mathrm{Im}(\beta/k_0)$ is fairly small (less than 2×10^{-5}) in this region and has a relatively big convergence error compared to the real part. The maximum relative errors for 100 and 120 elements are 19 and 8 percent compared to the results for 140 elements.

Based on these calculations, a standard value of 120 elements for each scatterer is chosen for the modelling of our model structures. We expect the real part of β/k_0

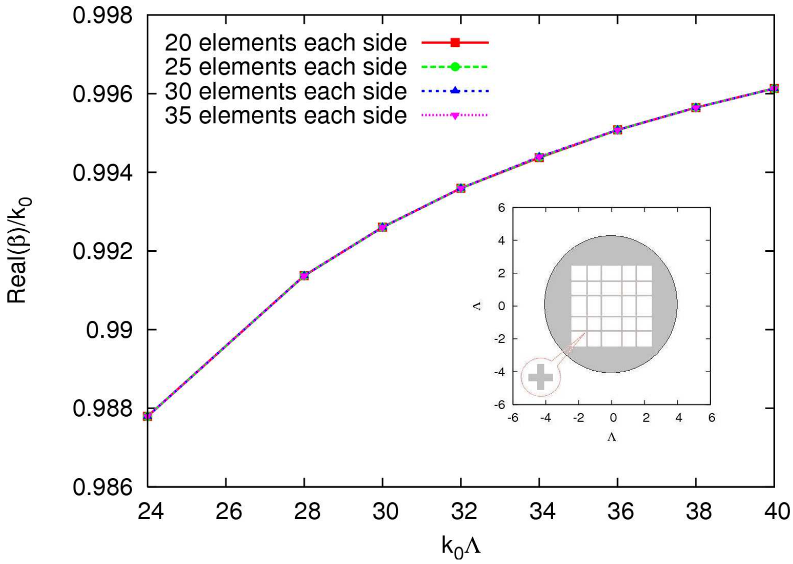

Figure 6.4: Convergence check for the real part of β for the vector governing equations. The 5×5 real rectangular PCF structure is shown in the inset.

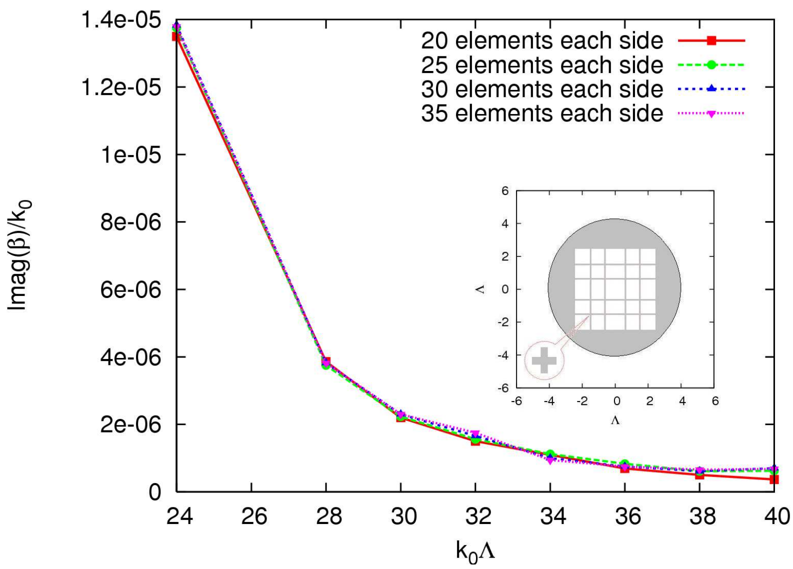

Figure 6.5: Convergence check for the imaginary part of β for the vector governing equations.

to be accurate up to 5 decimal places and the relative error for the imaginary part of β/k_0 to be of order 10%. Though this choice is determined by using the 5×5 real structure, it should be valid for other sizes of structures (e.g. 7×7 real structure) for the same range of frequency because we would expect convergence to be determined by the properties of the scatterers. However, for calculations at higher frequencies, the required number of elements will increase to obtain the same accuracy.

6.5 Computational efficiency

The matrix from which the β solution is found has been given in Eq.(5.61) in Section 5.5 for the vector governing equations. This enables us to estimate the required computer memory, where we assume that all the data is stored in the memory for optimised running speed. From the discussion in Section 5.5, if the number of elements for the j^{th} scatterer is Q_j, the size of final matrix $\underline{\underline{A}}$ is $4n_{tot}^2$, where n_{tot} is $\sum_j Q_j$. In the construction of this matrix, the other involved matrices are $\underline{\underline{G}}_D$, $\partial\underline{\underline{G}}_D/\partial n'$, $\underline{\underline{G}}_D^{-1}$, $\underline{\underline{G}}$, $\partial\underline{\underline{G}}/\partial n'$, $-\left[\frac{1}{2}\underline{\underline{1}} + \partial\underline{\underline{G}}/\partial n'\right]$, $\underline{\underline{G}}_D^{-1}\left[-\frac{1}{2}\underline{\underline{1}} + \partial\underline{\underline{G}}_D/\partial n'\right]$ and their sizes are all n_{tot}^2. Thus the total amount is about $11n_{tot}^2$. Each datum is complex corresponding to the complex β value, and must be double precision for accurate results. Therefore, the required computer memory can be estimated, as shown in Fig.6.6 for 5×5 real and 7×7 real structures. From the discussion in the last section, when the number of elements for each scatterer is chosen as 120, the required memory for the 5×5 real and 7×7 real structures are 1.58 and 6.09 Gigabytes respectively for the calculation of complex β. A powerful computer is needed in the larger calculation, and in our simulation the 64-bit computing cluster at the University of Bath is used, for which the maximum memory is 16 Gigabytes for each job.

Both the precision of integrals and number of boundary elements may affect the efficiency of calculations. It has been found that the improvement of the precision does not affect the CPU time very much, but an increment of the number of boundary elements will significantly increase the computational effort. We used the same computer to compare the CPU time for different number of elements for the 7×7 real structure. The total time to calculate one value of β is about 8.1 and 14.9 hours for 100 and 120 elements to obtain the real β, and 18.3 and 29.8 hours for 120 and 140 elements to obtain the complex β. As for a frequency, about 30 times of this calculation are performed in our simulation to give the

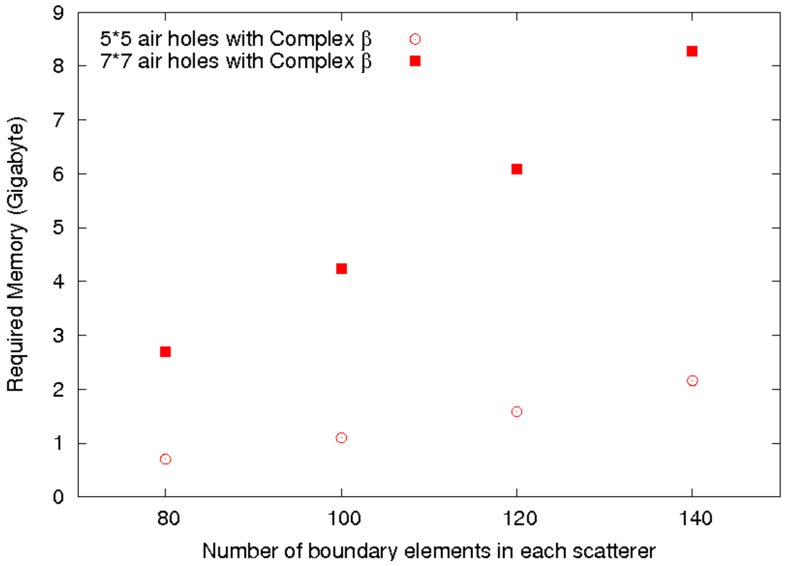

Figure 6.6: The dependence of the required computer memory for different sizes of structure on the number of boundary elements.

accurate β value.

In the next section, we present calculations for our model structures using a standard number of 120 elements for each air hole scatterer. For the high-index intersections in the ideal model structure, the number of elements is chosen as 20; this is sufficient because of the very small area of the intersections compared to the air holes.

6.6 Results and discussions

We start by restating the three model structures to be investigated: the 5×5 ideal structure, 5×5 real structure and 7×7 real structure. The comparison of the 5×5 ideal and 5×5 real structures allows the analysis of the difference between perfect guidance (i.e. the analytic solution) and a realistic case; and by comparing the 5×5 real and 7×7 real structures, the effect of the cladding on the guidance mechanism can be investigated.

Based on the structural parameters discussed in Section 6.1, the propagation constants for the 5×5 ideal and 5×5 real model structures are shown in Figures 6.7 and 6.8. Fig.6.7 shows the real part of the effective indices of the fundamental guided modes in a selected region of normalised frequency. Scalar and vector

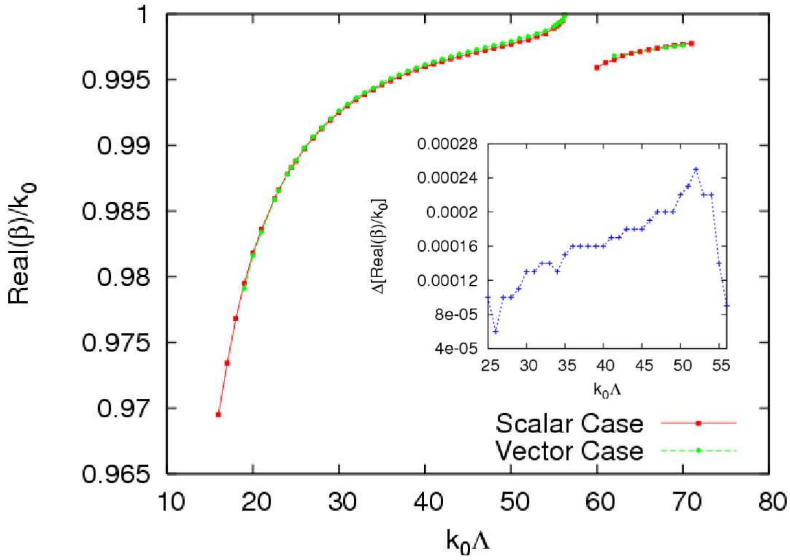

Figure 6.7: Variation of the real part of the effective index β/k_0 with the normalised frequency $k_0\Lambda$. The red and green points are for 5×5 ideal and real structures, which are governed by scalar and vector wave equations, respectively. The difference between the real and ideal case is shown in the inner figure.

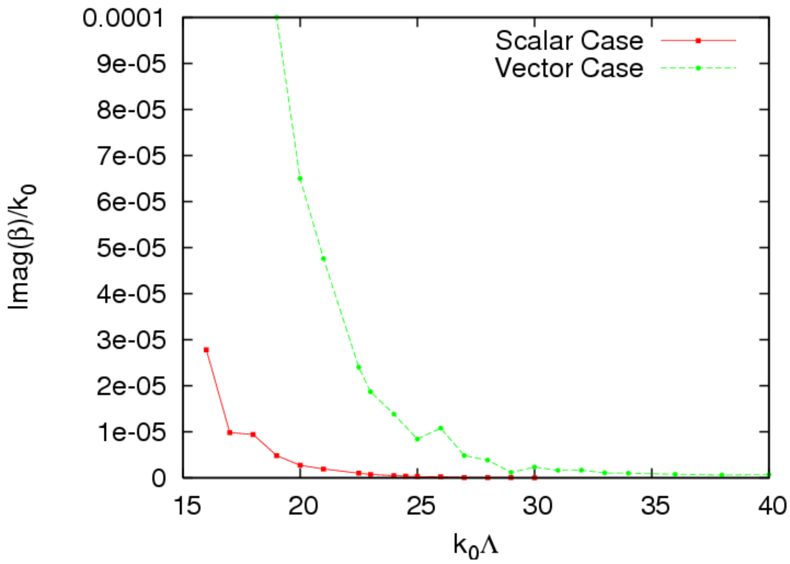

Figure 6.8: Variation of the imaginary part of the effective index β/k_0 with normalised frequency $k_0\Lambda$.

codes are used to calculate 5×5 ideal and 5×5 real structures respectively. It can be seen that the effective indices of the fundamental guided modes match closely. The exact value of the difference for the effective indices between the ideal and real cases, $\Delta\left[\mathrm{Re}(\beta)/k_0\right]$, is shown in the inset of Fig.6.7. It shows their difference is less than 3×10^{-4} over the selected range of $k_0\Lambda$ from 25 to 56. The maximum value of $\Delta\left[\mathrm{Re}(\beta)/k_0\right] = 2.5 \times 10^{-4}$ appears when $k_0\Lambda = 52$, and for the frequencies away from that, the difference roughly decreases monotonously. This indicates that the ideal scalar model may provide a useful starting point for analysis of guidance in more realistic structures. The features observed at $k_0\Lambda{\sim}58$ is due to a transverse resonance of the modes in the glass struts. A similar feature is seen for $k_0\Lambda{\sim}140$ in Fig.4.2 (c) for the hexagonal Kagome PCF. It will be discussed in more detail in Chapter 11.

Fig.6.8 compares the normalised frequency dependence of the imaginary part of β/k_0 for the scalar and vector cases in 5×5 ideal and 5×5 real structures. In both cases the loss drops rapidly with $k_0\Lambda$. We also find that the confinement loss for the real case is more than one magnitude larger than for the scalar case. Moreover, the imaginary part of the propagation constant for the real structure fluctuates more rapidly than for the ideal structure. The difference is caused by the perturbations in the real structure breaking the exponential localisation of the ideal case, as will be discussed in Chapters 9 and 10.

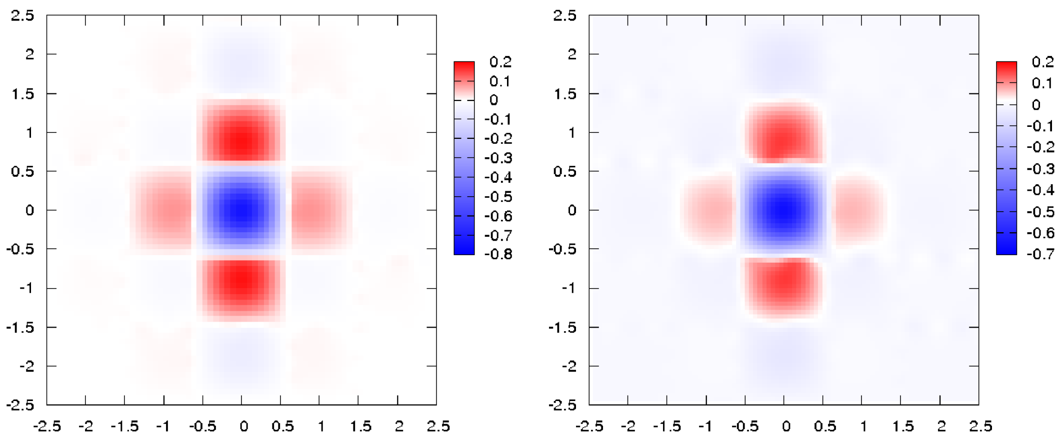

Figure 6.9: Plots of the magnetic field for fundamental guided modes in the 5×5 real structure. The left is for $k_0\Lambda = 25.0$, $\beta\Lambda$=(24.7218,0.00021), where the guided mode is confined well. The right is for $k_0\Lambda = 26.0$, $\beta\Lambda$=(25.7351,0.00028), where the fundamental mode is spreading compared to the left plot.

For some points (e.g. $k_0\Lambda = 26$), the value of the imaginary part of β for the vector case is larger than for nearby frequencies. This corresponds to a frequency where the modes are not 'clean' guided modes. Our simulations show that other modes appear and interact; this is similar to the surface crossings described in Chapter 4. Fig.6.9 shows the transverse magnetic fields for the fundamental guided modes in the 5×5 real structure. By comparing the magnitude of the fields in the central hole and cladding, we find that when $k_0\Lambda = 26$, the fundamental mode is not so well localised and interacts more with the cladding.

We have also investigated the effects of different amounts of the cladding structure. For the real structure governed by vector wave equations, the propagation constants for 5×5 and 7×7 rectangular hollow-core PCFs are plotted in Figs 6.10 and 6.11. The real parts of β for the 5×5 and 7×7 structures are very closely matched, up to 5 decimal places. However, for 7×7 real structure, the imaginary part of β is several times lower than for the 5×5 real structure (see Fig.6.11). This indicates that the confinement loss depends significantly on the size of cladding within three concentric square glass layers around the central air hole. An interesting feature of Fig.6.11 is that the relative high loss regions exist at the same frequencies for the two structures (e.g. when $k_0\Lambda = 26$), where the mode interaction is strong for both of them.

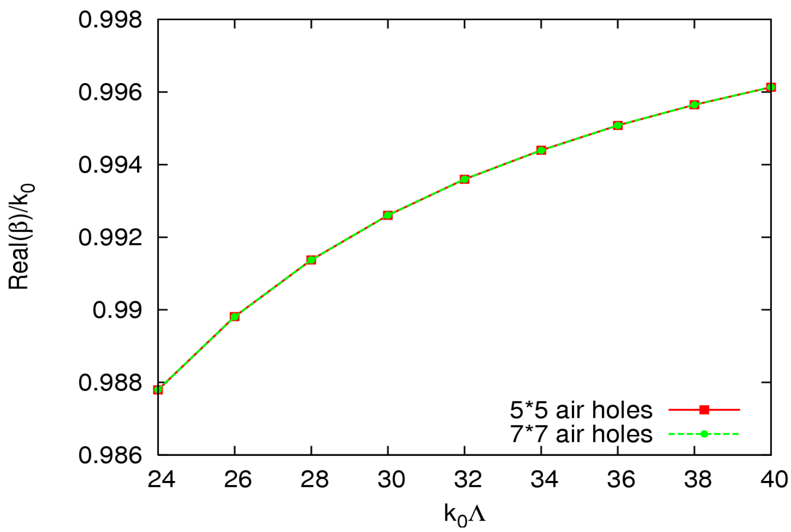

Figure 6.10: Variation of the real part of the effective index β/k_0 for fundamental guided mode with normalised frequency for different sizes of cladding structure. The results are calculated based on the real model structure and the vector governing equation.

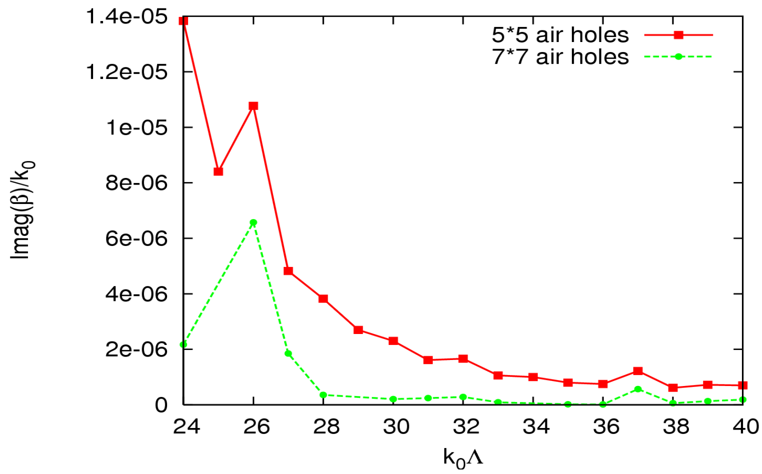

Figure 6.11: Variation of the imaginary part of the effective index β/k_0 with normalised frequency for different sizes of cladding structure.

6.7 Conclusions

We have presented calculations for rectangular hollow-core PCFs using the boundary element method. The particular model structures and operation of the program have been given and a circular fibre structure used to verify the accuracy of the calculations. The convergence and efficiency of the calculations has also been discussed. When calculating the model structures, a suitable choice of the number of elements for each scatterer should be made, taking into account both the required accuracy and a reasonable amount of computer memory and CPU time.

In our calculation, the propagation constants for 5×5 ideal and real model structures are compared. The difference of the real part of the effective index is at about the 10^{-4} level for normalised frequency varying from 19 to 56, and the imaginary part for the ideal model is more than one magnitude lower than for the real one. This shows that the perturbation of the modes plays the main role in the confinement loss. For a small size of cladding (e.g. 5×5 and 7×7 cells in our model structures), there exists a strong dependence of the confinement loss on the thickness of the cladding in rectangular hollow-core PCFs. However, the influence on the real part of the effective index is very small, of the order of 10^{-5} for $\beta\Lambda$ in the selected region of frequencies. It was also found that at some frequencies the confinement loss is more significant (e.g. $k_0\Lambda = 26$ in our model) regardless of the size of the cladding, and plots of the magnetic fields show that the interaction of the modes is strengthened.

Chapter 7

Analytic methods for the ideal model structure

The previous two chapters discussed the derivation and application of boundary element methods in the model PCF structures. In this chapter, we will demonstrate an analytic method to calculate the guidance for the ideal model.

The ideal model structure is an important part in understanding the guidance. First, as will be shown below, it can be solved exactly by using the scalar governing equation (i.e. Helmholtz equation), where the solution is separated into two independent one-dimensional expressions. The analytic results provide many benefits for the analysis of guidance, which has been discussed in Section 2.2 in Chapter 2. Second, the ideal model structure has perfect guided modes and exhibits an ideal confinement for this type of PCF. Third, the real structure can be analysed using perturbation theory to see how the difference from the ideal structure affects the guidance properties.

In the following sections of this chapter, analytic solutions for the ideal structure will be derived for both an infinite cladding and a supercell geometry. This work is based on the notes and codes completed by Professor Tim Birks and Dr. Greg Pearce. As a further development, we present an analytic method to determine the complete mode structure over a range of normalised frequencies in a supercell geometry.

This chapter is organised as follows: In Section 7.1, the scalar governing equations are separated along the orthogonal directions in the transverse plane. A set of new variables relating to the wave frequency and dielectric constant are established for the convenience of analysis. Expressions for the fields are developed in Section 7.2, where the transfer matrix is introduced to connect the neighbouring layers with different refractive indices. This transfer matrix will be widely employed in our analytic solutions. Section 7.3 gives the derivation of the field expressions for the periodic structure, where the fields satisfy Bloch's theorem. From this, we can find the photonic band structure. Sections 7.4 and 7.5 discuss the application to the model PCF structures with a central defect in either an infinite cladding or a supercell geometry. The method used to construct the whole mode map for a range of frequencies in the supercell structure is described in Section 7.6. Section 7.7 is the summary.

7.1 Separation of the governing equation

Due to the similar forms of the scalar electric and magnetic governing equations, we focus on the magnetic field in our derivations. As shown in Eq.(2.19), the scalar magnetic wave equation for the ideal structure is

$$[\nabla_t^2 + n^2(x,y)k_0^2 - \beta^2]h_t = 0, \tag{7.1}$$

where k_0 and β are the wavenumber and propagation constant, and the scalar expression h_t can be either x or y polarised. As discussed previously, the ideal model has identical arrangements for the dielectric constant $n^2(x,y)$ along both x and y directions in the transverse plane. This characteristic means that $n^2(x,y)$ can be separated as

$$n^2(x,y) = n_a^2 + \triangle n_x^2 + \triangle n_y^2, \tag{7.2}$$

where n_a^2 is the dielectric constant for the air holes, and $\triangle n_x^2$ and $\triangle n_y^2$ are the differences of the dielectric constants between the glass strips and air holes along the x and y directions respectively. By defining refractive index for the glass strips as n_g, we have

$$\triangle n_x^2 = \triangle n_y^2 = \begin{cases} n_g^2 - n_a^2 & \text{for the glass strips} \\ 0 & \text{for the air holes.} \end{cases} \tag{7.3}$$

In the boundary element calculations of Section 6.1, the refractive index for the high-index intersections was chosen to be $\sqrt{2n_g^2 - n_a^2}$. This can now be explained. Based on Eq.(7.3), we know that at the intersections of the strips the total dielectric constant contains three parts: the dielectric constant of the air holes is n_a^2, and the difference between the strips and air holes along both x and y directions is $(n_g^2 - n_a^2)$. The sum in Eq.(7.2) therefore gives $(2n_g^2 - n_a^2)$. Thus, the dielectric constant n^2 in the ideal model structure has three different values

$$n^2 = \begin{cases} n_a^2 & \text{for the air holes} \\ n_g^2 & \text{for the glass strips} \\ 2n_g^2 - n_a^2 & \text{for the high-index intersections.} \end{cases} \tag{7.4}$$

Because of the separable nature of the dielectric constant, the solutions of Eq.(7.1) can be written in the form

$$h(x, y) = X(x)Y(y). \tag{7.5}$$

By substituting Eqs.(7.2) and (7.5) into Eq.(7.1), we find

$$\begin{aligned} \frac{\partial^2 X(x)}{\partial x^2}Y(y) + \frac{\partial^2 Y(y)}{\partial y^2}X(x) + k_0^2 n_a^2 X(x)Y(y) + k_0^2 \triangle n_x^2(x)X(x)Y(y) \\ +k_0^2 \triangle n_y^2(y)X(x)Y(y) - \beta^2 X(x)Y(y) = 0, \end{aligned} \tag{7.6}$$

and by dividing by $X(x)Y(y)$, Eq.(7.6) can be separated into

$$\frac{d^2 X(x)}{dx^2} + p_x^2(x)X(x) = 0 \tag{7.7}$$

and

$$\frac{d^2 Y(y)}{dy^2} + p_y^2(y)Y(y) = 0, \tag{7.8}$$

where $p_x^2(x)$ and $p_y^2(y)$ are defined as

$$p_x^2(x) = k_0^2 n_a^2 + k_0^2 \triangle n_x^2(x) - \beta^2 - \alpha \tag{7.9}$$

$$p_y^2(y) = k_0^2 \triangle n_y^2(y) + \alpha. \tag{7.10}$$

Here the new variable α is the separation constant which couples the governing equations in the two different directions.

For convenience, we now rewrite Eqs.(7.9) and (7.10) in dimensionless forms. The definition of p_x^2 and p_y^2 shows that they have different values in different regions, so we can use p_{ig}^2 and p_{ia}^2 to express the value in the glass strips and air holes respectively, where i denotes x or y. In the high-index intersections, we define p_g^2 as the sum of the two components and write

$$p_g^2 = p_{xg}^2 + p_{yg}^2 = k_0^2(2n_g^2 - n_a^2) - \beta^2 = K_T^2. \tag{7.11}$$

K_T can be interpreted as the magnitude of the transverse wavevector in the high-index intersections. It can be seen that the separation constant α in Eqs.(7.9) and (7.10) describes how the 'available' wavevector is divided into x and y components. We can introduce trigonometric functions to replace α and express the transverse components of the wavevector in the glass strips as

$$p_{xg} = K_T \cos\theta \tag{7.12}$$

$$p_{yg} = K_T \sin\theta. \tag{7.13}$$

With this notation, the transverse wavevectors in the glass strips and air holes along the x and y directions can be written in the forms

$$p_{xg}^2 = \left[k_0^2\left(2n_g^2 - n_a^2\right) - \beta^2\right]\cos^2\theta \tag{7.14}$$

$$p_{yg}^2 = \left[k_0^2\left(2n_g^2 - n_a^2\right) - \beta^2\right]\sin^2\theta \tag{7.15}$$

$$p_{xa}^2 = \left[k_0^2\left(2n_g^2 - n_a^2\right) - \beta^2\right]\cos^2\theta - k_0^2\left(n_g^2 - n_a^2\right) \tag{7.16}$$

$$p_{ya}^2 = \left[k_0^2\left(2n_g^2 - n_a^2\right) - \beta^2\right]\sin^2\theta - k_0^2\left(n_g^2 - n_a^2\right). \tag{7.17}$$

An alternative variable $C = \cos(2\theta)$ can be used to describe the magnitude of K_T in the x and y directions as

$$C = \begin{cases} -1 & \text{when } \theta = \pm\pi/2;\, K_T \text{ along } \pm y \\ 0 & \text{when } \theta = \pm\pi/4, \pm 3\pi/4;\, K_T \text{ at } \pm\pi/4, \pm 3\pi/4 \\ 1 & \text{when } \theta = 0, \pi;\, K_T \text{ along } \pm x. \end{cases} \tag{7.18}$$

By using C to replace θ, the components of the wavevectors become

$$p_{xg}^2 = \left[k_0^2\left(2n_g^2 - n_a^2\right) - \beta^2\right]\frac{1+C}{2} \tag{7.19}$$

$$p_{yg}^2 = \Big[k_0^2\big(2n_g^2 - n_a^2\big) - \beta^2\Big]\frac{1-C}{2} \tag{7.20}$$

$$p_{xa}^2 = \Big[k_0^2\big(2n_g^2 - n_a^2\big) - \beta^2\Big]\frac{1+C}{2} - k_0^2\big(n_g^2 - n_a^2\big) \tag{7.21}$$

$$p_{ya}^2 = \Big[k_0^2\big(2n_g^2 - n_a^2\big) - \beta^2\Big]\frac{1-C}{2} - k_0^2\big(n_g^2 - n_a^2\big). \tag{7.22}$$

A constant pitch of Λ can be introduced, leading to normalised wavevector components, which are denoted as $p_{xj}\Lambda$ and $p_{yj}\Lambda$. We substitute normalised parameters

$$V = k_0 n_a \Lambda \tag{7.23}$$

$$n_R = n_g/n_a \tag{7.24}$$

$$b = \beta/(k_0 n_a) \tag{7.25}$$

into Eqs.(7.19) to (7.22), and the normalised wavevector components become

$$\big(p_{xg}\Lambda\big)^2 = \Big[\big(2n_R^2 - 1 - b^2\big) + C\big(2n_R^2 - 1 - b^2\big)\Big]\frac{V^2}{2} \tag{7.26}$$

$$\big(p_{yg}\Lambda\big)^2 = \Big[\big(2n_R^2 - 1 - b^2\big) - C\big(2n_R^2 - 1 - b^2\big)\Big]\frac{V^2}{2} \tag{7.27}$$

$$\big(p_{xa}\Lambda\big)^2 = \Big[\big(1 - b^2\big) + C\big(2n_R^2 - 1 - b^2\big)\Big]\frac{V^2}{2} \tag{7.28}$$

$$\big(p_{ya}\Lambda\big)^2 = \Big[\big(1 - b^2\big) - C\big(2n_R^2 - 1 - b^2\big)\Big]\frac{V^2}{2}. \tag{7.29}$$

Although we have defined the refractive indices to be those for glass and air, it can be seen that the analysis could be applied to any two materials. In our particular case, when $n_a = 1$, V is the usual frequency parameter $k_0\Lambda$, n_R is just n_g, and b is the effective index of the mode.

By looking at the normalised wavevectors for the x and y components in Eqs.(7.26) to (7.29), we can sort the modes into two different types: 'symmetric modes' (with $C = 0$) and 'non-symmetric modes' (with $C \neq 0$). These have the same and different transverse wavevector components in the x and y directions, respectively. As we shall see, solutions for $C = 0$ are important because, from them, we can derive solutions for other values of C.

7.2 Matrix expression for the fields

In this section, we will solve the one-dimensional governing equations, Eqs.(7.7) and (7.8), by applying the boundary conditions to express the fields in a matrix form. Field expressions in a periodic cladding structure have been given in Ref. [101] in a discussion of the photonic band structure of a dielectric stack. Here we develop more general expressions, which can be applied both in periodic and non-periodic arrangements of one-dimensional structures with different refractive indices.

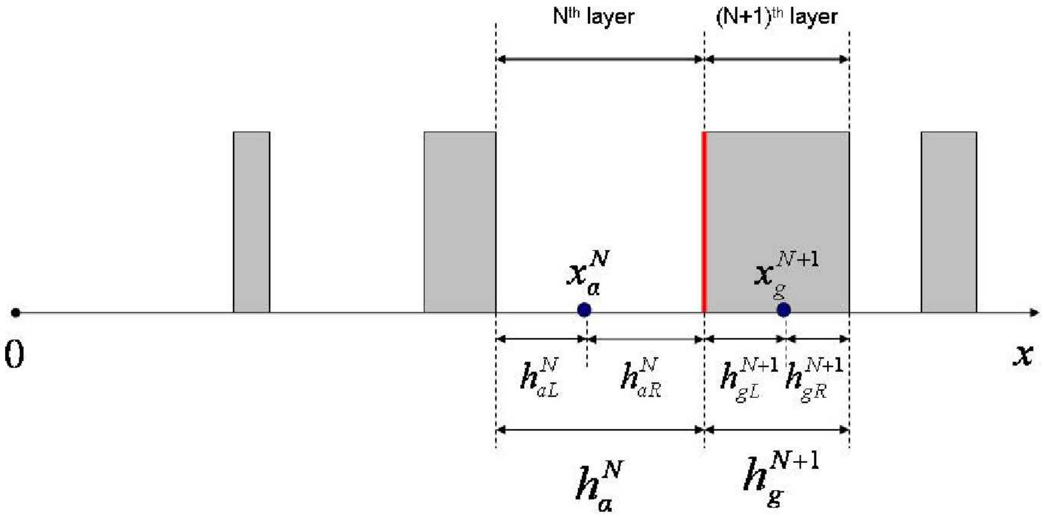

Figure 7.1: Sketch of a general one-dimensional arrangement of air and glass regions. The light and dark colours represent air and glass, respectively. The widths of the N^{th} air and $(N+1)^{th}$ glass regions are h_a^N and h_g^{N+1}. x_a^N and x_g^{N+1} are two arbitrary points within the air and glass.

A schematic of the structure considered is shown in Fig.7.1, where the structural parameters are defined for the N^{th} and $(N+1)^{th}$ layers of an extended structure. Here we assume that the layers are composed of air and glass. The lengths of the selected regions are taken to be h_a^N and h_g^{N+1}, where the subscripts a and g represent the air and glass respectively. Similarly to the treatment in Ref. [101], two points within the air and glass regions are selected and denoted as x_a^N and x_g^{N+1}. The one-dimensional waves satisfying Eqs.(7.7) in the N^{th} layer of this structure can be written as [101]

$$X_j^N(x) = a_j^N \cos\left[p_{xj}\left(x - x_j^N\right)\right] + b_j^N \frac{\sin\left[p_{xj}\left(x - x_j^N\right)\right]}{p_{xj}}, \tag{7.30}$$

where a_j^N and b_j^N are arbitrary constants, $j = a, g$ represents the materials of the structure, and p_{xj} is the wavevector component referring to material j. The equivalent expression with respect to the normalised wavevectors and dimensionless variables has the form

$$X_j^N(x') = a'^N_j \cos\Big[(p_{xj}\Lambda)\big(x' - x'^N_j\big)\Big] + b'^N_j \frac{\sin\Big[(p_{xj}\Lambda)\big(x' - x'^N_j\big)\Big]}{\big(p_{xj}\Lambda\big)}, \tag{7.31}$$

where $x' = x/\Lambda$ and $x'^N_j = x_j^N/\Lambda$, and the dimensionless lengths are $h'^N_a = h_a^N/\Lambda$ and $h'^{N+1}_g = h_g^{N+1}/\Lambda$. a'^N_j and b'^N_j are new field coefficients corresponding to the dimensionless case. We note that the following derivation will be based on this dimensionless notation, therefore x', h'^N_a, h'^{N+1}_g, a'^N_j and b'^N_j are replaced by x, h_a^N, h_g^{N+1}, a_j^N and b_j^N for simplification.

The fields and their derivatives at the boundary between the N^{th} and $(N+1)^{th}$ layers, which is denoted by the red line in Fig.7.1, can be expressed as

$$X_a^N\Big(h_{aR}^N\Big) = a_a^N \cos\Big[(p_{xa}\Lambda)h_{aR}^N\Big] + \frac{b_a^N}{p_{xa}\Lambda} \sin\Big[(p_{xa}\Lambda)h_{aR}^N\Big] \tag{7.32}$$

$$X'^N_a\Big(h_{aR}^N\Big) = -a_a^N(p_{xa}\Lambda) \sin\Big[(p_{xa}\Lambda)h_{aR}^N\Big] + b_a^N \cos\Big[(p_{xa}\Lambda)h_{aR}^N\Big] \tag{7.33}$$

$$X_g^{N+1}\Big(-h_{gL}^{N+1}\Big) = a_g^{N+1} \cos\Big[(p_{xg}\Lambda)h_{gL}^{N+1}\Big] - \frac{b_g^{N+1}}{p_{xg}\Lambda} \sin\Big[(p_{xg}\Lambda)h_{gL}^{N+1}\Big] \tag{7.34}$$

$$X'^{N+1}_g\Big(-h_{gL}^{N+1}\Big) = a_g^{N+1}(p_{xg}\Lambda) \sin\Big[(p_{xg}\Lambda)h_{gL}^{N+1}\Big] + b_g^{N+1} \cos\Big[(p_{xg}\Lambda)h_{gL}^{N+1}\Big], \tag{7.35}$$

where additional subscripts L and R are introduced, as shown in Fig.7.1. In the scalar case, both the fields and their derivatives are continuous at the interface. So Eqs.(7.32) to (7.35) can be expressed in a matrix form as

$$\begin{pmatrix} \cos\big[(p_{xa}\Lambda)h_{aR}^N\big] & \sin\big[(p_{xa}\Lambda)h_{aR}^N\big]/(p_{xa}\Lambda) \\ -(p_{xa}\Lambda)\sin\big[(p_{xa}\Lambda)h_{aR}^N\big] & \cos\big[(p_{xa}\Lambda)h_{aR}^N\big] \end{pmatrix} \begin{pmatrix} a_a^N \\ b_a^N \end{pmatrix} =$$
$$\begin{pmatrix} \cos\big[(p_{xg}\Lambda)h_{gL}^{N+1}\big] & -\sin\big[(p_{xg}\Lambda)h_{gL}^{N+1}\big]/(p_{xg}\Lambda) \\ (p_{xg}\Lambda)\sin\big[(p_{xg}\Lambda)h_{gL}^{N+1}\big] & \cos\big[(p_{xg}\Lambda)h_{gL}^{N+1}\big] \end{pmatrix} \begin{pmatrix} a_g^{N+1} \\ b_g^{N+1} \end{pmatrix}. \tag{7.36}$$

Based on Eq.(7.36), in order to connect the fields for all the layers in the structure, both h_{jL} and h_{jR} are required. To avoid this complexity, the reference point x_j^N can be chosen as the centre of each layer so that $h_{jL}^N = h_{jR}^N = h_j^N/2$. Eq.(7.36) then reduces to

$$\left(\begin{array}{cc} \cos\left[(p_{xa}\Lambda)\frac{h_a^N}{2}\right] & \sin\left[(p_{xa}\Lambda)\frac{h_a^N}{2}\right]/(p_{xa}\Lambda) \\ -(p_{xa}\Lambda)\sin\left[(p_{xa}\Lambda)\frac{h_a^N}{2}\right] & \cos\left[(p_{xa}\Lambda)\frac{h_a^N}{2}\right] \end{array}\right)\left(\begin{array}{c} a_a^N \\ b_a^N \end{array}\right) =$$

$$\left(\begin{array}{cc} \cos\left[(p_{xg}\Lambda)\frac{h_g^{N+1}}{2}\right] & -\sin\left[(p_{xg}\Lambda)\frac{h_g^{N+1}}{2}\right]/(p_{xg}\Lambda) \\ (p_{xg}\Lambda)\sin\left[(p_{xg}\Lambda)\frac{h_g^{N+1}}{2}\right] & \cos\left[(p_{xg}\Lambda)\frac{h_g^{N+1}}{2}\right] \end{array}\right)\left(\begin{array}{c} a_g^{N+1} \\ b_g^{N+1} \end{array}\right). \qquad (7.37)$$

The matrices in front of the field coefficients in Eq.(7.37) have a similar form, which allows Eq.(7.37) to be written as

$$\underline{\underline{m}}\Big(\frac{h_a^N}{2}, p_{xa}\Lambda\Big)\,\underline{a}_a^N = \underline{\underline{m}}\Big(-\frac{h_g^{N+1}}{2}, p_{xg}\Lambda\Big)\,\underline{a}_g^{N+1}, \qquad (7.38)$$

where

$$\underline{a}_j^N = (a_j^N, b_j^N)^T \qquad (7.39)$$

$$\underline{a}_j^{N+1} = (a_j^{N+1}, b_j^{N+1})^T, \qquad (7.40)$$

and

$$\underline{\underline{m}}(h,p) = \left(\begin{array}{cc} \cos(hp) & \sin(hp)/p \\ -p\sin(hp) & \cos(hp) \end{array}\right). \qquad (7.41)$$

Eq.(7.38) can then be written in an alternative form to express the field coefficients in the $(N+1)^{th}$ layer in terms of those in the N^{th} layer

$$\underline{a}_g^{N+1} = \underline{\underline{m}}\Big(-\frac{h_g^{N+1}}{2}, p_{xg}\Lambda\Big)^{-1}\,\underline{\underline{m}}\Big(\frac{h_a^N}{2}, p_{xa}\Lambda\Big)\,\underline{a}_a^N. \qquad (7.42)$$

Eq.(7.42) is the transfer matrix expression to connect the field coefficients between neighbouring layers. The transfer matrix can also be written as matrix $\underline{\underline{T}}$, and Eq.(7.38) becomes

$$\underline{a}_g^{N+1} = \underline{\underline{T}}\Big(\frac{h_a^N}{2}, p_{xa}\Lambda; \frac{h_g^{N+1}}{2}, p_{xg}\Lambda\Big)\,\underline{a}_a^N, \qquad (7.43)$$

with

$$\underline{\underline{T}} = \underline{\underline{m}}\Big(-\frac{h_g^{N+1}}{2}, p_{xg}\Lambda\Big)^{-1}\,\underline{\underline{m}}\Big(\frac{h_a^N}{2}, p_{xa}\Lambda\Big). \qquad (7.44)$$

By applying Eqs.(7.43) and (7.44), the whole field profile can be derived from the field coefficients for an arbitrary layer. In the following derivations, Λ is chosen as the pitch of the cladding structure.

7.3 Full periodic structure

The preceding section is based on a general one-dimensional arrangement of two optical materials. We now consider the transfer matrix for a completely periodic system composed of air and glass regions. By calculating all the allowed propagation constants for a range of frequencies in this configuration, the photonic density of states can be plotted.

The field coefficients for the $(N+2)^{th}$ and N^{th} glass strips have the relation

$$\underline{a}_g^{N+2} = \underline{\underline{T}}\Big(\frac{h_a}{2}, p_{xa}\Lambda; \frac{h_g}{2}, p_{xg}\Lambda\Big)\,\underline{\underline{T}}\Big(\frac{h_g}{2}, p_{xg}\Lambda; \frac{h_a}{2}, p_{xa}\Lambda\Big)\underline{a}_g^N \equiv \underline{\underline{M}}\;\underline{a}_g^N, \qquad (7.45)$$

where the transfer matrix expression Eq.(7.43) is used twice to pass through the $(N+1)^{th}$ air region between the $(N+2)^{th}$ and N^{th} glass strips. Because the structure is periodic, h_a and h_g no longer need the N label. The field coefficients $\underline{a}_g^{N+2}$ and $\underline{a}_g^N$ in Eq.(7.45) are for equivalent points in the periodic structure. By Bloch's theorem, the fields in the $(N+2)^{th}$ glass layer differ only by a phase factor, $e^{ik_x\Lambda}$, from that in the N^{th} glass layer, i.e.,

$$\underline{a}_g^{N+2} = e^{ik_x\Lambda}\underline{a}_g^N. \qquad (7.46)$$

If k_x is real, the mode exists and can propagate. If k_x has an imaginary part, the Bloch waves are exponentially evanescent along the layers, and no mode can exist in an infinite cladding, as has been discussed in Chapter 3.2.

Comparing Eqs.(7.45) and (7.46), we know that $e^{ik_x\Lambda}$ must be an eigenvalue of $\underline{\underline{M}}$. In our particular case, by looking at the composition of $\underline{\underline{M}}$ contained in Eq.(7.45), it can be written as [101]

$$\underline{\underline{M}} = \begin{pmatrix} A & B \\ C & A \end{pmatrix}, \qquad (7.47)$$

where $BC = A^2 - 1$ and the determinant of $\underline{\underline{M}}$ is 1. The corresponding eigenvalues, λ, and eigenvectors $\underline{f}$ can then be written as [101]

$$\lambda_{\pm} = A \pm \sqrt{BC} \qquad (7.48)$$

$$\underline{f}_{\pm} = (\sqrt{B}, \pm\sqrt{C})^T. \tag{7.49}$$

Based on Eq.(7.48), the Bloch wavevector k_x takes the form [101]

$$k_x = \cos^{-1}(A)/\Lambda. \tag{7.50}$$

The condition for a real k_x in Eq.(7.46) is that $|A|\leq 1$; if $|A| > 1$, k_x is imaginary and the mode is not propagating.

The photonic bandstructure shows the allowed and forbidden regions for the propagation constant $\beta\Lambda$ (equivalent to b) as a function of frequency $k_0\Lambda$ (equivalent to V). The polarisation factor C is a hidden variable in these plots. In our calculations, for a given frequency, we search a range of $\beta\Lambda$ values near to the air-line. For each $\beta\Lambda$, C is varied from -1 to 1 to check whether any C value can make both k_x and k_y real (i.e. $|A|\leq 1$ for matrix $\underline{\underline{M}}$ in both x and y directions). If there is no such a value, then this $\beta\Lambda$ is forbidden and must lie in a photonic bandgap. Examples of these calculations will be presented in the next chapter.

7.4 Central defect structure

In this section, we derive the formulae to calculate the propagation constant for a central defect in an infinite cladding structure. In our modelling, the movement of the four glass strips enclosing the central air hole differentiates the full structure into two parts: the central defect and the outer cladding, as shown in Fig.7.2.

The field coefficients in the defect core and the first glass strip are defined as $\underline{a}_a^A = (a_a^A, b_a^A)^T$ and $\underline{a}_g^B = (a_g^B, b_g^B)^T$ respectively, and they are related by

$$\underline{a}_g^B = \underline{\underline{T}}\Big(\frac{h_c}{2}, p_{xa}\Lambda; \frac{h_g}{2}, p_{xg}\Lambda\Big)\,\underline{a}_a^A. \tag{7.51}$$

The connections between the next air hole and glass strip are

$$\underline{a}_a^C = \underline{\underline{T}}\Big(\frac{h_g}{2}, p_{xg}\Lambda; \frac{h_c'}{2}, p_{xa}\Lambda\Big)\,\underline{a}_g^B \tag{7.52}$$

$$\underline{a}_g^D = \underline{\underline{T}}\Big(\frac{h_c'}{2}, p_{xa}\Lambda; \frac{h_g}{2}, p_{xg}\Lambda\Big)\,\underline{a}_a^C, \tag{7.53}$$

where the labelled regions from A to D have been shown in Fig.7.2.

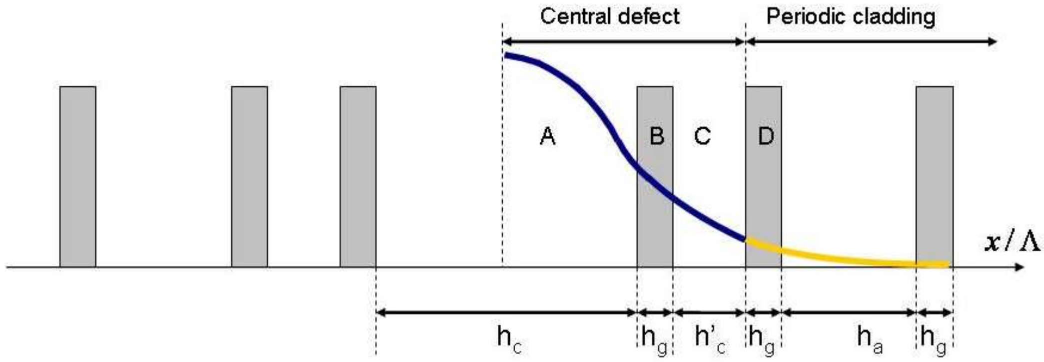

Figure 7.2: The one-dimensional central defect with infinite cladding. The light and dark colours represent the air holes and glass strips, respectively. The one-dimensional field is confined in the central defect regions A, B and C (as shown in blue) and exponentially decays after entering the periodic cladding region D (as shown in yellow). The lengths of the defect air holes are indicated by h_c and h'_c, and the lengths of the air holes and glass strips in the cladding are h_a and h_g.

By combining Eqs.(7.51) to (7.53) we find

$$\underline{a}_a^A = \left[\underline{\underline{T}}\left(\frac{h_c}{2}, p_{xa}\Lambda; \frac{h_g}{2}, p_{xg}\Lambda\right)^{-1} \underline{\underline{T}}\left(\frac{h_g}{2}, p_{xg}\Lambda; \frac{h'_c}{2}, p_{xa}\Lambda\right)^{-1} \cdot \underline{\underline{T}}\left(\frac{h'_c}{2}, p_{xa}\Lambda; \frac{h_g}{2}, p_{xg}\Lambda\right)^{-1}\right] \underline{a}_g^D. \tag{7.54}$$

In Eq.(7.54), the field coefficients for the central defect $\underline{a}_a^A$ are expressed in terms of those of the glass strip $\underline{a}_g^D$. The field coefficients $\underline{a}_g^D$ can then be expressed in terms of those of the next glass strip in the periodic cladding. The transfer matrix involved is same as Eq.(7.45). Therefore, $\underline{a}_g^D$ must also be an eigenvector of matrix $\underline{\underline{M}}$.

In our calculation, three conditions are used to determine the propagation constant of the fundamental guided mode for a specific frequency. The first is that the fundamental mode should be symmetric with respect to the x and y directions, and therefore it will have $C = 0$. The second is that the wavefunction in the semi-infinite cladding must decay exponentially. This is different from the case described for the infinite cladding; it means that the eigenvalue has an imaginary k_x and requires $|A| > 1$ in Eq.(7.47). The third condition is that the one-dimensional wavefunctions should be even with respect to the central defect. This property requires that the field coefficient b_a^A related to sine function in Eq.(7.31) should be zero. By employing these conditions, we search a range of $\beta\Lambda$ values with $C = 0$ to calculate the matrix $\underline{\underline{M}}$ in Eq.(7.45) at a specific frequency. Only the eigenvectors satisfying $|A| > 1$ are chosen as the field coefficients of $\underline{a}_g^D$. There are a number of $\beta\Lambda$ satisfying this condition. By using Eq.(7.54), $\underline{a}_a^A$ can then be determined from $\underline{a}_g^D$. By tracking the value of b_a^A/a_a^A in the central defect and looking for this ratio to approach zero, we obtain the $\beta\Lambda$ value for the fundamental guided mode.

After finding the propagation constant, the field coefficient in the central defect $\underline{a}_a^A$ can be written as $(1, 0)^T$. The whole field profile can then be obtained by using the transfer matrix and field expressions, as shown in Eqs.(7.43) and (7.31). It should be noted that the fields are calculated as relative values rather than absolute values. Although the guided mode can be normalised, the unguided modes that also exist in this structure can not easily be normalised.

For any frequency, the cladding modes within this structure can also be calculated. As will be shown in the next chapter, cladding modes with $C \neq 0$ can exist with exactly the same propagation constant as the mode guided in the central defect. Here we briefly describe this calculation process. The first step is to check on the existence of these cladding modes for a given frequency; this is equivalent to determining whether this $(k_0\Lambda, \beta\Lambda)$ combination is located within the photonic bands or not. The calculation here is same as those described in Section 7.3, but we only need to consider this particular $(k_0\Lambda, \beta\Lambda)$. If there exists a set of C values that make $|A|\leq 1$ in matrix $\underline{\underline{M}}$, then cladding modes are coexisting. By choosing a C from this and setting the field coefficients to be $(1, 0)^T$ in the central defect, the whole field for this cladding mode can be plotted by using the transfer matrix.

7.5 Symmetric modes of the supercell structure

In order to obtain a finite number of normalisable modes for the later perturbation calculations, a supercell structure has been introduced. Each supercell can be viewed a large 'unit cell', which contains $N \times N$ cells in the transverse plane. A supercell geometry is often used in computational solutions where a plane-wave basis is used. The size of a supercell should be large enough so that the coupling between the neighbouring supercells can be neglected [102, 103].

We now calculate the transfer matrix for the fields from the central defect of one supercell, $\underline{a}_a^{c(M)}$, to the neighbouring centre, $\underline{a}_a^{c(M+1)}$, as shown in Fig.7.3. Here we choose four points to denote the whole transfer matrix, where P_1 and P_4

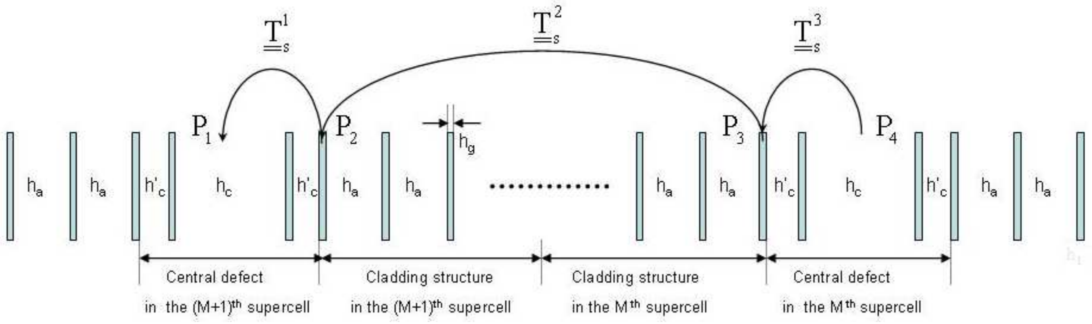

Figure 7.3: The transfer matrices in a supercell. P_1 to P_4 are four points where the fields coefficients are related. The whole transfer matrix contains three calculation steps, which are indicated by matrices $\underline{\underline{T}}_s^1$ to $\underline{\underline{T}}_s^3$.

represent the field coefficients at the central defects of neighbouring supercells, P_2 and P_3 are the field coefficients at the boundary between the central defects and the cladding. The transfer matrix $\underline{\underline{T}}_s^1$ from P_2 to P_1 can be expressed as

$$\underline{\underline{T}}_s^1 = \underline{\underline{T}}\Big(\frac{h_g}{2}, p_{xg}\Lambda; \frac{h_c}{2}, p_{xa}\Lambda\Big)\underline{\underline{T}}\Big(\frac{h_{c'}}{2}, p_{xa}\Lambda; \frac{h_g}{2}, p_{xg}\Lambda\Big)\underline{\underline{T}}\Big(\frac{h_g}{2}, p_{xg}\Lambda; \frac{h_{c'}}{2}, p_{xa}\Lambda\Big). \tag{7.55}$$

Similarly, we have (where $\underline{\underline{T}}_s^2$ and $\underline{\underline{T}}_s^3$ are defined in Fig.7.3)

$$\underline{\underline{T}}_s^2 = \left[\underline{\underline{T}}\Big(\frac{h_a}{2}, p_{xa}\Lambda; \frac{h_g}{2}, p_{xg}\Lambda\Big)\underline{\underline{T}}\Big(\frac{h_g}{2}, p_{xg}\Lambda; \frac{h_a}{2}, p_{xa}\Lambda\Big)\right]^{N-3} \tag{7.56}$$

$$\underline{\underline{T}}_s^3 = \underline{\underline{T}}\Big(\frac{h_{c'}}{2}, p_{xa}\Lambda; \frac{h_g}{2}, p_{xg}\Lambda\Big)\underline{\underline{T}}\Big(\frac{h_g}{2}, p_{xg}\Lambda; \frac{h_{c'}}{2}, p_{xa}\Lambda\Big)\underline{\underline{T}}\Big(\frac{h_c}{2}, p_{xa}\Lambda; \frac{h_g}{2}, p_{xg}\Lambda\Big). \tag{7.57}$$

The fields at the centres of the adjacent supercells can therefore be expressed as

$$\underline{a}_a^{c(M+1)} = \underline{\underline{T}}_s \underline{a}_a^{c(M)}, \tag{7.58}$$

where the overall transfer matrix $\underline{\underline{T}}_s$ is given by

$$\underline{\underline{T}}_s = \underline{\underline{T}}_s^1 \underline{\underline{T}}_s^2 \underline{\underline{T}}_s^3. \tag{7.59}$$

We analyse only those modes at the Γ point of the supercell Brillouin zone, which means that the field coefficients in the central defects of neighbouring supercells should be same for all modes. We also, for the moment, restrict our analysis to symmetric modes with the same transverse wavevector in the x and y directions, that is those with $C = 0$. Because of the symmetry of the structure, the allowed solutions will have either even or odd symmetry with respect to the centre of the central defect. The field coefficients $\underline{a}_a^{c(M)}$ can therefore be chosen to be either $(1,0)^T$ or $(0,1)^T$ for even and odd solutions respectively. The field coefficients at the central core of the $(M+1)^{th}$ supercell must then have the same value as those at the centre of the M^{th} supercell. This condition means that the matrix $\underline{\underline{T}}_s$ must have an eigenvector of $(1,0)^T$ or $(0,1)^T$ with unit eigenvalue. The propagation constants of the allowed modes can therefore be obtained by searching for these solutions of matrix $\underline{\underline{T}}_s$ with $C = 0$. After obtaining the propagation constants for the allowed modes, their fields can be plotted by using the transfer matrix from the central air hole to the cladding air and glass layers. The fundamental air-guided mode can be differentiated by finding the propagation constant nearest to the air line, or by obtaining a field confined within the central defect.

Because the field coefficients at the each centre of the supercell are assumed to be either $(1,0)^T$ or $(0,1)^T$, the calculated field expressions, $h^u(x,y)$, are relative values. The supercell structure means that all the modes, m, can be normalised by multiplying by a normalisation factor Q_m. We can write

$$h_m(x,y) = Q_m h_m^u(x,y), \tag{7.60}$$

where Q_m is given by

$$Q_m = \frac{1}{[\int X_m^u(x)^2 dx \int Y_m^u(y)^2 dy]^{1/2}}. \tag{7.61}$$

X_m^u and Y_m^u are the one-dimensional wavefunctions corresponding to the unnormalised fields, and the integrals are performed over one supercell. The particular trigonometric formulae for these integrals will be given in Chapter 9.

7.6 Non-symmetric modes for the supercell

In the previous section, the propagation constants and corresponding fields for symmetric modes with $C = 0$ have been derived for the supercell structure. However, in order to apply perturbation methods, all the modes with propagation constants close to the guided mode are required. In this section we show how all the modes of the supercell can be obtained from the symmetric modes.

To demonstrate the relationship between the symmetric and non-symmetric modes, we rewrite the governing equations, Eqs.(7.7) and (7.8) as the dimensionless forms

$$\frac{d^2X(x)}{dx^2} + \left[p_x(x)\Lambda\right]^2 X(x) = 0 \tag{7.62}$$

$$\frac{d^2Y(y)}{dy^2} + \left[p_y(y)\Lambda\right]^2 Y(y) = 0. \tag{7.63}$$

We first note that the solutions of the Helmholtz equations (7.62) and (7.63) depend only on the values of the wavevector components given by Eqs.(7.26) to (7.29). By introducing a new variable $\alpha = 2n_R^2 - 1 - b^2$, these equations are rewritten as

$$\left(p_{xg}\Lambda\right)^2 = (1+C)\alpha\frac{V^2}{2} \tag{7.64}$$

$$\left(p_{yg}\Lambda\right)^2 = (1-C)\alpha\frac{V^2}{2} \tag{7.65}$$

$$\left(p_{xa}\Lambda\right)^2 = \left[(1+C)\alpha - 2n_R^2 + 2\right]\frac{V^2}{2} \tag{7.66}$$

$$\left(p_{ya}\Lambda\right)^2 = \left[(1-C)\alpha - 2n_R^2 + 2\right]\frac{V^2}{2}. \tag{7.67}$$

When C is zero (i.e. for modes that are equivalent in x and y), we write allowed values of α and b as α_0 and b_0. For a given pair of (b, C) values, $(p_{xj}\Lambda)$ and $(p_{yj}\Lambda)$ can be determined by Eqs.(7.64) to (7.67). If these values make the field coefficients in $X(x)$ and $Y(y)$ equal to $(1,0)^T$ or $(0,1)^T$ at the centre of each supercell, then (b, C) correspond to a solution of the supercell structure.

In the x direction, there are a number of $(p_{xj}\Lambda)$ values that satisfy the Helmholtz equation. Whether C is zero or not, these $(p_{xj}\Lambda)$ values are unique because they are the only variable in the Helmholtz equation. If we look at the symmetric modes with $C = 0$, these $(p_{xj}\Lambda)$ values are determined only by a set of $\alpha_0^{(m)}$, where m labels the solutions. The solutions for non-symmetric modes can then be derived by using the following relationship

$$(1 + C^{(m)})\alpha^{(m)} = \alpha_0^{(m)}, \tag{7.68}$$

which ensures that Eqs.(7.64) and (7.66) give the same $p_{xj}\Lambda$ values. An equivalent expression for Eq.(7.68) is

$$C^{(m)} = \frac{\alpha_0^{(m)}}{\alpha^{(m)}} - 1 = \frac{b^{(m)^2} - b_0^{(m)^2}}{2n_R^2 - 1 - b^{(m)^2}}. \tag{7.69}$$

In the x direction, this gives a set of identical solutions in the (b, C) space; the trajectory of the solutions is determined from Eq.(7.69) once the solution corresponding to $C = 0$ has been found.

In the y direction, an equivalent analysis yields

$$(1 - C^{(n)})\alpha^{(n)} = \alpha_0^{(n)}, \tag{7.70}$$

where the label n is used to indicate solutions for the y direction. Eq.(7.70) can be rewritten as

$$C^{(n)} = 1 - \frac{\alpha_0^{(n)}}{\alpha^{(n)}} = \frac{b_0^{(n)^2} - b^{(n)^2}}{2n_R^2 - 1 - b^{(n)^2}}. \tag{7.71}$$

Allowed solutions for the supercell must satisfy the Helmholtz equations in both the x and y directions, which requires $b^{(m)} = b^{(n)}$ and $C^{(m)} = C^{(n)}$. By combining Eqs.(7.69) and (7.71) we find

$$\frac{b^2 - b_0^{(m)^2}}{2n_R^2 - 1 - b^2} = \frac{b_0^{(n)^2} - b^2}{2n_R^2 - 1 - b^2}, \tag{7.72}$$

which can be simplified as

$$b^2 = \frac{b_0^{(n)^2} + b_0^{(m)^2}}{2}. \tag{7.73}$$

Eq.(7.73) gives the relationship between the propagation constants of the symmetric and the non-symmetric modes. A non-symmetric mode (b, C), which is determined by the symmetric solutions $(b_0^{(m)}, 0)$ and $(b_0^{(n)}, 0)$ has the same $p_{xj}\Lambda$ value as the symmetric mode $(b_0^{(m)}, 0)$ and same $p_{yj}\Lambda$ value as the symmetric mode $(b_0^{(n)}, 0)$. Therefore, the full set of non-symmetric modes of the supercell can be derived based only on the symmetric modes. In practice, we are interested in modes where b is close to the air line. We note that, to obtain such modes, modes with a wide range of b_0^2 must be considered, including those where $b_0^{(m)^2}$ or $b_0^{(n)^2}$ may be less than zero.

7.7 Summary

In this chapter, a transfer matrix formulation for a one-dimensional structure has been derived. This method can be applied to the ideal rectangular model PCF structures due to the separable property of the scalar governing equations.

Based on the transfer matrix, methods to calculate the photonic band structure and field profiles have been discussed. This will be applied in the next chapter to the ideal model PCF structure.

Chapter 8

Results for the ideal model structure

The analytic method for the ideal model structure governed by the scalar wave equation has been discussed in Chapter 7. In this chapter, we present computational results based on the preceding derivation. Section 8.1 describes the different types of ideal structures applied in the analytic and previous boundary element calculations, and the motivation to analyse the various cases is discussed. In Sections 8.2 and 8.3, the band structure and guidance properties for a defect in the infinite cladding structure are shown. Field profiles of the modes in both the bands and bandgaps are plotted. Section 8.4 describes the symmetric modes for the supercell structure and classifies them based on their characteristics. These symmetric modes not only serve as an essential step to derive and understand the complete mode distribution, but also provide key information for the analysis of the types of modes in our ideal model structure. The whole mode structure for the supercell is found in Section 8.5 by using the results of Section 8.4. The conclusion is given in Section 8.6.

8.1 Structural details for the analytic methods

In our analytic modelling, for consistency with the results of boundary element calculations, we assume the ideal structure is made from the same materials: the refractive indices are 1.0 for the air holes and 1.5 for the glass strips, and the intersections of glass strips have a higher refractive index of 1.8708 (i.e. $\sqrt{2n_g^2 - n_a^2}$, where n_g and n_a are refractive indices for glass and air). The thickness of the glass strips is still 0.05Λ, where Λ is the pitch of the perfect periodic structure. There are three different configurations used in our analytic simulations. One is the perfect periodic cladding structure, the other two contain the same size of central defects, where the four glass strips enclosing the central air hole are moved outward by a distance of 0.125Λ. The difference between these two lies in the cladding. By including the previous ideal structure used in boundary element calculations, it is useful to list all the ideal configurations that we have simulated (as shown in Table 8.1). In these ideal systems, by comparing the structures $I1$ and $I2$, the dependence of the guidance on the photonic bandgap can be found. Furthermore, the comparison of $I2$ and $I3$ can effectively test the correctness of the analytic methods developed in Chapter 7. In the application of the perturbation methods in Chapters 9 and 10, $I4$ is an essential step because all the modes can be found and normalised for a supercell geometry.

Labels	Structures	Methods	Purpose
$I1$	Infinite without defect	Analytic	Get bandstructure
$I2$	Defect in infinite cladding	Analytic	Get perfect guidance
$I3$	Defect in finite cladding	BE	Get confinement loss due to finite cladding
$I4$	Defect in supercell geometry	Analytic	Get whole mode map for later perturbation theory

Table 8.1: The variety of ideal model structures employed in analytic and numerical simulations.

8.2 Bandstructure for infinite ideal model

The allowed and forbidden propagation constants for the perfect cladding structure can be calculated using the method described in Section 7.3. These values form the photonic bands and bandgaps in $(k_0\Lambda, \beta\Lambda)$ space for our ideal rectangular model structure. Fig.8.1 shows the comparison of bandstructures for the ideal rectangular PCF (a), a typical bandgap-guiding hollow-core PCF (b), and a reported Kagome hollow-core PCF (c). The range of normalised frequency for the ideal rectangular PCF is from 10 to 22; calculations have been performed for 400 $k_0\Lambda$ values. At each normalised frequency, n_{eff} (i.e. β/k_0) is evenly divided into 5000 values from 0.95 to 1.05, and 1000 values for the factor C are checked from -1 to 1.

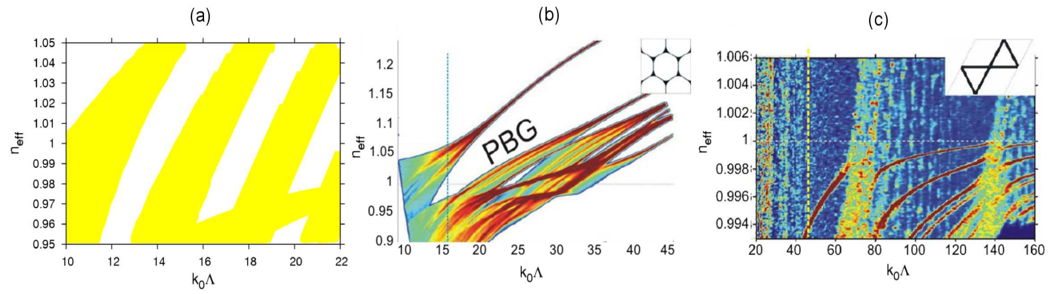

Figure 8.1: Photonic bandstructures for the ideal rectangular hollow-core PCF (a), typical bandgap-guiding PCF (b), and Kagome PCF (c). The x and y axes represent the normalised frequency $k_0\Lambda$ and effective index β/k_0, respectively. The coloured regions are photonic bands, and the white areas are photonic bandgaps. Figures (b) and (c) taken from Ref. [104].

Like the typical bandgap-guiding PCFs, the ideal model rectangular PCF has photonic bandgaps, as shown by the white areas in Fig.8.1. This property is different from Kagome PCFs. However, the shape of the bandgaps in rectangular hollow-core PCFs differs from that in bandgap-guiding hollow-core PCFs, where a single bandgap exists. In contrast, the ideal model structure has a succession of narrow bandgaps.

8.3 Guided modes within photonic bands

By using the method discussed in Chapter 7.4 we have calculated the fundamental guided mode for the ideal model structure with a central defect. The variation of the normalised propagation constant versus the normalised frequency is shown by the red line in Fig.8.2. For comparison, we also plot (with blue points) the results of boundary element calculations for a finite cladding with 5×5 air holes. The analytic and boundary element values for β/k_0 agree to four decimal places over the range of normalised frequency from 10 to 40. This indicates that the real part of β does not depend on the thickness of the cladding.

Fig.8.2 shows a striking phenomenon. In rectangular hollow-core PCFs, the fundamental guided modes exist both in the bands and bandgaps of the cladding, and they extend over a very wide range of frequencies. This property is contradictory with the mechanism of bandgap guidance. Both the independence of guidance on the bandstructure and the broad range of guidance frequencies are similar to the Kagome hollow-core PCFs. It is for this reason that we argue that rectangular hollow-core PCFs belong to the family of 'weak interaction guidance' fibres.

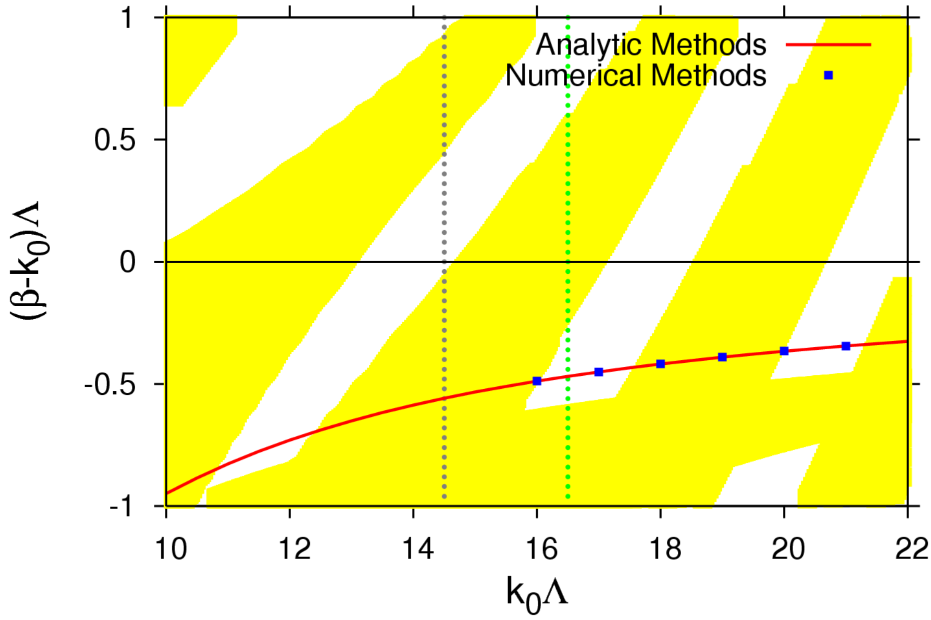

Figure 8.2: Propagation constant versus normalised frequency for the scalar governing equations in the ideal model structure. The red line and blue points are analytic and boundary element results, which are calculated for an infinite and finite (5×5 air holes) cladding respectively. The yellow and white backgrounds represent the photonic bands and bandgaps, respectively. The black and green dashed lines are two selected frequencies for which guided modes are plotted.

In order to look at the field patterns for the guided modes in both bands and bandgaps, two frequencies are selected, as shown by the black ($k_0\Lambda = 14.5$ in the band) and green ($k_0\Lambda = 16.5$ in the bandgap) dashed lines in Fig.8.2. The propagation constants, $\beta\Lambda$, for them are 13.9414 (for $k_0\Lambda = 14.5$) and 16.0312 (for $k_0\Lambda = 16.5$). The magnetic fields of the fundamental guided modes are shown in Fig.8.3 a(1) and b, respectively. They are both symmetric along the two directions and exhibit similar field shapes. Both are localised within the central defect and have exponentially decaying fields away from the defect. In addition, at $k_0\Lambda = 14.5$, it is possible to find a set of cladding modes with the same $\beta\Lambda$ as the fundamental guided mode, as discussed at the end of Section 7.4. In Fig.8.3 a(2), we show an example of these cladding modes, where $C = 0.159723$. By presenting the fundamental guided and cladding modes for the same normalised frequency and propagation constant we again confirm that guided modes can occur within the photonic bands.

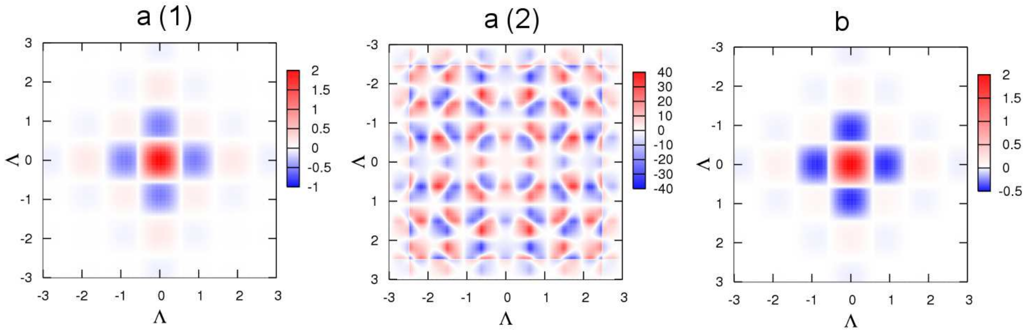

Figure 8.3: Plots of air-guided modes in the infinite cladding structure. $a(1, 2)$ are the fundamental guided mode and a cladding mode with the same frequency and propagation constant, for which $(k_0\Lambda, \beta\Lambda)$=$(14.5, 13.9414)$. b is the fundamental guided mode with $(k_0\Lambda, \beta\Lambda)$=$(16.5, 16.0312)$. $a(1, 2)$ and b are situated in the photonic band and bandgap, respectively.

It is instructive at this point to look back at the results of boundary element calculations for the confinement loss over a range of frequencies. Different guidance mechanisms result in different levels of leakage; for light guided by weak interaction guidance, the confinement loss has been found to be relatively larger than that for bandgap guidance [66,68]. The imaginary part of β for both scalar (in the 5×5 ideal structure) and vector (in the 5×5 real structure) governing equations in rectangular hollow-core PCFs has been obtained by using boundary element method in Chapter 6. Fig.6.8 shows that in both cases there is a continuous change of the confinement loss. There is no sign of a variation in confinement loss that mirrors the alternation of bands and bandgaps shown in Fig.8.2. The existence of weak interaction guidance in rectangular hollow-core PCFs indicates that this structure can serve in an analysis of this guidance mechanism.

For a deeper understanding of the weak interaction guidance, the interaction between the fundamental guided and cladding modes should be analysed. For perturbation theory to be applied, the number of modes and their amplitudes are critical information. In an infinite cladding structure, counting the number of modes and normalisation of the fields are difficult. Because of this we have used calculations based on the supercell geometry, as will be discussed in the following section.

8.4 Symmetric modes for the supercell structure

In this section, we apply analytic methods to the supercell structure to find and analyse the symmetric modes (i.e. $C = 0$) for a given frequency. The size of the supercell is assumed to be 8×8 unit cells, which means that the length of one supercell is 8Λ along both the x and y directions in the transverse plane. We choose $k_0\Lambda = 40$ as an example frequency in the computation and the following perturbation calculations. This selected frequency is located in a band for our model structure.

In our calculations, the symmetric modes are obtained by finding the even or odd one-dimensional wavefunctions with respect to the central defect, as has been discussed in Section 7.5. For even solutions we require that the value of $\left[(a-1)^2+b^2\right]$ approaches zero in the neighbouring central defect, where a and b are the field coefficients of the cosine and sine functions in Eq.(7.31). The equivalent function for odd solutions is $[a^2 + (b-1)^2]$. In our root finding, these values are tracked until they are less than 10^{-30}. This very small value is required to obtain all the solutions because the fields for some of them are small in the central defect. Quadruple precision is used to provide the required level of numerical accuracy.

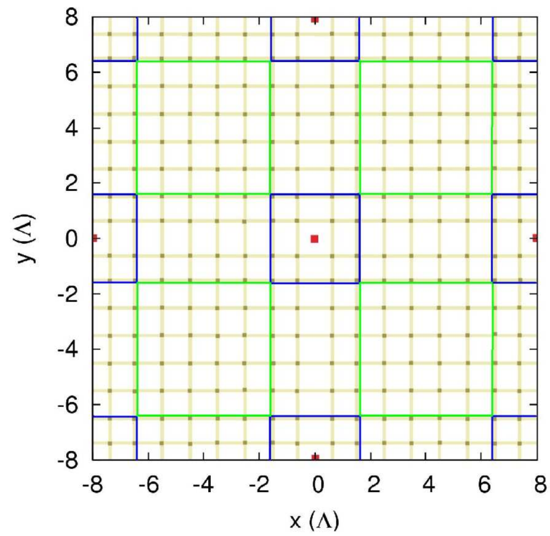

Figure 8.4: Schematic of the supercell showing the defect region surrounded by blue lines and with a red point at the centre, and the perfect cladding region surrounded by green lines.

In order to analyse and describe the modes it is convenient to divide the supercell into different regions, as shown in Fig.8.4. The central defect region has 9 air holes, while the perfect cladding region has 25 air holes. In the following sections the symmetric modes with $C = 0$ will be categorised in terms of their β values and where in the supercell the field is concentrated.

8.4.1 Results for the air-guided modes

Due to factor C being zero, the one-dimensional wavefunctions along both the x and y directions will have the same parity. They can therefore be described as 'both-even' and 'both-odd' modes. Our calculations show that there is a group of modes that exist in a range of β/k_0 from 0.991 to 0.997. These modes are relatively isolated from the others in terms of their propagation constants and they include the fundamental defect guided mode; thus we call this region the 'guided area'. The both-even and both-odd modes in the guided area are listed in Tables 8.2 and 8.3, respectively.

Label	(b^2,C)	Label	(b^2, C)
A(1)	(0.99195051980024, 0)	A(2)	(0.98847913625764, 0)
A(3)	(0.98738164082161, 0)	A(4)	(0.98596345041728, 0)
A(5)	(0.98295725827093, 0)		

Table 8.2: The both-even symmetric modes in the guided area at $k_0\Lambda = 40$ for the 8×8 ideal supercell structure. The variable b^2 is defined by $b^2 = (\beta/k_0)^2$, and the factor C is zero.

Label	(b^2,C)	Label	(b^2, C)
B(1)	(0.98804490266687, 0)	B(2)	(0.98662722200955, 0)
B(3)	(0.98318048286092, 0)		

Table 8.3: The both-odd symmetric modes in the guided area at $k_0\Lambda = 40$ for the 8×8 ideal supercell structure.

There are five both-even and three both-odd modes in this β range. Among them is the fundamental air-guided mode, labelled by $A(1)$ in Table.8.2. The $\beta\Lambda$ value of this mode is 39.838685, which agrees to at least six decimal places with the result for the infinite cladding. This illustrates that the supercell calculation is very accurate, and shows that the interactions between supercells can be neglected.

The transverse field profiles for all these symmetric modes are shown in Fig.8.5.

Because of the range of β chosen, these modes have fields which are situated mainly in the air holes of the structure. It is also seen that the total number of symmetric modes near to the fundamental guided mode (including the guided mode itself) is 8, which is associated with the size of 8×8 supercell.

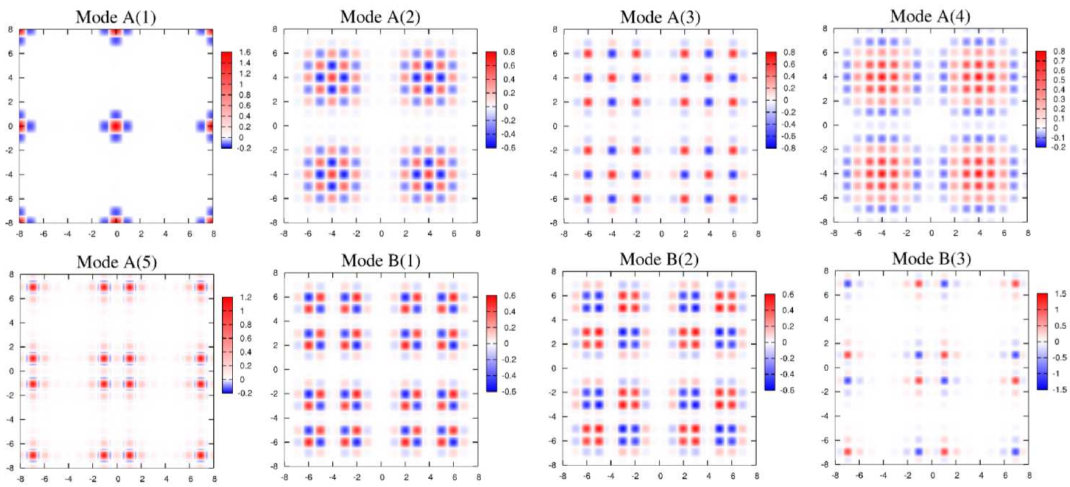

Figure 8.5: Field plots in the transverse plane for the symmetric modes (i.e. $C = 0$) in the guided area when $k_0\Lambda = 40$. The wave functions in modes $A(1)$ to $A(5)$ are both even along two different directions, and in modes $B(1)$ to $B(3)$ are both odd. The mode $A(1)$ is the fundamental guided mode. The propagation constants of these modes are given in Tables 8.2 and 8.3.

8.4.2 High-index modes

When the propagation constant is much higher than for the guided area, other groups of modes are found and are shown in Tables 8.4 and 8.5, corresponding to the both-even and both-odd parities. The normalised propagation constants for them are large, but also show an extremely narrow difference between them, with $\beta\Lambda$ varying from 60.09612950777 to 60.09612950785. Due to this property, these modes are named 'high-index modes' in this thesis.

Label	(b^2, C)	Label	(b^2, C)
C(1)	(2.257215488640370478, 0)	C(2)	(2.257215488637439480, 0)
C(3)	(2.257215488637311172, 0)	C(4)	(2.257215488634322805, 0)

Table 8.4: The both-even symmetric modes (higher than the guided area) at $k_0\Lambda = 40$ for the 8×8 ideal supercell model.

The field profiles for these modes are shown in Fig.8.6, where it can be seen that

Label	(b^2, C)	Label	(b^2, C)
D(1)	(2.257215488640370458, 0)	D(2)	(2.257215488637382090,0)
D(3)	(2.257215488637253782, 0)	D(4)	(2.257215488634322784, 0)

Table 8.5: The both-odd symmetric modes (higher than the guided area) at $k_0\Lambda = 40$ for the 8×8 ideal supercell model.

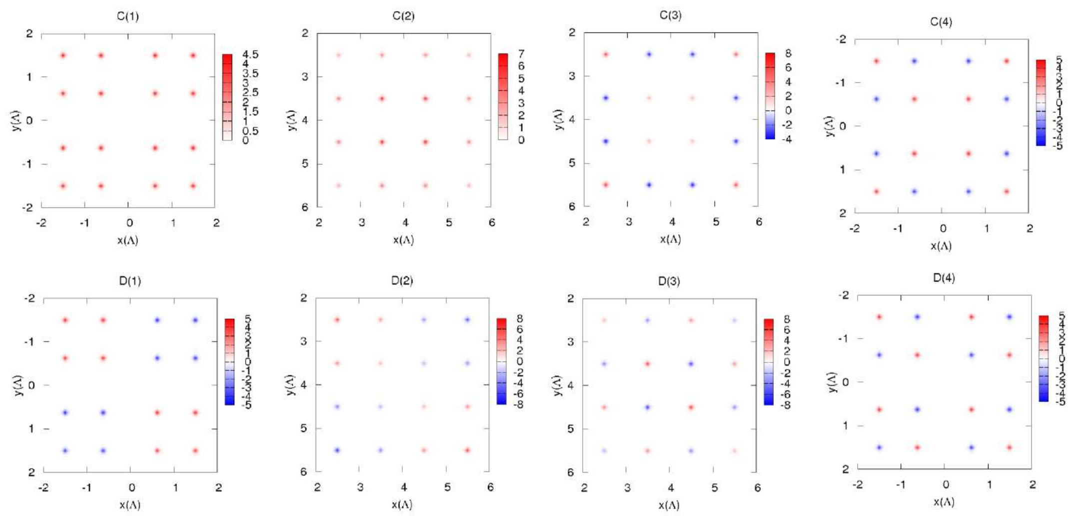

Figure 8.6: Field plots in the transverse plane for the symmetric high-index modes when $k_0\Lambda = 40$. The modes labelled by C(1-4) and D(1-4) correspond to Tables 8.4 and 8.5, respectively. C(1-4) are both-even symmetric modes, and D(1-4) are both-odd symmetric modes.

the modes are localised in the high-index intersections of the ideal structure. It should be noted that different regions of the supercell are shown for the different modes; modes C(1), C(4), D(1), D(4) are localised near to the central defect, while the other modes are localised in the perfect cladding region (as shown in Fig.8.4).

8.4.3 Delocalised modes

There are also many symmetric modes with $C = 0$ in the region below the guided area. We have listed the both-even modes in Table 8.6 for a selected range of b^2 from -0.22 to 0.35. The both-odd modes are omitted here because, based on our following calculations, their final β values are located away from guided area when $k_0\Lambda = 40$. However, both even and odd types need to be examined for a general calculation. Here, it is worth noting that when b^2 is positive, these modes exist in the model structure, but when b^2 is negative, these symmetric solutions (e.g. $E(8-11)$) do not exist as propagating modes. The reason for

Label	(b^2, C)	Label	(b^2, C)
E(1)	(0.33438003975791,0)	E(2)	(0.31140439521518,0)
E(3)	(0.23173791606480, 0)	E(4)	(0.18577898295556,0)
E(5)	(0.13794479117554,0)	E(6)	(0.05971611218204,0)
E(7)	(0.02716288416217,0)	E(8)	(-0.02597519955558,0)
E(9)	(-0.08454562877624,0)	E(10)	(-0.13018465013018,0)
E(11)	(-0.21548602587866,0)		

Table 8.6: Selected both-even symmetric modes (lower than the guided area) at $k_0\Lambda = 40$ for the 8×8 ideal supercell structure.

calculating the negative b^2 solution is as follows. The complete mode structure contains both symmetric ($C = 0$) and non-symmetric ($C \neq 0$) modes, and we can locate the non-symmetric modes from the symmetric modes by using Eq.(7.73); the symmetric modes with negative b^2 are only useful in the determination of the non-symmetric modes with positive b^2. This also explains the range of b^2 values that we consider; the modes in Table 8.6 are those which can generate non-symmetric modes with β values close to the fundamental guided mode.

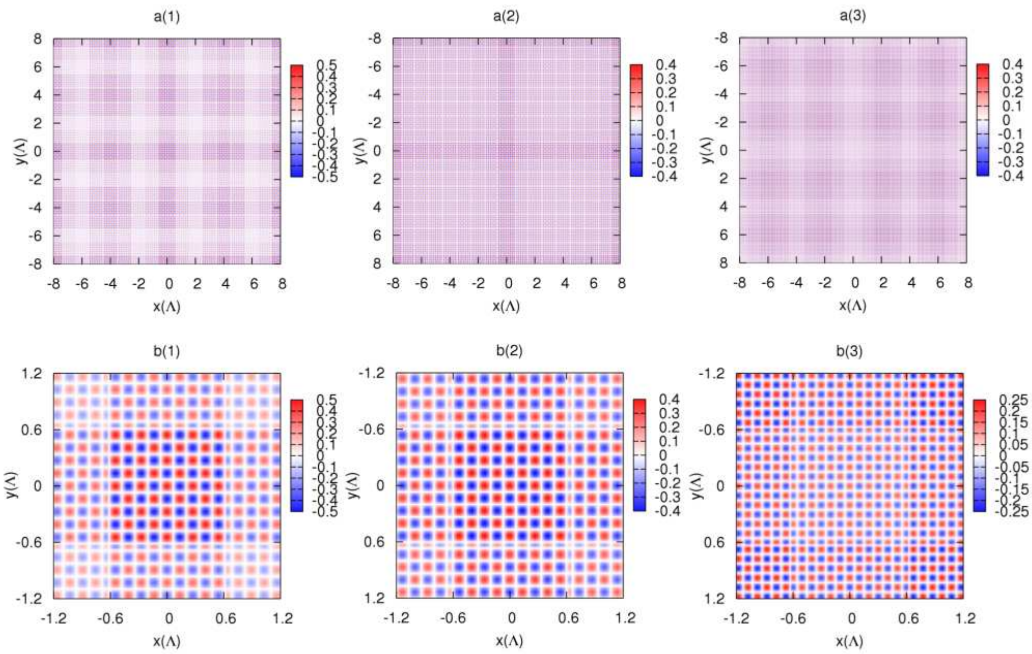

Figure 8.7: Field profiles for selected delocalised modes. Figures a(1-3) correspond to the solutions E(1), E(2) and E(11) respectively, as shown in Table 8.6. The b^2 values for a(1), a(2) and a(3) are 0.3344, 0.3114 and -0.2155. These delocalised solutions will be combined with high-index modes to generate the complete mode map. Figures b(1-3) are the enlarged plots of the fields shown in a(1-3), respectively.

Selected plots of the transverse field for these solutions are shown in Fig.8.7. With a lower value of b^2, the fields of these 'delocalised modes' are no longer confined and spread throughout the supercell. In addition the transverse oscillation of the modes is greatly enhanced, as shown in the comparison of Figs.8.7.b(1-3); this property is important for our development of perturbation theory in the following chapters.

8.5 Complete mode map for the supercell structure

The relation between the symmetric and non-symmetric modes for a supercell structure has been discussed in Section 7.6. The propagation constant and polarisation factor (i.e. C value) for non-symmetric modes can be obtained from Eq.(7.73) and Eq.(7.69) (or Eq.(7.71)). In principle, every possible pair of symmetric modes can be combined to give two non-symmetric modes. Fig.8.8 gives a schematic drawing of these modes. The b^2 values for a pair of symmetric modes are given by b_1^2 and b_2^2, where we assume that $b_1^2 > b_2^2$. The two non-symmetric modes have the same b^2, and equal and opposite values of C. Furthermore, the non-symmetric mode with $C < 0$ has the same p_x and p_y as the symmetric modes with (b_1^2,0) and (b_2^2,0) respectively. The p_x and p_y values for the other non-symmetric mode are equivalent to (b_2^2,0) and (b_1^2,0).

Fig.8.9 shows an example of how symmetric modes combine to give a non-symmetric mode. The upper three figures are field plots for the modes labelled by A(1), A(3) (see Table 8.2) and their combined non-symmetric mode, which has identical p_x and p_y with A(1) and A(3) respectively. The lower figures are corresponding drawings for the field regions. For modes A(1) and A(3) , the one-dimensional fields are the same along the x and y directions. The intersections of the one-dimensional regions, which are indicated by darker colours, therefore satisfy the two-dimensional field equations and represent the regions where the fields are maximised. The one-dimensional confined regions for the non-symmetric mode are the same as those in A(1) and A(3) along the x and y directions respectively. The two-dimensional field regions can thus be located, as shown by dark colours in Fig.8.9 b(3).

In the previous section, three groups of symmetric modes were discussed. In practice, we are only interested in modes that lie close (in β value) to the funda-

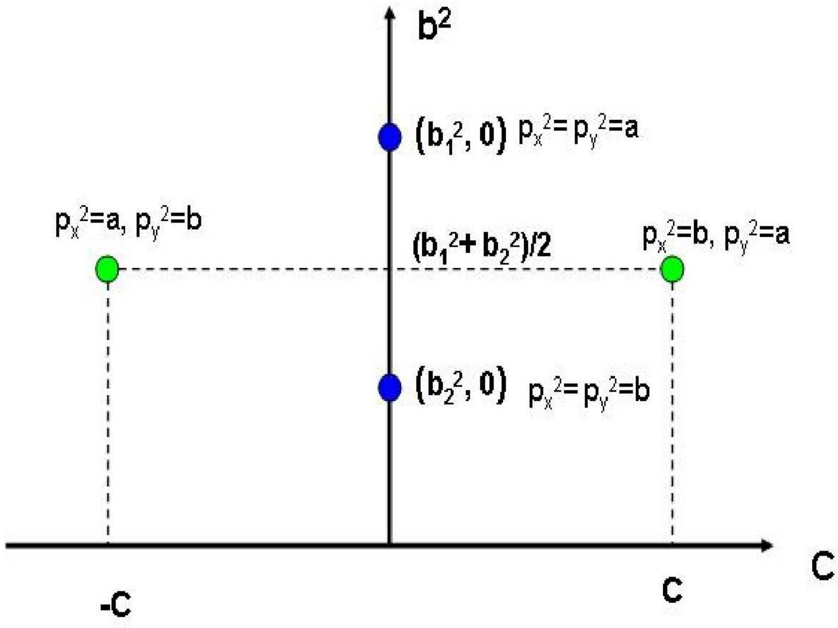

Figure 8.8: The relationship between a pair of symmetric modes (shown by blue points) and the derived non-symmetric modes (shown by green points) in (b^2, C) space.

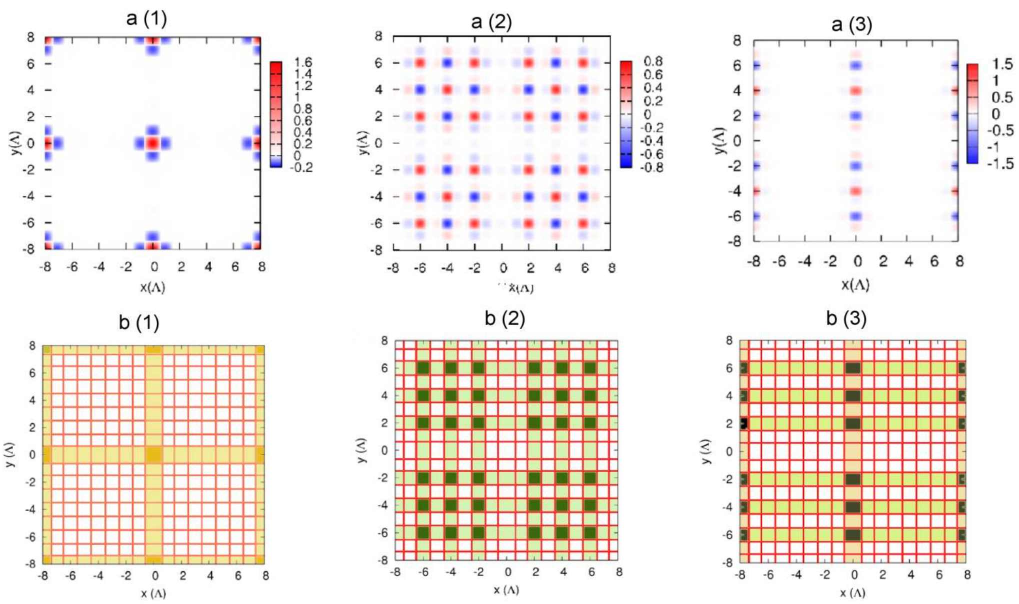

Figure 8.9: Comparison of the realistic (a(1-3)) and corresponding schematic (b(1-3)) field regions in the supercell structure. a(1) and a(2) are the symmetric modes A(1) and A(3) shown in Table.8.2. a(3) is a non-symmetric mode, which has the same p_x and p_y as A(1) and A(3) respectively. The one-dimensional field regions are indicated by the light colours in b(1-3). The dark colours are regions where the two-dimensional field is confined.

mental air-guided mode. There are two choices of symmetric mode combination that lead to modes located near to the fundamental guided mode. One is the internal combination for the group in the guided area; the other is the external combination from the groups higher and lower than the guided area. In the following sections, the whole mode map will be built up and discussed based on these groups.

8.5.1 Air-guided mode map

We first look at the mode map of Fig.8.10 constructed from symmetric modes in the air-guided area. The fields of all these modes are concentrated in the air holes. The modes can be divided into three types: even one-dimensional functions in both x and y (red dots), odd functions in both x and y (blue dots), and hybrid modes with one even and one odd function (green dots). It can also be seen that all the airy modes have a small C value (the absolute values are less than 0.002).

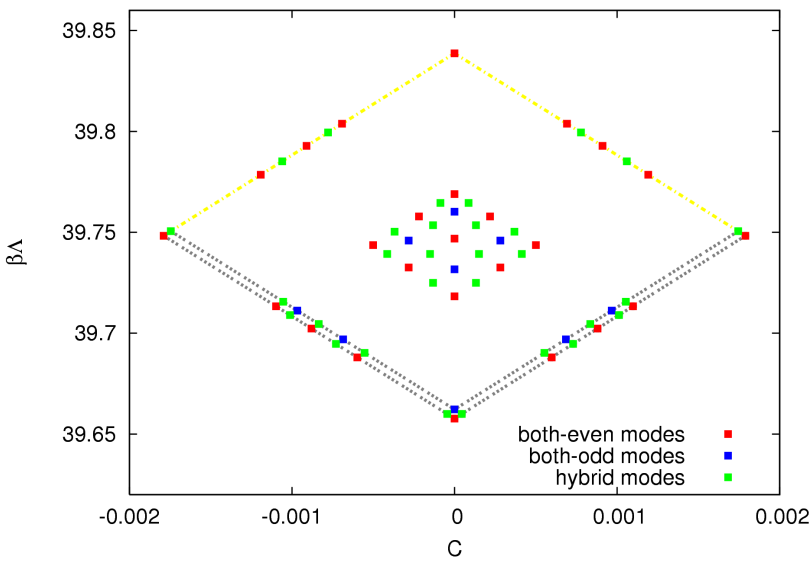

Figure 8.10: Mode diagram in the air-guided region for a 8×8 ideal supercell structure for $k_0\Lambda = 40$. The x and y axes represent the polarisation factor and normalised propagation constant, respectively. Red, green, and blue points denote 'both-even', 'both-odd' and 'hybrid' modes, which are defined by their one-dimensional wavefunctions. The modes connected by the yellow and grey dashed lines are situated in the defect air holes.

The regions where the field is most intense for the air-guided modes can be classified into three types. The first is the 'inner defect region', for which the width and/or length of the air holes is enlarged when the central defect is created. The second is the 'outer defect region', where the width and/or length of the air holes are decreased in the formation of the central defect. The third is air holes located the perfect cladding region. We find that the modes with same p_j ($j = x, y$) as the fundamental guided mode A(1) belong to the first type. Modes with p_j corresponding to A(5) or B(3) belong to the second type. The other modes correspond to the third type. The airy modes belonging to the first and second types are shown by the points on the yellow and grey dashed lines in Fig.8.10, respectively.

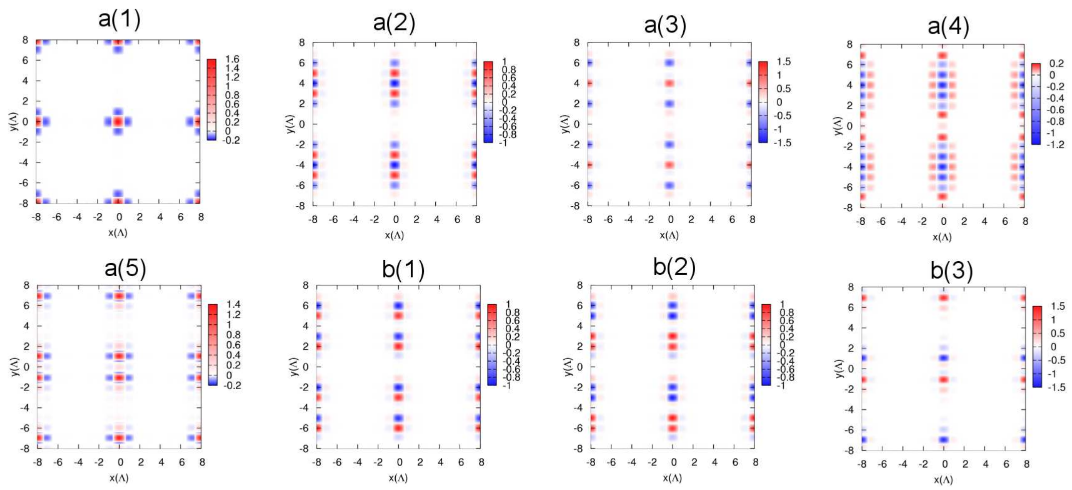

Figure 8.11: Fields of the air-guided modes in the inner defect regions. They have the same p_x as the fundamental guided mode A(1). The p_y values for figures a(1-5) and b(1-3) are equivalent to the symmetric modes A(1-5) and B(1-3), respectively.

Examples of the field plots in the inner defect regions are shown in Fig.8.11. These modes are indicated by the yellow dashed line in the left hand side of Fig.8.10 (i.e. containing the same p_x as the fundamental guided mode A(1)).

Fig.8.12 shows field plots for modes located in the outer defect regions. The relevant modes are indicated by the lower right grey dashed line in Fig.8.10 and thus have the same p_x as the symmetric mode A(5).

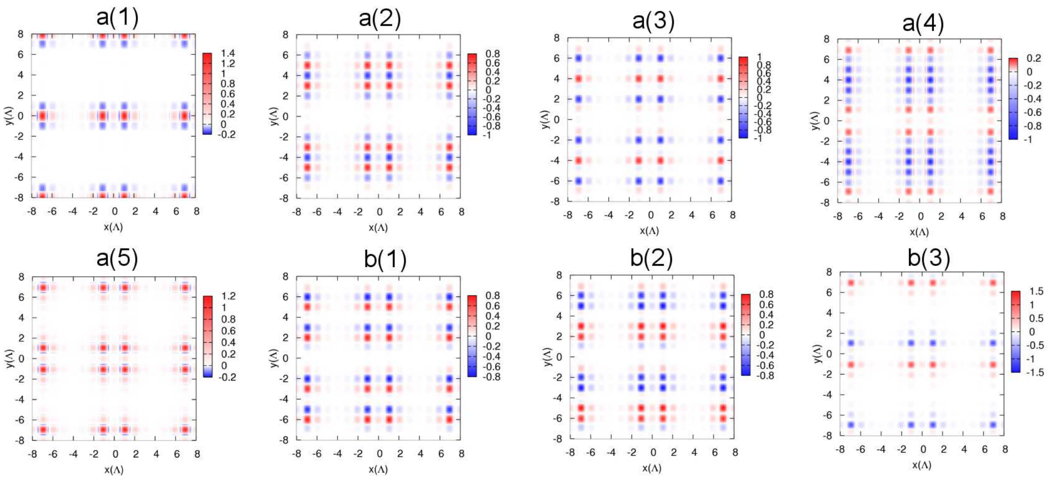

Figure 8.12: Fields of the air-guided modes in the outer defect regions. The p_x value is the same as for the symmetric mode A(5). Figures a(1-5) and b(1-3) have the same p_y values as the symmetric modes A(1-5) and B(1-3), respectively.

8.5.2 Glass-guided mode map

The other possibility for constructing modes is the combination between the high-index modes (as shown in Tables.8.4 and 8.5) and the delocalised modes (as shown in Table.8.6). This leads to a large set of non-symmetric modes, with relatively large absolute C values (varying from 0.43 to 0.52). The large C values means that the modes are strongly asymmetric with respect to the x and y directions. As for the glass-guided modes, they also have different field profiles, such as 'both-even' and 'hybrid' modes.

As mentioned before, we are interested in modes with propagation constants near to the fundamental guided mode. Based on this consideration, three groups can be chosen: $C(1-4)$ and $D(1-4)$ with $E(1)$, $E(2)$ or $E(11)$. In the first two choices, the b^2 values are about 1.295798 and 1.284310 for the scalar governing equation. The reason to select these modes is that the b^2 values for some of them have a large shift to about 1.001375 and 0.992287 when vector and high-index effects are considered, which brings them into the air-guided region. For the third case, the b^2 value for the non-symmetric modes is about 1.020865, which is in the vicinity of the guided area after a small shift. This will be discussed further in Chapters 9 and 10. In this section, we will discuss the general properties of these types of modes.

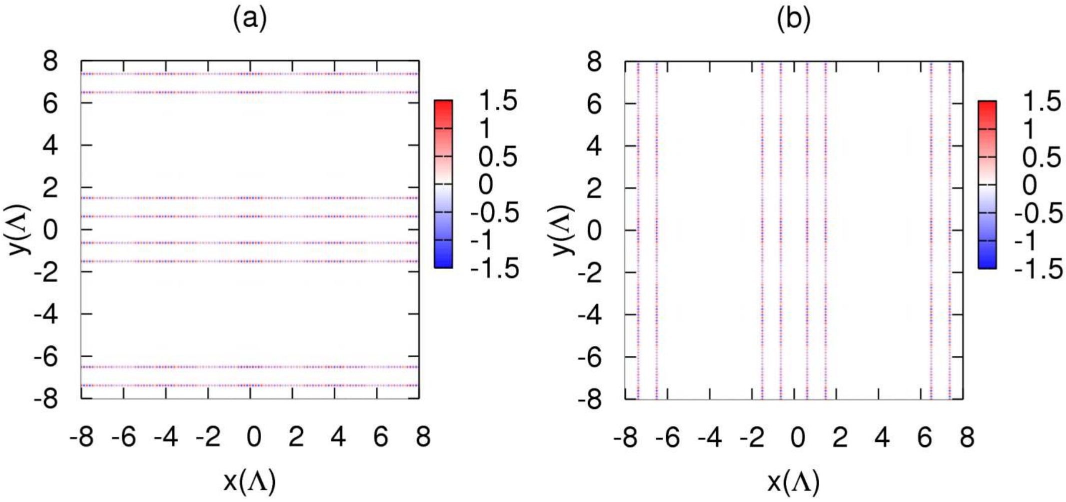

Figure 8.13: Sample of the field patterns for two non-symmetric modes close to the guided area. The mode (a) has the same p_x as E(1) and p_y as C(1). The mode (b) has the same p_x and p_y as C(1) and E(1), respectively.

Fig.8.13 shows field plots for the two non-symmetric modes derived from a pair of high-index and delocalised modes. We find that the field regions for all of these modes are concentrated within the glass strips. Thus, we call these modes 'glass-guided modes'. This property can be explained by looking at the one-dimensional fields as was done in Fig.8.9. Each glass-guided mode has the same p_i as a high-index mode and the same p_j as a delocalised mode, where i, j represent the x and y axes. In the i direction, p_i ensures that the field is well confined in the glass strips. Along the j direction, the field extends along the glass strips because this is true of one-dimensional fields of the delocalised modes, as can been seen in Fig.8.7.

In correspondence with the high-index modes, the glass-guided modes also tend to be localised in two different regions. Some are concentrated in the glass strips passing through the central defect area (as shown by the area enclosed by blue lines in Fig.8.4). The others are located in those strips passing through the region of the perfect cladding structure (the area surrounded by green lines in Fig.8.4).

A key property of the field profiles for the glass-guided modes is their rapid oscillation, as indicated by the changing red and blue colours in Fig.8.13. An enlarged view close to the central defect is shown in Fig.8.14 (a). Two parameters can be introduced to describe these fields. One is the period of the field oscillation along the glass strips; the other is the relative phase of the fields between the strips. The period is the same in all the glass strips for a glass-guided mode, but the phases may be different. The relative phase is determined by the parity of the relevant high-index mode because this controls the field variation in the direction perpendicular to the field extension.

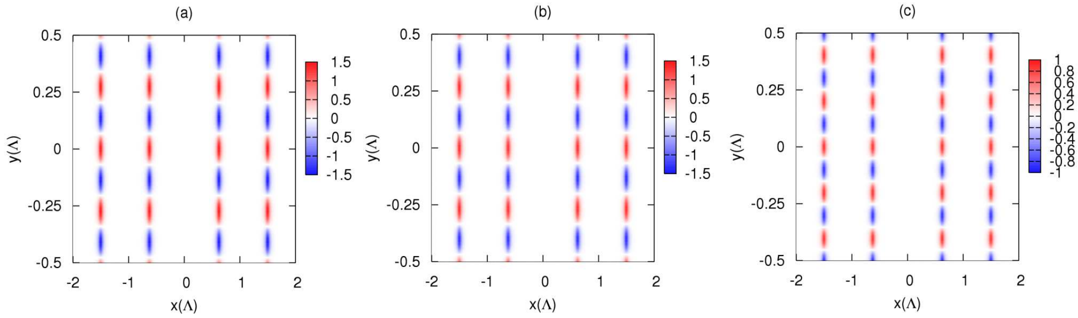

Figure 8.14: Examples of fields for the glass-guided modes. They all have the same p_x as the high-index mode $C(1)$. The p_y values for (a), (b) and (c) are identical with the delocalised modes E(1), E(2) and E(11), respectively.

Fig.8.14 shows glass-guided modes with the same p_x value as the high-index mode C(1). The p_y values are different and equivalent to the symmetric modes E(1), E(2) and E(11) respectively. As shown in Eqs.(7.64) and (7.65), a symmetric mode with a larger b^2 has a smaller p_x and p_y, i.e. a lower oscillation frequency in the one-dimensional wavefunctions. Therefore, the oscillation frequency of the field in Fig.8.14 (c) is relatively higher than for the other two because the b^2 value of the symmetric modes E(1) and E(2) is larger than that for E(11), as shown in Table 8.6. Because the b^2 values for the symmetric high-index modes are very similar to each other, the oscillation frequency of all the glass-guided modes is determined by the b^2 value of the relevant delocalised mode.

8.6 Conclusions

Analytic solutions for the modes of the ideal model structure with the scalar governing equations have been presented in this chapter. It has been shown that for the infinite structure, the guidance of rectangular hollow-core PCFs does not depend on the existence of a photonic bandgap but instead exhibits guidance over a broad frequency range. This point has been demonstrated by the coexistence of the fundamental guided and cladding modes with the same frequency and propagation constant. These properties are similar to those of Kagome PCFs, thus the rectangular hollow-core PCFs can be identified as prototypes of weak interaction guidance fibres.

The calculated propagation constants for the fundamental guided mode in the infinite cladding and a supercell geometry are the same to at least six decimal places. This indicates that the supercell geometry is suitable for highly accurate calculations for rectangular hollow-core PCFs.

We have shown that a full set of modes can be calculated for the supercell geometry. The modes close to the fundamental guided mode are of two distinct types: air-guided modes and glass-guided modes. An analysis of these modes has been presented, and this analysis will form the basis of our perturbation calculations in the next two chapters.

Chapter 9

Perturbation methods for model PCF structures

Analytic solutions for the ideal model structure using the scalar wave equation have been discussed in the previous two chapters. In order to achieve a better understanding of the guidance of rectangular hollow-core PCFs, we will develop a perturbation method. This allows us to discuss the real model structure with a vector governing equation. In our application, the ideal structure with a scalar governing equation is viewed as the unperturbed system. The perturbation then consists of the factors required to consider the real model structure with a vector governing equation. Our aim is to quantify and analyse the effect of the perturbation terms on the light propagation.

In Section 9.1 we derive the perturbation matrix for PCFs. The derivation of the matrix elements is presented in Section 9.2 for the magnetic field. The calculation of the photonic density of states (PDOS) is presented in Section 9.3, which provides a quantitative analysis of the interaction of cladding modes with the fundamental guided mode. Section 9.4 is the summary. Computational results, based on the theory discussed in this chapter, are presented in Chapters 10 and 11.

9.1 Matrix formulation of perturbation theory

With the scalar governing equation, the polarisation of the fields can be omitted because the solutions are degenerate for polarisations along the x and y directions in the transverse plane. Hence we can express the scalar wave equations, (2.18) and (2.19), in a concise form

$$L_0 \Psi_n = \beta_{0n}^2 \Psi_n, \tag{9.1}$$

where L_0 denotes $[\nabla_t^2 + n_i^2 k_0^2]$, and n_i^2 is the dielectric function for the ideal model structure. β_{0n}^2 and Ψ_n are the eigenvalues and eigenstates of the operator L_0, corresponding to the square of the propagation constants and their associated fields. The subscript n labels the modes. Analytic solutions for Eq.(9.1) have been derived within a supercell geometry in Chapter 7. In our perturbation theory, these results will serve as the unperturbed solutions.

In contrast, solutions of the vector governing equation are polarised modes. Therefore, we require scalar solutions which are polarised. We write Eq.(9.1) as

$$L_0 \boldsymbol{\Psi}_n = \beta_{0n}^2 \boldsymbol{\Psi}_n, \tag{9.2}$$

where the vector field solution $\boldsymbol{\Psi}_n$ is

$$\boldsymbol{\Psi}_n = \Psi_n \hat{\mathbf{e}}_n \tag{9.3}$$

with $\hat{\mathbf{e}}_n = \hat{\mathbf{x}}$ or $\hat{\mathbf{y}}$.

The vector wave equation for the real model structure can be written in a similar form as

$$L_0 \boldsymbol{\Phi} + \delta L(\boldsymbol{\Phi}) = \beta^2 \boldsymbol{\Phi}, \tag{9.4}$$

where L_0 is the same as in Eq.(9.1) and the perturbation term, $\delta L(\boldsymbol{\Phi})$, is a linear vector function of $\boldsymbol{\Phi}$. The eigenvalue β^2 and eigenvector $\boldsymbol{\Phi}$ now denote the square of the propagation constant and field for the realistic system. In our model, the correction term $\delta L(\boldsymbol{\Phi})$ consists of two parts. One comes from the vector term in the governing equation; the other comes from the difference of the dielectric constant between the realistic and ideal structures. Thus they are called the 'vector terms' and 'high-index terms' respectively.

We look for solutions of Eq.(9.4) by using solutions of Eq.(9.2) as basis functions:

$$\mathbf{\Phi} = \sum_n a_n \mathbf{\Psi}_n, \tag{9.5}$$

where the a_n is the expansion coefficient. Substituting this expression into Eq.(9.4), we obtain

$$L_0\big(\sum_n a_n \mathbf{\Psi}_n\big) + \delta L\big(\sum_n a_n \mathbf{\Psi}_n\big) = \beta^2 \sum_n a_n \mathbf{\Psi}_n, \tag{9.6}$$

which, using Eq.(9.2), leads to

$$\sum_n a_n \beta_{0n}^2 \mathbf{\Psi}_n + \sum_n a_n \delta L(\mathbf{\Psi}_n) = \beta^2 \sum_n a_n \mathbf{\Psi}_n. \tag{9.7}$$

Eq.(9.7) is multiplied on both sides by $\mathbf{\Psi}_m^*$ to give

$$\sum_n a_n \beta_{0n}^2 \mathbf{\Psi}_m^* \cdot \mathbf{\Psi}_n + \sum_n a_n \mathbf{\Psi}_m^* \cdot \delta L(\mathbf{\Psi}_n) = \beta^2 \sum_n a_n \mathbf{\Psi}_m^* \cdot \mathbf{\Psi}_n \tag{9.8}$$

and by integrating over one supercell, with the ortho-normalisation formula $\int\int \mathbf{\Psi}_m^* \cdot \mathbf{\Psi}_n dA = \delta_{mn}$ we obtain

$$a_m \beta_{0m}^2 + \sum_n a_n \delta L_{mn} = \beta^2 a_m, \tag{9.9}$$

where

$$(\delta L)_{mn} = \int\int \mathbf{\Psi}_m^* \cdot \delta L(\mathbf{\Psi}_n) dA. \tag{9.10}$$

Eq.(9.9) can be written in a matrix form as

$$(\underline{\underline{L}}_0 + \underline{\underline{\delta L}})\underline{a} = \beta^2 \underline{a}, \tag{9.11}$$

where the elements in $\underline{\underline{L}}_0$ are

$$(L_0)_{mn} = \delta_{mn} \beta_{0m}^2, \tag{9.12}$$

and the elements in $\underline{\underline{\delta L}}$ take the same form as Eq.(9.10). Eq.(9.11) gives the perturbation matrix for PCFs. In order to provide a direct connection with the scalar field expression (i.e. Eq.(9.1)), $\mathbf{\Psi}_m$ is replaced by $\Psi_m \hat{\mathbf{e}}_m$. The matrix elements Eqs.(9.10) and (9.12) can then be written as

$$\delta L_{mn_{(e_m e_n)}} = \int\int (\Psi_m \hat{\mathbf{e}}_m)^* \cdot \delta L(\Psi_n \hat{\mathbf{e}}_n)\, dA, \tag{9.13}$$

$$(L_0)_{mn_{(e_m e_n)}} = \delta_{e_m e_n} \delta_{mn} \beta_{0m}^2 \tag{9.14}$$

where the subscripts $(e_m e_n)$ denote the polarisations of the fields Ψ_m and Ψ_n. The corresponding perturbation matrix then becomes

$$\left\{ \begin{bmatrix} \underline{\underline{L}}_{0(xx)} & 0 \\ 0 & \underline{\underline{L}}_{0(yy)} \end{bmatrix} + \begin{bmatrix} \underline{\underline{\delta L}}_{(xx)} & \underline{\underline{\delta L}}_{(xy)} \\ \underline{\underline{\delta L}}_{(yx)} & \underline{\underline{\delta L}}_{(yy)} \end{bmatrix} \right\} \underline{a} = \beta^2 \underline{a}. \tag{9.15}$$

Expressions for the elements in the second matrix will be derived in Section 9.2 for the magnetic field.

The matrix elements δL_{mn} that appear in Eq.(9.11) (or Eq.(9.15)) can be classified into three types. First we consider the diagonal matrix elements, δL_{mm}. These cause a 'shift' of the propagation constant for each mode but, by themselves, do not lead to any interaction between the modes and therefore do not affect the loss. If only these term are considered, the propagation constants are given by

$${\beta'_{0m}}^2 = \beta_{0m}^2 + \delta L_{mm}, \tag{9.16}$$

and the fields of the modes are unchanged. As we shall see in the next chapter, the diagonal matrix elements are substantially larger than the off-diagonal elements. We therefore use the shifted propagation constants given by (9.16) to decide which modes to include in the perturbation calculation. Only the modes with shifted propagation constants located close to the fundamental guided mode are selected.

The second type of matrix element in Eq.(9.11) is $\delta L_{m_0 n}$ and $\delta L_{n m_0}$, where m_0 labels the fundamental guided mode and n labels another mode of the supercell. Coupling of this type will lead to confinement loss due to light leaking from the guided mode into cladding modes. The third type of matrix element is δL_{mn} and δL_{nm} (where $m, n \neq m_0$); these reflect interactions between the cladding modes.

9.2 Calculation of matrix elements

For the magnetic field, the scalar and vector governing equations given in Eqs.(2.19) and (2.14) are

$$\big(\nabla_t^2 + n_i^2 k_0^2\big)\mathbf{h}_t = \beta_0^2 \mathbf{h}_t \tag{9.17}$$

$$\big(\nabla_t^2 + n_r^2 k_0^2\big)\mathbf{h}_t^r - \big(\nabla_t \times \mathbf{h}_t^r\big) \times \nabla_t \ln n_r^2 = \beta^2 \mathbf{h}_t^r, \tag{9.18}$$

where β_0 and $\mathbf{h}_t$ are the propagation constant and transverse field for the scalar governing equation and the ideal structure, β and $\mathbf{h}_t^r$ are those for the vector governing equation with the realistic structure, and the dielectric functions n_i^2 and n_r^2 are for the ideal and real model structures respectively. The relationship between the ideal and realistic dielectric functions is expressed as

$$n_r{}^2 = n_i{}^2 + \Delta n^2, \tag{9.19}$$

where, as shown in Section 7.1, Δn^2 is given by

$$\Delta n^2 = \begin{cases} n_a^2 - n_g^2 & \text{for the glass intersections} \\ 0 & \text{for other regions,} \end{cases} \tag{9.20}$$

where n_a and n_g are the refractive indices for air and glass.

By comparison of Eqs.(9.17) and (9.18), the perturbation term for the magnetic field of mode n is found to be

$$\delta L(\mathbf{h}_n) = -\big(\nabla_t \times \mathbf{h}_n\big) \times \nabla_t \ln n_r^2 + \Delta n^2 k_0^2 \mathbf{h}_n. \tag{9.21}$$

The perturbation matrix in Eq.(9.15) can then be written as

$$\underline{\underline{\delta L}}_{(e_m e_n)} = \underline{\underline{\delta L}}^a{}_{(e_m e_n)} + \underline{\underline{\delta L}}^b{}_{(e_m e_n)}, \tag{9.22}$$

where the a and b labels are for the vector terms and high-index terms respectively. The matrix elements are

$$\delta L^a_{mn(e_m e_n)} = -\int\!\!\int h_m \hat{\mathbf{e}}_m \cdot \Big[\big(\nabla_t \times (h_n \hat{\mathbf{e}}_n)\big) \times \nabla_t \ln n_r^2\Big]\, dA \tag{9.23}$$

$$\delta L^b_{mn(e_m e_n)} = \int\!\!\int h_m \hat{\mathbf{e}}_m \cdot (\Delta n^2 k_0^2) h_n \hat{\mathbf{e}}_n \, dA', \tag{9.24}$$

where dA and dA' are the integration elements for the whole supercell and for only the intersections of the glass strips, respectively. In the following sections, analytic expressions for these terms will be derived.

9.2.1 Vector terms

The vector perturbation term, Eq.(9.23), can be written as

$$\delta L^a_{mn} = -\int\int h_m \hat{\mathbf{e}}_m \cdot \left[(\frac{\partial}{\partial x}\hat{\mathbf{x}} + \frac{\partial}{\partial y}\hat{\mathbf{y}}) \times (h_n \hat{\mathbf{e}}_n) \times \nabla_t \ln n_r^2 \right] dA. \tag{9.25}$$

The directions of $\hat{\mathbf{e}}_m$ and $\hat{\mathbf{e}}_n$ have four possible combinations in the perturbation matrix, as shown in Eq.(9.15); the corresponding expressions become

$$\delta L^a_{mn_{(xx)}} = -\int\int h_m \hat{\mathbf{x}} \cdot \left\{ -\frac{\partial h_n}{\partial y} \hat{\mathbf{z}} \times \nabla_t \ln n_r^2 \right\} dA \tag{9.26}$$

$$\delta L^a_{mn_{(yy)}} = -\int\int h_m \hat{\mathbf{y}} \cdot \left\{ \frac{\partial h_n}{\partial x} \hat{\mathbf{z}} \times \nabla_t \ln n_r^2 \right\} dA \tag{9.27}$$

$$\delta L^a_{mn_{(xy)}} = -\int\int h_m \hat{\mathbf{x}} \cdot \left\{ \frac{\partial h_n}{\partial x} \hat{\mathbf{z}} \times \nabla_t \ln n_r^2 \right\} dA \tag{9.28}$$

$$\delta L^a_{mn_{(yx)}} = -\int\int h_m \hat{\mathbf{y}} \cdot \left\{ -\frac{\partial h_n}{\partial y} \hat{\mathbf{z}} \times \nabla_t \ln n_r^2 \right\} dA, \tag{9.29}$$

where ($\hat{\mathbf{e}}_m$, $\hat{\mathbf{e}}_n$) are ($\hat{\mathbf{x}}$, $\hat{\mathbf{x}}$), ($\hat{\mathbf{y}}$, $\hat{\mathbf{y}}$), ($\hat{\mathbf{x}}$,$\hat{\mathbf{y}}$) and ($\hat{\mathbf{y}}$,$\hat{\mathbf{x}}$), respectively.

In these formulae, $\nabla_t \ln n_r^2$ is the derivative of a step function with a non-zero value only at the interfaces between the glass and air. In our model structure we have [105]

$$(\nabla_t \ln n_r^2) dA = \begin{cases} \hat{\mathbf{y}} \ln \left(\frac{n^2_{r(y+)}}{n^2_{r(y-)}} \right) \delta(B)\, dx dB & \text{for interfaces parallel to the } x \text{ axis} \\ \hat{\mathbf{x}} \ln \left(\frac{n^2_{r(x+)}}{n^2_{r(x-)}} \right) \delta(B)\, dy dB & \text{for interfaces parallel to the } y \text{ axis.} \end{cases} \tag{9.30}$$

The subscripts + and − represent positions on either side of the interface, $\delta(B)$ is a delta function in the coordinate perpendicular to the boundary, and the integration element dx or dy is along the boundary. The direction of $\nabla_t \ln n_r^2$ must be $\hat{\mathbf{y}}$ in Eqs.(9.26) and (9.28), and $\hat{\mathbf{x}}$ in Eqs.(9.27) and (9.29) for non-zero values. Substitution of Eq.(9.30) into Eqs.(9.26) to (9.29) leads to the following expressions

$$\begin{aligned}
\delta L^a_{mn(xx)} &= -\sum_{\{l_x\}} \int h_m \hat{\mathbf{x}} \cdot \left\{ \frac{\partial h_n}{\partial y} (-\hat{\mathbf{z}}) \times \hat{\mathbf{y}} \ln \left(\frac{n^2_{r(y+)}}{n^2_{r(y-)}} \right) \delta(B) dx dB \right\} \\
&= -\sum_{\{l_x\}} \ln \left(\frac{n^2_{r(y+)}}{n^2_{r(y-)}} \right) \int h_m \frac{\partial h_n}{\partial y} dx \qquad (9.31)
\end{aligned}$$

$$\begin{aligned}
\delta L^a_{mn(yy)} &= -\sum_{\{l_y\}} \int h_m \hat{\mathbf{y}} \cdot \left\{ \frac{\partial h_n}{\partial x} \hat{\mathbf{z}} \times \hat{\mathbf{x}} \ln \left(\frac{n^2_{r(x+)}}{n^2_{r(x-)}} \right) \delta(B) dy dB \right\} \\
&= -\sum_{\{l_y\}} \ln \left(\frac{n^2_{r(x+)}}{n^2_{r(x-)}} \right) \int h_m \frac{\partial h_n}{\partial x} dy \qquad (9.32)
\end{aligned}$$

$$\begin{aligned}
\delta L^a_{mn(xy)} &= -\sum_{\{l_x\}} \int h_m \hat{\mathbf{x}} \cdot \left\{ \frac{\partial h_n}{\partial x} \hat{\mathbf{z}} \times \hat{\mathbf{y}} \ln \left(\frac{n^2_{r(y+)}}{n^2_{r(y-)}} \right) \delta(B) dx dB \right\} \\
&= \sum_{\{l_x\}} \ln \left(\frac{n^2_{r(y+)}}{n^2_{r(y-)}} \right) \int h_m \frac{\partial h_n}{\partial x} dx \qquad (9.33)
\end{aligned}$$

$$\begin{aligned}
\delta L^a_{mn(yx)} &= -\sum_{\{l_y\}} \int h_m \hat{\mathbf{y}} \cdot \left\{ \frac{\partial h_n}{\partial y} (-\hat{\mathbf{z}}) \times \hat{\mathbf{x}} \ln \left(\frac{n^2_{r(x+)}}{n^2_{r(x-)}} \right) \delta(B) dy dB \right\} \\
&= \sum_{\{l_y\}} \ln \left(\frac{n^2_{r(x+)}}{n^2_{r(x-)}} \right) \int h_m \frac{\partial h_n}{\partial y} dy, \qquad (9.34)
\end{aligned}$$

where the integrals include all the interfaces $\{l_x\}$ and $\{l_y\}$ in one supercell for the real model structure.

In Eqs.(9.31) to (9.34), the vector terms are expressed using the two-dimensional scalar fields h_m and h_n, which are solutions of the scalar governing equation for the ideal model structure. As discussed in Chapter 7, they can be written in terms of one-dimensional separable fields $X(x)$ and $Y(y)$:

$$h_m = X_m(x) Y_m(y) \qquad (9.35)$$

$$h_n = X_n(x) Y_n(y) \qquad (9.36)$$

which, when substituted into Eqs.(9.31) to (9.34), give

$$\begin{aligned}
\delta L^a_{mn_{(xx)}} &= -\sum_{\{l_x\}} \ln\left(\frac{n^2_{r(y+)}}{n^2_{r(y-)}}\right) \int \left[X_m(x)Y_m(y)\right]\left[X_n(x)Y'_n(y)\right]dx \\
&= -\sum_{\{l_x\}} \ln\left(\frac{n^2_{r(y+)}}{n^2_{r(y-)}}\right) \Big[Y_m(y)Y'_n(y)\Big]_{int} \int_{l_x} X_m(x)X_n(x)dx \quad (9.37)
\end{aligned}$$

$$\begin{aligned}
\delta L^a_{mn_{(yy)}} &= -\sum_{\{l_y\}} \ln\left(\frac{n^2_{r(x+)}}{n^2_{r(x-)}}\right) \int \left[X_m(x)Y_m(y)\right]\left[X'_n(x)Y_n(y)\right]dy \\
&= -\sum_{\{l_y\}} \ln\left(\frac{n^2_{r(x+)}}{n^2_{r(x-)}}\right) \Big[X_m(x)X'_n(x)\Big]_{int} \int_{l_y} Y_m(y)Y_n(y)dy \quad (9.38)
\end{aligned}$$

$$\begin{aligned}
\delta L^a_{mn_{(xy)}} &= \sum_{\{l_x\}} \ln\left(\frac{n^2_{r(y+)}}{n^2_{r(y-)}}\right) \int \left[X_m(x)Y_m(y)\right]\left[X'_n(x)Y_n(y)\right]dx \\
&= \sum_{\{l_x\}} \ln\left(\frac{n^2_{r(y+)}}{n^2_{r(y-)}}\right) \Big[Y_m(y)Y_n(y)\Big]_{int} \int_{l_x} X_m(x)X'_n(x)dx \quad (9.39)
\end{aligned}$$

$$\begin{aligned}
\delta L^a_{mn_{(yx)}} &= \sum_{\{l_y\}} \ln\left(\frac{n^2_{r(x+)}}{n^2_{r(x-)}}\right) \int \left[X_m(x)Y_m(y)\right]\left[X_n(x)Y'_n(y)\right]dy \\
&= \sum_{\{l_y\}} \ln\left(\frac{n^2_{r(x+)}}{n^2_{r(x-)}}\right) \Big[X_m(x)X_n(x)\Big]_{int} \int_{l_y} Y_m(y)Y'_n(y)dy, \quad (9.40)
\end{aligned}$$

where the subscript *int* means the values at the relevant interface. Eqs.(9.37) to (9.40) are our final expressions for the vector perturbation terms. They consist of two parts: a non-integral component (e.g. $Y_m(y)Y'_n(y)$ in Eq.(9.37)) and an integral component (e.g. $\int X_m(x)X_n(x)dx$ in Eq.(9.37)). The values of the non-integral component can be calculated directly from the one-dimensional field expressions given in Chapter 7. The integral components contain terms like $\int X_m(x)X_n(x)dx$, $\int Y_m(y)Y_n(y)dy$, $\int X_m(x)X'{}_n(x)dx$ and $\int Y_m(y)Y'_n(y)dy$. All of these integrals can be performed analytically; here we show an example to perform the calculation the integral of $\int X_m(x)X_n(x)dx$.

At any point in the structure (we suppose the layer index N) the field can be expressed in dimensionless variables as (See Eq.(7.31))

$$X_m(x) = a_x^m \cos\left[(p_x^m\Lambda)(x-x_c)\right] + b_x^m \frac{\sin\left[(p_x^m\Lambda)(x-x_c)\right]}{p_x^m\Lambda} \tag{9.41}$$

where m labels the mode, x_c represents the centre of the layer in the x direction and a_x^m, b_x^m are the field coefficients. Using Eq.(9.41), the example integral becomes

$$\begin{aligned}\int X_m(x)X_n(x)dx = &\int_{x_c-\frac{t}{2}}^{x_c+\frac{t}{2}} \left\{a_x^m \cos\left[(p_x^m\Lambda)(x-x_c)\right] + b_x^m \frac{\sin\left[(p_x^m\Lambda)(x-x_c)\right]}{p_x^m\Lambda}\right\} \\ &\cdot\left\{a_x^n \cos\left[(p_x^n\Lambda)(x-x_c)\right] + b_x^n \frac{\sin\left[(p_x^n\Lambda)(x-x_c)\right]}{p_x^n\Lambda}\right\}dx,\end{aligned} \tag{9.42}$$

where t is the dimensionless width of the air or glass layer over which we integrate. In the particular application of this formula in Eq.(9.37), the integration is calculated along the interfaces between the air and glass regions. The integral is simple to perform, yielding

$$\begin{aligned}\int X_m(x)X_n(x)dx = &a_x^m a_x^n\left[\frac{\sin(\frac{p_x^m\Lambda+p_x^n\Lambda}{2}t)}{p_x^m\Lambda+p_x^n\Lambda} + \frac{\sin(\frac{p_x^m\Lambda-p_x^n\Lambda}{2}t)}{p_x^m\Lambda-p_x^n\Lambda}\right] \\ &+\frac{b_x^m b_x^n}{(p_x^m\Lambda)(p_x^n\Lambda)}\left[\frac{\sin(\frac{p_x^m\Lambda-p_x^n\Lambda}{2}t)}{p_x^m\Lambda-p_x^n\Lambda} - \frac{\sin(\frac{p_x^m\Lambda+p_x^n\Lambda}{2}t)}{p_x^m\Lambda+p_x^n\Lambda}\right].\end{aligned} \tag{9.43}$$

In a similar way, the other integrals become

$$\begin{aligned}\int Y_m(y)Y_n(y)dy = &a_y^m a_y^n\left[\frac{\sin(\frac{p_y^m\Lambda+p_y^n\Lambda}{2}t)}{p_y^m\Lambda+p_y^n\Lambda} + \frac{\sin(\frac{p_y^m\Lambda-p_y^n\Lambda}{2}t)}{p_y^m\Lambda-p_y^n\Lambda}\right] \\ &+\frac{b_y^m b_y^n}{(p_y^m\Lambda)(p_y^n\Lambda)}\left[\frac{\sin(\frac{p_y^m\Lambda-p_y^n\Lambda}{2}t)}{p_y^m\Lambda-p_y^n\Lambda} - \frac{\sin(\frac{p_y^m\Lambda+p_y^n\Lambda}{2}t)}{p_y^m\Lambda+p_y^n\Lambda}\right]\end{aligned} \tag{9.44}$$

$$\begin{aligned}\int X_m(x)X_n'(x)dx = &a_x^m b_x^n\left[\frac{\sin(\frac{p_x^m\Lambda+p_x^n\Lambda}{2}t)}{p_x^m\Lambda+p_x^n\Lambda} + \frac{\sin(\frac{p_x^m\Lambda-p_x^n\Lambda}{2}t)}{p_x^m\Lambda-p_x^n\Lambda}\right] \\ &-\frac{b_x^m a_x^n(p_x^n\Lambda)}{(p_x^m\Lambda)}\left[\frac{\sin(\frac{p_x^m\Lambda-p_x^n\Lambda}{2}t)}{p_x^m\Lambda-p_x^n\Lambda} - \frac{\sin(\frac{p_x^m\Lambda+p_x^n\Lambda}{2}t)}{p_x^m\Lambda+p_x^n\Lambda}\right]\end{aligned} \tag{9.45}$$

$$\int Y_m(y)Y_n'(y)dy = a_y^m b_y^n\left[\frac{\sin(\frac{p_y^m\Lambda+p_y^n\Lambda}{2}t)}{p_y^m\Lambda+p_y^n\Lambda}+\frac{\sin(\frac{p_y^m\Lambda-p_y^n\Lambda}{2}t)}{p_y^m\Lambda-p_y^n\Lambda}\right]$$
$$-\frac{b_y^m a_y^n(p_y^n\Lambda)}{(p_y^m\Lambda)}\left[\frac{\sin(\frac{p_y^m\Lambda-p_y^n\Lambda}{2}t)}{p_y^m\Lambda-p_y^n\Lambda}-\frac{\sin(\frac{p_y^m\Lambda+p_y^n\Lambda}{2}t)}{p_y^m\Lambda+p_y^n\Lambda}\right]. \tag{9.46}$$

For the special case when $p_x^m = p_x^n$ or $p_y^m = p_y^n$, we find

$$\int X_m(x)X_n(x)dx = \frac{a_x^m a_x^n}{2}\left[t+\frac{\sin\left[(p_x\Lambda)t\right]}{p_x\Lambda}\right]+\frac{b_x^m b_x^n}{2(p_x\Lambda)^2}\left[t-\frac{\sin\left[(p_x\Lambda)t\right]}{p_x\Lambda}\right] \tag{9.47}$$

$$\int Y_m(y)Y_n(y)dy = \frac{a_y^m a_y^n}{2}\left[t+\frac{\sin\left[(p_y\Lambda)t\right]}{p_y\Lambda}\right]+\frac{b_y^m b_y^n}{2(p_y\Lambda)^2}\left[t-\frac{\sin\left[(p_y\Lambda)t\right]}{p_y\Lambda}\right] \tag{9.48}$$

$$\int X_m(x)X_n'(x)dx = \frac{a_x^m b_x^n}{2}\left[t+\frac{\sin\left[(p_x\Lambda)t\right]}{p_x\Lambda}\right]-\frac{a_x^n b_x^m}{2}\left[t-\frac{\sin\left[(p_x\Lambda)t\right]}{p_x\Lambda}\right] \tag{9.49}$$

$$\int Y_m(y)Y_n'(y)dy = \frac{a_y^m b_y^n}{2}\left[t+\frac{\sin\left[(p_y\Lambda)t\right]}{p_y\Lambda}\right]-\frac{a_y^n b_y^m}{2}\left[t-\frac{\sin\left[(p_y\Lambda)t\right]}{p_y\Lambda}\right]. \tag{9.50}$$

By using these expressions in Eqs.(9.37) to (9.40), we are able to calculate the vector perturbation terms for the magnetic field.

9.2.2 High-index terms

We now consider the high-index term, δL_{mn}^b, given by

$$\delta L_{mn(e_m e_n)}^b = \int\int h_m\hat{\mathbf{e}}_m\cdot\left(\Delta n^2 k_0^2\right)h_n\hat{\mathbf{e}}_n\,dA', \tag{9.51}$$

where the integration is over only the area of the intersections of the glass strips in the rectangular PCF structure. As for the vector terms, δL_{mn}^b also has four different forms related to the directions of the fields h_m and h_n. They are given by

$$\delta L_{mn_{(xx)}}^b = \delta L_{mn_{(yy)}}^b = \int\int\left(\Delta n^2 k_0^2\right)h_m h_n\,dA' \tag{9.52}$$

$$\delta L_{mn_{(xy)}}^b = \delta L_{mn_{(yx)}}^b = 0. \tag{9.53}$$

Substituting the separable field expressions Eqs.(9.35) and (9.36) into Eq.(9.52) leads to

$$\delta L_{mn_{(xx)}}^b = \delta L_{mn_{(yy)}}^b = \int\int_{A'}(\Delta n^2 k_0^2)\left[X_m(x)Y_m(y)\right]\left[X_n(x)Y_n(y)\right]dxdy, \tag{9.54}$$

where the label A' shows that the two one-dimensional integrals are performed within the intersections of the glass strips. We introduce labels j and k to represent the j^{th} and k^{th} layer along the x and y directions respectively from the centre of one supercell to the centre of the next. For the $N \times N$ supercell structure, j and k start from 0 (i.e. the air hole centre) to $2N$ (i.e. the next air hole centre). Because of the alternation of air holes and glass strips in our model structure, even and odd values of j and k represent the air holes and glass strips respectively. At the intersections of the strips, j and k are both odd. Thus Eq.(9.54) can be written as

$$\begin{aligned}
&\delta L^b_{mn_{(xx)}} = \delta L^b_{mn_{(yy)}} \\
&= (\Delta n^2 k_0^2) \sum_{\substack{j=1,3,..,\\2N-1}} \sum_{\substack{k=1,3,..,\\2N-1}} \int_{x_j-\frac{t_j}{2}}^{x_j+\frac{t_j}{2}} X_m(x)X_n(x)dx \int_{y_k-\frac{t_k}{2}}^{y_k+\frac{t_k}{2}} Y_m(y)Y_n(y)dy, \quad (9.55)
\end{aligned}$$

where x_j and y_k are the centres of the j^{th} and k^{th} layers in the x and y directions respectively, and t_j and t_k are the corresponding thicknesses. The two integrals in Eq.(9.55) are given by Eqs.(9.43) and (9.44); they reduce to Eqs.(9.47) and (9.48) when $p_x^m = p_x^n$ and $p_y^m = p_y^n$.

9.3 Projected density of states

9.3.1 Analysis of the perturbation matrix

The expressions derived in Section 9.2 can be used to construct the perturbation matrices in Eq.(9.11) or (9.15). By solving these equations we can not only obtain the propagation constant for the realistic case, but we can also derive information about the interactions between the modes.

The general matrix $\underline{\underline{L}}$, which is used to replace $\{\underline{\underline{L}}_0 + \underline{\underline{\delta L}}\}$ in Eq.(9.11), has both right and left eigenvectors defined as

$$\underline{\underline{L}}\,\underline{a}_R^{(k)} = \beta^{(k)^2}\,\underline{a}_R^{(k)} \quad (9.56)$$

$$\underline{a}_L^{(k)}\,\underline{\underline{L}} = \beta^{(k)^2}\,\underline{a}_L^{(k)}, \quad (9.57)$$

where k labels the eigenvector and the R, L subscripts denote the right and left eigenvectors respectively. For a Hermitian matrix, we have $\underline{a}_L^{(k)} = \underline{a}_R^{(k)^{*T}}$, but this is not true for a non-Hermitian problem (the vector term in Eq.(9.18) is non-Hermitian). The eigenvectors obey the orthogonality and completeness relations:

$$\sum_i a_{Li}^{(k)}\, a_{Ri}^{(k')} = \delta_{kk'} \tag{9.58}$$

$$\sum_k a_{Li}^{(k)}\, a_{Rj}^{(k)} = \delta_{ij}, \tag{9.59}$$

where i labels the i^{th} element in the k^{th} eigenvector .

In electronic structure calculations, the projected density of states is widely used to express the total density of states weighted by the probability of finding an electron in a particular energy state [106]. Here we can define the projected photonic density of states for any basis function i, where i represents a solution of the unperturbed problem:

$$\rho_i(\beta^2) = \sum_k a_{Li}^{(k)}\, a_{Ri}^{(k)}\, \delta\Big(\beta^2 - \beta^{(k)^2}\Big). \tag{9.60}$$

The coefficient $\{a_{Li}^{(k)}\, a_{Ri}^{(k)}\}$ in front of the delta function can be expressed as $W_i^{(k)}$, representing the weight of the i^{th} unperturbed mode in the k^{th} perturbed mode. $\rho_i(\beta^2)$ gives a picture of how each unperturbed mode i is 'spread out' over a range of propagation constants in the full problem. In particular, if i represents the fundamental guided mode (i.e. if $i \equiv m_0$), $\rho_{m_0}(\beta^2)$ will show how strongly the guided mode interacts with cladding modes when the perturbation is present. As we shall show below, the width of $\rho_{m_0}(\beta^2)$ gives an indication of the confinement loss caused by this interaction.

9.3.2 Analytic expression for the projected density of states

Following the discussion at the end of Section 9.1 it is convenient to rewrite the operator $\underline{\underline{L}}$ in Eq.(9.56) as

$$\underline{\underline{L}} = \underline{\underline{L}}_0 + \underline{\underline{\delta L}}_0 + \underline{\underline{\delta L}}' + \underline{\underline{\delta L}}'', \tag{9.61}$$

where $\underline{\underline{L}}_0$ is the unperturbed matrix, $\underline{\underline{\delta L}}_0$ is the diagonal matrix constructed from the first type of elements δL_{mm}, $\underline{\underline{\delta L}}'$ contains the second type with terms linking the fundamental guided mode to the cladding modes: $\delta L_{m_0 n}$, and $\delta L_{n m_0}$, and $\underline{\underline{\delta L}}''$ includes the remaining (i.e. cladding-cladding) terms. In general, we can define the Green's function matrix $\underline{\underline{G}}(\beta^2)$ for the operator in Eq.(9.61) by

$$\left(\underline{\underline{L}} - \beta^2\underline{\underline{I}}\right)\underline{\underline{G}}(\beta^2) = -\underline{\underline{I}}, \tag{9.62}$$

where $\underline{\underline{I}}$ is the identity matrix. As usual, we can express the elements of $\underline{\underline{G}}$ in terms of the eigenvalues and eigenvectors of $\underline{\underline{L}}$:

$$G_{pq} = \sum_k \frac{a_{Lq}^{(k)} a_{Rp}^{(k)}}{\beta^2 - \beta^{2(k)} - i\varepsilon}, \tag{9.63}$$

where ε approaches 0 from above. The reason for introducing the Green's function can be seen by using the identity [107]

$$\lim_{y\to 0} \frac{1}{x - iy} = P\frac{1}{x} + i\pi\delta(x), \tag{9.64}$$

where P is the principal value and $\delta(x)$ is a Dirac delta function. The elements of the Green's function become

$$G_{pq} = \sum_k \left[P\frac{a_{Lq}^{(k)} a_{Rp}^{(k)}}{\beta^2 - \beta^{2(k)}} + i\pi a_{Lq}^{(k)} a_{Rp}^{(k)} \delta\left(\beta^2 - \beta^{2(k)}\right)\right], \tag{9.65}$$

and by comparison with Eq.(9.60) we find

$$\rho_i(\beta^2) = \frac{1}{\pi} Im[G_{ii}]. \tag{9.66}$$

Therefore, if we can calculate the Green's function we can determine the projected density of states.

In general, it is not possible to derive analytic expressions for the Green's function. However, there is a useful approximation we can make that enables us to derive an expression for $\rho_{m_0}(\beta^2)$. We ignore the $\underline{\underline{\delta L}}''$ term in Eq.(9.61) and write

$$\underline{\underline{L}} = \underline{\underline{L}}_0' + \underline{\underline{\delta L}}', \tag{9.67}$$

where $\underline{\underline{L}}_0' = \underline{\underline{L}}_0 + \underline{\underline{\delta L}}_0$ is a diagonal matrix whose elements are the shifted propagation constants given by Eq.(9.16). This approximate equation is closely related to a problem that is familiar in electronic structure calculations, where a localised impurity orbital is embedded in an electron gas, and our analysis follows that in Ref. [108]. In the electronic case, the localised orbital broadens into a resonance, and the width of the resonance is related to the lifetime of the electron in the localised state. In our case the interaction of the fundamental guided mode with cladding modes leads to a broadening of the projected density of states and to attenuation of the guided mode.

For the unperturbed but shifted system, we can define a Green's function $\underline{\underline{G}}_0$ that satisfies

$$\left(\underline{\underline{L}}_0' - \beta^2 \underline{\underline{I}}\right) \underline{\underline{G}}_0 = -\underline{\underline{I}}, \tag{9.68}$$

where the elements of the diagonal matrix $\underline{\underline{G}}_0$ have the form

$$G_{0mm} = \frac{1}{\beta^2 - \beta_{0m}'^2 - i\varepsilon}. \tag{9.69}$$

The two Green's function matrices $\underline{\underline{G}}$ and $\underline{\underline{G}}_0$ are related by the Dyson equation [107]

$$\underline{\underline{G}} = \underline{\underline{G}}_0 + \underline{\underline{G}}_0 \underline{\underline{\delta L'}} \underline{\underline{G}}, \tag{9.70}$$

where $\underline{\underline{\delta L'}}$ has non-zero elements only when one of the indices is m_0. The elements in Eq.(9.70) can be expressed as

$$G_{ab} = G_{0aa}\delta_{ab} + G_{0aa} \sum_c \delta L'_{ac} G_{cb}. \tag{9.71}$$

When the subscripts $\{ab\}$ are chosen as $\{m_0 m_0\}$, $\{m m_0\}$, $\{m_0 m\}$, Eq.(9.71) becomes

$$G_{m_0 m_0} = G_{0 m_0 m_0} + G_{0 m_0 m_0} \sum_m \delta L'_{m_0 m} G_{m m_0} \tag{9.72}$$

$$G_{m m_0} = G_{0mm} \delta L'_{m m_0} G_{m_0 m_0} \tag{9.73}$$

$$G_{m_0 m} = G_{0 m_0 m_0} \sum_m \delta L'_{m_0 m} G_{mm}. \tag{9.74}$$

Substituting Eq.(9.73) into Eq.(9.72), we obtain

$$G_{m_0 m_0} = G_{0 m_0 m_0} + G_{0 m_0 m_0} G_{m_0 m_0} \sum_m \delta L'_{m_0 m} G_{0mm} \delta L'_{m m_0}. \tag{9.75}$$

Eq.(9.75) can be rearranged to give

$$G_{m_0 m_0} = \frac{G_{0 m_0 m_0}}{1 - G_{0 m_0 m_0} \sum_m \delta L'_{m_0 m} G_{0mm} \delta L'_{m m_0}} \tag{9.76}$$

and by placing Eq.(9.69) into Eq.(9.76) we obtain an analytic expression for the element of the Green's function we are interested in:

$$G_{m_0m_0} = \frac{1}{\beta^2 - {\beta'}_{0m_0}^2 - i\varepsilon - \sum_m \frac{\delta L'_{m_0m}\delta L'_{mm_0}}{\beta^2 - {\beta'}_{0m}^2 - i\varepsilon}}. \tag{9.77}$$

By comparing Eqs.(9.69) and (9.77), we can interpret the effect of the perturbation on the fundamental guided mode as a change in its value of β^2, given by

$$\Delta\beta_{m_0}^2 = \sum_m \frac{\delta L'_{m_0m}\delta L'_{mm_0}}{\beta^2 - {\beta'}_{0m}^2 - i\varepsilon}. \tag{9.78}$$

It is important to note that this expression has both real and imaginary parts. By using Eq.(9.64) we can write

$$\Delta\beta_{m_0}^2 = \Delta\beta_{m_0}^2(Re) + i\Delta\beta_{m_0}^2(Im), \tag{9.79}$$

where

$$\Delta\beta_{m_0}^2(Re) = P\sum_m \frac{\delta L'_{m_0m}\delta L'_{mm_0}}{\beta^2 - {\beta'}_{0m}^2}, \tag{9.80}$$

where P is the principal value, and

$$\Delta\beta_{m_0}^2(Im) = \pi\sum_m \delta L'_{m_0m}\delta L'_{mm_0}\delta\Big(\beta^2 - {\beta'}_{0m}^2\Big). \tag{9.81}$$

As we shall see in the next chapter, the shift of the real part is not very important, but the existence of an imaginary part leads directly to an attenuation of the guided mode due to the effects of the perturbation. The relationship of this with the projected density of states can be seen by writing

$$G_{m_0m_0} = \frac{1}{\beta^2 - {\beta'}_{0m_0}^2 - \Delta\beta_{m_0}^2(Re) - i\Delta\beta_{m_0}^2(Im)}, \tag{9.82}$$

where $i\varepsilon$ is omitted because it is tiny compared to the term $i\Delta\beta_{m_0}^2(Im)$. It is straightforward to show that the imaginary part of $G_{m_0m_0}$ becomes

$$Im[G_{m_0m_0}] = \frac{\Delta\beta_{m_0}^2(Im)}{\big(\beta^2 - {\beta'}_{0m_0}^2\big)^2 + \big(\Delta\beta_{m_0}^2(Im)\big)^2}, \tag{9.83}$$

where the small term $\Delta\beta_{m_0}^2(Re)$ has been neglected. The projected photonic density of states then becomes

$$\rho_{m_0}(\beta^2) = \frac{1}{\pi} \frac{\Delta\beta^2_{m_0}(Im)}{(\beta^2 - {\beta'}^2_{0m_0})^2 + \left(\Delta\beta^2_{m_0}(Im)\right)^2}. \tag{9.84}$$

Eq.(9.84) is a Lorentzian function in β^2, for which the full width at half maximum (FWHM) is $2\Delta\beta^2_{m_0}(Im)$. This shows the relationship between the width of the projected density of states and the attenuation of the fundamental mode.

9.4 Summary

In this chapter we have developed a perturbation method to analyse the real model PCF structures with a vector governing equation. The perturbation matrix for the magnetic fields has been derived, and we have shown that the matrix elements can be expressed analytically by using the one-dimensional field equations. The correction of the propagation constant for the real case can be viewed in two steps. The first is a shift of the propagation constant, and the second involves the interaction of these shifted solutions. The perturbation also has two parts: the vector terms of the governing equation, and the difference between the real and ideal fibre structures. In our investigation, these effects can be analysed individually or together, which enables us to obtain a useful comparison. We have also discussed the way in which we can analyse the effect on the fundamental guided mode due to the interactions with the cladding modes. In the next chapter we will present numerical results based on the theory we have developed.

Chapter 10

Perturbation results

In this chapter, we perform perturbation calculations based on the theory presented in the previous chapter. The aim is to analyse the strength of the mode interactions, and to provide a physical explanation for the weak interaction guidance.

In Section 10.1 we discuss the shift of the guided modes due to the diagonal elements of the perturbation matrix. The perturbed propagation constants and the general pattern of the mode interactions are discussed in Section 10.2. The weight of the unperturbed fundamental guided mode in the perturbed guided modes is calculated and analysed in Section 10.3. In Section 10.4 we investigate the perturbed field for both the fundamental guided mode and the cladding modes with the largest weightings from the unperturbed fundamental mode. Calculations of the imaginary part of the propagation constant from perturbation theory are presented in Section 10.5. Section 10.6 is the conclusion.

10.1 Shift of the propagation constants

In Chapter 8, we used an ideal 8×8 supercell model structure to calculate the full set of the modes for the scalar wave equation for $k_0\Lambda = 40$. In our perturbation calculations, we choose the same frequency. As discussed in Section 9.1, the diagonal elements of the perturbation matrix correspond to a shift of the propagation constant. In this section, we present results for this shift, based on the expressions derived in Section 9.1. A comparison between the shifted and unshifted $\beta\Lambda$ is shown in Fig.10.1. It contains two sets of modes for the x (the upper figures) and y (the lower figures) polarisations. As discussed in Section 8.5, the full set of supercell modes can be divided into air-guided and glass-guided modes. The air-guided modes with a small value of C are shown in the middle figures; the glass-guided modes with large values of C are shown in the two side panels. The air-guided modes consist of the combinations of modes $A(1-5)$ and $B(1-3)$, and the glass-guided modes are formed by combinations of the symmetric modes $C(1-4)/D(1-4)$ with $E(1/2/11)$ (see Tables 8.2 to 8.6).

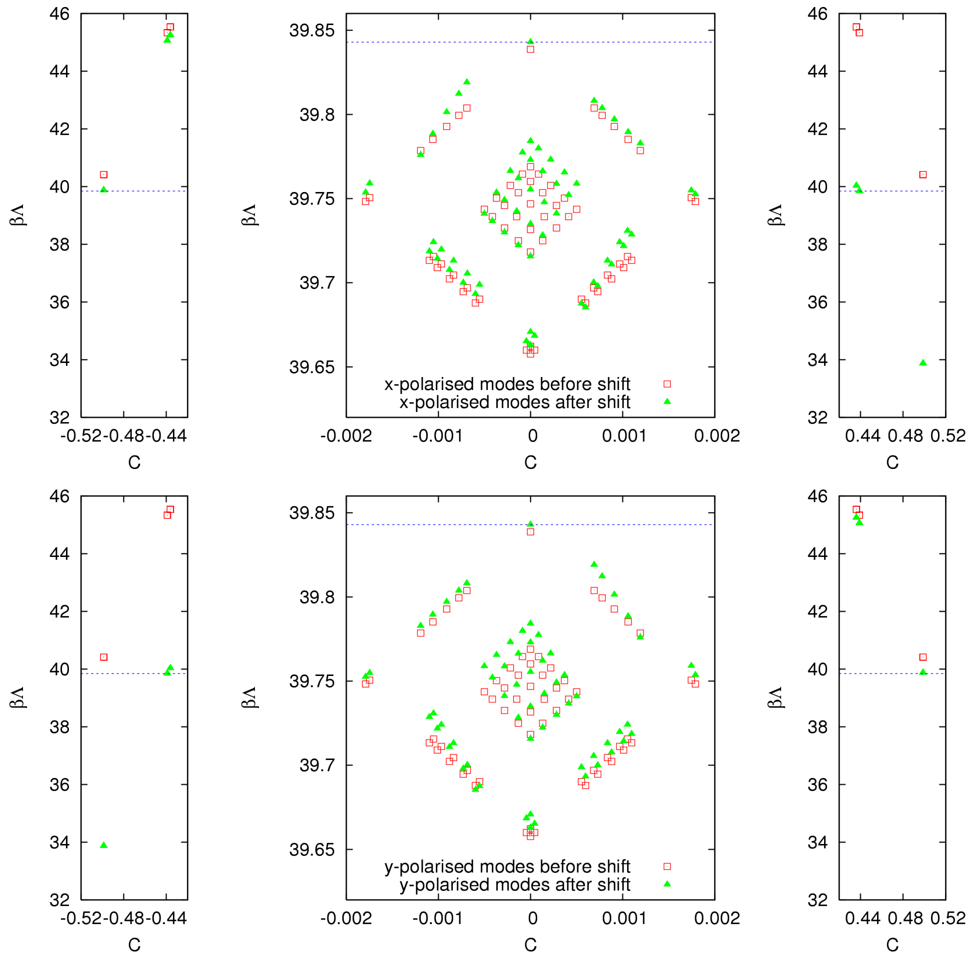

Figure 10.1: Shifts of air-guided and glass-guided modes. The upper three and lower three figures are for x and y polarised modes respectively. The middle figures are shifts of the air-guided modes, and the side figures are shifts of the glass-guided modes. The red and green points show the unshifted and shifted modes, respectively. The blue lines indicate the shifted $\beta\Lambda$ value of 39.842977 for the fundamental guided mode.

For the air-guided modes, it is found that the shifts are relatively small. For example, when $k_0\Lambda = 40$, the $\beta\Lambda$ value for the fundamental guided mode after the diagonal shift is 39.842977, which is 4.292×10^{-3} greater than the unperturbed solution (where $\beta\Lambda = 39.838685$). In addition, the shifts arising from the vector terms and high-index terms can be calculated separately. With only the vector terms, the shifted $\beta\Lambda$ is 39.842980, and with only the high-index terms, it is 39.838681. The difference between these and the scalar solutions are 4.295×10^{-3} and -4×10^{-6}, respectively. This shows that the shift of $\beta\Lambda$ is mainly caused by the vector terms. For all of the air-guided modes the shift due to the vector terms is about three orders of magnitude greater than that of the high-index terms.

The glass-guided modes are affected much more strongly than the air-guided modes, as can be seen from the side figures of Fig.10.1. The propagation constants for some of the glass-guided modes exhibit a very large shift. Specifically, for the x polarised glass-guided modes, the large shift occurs only when the transverse field extends along the x direction (e.g. Fig.8.13(a) in Section 8.5.2), while for the y polarised modes, the fields spreading along the y direction have a large shift (e.g. Fig.8.13 (b)). The shifts of the glass-guided modes are dominated either by vector terms or by high-index terms. We find that for those modes with a large shift the vector effect is about one order of magnitude larger than the high-index effect in the change of $\beta\Lambda$ values; for the others the vector effect is about one order of magnitude lower than the high-index effect. The large shifts require us to calculate a wide range of glass-guided modes in order to ensure that we consider all the modes with a shifted β in the guided area. For example, the modes formed by combining the symmetric modes of $C(1-4)/D(1-4)$ with the delocalised modes $E(1/2)$ should be included, even though their scalar propagation constants are very different from the fundamental guided mode.

The shifted $(\beta\Lambda)^2$ value for the fundamental guided mode is 1587.4629. The $(\beta\Lambda)^2$ values for the cladding modes nearest to the fundamental guided mode after the diagonal shift are 1585.5579 and 1587.6618 for air-guided and glass-guided modes respectively, which are produced by $A(1)$ combined with $A(2)$, and $C(1-4)/D(1-4)$ combined with $E(2)$.

The modes found with the scalar wave equation and the ideal model structure are either two-fold degenerate (i.e. x and y polarisations with $C = 0$) or four-fold degenerate (i.e. x and y polarisations and $C \to -C$). After the shift, all modes are doubly degenerate, with the factor C and the polarisation being related by $(C, x) \leftrightarrow (-C, y)$, as can be seen in Fig.10.1.

10.2 Perturbed propagation constant

By using the expressions for the matrix elements derived in Section 9.2 in Eq.(9.15), we can construct the full perturbation matrix and calculate its eigenvalues and eigenvectors. The eigenvalues in Eq.(9.15) are the square of normalised propagation constant, and the corresponding eigenvectors represent the coefficients of the unperturbed modes in the expansion of the perturbed field, as shown in Eq.(9.5).

The modes included in the perturbation matrix come from those shown in Fig.10.1, for which the shifted propagation constants with either x or y polarisation are in the vicinity of the shifted fundamental guided mode. For each polarisation, this gives 64 basis states from air-guided modes and 48 basis states from glass-guided modes. The perturbation matrix shown in the second term of the left hand side of Eq.(9.15) consists of four parts, arising from the different polarisations. The size of each sub-matrix is 112×112, and each contains four blocks: one with 64×64 elements for the air-air mode interaction, one with 48×48 elements for the glass-glass mode interaction and two with 64×48 or 48×64 elements for the air-glass mode interaction. Each element is a sum of a vector term (as described in Section 9.2.1) and a high-index term (as described in Section 9.2.2).

It is interesting to look at the magnitude of the different elements of the perturbation matrix. We first consider the vector terms. The maximum absolute values of the diagonal perturbation terms are 1.2146 and 445.4972 for air-guided and glass-guided modes respectively, which correspond to the largest shifts of $(\beta\Lambda)^2$. Average absolute values are 0.6037 and 222.7065 respectively. By comparison, the off-diagonal elements are considerably smaller. The largest magnitudes for modes with the same polarisation (i.e. within δL_{xx} and δL_{yy}) are 0.5629, 8.4828 and 8.5495×10^{-2} for the air-air, glass-glass and air-glass mode interactions respectively. More typical values are of order 10^{-1}, 10^{0} and 10^{-3} respectively for these three types. For the interaction between different polarisations (i.e. within δL_{xy} and δL_{yx}), the maximum values are 5.0883×10^{-4}, 12.8871 and 0.2951 and typical values are of order 10^{-5}, 10^{0} and 10^{-2} for the three groups.

The high-index term has a rather different effect. The largest magnitudes of the diagonal shifts for the air-guided and glass-guided modes are 1.7236×10^{-3}, 49.0511 respectively (average values are 9.1295×10^{-4} and 32.7054), which are significantly smaller than for the vector terms. The largest magnitudes of the off-diagonal elements in δL_{xx} and δL_{yy} are 2.5187×10^{-4}, 14.6505 and 0.1025 for the air-air, glass-glass and air-glass mode interactions; more typical values are 10^{-5}, 10^{0} and 10^{-2} respectively. The δL_{xy} and δL_{yx} elements are identically zero for the high-index term. In general, we can conclude that, apart from the diagonal shift, the magnitude of the perturbation is relatively small, which gives us confidence that the solutions of the ideal model structure provide a useful basis to analyse real fibre structures. We also note that the vector effects and high-index effects are both significant; neither can be neglected in performing perturbation calculations.

Before looking in detail at the effect of the perturbation on the fundamental guided mode, we first note some general properties of the solutions of the perturbation matrix. After perturbation, investigation of the eigenvectors shows that it is still possible to distinguish between modes that are predominantly air-guided and those which are predominantly glass-guided. This is what would be expected from the magnitude of the air-glass matrix elements. The very different nature of the fields of the unperturbed air-guided and glass-guided modes means that the air-glass matrix elements are small (typically of order 10^{-2}) relative to the typical separation between the shifted $(\beta\Lambda)^2$ values, leading to only a small amount of mixing between air-guided and glass-guided modes. The magnitude of the off-diagonal matrix elements also gives an indication of how much mixing there is within the air-guided and glass-guided modes. The glass-glass matrix elements are substantially larger (by more than one order of magnitude) than the other types of elements. The strong mixing that this leads to means that the perturbed glass-guided modes typically have contributions from a number of glass-guided unperturbed modes. The situation is different, however, for the air-guided modes, where the matrix elements are relatively small compared with the typical spacing of the shifted $(\beta\Lambda)^2$ values. This means that, for nearly all of the perturbed air-guided modes, either one unperturbed mode is dominant or two unperturbed modes have fairly equal weightings.

There is one important exception to this general pattern. We find that the fundamental air-guided mode mixes strongly with some glass-guided modes, leading to two degenerate pairs of perturbed 'fundamental' modes with $\beta\Lambda$ values of

39.843577 and 39.843715 respectively. The relevant unperturbed glass-guided modes are those constructed from $C(2/4)$ and $E(2)$. The shifted $(\beta\Lambda)^2$ values of the unperturbed fundamental air-guided mode and these glass-guided modes are 1587.4629 and 1587.6618 respectively; the closeness of these values explains why even the relatively weak air-glass matrix elements can produce a significant amount of mixing. It is important to emphasise that this strong mixing of the fundamental mode is not a special property of this mode. Within our 8×8 supercell structure there are a finite number of modes and it is a largely a matter of 'luck' whether, for a given frequency $k_0\Lambda$, there is a strong mixing between any given modes. The typical sizes of the matrix elements given above are not a matter of luck; they do give a good indication of the strength of the mode interaction. The finite spacing of the modes, however, depends on the size of the supercell used and therefore the strong mixing of the fundamental mode we have found at $k_0\Lambda = 40$ is more a reflection of the size of supercell used than a property of the model fibre. We have confirmed this by performing calculations at other frequencies; for example, at $k_0\Lambda = 40.1$ the fundamental mode is 'clean' and does not mix strongly with glass-guided modes.

10.3 Projected weighting of the fundamental guided mode

In this section we look in more detail at the properties of the fundamental air-guided mode. In order to obtain a clearer understanding the effect of the cladding modes on the leakage from the fundamental guided mode, it is useful to analyse the projected density of states on the unperturbed fundamental guided mode, based on Eq.(9.60). Because of the finite number of modes in the supercell geometry, instead of trying to calculate Eq.(9.60) directly, we look at the individual states that make up the projected density of states, and plot the weighting $W_{m_0}^{(k)} = a_{Lm_0}^{(k)} a_{Rm_0}^{(k)}$ of the unperturbed fundamental mode m_0 in each perturbed state k with eigenvalue $\beta^{(k)}$. As discussed in the previous section, there is a clear separation of the perturbed modes into those derived mainly from air-guided modes and those from glass-guided modes and so we consider these groups of modes separately.

The weights $W_{m_0}^{(k)}$ for the air-guided modes are shown in Fig.10.2 (a). These have been calculated for the x polarised unperturbed fundamental mode; the results for the y polarisation are equivalent. The red, green and blue points represent weights larger than 0.1, between 10^{-5} and 0.1 and less than 10^{-5}, respectively.

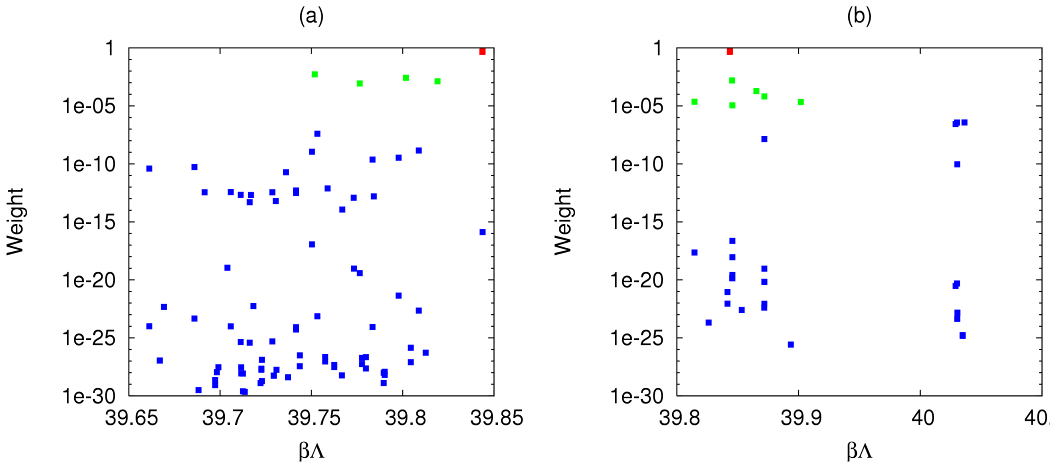

Figure 10.2: Projected weights of the x polarised fundamental mode on the perturbed modes. (a) and (b) are for the air-guided and glass-guided modes respectively. The different colours indicate the different magnitudes of the projected weight.

The largest two weights, as shown by the overlapping red points in Fig.10.2 (a), correspond to the projection on the perturbed fundamental guided modes with the same x polarisation. The weights are 0.4540 and 0.5340 for $\beta\Lambda = 39.843577$ and 39.843715 respectively; these modes also have a large contribution from glass-guided modes, as discussed in the previous section. The group of modes with the second highest weights (green colour) are derived from unperturbed air-guided modes with the same p_x value as the fundamental guided mode $A(1)$ and the same p_y value as the both-even modes $A(2-5)$. The exact value of the projected weighting varies from 8.6503×10^{-4} to 5.2552×10^{-3}. All other modes shown in blue have a very small contribution from the unperturbed fundamental mode.

The weights of the x polarised fundamental guided mode in the perturbed glass-guided modes are shown in Fig.10.2 (b). The red points shown in Fig.10.2 (b) are the same as those in Fig.10.2 (a), showing that these modes also have a considerable contribution from glass-guided modes. The perturbed modes shown in green have weights between 1.1111×10^{-5} and 1.5728×10^{-3}, a similar magnitude to those of the 'strongest' air-guided modes. Unlike the perturbed air-guided modes, each perturbed glass-guided mode has contributions from several unperturbed glass-guided modes; this will be discussed further in the next section.

Fig.10.2 shows that, within our supercell geometry, there exists a number of air-guided and glass-guided modes that have relatively strong contributions from the unperturbed fundamental mode for the selected frequency. The most prominent are two perturbed fundamental guided modes. In addition, four air-guided modes and six glass-guided modes have a projected weighting of order between 10^{-5} and 10^{-3}; the weighting of the other modes is less than 10^{-5}. In the next section, the perturbed fields for these strongly interacting modes will be plotted and analysed. From this we can understand the characteristics of the perturbed fundamental modes better, and gain a better understanding of the effects of the perturbation on the air-guided and glass-guided modes.

10.4 Perturbed field profiles

The field profiles can be calculated from Eq.(9.5) by treating the eigenvectors of the perturbation matrix as a set of coefficients. The perturbed field is then expressed as an expansion over a full set of unperturbed modes. As in the previous section, for any perturbed mode k we can also calculate the weighting $W_i^{(k)}$ of each unperturbed mode i. The unperturbed modes are either purely x or y polarised. After the perturbation, the perturbed field has contributions from both polarisations. However, since we are concentrating on the x polarised unperturbed fundamental mode, the majority polarisation of the field of the perturbed modes that have the largest weights in Fig.10.2 remains in the x direction. For example, for the modes shown in red in Fig.10.2, the highest magnitude of the field in the y direction is found to be about three orders of magnitude lower than for the x polarisation.

The fields for the two perturbed fundamental guided modes (i.e. the red points in Fig.10.2) are shown in Fig.10.3, where a(1) and a(2) correspond to $\beta\Lambda =$ 39.843577 and 39.843715, respectively. The largest weightings of unperturbed modes are from the fundamental guided modes (with weights 0.4540 and 0.5340 respectively) and from the glass-guided modes formed from $E(2)$ and $C(1-4)$ (see Tables 8.4 and 8.6), where the total weights are 0.5404 and 0.4602 for a(1) and a(2). In addition, there are smaller but significant contributions from the air-guided modes formed from $A(1)$ with $A(2-5)$, for which the total weights are 0.0048 and 0.0053 respectively. The effect of the strong mixing can be clearly seen in Fig.10.3, where the field spreads from the central defect into the surrounding glass strips; specifically those parallel to the x axis. Figs.10.3 b(1-2) show a

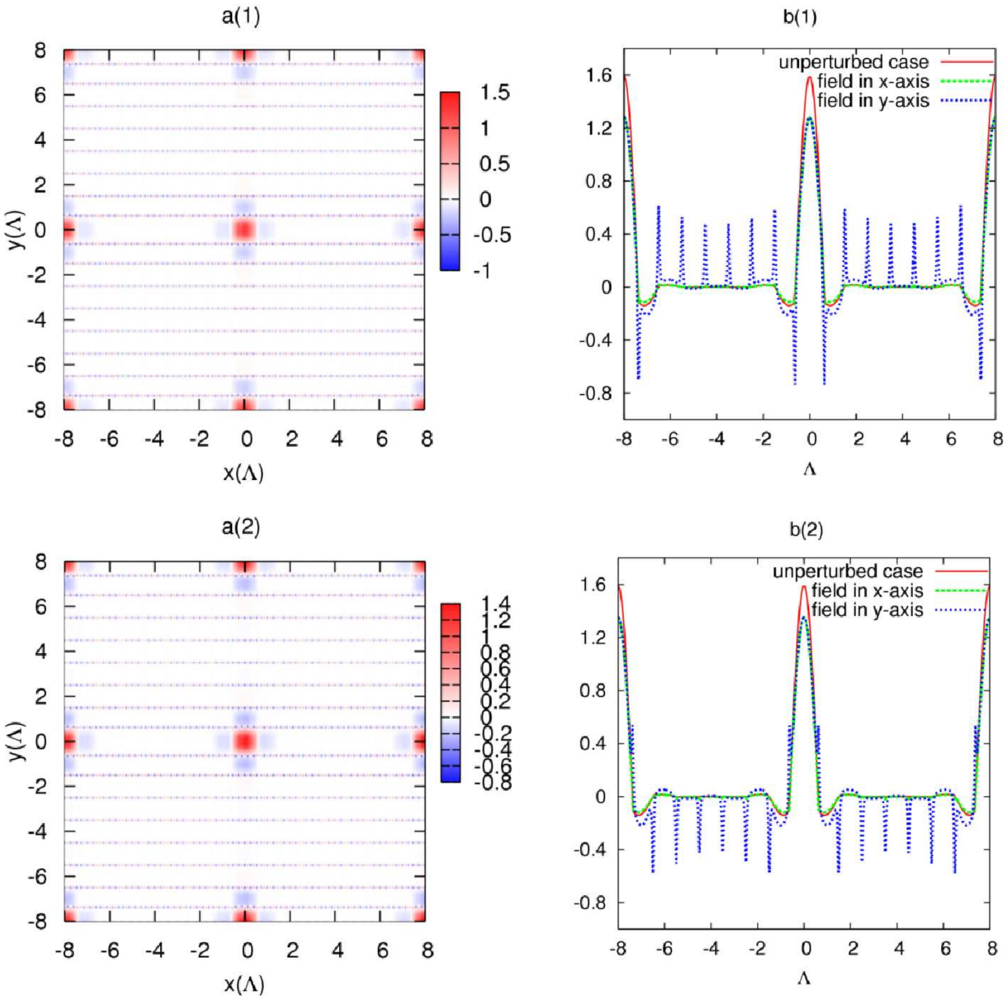

Figure 10.3: Field profiles in the supercell geometry for the perturbed fundamental guided modes when $k_0\Lambda = 40$. a(1-2) correspond to the two propagation constants of $\beta\Lambda = 39.843577$ and 39.843715 respectively. b(1-2) are their corresponding amplitudes along the x (the green lines) and y (blue lines) axes. The red lines in b(1-2) are for the unperturbed fundamental field.

comparison of the perturbed fields with the unperturbed fundamental mode. The interaction with the cladding is again clear and we can also see that the field in the central defect becomes weaker. A fairly small enhanced amplitude in the outer defect regions arising from the air-guided modes can also be observed.

We now turn to the cladding modes that have the largest projected weighting of the fundamental guided mode. Fig.10.4 shows the field profiles for the perturbed air-guided modes corresponding to the green points in Fig.10.2 (a). In each of these perturbed modes, we find a single dominant projected weighting (between 0.9584 and 0.9976) from an unperturbed air-guided mode; these have been plotted in Figs.8.11 a(2-5). The comparison between the unperturbed and perturbed fields shows that these modes are relatively 'clean', with a limited interaction with glass-guided modes. These perturbed fields reflect a more typical case for the air-guided modes in the 8×8 supercell, rather than the unusually perturbed fundamental guided mode. By looking at the plots in Figs.10.4 b(1-4) and c(1-4), we find that the field along the y direction is more heavily affected than that along the x direction; the perturbation occurs mainly in the inner defect regions along the y axis. Figs.10.4 b(1-4) show a clear change of amplitude at the centre of the supercell, varying from an increase between 0.0671 to 0.1039. This increase comes mainly from the contribution of the fundamental guided mode to these perturbed modes.

The glass-guided modes interact strongly due to their close $\beta\Lambda$ values and therefore their perturbed fields are complicated. The fields of the six modes shown in green in Fig.10.2 (b) are plotted in Fig.10.5. By looking at the projected weightings for all the unperturbed modes, we find these perturbed modes come mainly from the glass-guided modes with the same (p_x, p_y) values as $(E(2), C(1-4))$ and $(C(1-4), E(11))$ (see Tables 8.4 and 8.6). All of these modes also have a contribution from the fundamental guided mode; this is most clearly seen in figure b(1), which corresponds to the highest green point in Fig.10.2 (b).

10.5 Imaginary part of the propagation constant

In the previous sections we have analysed the interaction between the fundamental guided mode and the cladding modes, by looking at the contributions to the projected weighting given in Eq.(9.60) and by plotting the fields of the perturbed modes. However, there is one important aspect of the interaction that we have

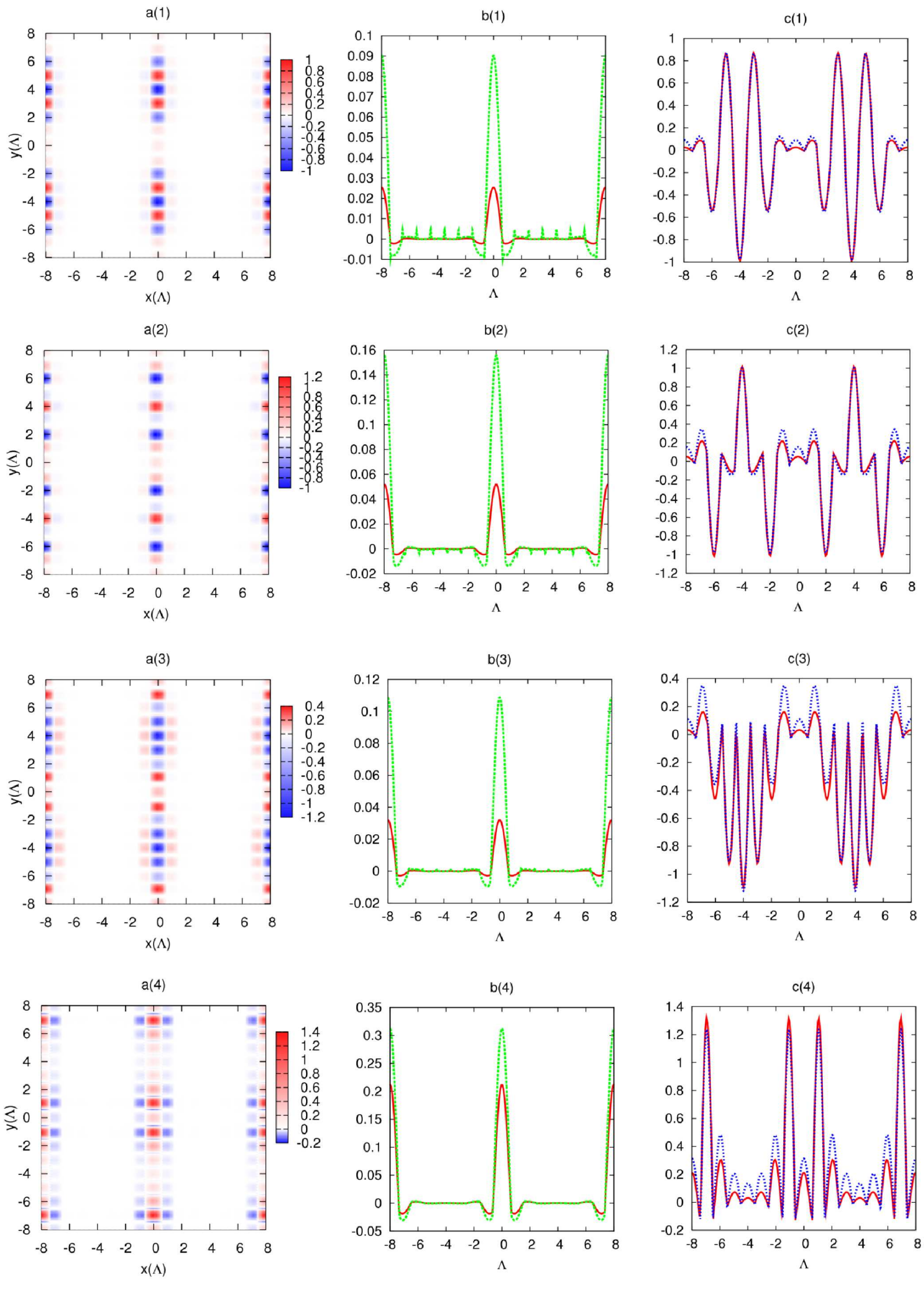

Figure 10.4: Field profiles of the perturbed air-guided modes containing the largest weighting from the x polarised fundamental guided mode (as shown by the green points in Fig.10.2 (a)). Their major components come from the unperturbed modes shown in Figs.8.11 a(2-5). b(1-4) and c(1-4) show comparisons of the amplitude of the field along the x and y axes respectively. The red and green/blue lines show the unperturbed and perturbed cases.

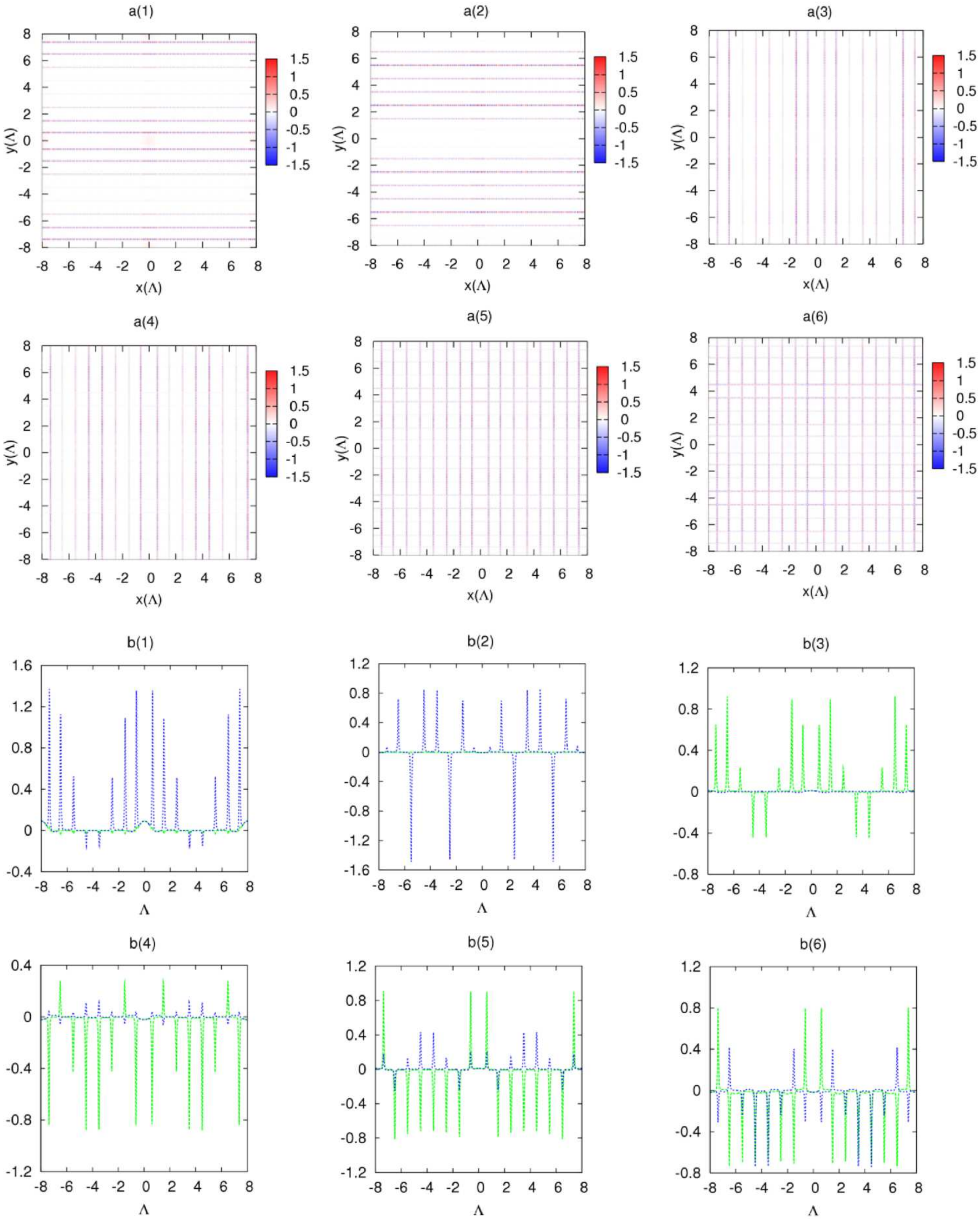

Figure 10.5: Field profiles of the perturbed glass-guided mode containing the largest weighting from the fundamental unperturbed guided mode. a(1-6) are the transverse fields after the perturbation. b(1-6) are the corresponding field amplitudes along the x and y axes, as shown by the green and blue lines respectively.

not yet discussed: the attenuation or confinement loss of the fundamental guided mode that this interaction causes. In the ideal scalar model, the confinement of the fundamental guided mode is perfect and, in the case of an infinite cladding, the attenuation would be zero. In the real structure the effects of the high-index and vector terms cause an interaction between the fundamental guided mode and the cladding modes and, because there is no bandgap, light can leak out from the guided modes into the surrounding cladding. This leakage would be modelled in the theory as an imaginary part of the propagation constant β and would be measured as an attenuation of the guided mode.

As was discussed in Section 9.3, the width of the density of states projected onto the fundamental guided mode gives a measure of the strength of the interaction and the confinement loss. Although we can analyse the individual components of the projected density of states in our supercell calculations, the discrete nature of the modes of the supercell and the weakness of the interaction (as shown in Fig.10.2) mean that it is not possible to define the width of $\rho_{m_0}(\beta^2)$. The usual way to define a continuous function (like the density of states in Eq.(9.60)) from a discrete set of calculated values is to use a smoothing method, for example, by replacing the delta function in Eq.(9.60) with Gaussian functions. However, this can not be done with the density of states projected onto the fundamental guided mode, because the gaussian width needed to obtain a smooth function would be greater than the intrinsic width $\rho_{m_0}(\beta^2)$. In principle this problem could be solved by using a larger supercell, but the interaction is so weak that the size of supercell required would be too large.

In order to discuss the attenuation of the fundamental guided mode we therefore turn to the approximate theory discussed in Section 9.3.2. By neglecting the cladding-cladding interaction terms, we were able to derive expressions for the Green's function from which analytic expressions for the projected density of states and the imaginary part of propagation constant were obtained. It is difficult to make a quantitative estimate of the effect of neglecting the cladding-cladding terms, but it is reasonable to expect that the major contributions to the attenuation of the fundamental guided mode are contained in the analysis of Section 9.3.2. The key result is expression Eq.(9.81) for the imaginary part of the propagation constant, which shows that the attenuation is governed by the matrix elements between the unperturbed mode m_0 and the other modes m. The mixing of the glass-guided modes that would be caused by the neglected terms will change the details of the interaction, but not the basic magnitude of the terms in Eq.(9.81). In this section, therefore, we use the analysis of Section 9.3.2 and, in particular, expression Eq.(9.81) to analyse the attenuation of the fundamental guided mode caused by the perturbation of the high-index and vector terms.

Equation (9.81) gives the imaginary part of the shift of the value of β^2 of the fundamental guided mode due to the high-index and vector perturbation terms. It consists of two parts, the matrix elements $\delta L'_{mm_0}\delta L'_{m_0m}$ and the density of states term represented by the delta function. In evaluating Eq.(9.81) two questions arise: at what value of β^2 should Eq.(9.81) be calculated, and which states m should be included in the sum?

Although we will need $\Delta(\beta_{m_0}\Lambda)^2_{[Imag]}$ at a particular value of β^2, it is useful first to consider Eq.(9.81) as a function of β^2, for values of β^2 close to the fundamental guided mode. To do this we smooth the delta functions in Eq.(9.81) by replacing them with gaussian functions and calculate

$$\Delta(\beta_{m_0}\Lambda)^2_{[Imag]} = \pi\sum_m \frac{1}{\sqrt{2\pi}\sigma} e^{-\frac{\left[\left((\beta\Lambda)^2-(\beta'_{0m}\Lambda)^2\right)/\sigma\right]^2}{2}} \delta L'_{mm_0}\delta L'_{m_0m}. \qquad (10.1)$$

where $1/\sigma\sqrt{2\pi}$ is a normalisation factor. The width of each mode is controlled by σ; a small value of σ represents little smoothing and a sharp peak in the plots.

Since the unperturbed cladding modes can be divided into air-guided and glass-guided modes, we can consider the weighted density of states Eq.(10.1) of these modes separately. The air-guided modes have a much high density of states than the glass-guided modes; a larger value of σ is therefore generally required for the latter to obtain a smooth density of states.

For the purpose of the high accuracy, the gaussian function should approach the delta function. We therefore want to use as small a value of σ as possible; this requires a very big supercell for reliably converged results. However, a problem arises if the supercell size becomes too large. As discussed in Chapter 7, the modes are found by searching for identical wave functions in neighboring supercells through a transfer matrix. As the size of the supercell increases, the transfer matrix passes through more air and glass layers. For some of the modes, especially the fundamental guided mode, the fields are well localised within a few layers and decay exponentially through the outer regions. To find these modes in a large supercell requires calculations with a high precision. For some fibre configurations, for example exceeding 32×32 supercells, we have found that even quadruple precision is insufficient. We have therefore chosen a set of supercells no more than 32×32 in our calculation.

Plots of the matrix element weighted density of states Eq.(10.1) for the air-guided and glass-guided modes are shown in Figs.10.6 and 10.7, respectively. In each supercell, the shifted $(\beta\Lambda)^2$ values of the fundamental mode are identical to at least five decimal places, therefore they can be indicated by an identical black arrow in these figures. The plotted range of $(\beta\Lambda)^2$ for air-guided and glass-guided modes are chosen to be 10 and 50 respectively so that the patterns close to the shifted fundamental guided mode can be examined clearly.

Fig.10.6 displays the calculated imaginary part of $\Delta(\beta\Lambda)^2$ caused by interaction of the fundamental guided mode with the air-guided modes. There exists an extremely high peak at around $(\beta\Lambda)^2 = 1580$; its magnitude varies from 4 to 1 for σ values between 0.1 and 0.4. This strong interaction comes from one air-guided mode with the field located in the outer defect regions. A comparison of Figs.10.6 (a-d) shows that both larger σ values and supercell sizes make the results smoother. For well-converged results the minimum acceptable value of σ in this set of supercells is 0.3, for which the difference of $\Delta(\beta_{m_0}\Lambda)^2_{[Imag]}$ between 28×28 and 32×32 supercells is less than 1%. In Fig.10.7, the weighted density of states for glass-guided modes exhibits a broad distribution over a wider range of $(\beta\Lambda)^2$. These figures show that the smallest acceptable value of σ is 10 for the largest supercell we have used. At this value, the difference between 28×28 and 32×32 supercells is less than 2%.

Based on these findings we return to the questions asked earlier in this section. The analysis of Chapter 9 shows that we require $\Delta(\beta_{m_0}\Lambda)^2_{[Imag]}$ at the β^2 value of the fundamental guided mode. Figs.10.6 and 10.7 show that, with the smoothing method described by Eq.(10.1), we can have confidence in determining this value of $\Delta(\beta_{m_0}\Lambda)^2_{[Imag]}$. In general, the values in Fig.10.6 are larger than those in Fig.10.7, and they vary more rapidly with $(\beta\Lambda)^2$. We see that the variation in Fig.10.7 is very smooth, and that there is clearly a non-zero value of $\Delta(\beta_{m_0}\Lambda)^2_{[Imag]}$ at the β^2 value of the fundamental mode, because the density of glass-guided modes is non-zero. In contrast, we see that the value of $\Delta(\beta_{m_0}\Lambda)^2_{[Imag]}$ is zero at the β^2 value of the fundamental mode for the air-guided modes in Fig.10.6. In

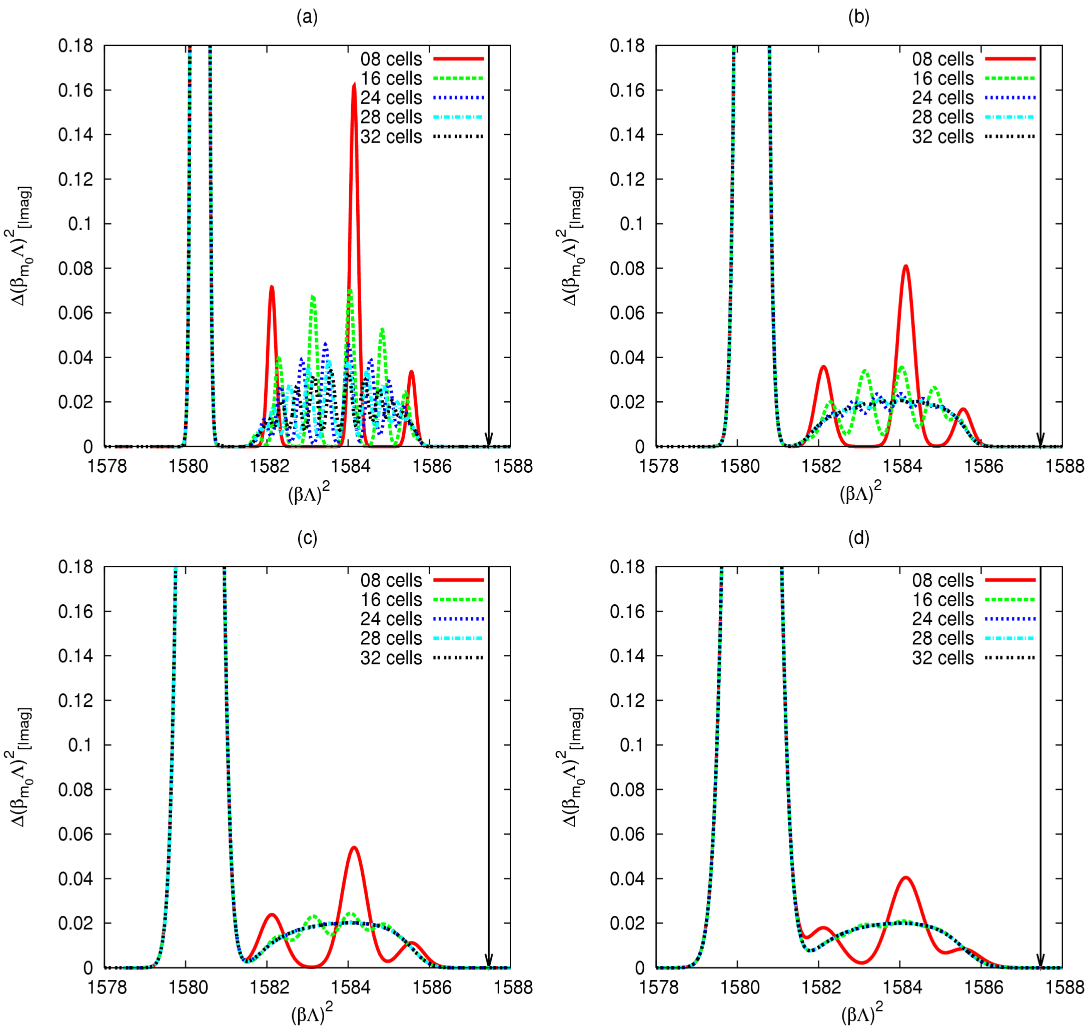

Figure 10.6: Density of states of the air-guided modes weighted by the perturbation matrix elements. σ values are 0.1, 0.2, 0.3 and 0.4 for figures (a-d) respectively. The black arrows indicate the location of the shifted fundamental guided mode with $(\beta\Lambda)^2 = 1587.46$ for all the sizes of supercells.

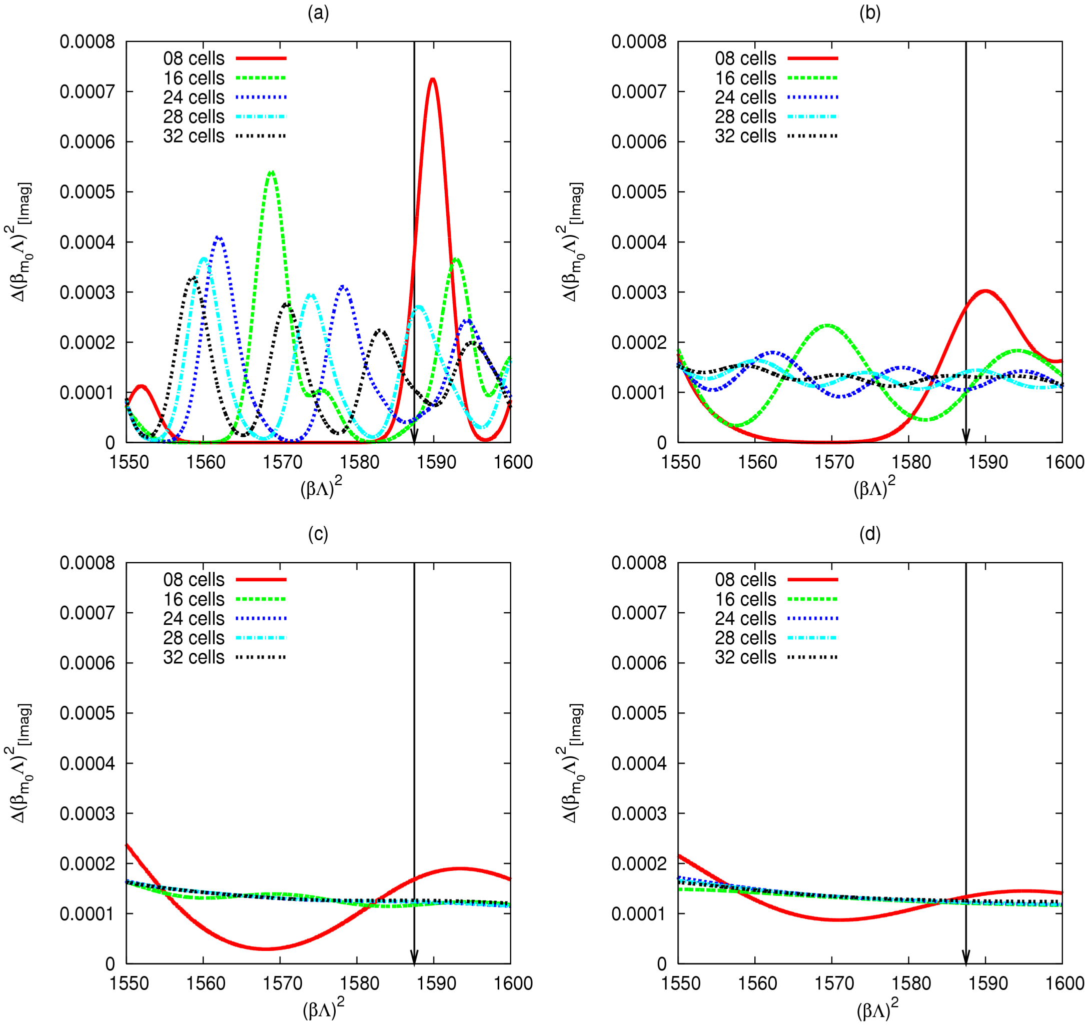

Figure 10.7: Density of states of the glass-guided modes weighted by the perturbation matrix elements. σ values are 2, 5, 10 and 15 for figures (a-d) respectively. The black arrows show the shifted fundamental guided mode, as in Fig.10.6.

effect, there is a bandgap for the air-guided modes. Therefore, for $k_0\Lambda = 40$ we consider only the glass-guided modes and calculate $\Delta(\beta_{m_0}\Lambda)^2_{[Imag]}$ for $(\beta\Lambda)^2 = 1587.46$. Although this analysis is for only a sample frequency in our model structure, it should be equally valid within the high-transmission windows for the family of weak interaction guidance PCF. As will be discussed in the next chapter, there also exist regions of frequency for which the confinement loss is significantly enhanced. The value of the leakage in these high-loss regions is not very important, but the attenuation in the high-transmission windows is one of the most crucial issues in the performance of PCFs.

10.6 Conclusions

Perturbation calculations and analysis have been performed in this chapter, based on the results of Chapter 8 and the derivation in Chapter 9. We have calculated the perturbation matrix and calculated its eigenvalues and eigenvectors. The results show that the glass-guided modes interact more strongly than the air-guided modes. For the fundamental guided mode, the projected weighting and the perturbed fields have been investigated. It was found that the coupling of the fundamental guided mode with the air-guided and glass-guided modes have similar orders of magnitude. However, the effect of the glass-guided modes is more significant due to the closer β values.

The approximate analytic expression for the attenuation derived in Chapter 9 has been used to calculate the change of the propagation constant of the fundamental guided mode after perturbation. By investigating the convergence of these results with respect to the supercell size and the width of the gaussian smoothing, we have selected a set of calculation parameters that provide reliable results. In the next chapter we will carry out a systematic analysis of the attenuation with respect to frequency and the structure of the rectangular PCF.

Chapter 11

The frequency and structural dependence of the attenuation

In this chapter, we will use the results of the last chapter to calculate the leakage of the fundamental mode due to vector and high-index perturbations and investigate the influence on the attenuation of the frequency, glass thickness and core size. This work provides us with an insight into the guidance in rectangular hollow-core PCFs and offers some perspectives in optimising fibre structures.

The method to calculate the attenuation is presented in Section 11.1. In Section 11.2 we present results for the attenuation as a function of frequency. The effect of the thickness of the glass strips is discussed in Section 11.3, and Section 11.4 discusses the effect of varying the size of the central defect. Section 11.5 presents the density of states of cladding modes, which is compared and discussed with the attenuation shown in Section 11.2. The conclusion is drawn in Section 11.6.

11.1 Calculation of the imaginary part of the propagation constant

An expression for the imaginary part of $\Delta(\beta\Lambda)^2$ for the fundamental guided mode has been given in Eq.(10.1). The perturbation leads to a complex value of

$(\beta_{m_0}\Lambda)^2$, which is related to its shifted value of $(\beta'_{0m_0}\Lambda)^2$ by

$$(\beta_{m_0}\Lambda)^2_{[Cmplx]} = (\beta'_{0m_0}\Lambda)^2_{[Real]} + \Delta(\beta_{m_0}\Lambda)^2_{[Cmplx]}, \tag{11.1}$$

where the labels $[Cmplx]$ and $[Real]$ represent complex and real types. The effect of the real part of $\Delta(\beta_{m_0}\Lambda)^2_{[Cmplx]}$ is small compared to the value of $(\beta'_{0m_0}\Lambda)^2$, therefore we write $\Delta(\beta_{m_0}\Lambda)^2_{[Cmplx]} = i\Delta(\beta_{m_0}\Lambda)^2_{[Imag]}$. Eq.(11.1) then becomes

$$(\beta_{m_0}\Lambda)_{[Cmplx]} = \sqrt{(\beta'_{0m_0}\Lambda)^2_{[Real]} + i\Delta(\beta_{m_0}\Lambda)^2_{[Imag]}}, \tag{11.2}$$

and by using a first order Taylor expansion on the square root in Eq.(11.2), the imaginary part of propagation constant is given by

$$\left(\beta_{m_0}\Lambda\right)_{[Imag]} = i\frac{\Delta(\beta_{m_0}\Lambda)^2_{[Imag]}}{2(\beta'_{0m_0}\Lambda)_{[Real]}}. \tag{11.3}$$

The combination of Eqs.(10.1) and (11.3) allows us to calculate the attenuation in rectangular hollow-core PCFs.

11.2 Frequency dependence

By substituting the value of $\Delta(\beta_{m_0}\Lambda)^2_{[Imag]}$ for $k_0\Lambda = 40$ into Eq.(11.3), the attenuation is calculated to be $\left(\beta_{m_0}\Lambda\right)_{[Imag]} = 1.58 \times 10^{-6}$. This shows that the leakage is small in our model structure. However, it is expected that the confinement loss will significantly increase at some frequencies due to a resonance of the glass strips [65, 66, 90–92]. This occurs when a new one-dimensional mode is just trapped in the transverse direction across the glass strips [77]. Based on the one-dimensional field expression Eq.(7.30), the resonance condition can be written as

$$p_x \cdot t = j\pi, \tag{11.4}$$

where j is an integer. Substituting the dimensionless expression for p_x, Eq.(7.19), into Eq.(11.4) gives

$$\sqrt{\frac{(k_0\Lambda)^2(2n_g^2 - n_a^2) - (\beta\Lambda)^2}{2}} \cdot \frac{t}{\Lambda} = j\pi, \tag{11.5}$$

where n_g and n_a are the refractive indices for the glass and air respectively. By assuming that the fundamental guided mode is located on the air line, i.e. $\beta = k_0$, Eq.(11.5) can be simplified as [65]

$$k_0\Lambda\sqrt{n_g^2 - n_a^2}\cdot\frac{t}{\Lambda} = j\pi. \tag{11.6}$$

Eq.(11.6) determines the high-attenuation regions with respect to variation of the normalised frequency $k_0\Lambda$ or the dimensionless thickness of the glass strips t/Λ. An example of this effect can be seen from the guidance features of Kagome hollow-core PCFs in Fig.4.3 of Chapter 4. The resonance causes a low level of transmission over a region of about $200nm$ [66]. In our standard model structure, the value of t/Λ is set to be 0.05, therefore the first high-transmission window is $k_0\Lambda < 56.2$ (i.e. between $j = 0$ and 1). Alternatively, we can fix $k_0\Lambda = 40$ and change the thickness of the glass-strips to investigate the effect of the fibre structure. In this situation, the t/Λ value is required to be less than 0.070 so that the guidance is limited to the first high-transmission window.

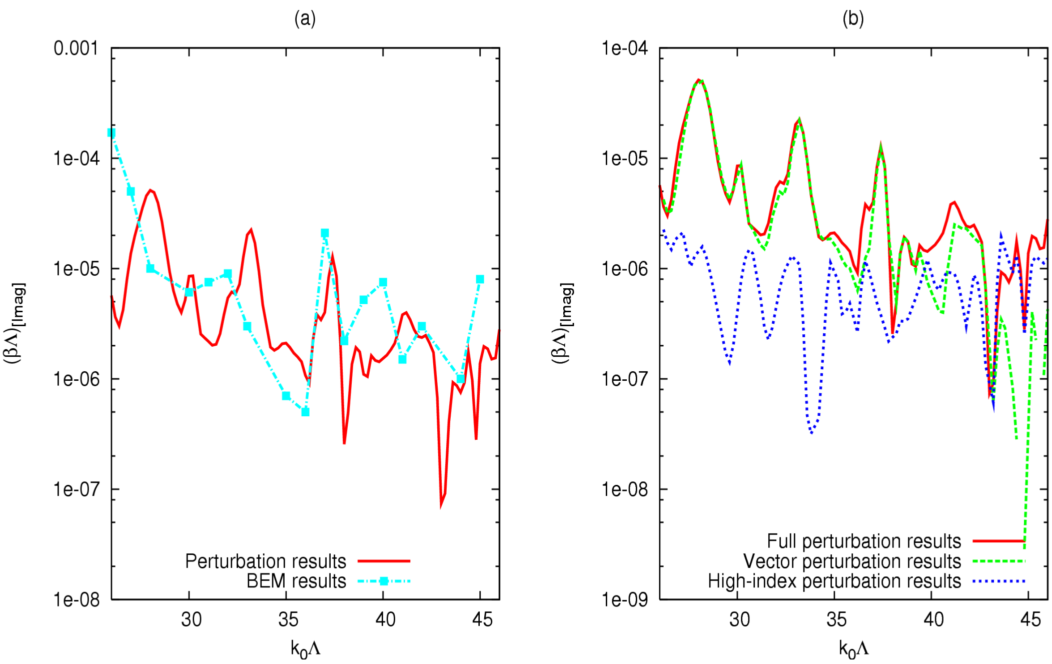

Figure 11.1: Imaginary part of the propagation constant over a range of frequencies in the first transmission window. Figure (a) is the comparison between the perturbation and boundary element methods. The effect of the perturbation terms is shown in Figure (b), where the red line gives the full perturbation results; the green and blue lines are results that include only the vector and high-index perturbation terms, respectively.

Fig.11.1 shows the variation of the attenuation in the first high-transmission window over a range of frequencies from $k_0\Lambda = 26$ to 46 at an interval of 0.2.

The attenuation exhibits a strong variation, which is similar to the previously reported Kagome and hollow-core square lattice PCFs [65, 66, 89–92]. There are three peaks at $k_0\Lambda = 28.0$, 33.2 and 37.4, for which the attenuation varies from 5.1×10^{-5} to 1.3×10^{-5}. The attenuation generally shows a decreasing trend with increasing frequency in our selected region. In Section 6.6, we performed boundary element calculations for the 7×7 cell structure. Fig.11.1 (a) shows a comparison of the perturbation results and the boundary element simulations. They exhibit good agreement of the order of magnitude of the attenuation and they show a similar range of variation with frequency. The details do not match very well, but this is to be expected because the calculated structures are not the same. Leakages for Kagome and hollow-core square lattice PCFs have also been measured in experiments for the same high-transmission window [66, 91], although their resonance frequencies are different due to the fibre structures. In these experiments the confinement losses vary about from $0.5dB/m$ to $1.5dB/m$ in Kagome PCFs (with pitch $\Lambda = 10.9\mu m$) [66], and from $1dB/m$ to $4dB/m$ in hollow-core square lattice PCFs (with pitch $\Lambda = 17\mu m$) [91] for a continuous range of frequencies; this can also be seen in Figs.4.3 and 4.4. In both the boundary element and perturbation methods, the attenuation exhibits a typical value of $(\beta\Lambda)_{[imag]}$ between 10^{-6} and 10^{-5} in a relatively flat range after the peaks. The corresponding confinement loss is about $0.58dB/m$ to $5.8dB/m$ (if the pitch $\Lambda = 15\mu m$), in accord with the experimental values.

The vector and high-index perturbation results are also compared in Fig.11.1 (b), as shown by green and blue curves respectively. It is found that the vector terms are the dominant factor in the attenuation and significantly contribute to the higher loss regions (i.e. the peaks) in the guidance window. In contrast, the high-index perturbation is maintained at a relatively low level. Only for the lowest losses is its effect comparable to the vector perturbation term.

When approaching the resonance frequency, the calculated attenuation values become negative and therefore unphysical. In this case, our choice of considering only the glass-guided modes with high value of C (as discussed in Section 8.5.2) is not sufficient to calculate the attenuation. In this region, a number of modes are located very close to the fundamental guided mode. Their fields occupy both the air and glass regions, showing that they are 'precursors' to the set of higher-order glass-guided modes that are about to become trapped. These characteristics lead to a strong interaction with the fundamental guided mode, giving rise to contributions to attenuations that are not included in our model.

11.3 The effect of glass thickness on the attenuation

For a given frequency of $k_0\Lambda = 40$, the confinement loss can also be calculated as a function of the thickness of the glass strips. In our calculation, the centres of the air and glass regions are unchanged and only the thickness of each glass strip is varied.

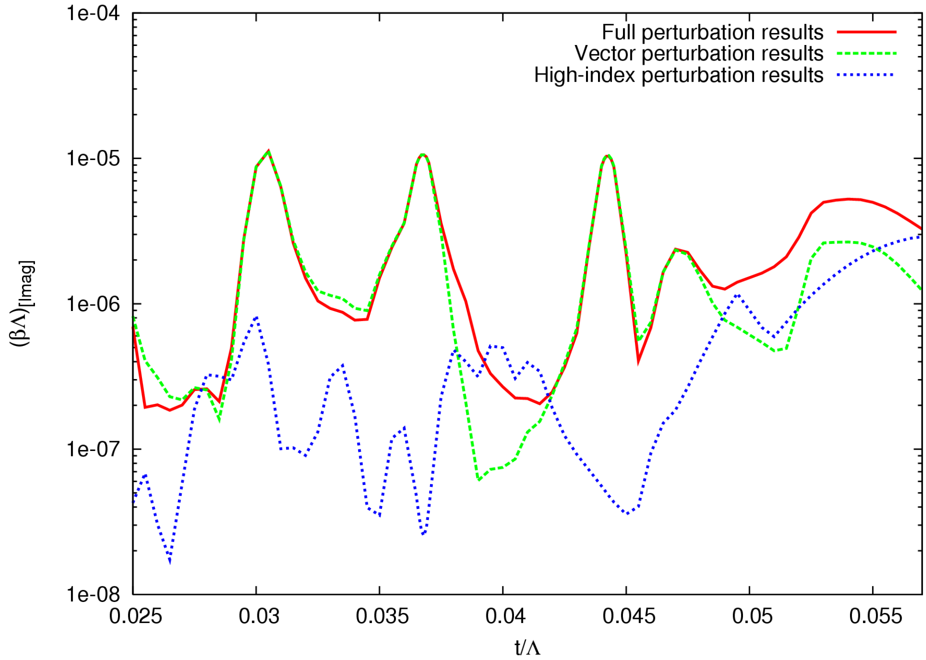

Figure 11.2: Imaginary part of the propagation constant as a function of the glass strip thickness in the first transmission window. The full, vector and high-index perturbation results are shown by red, green and blue colours, respectively.

Fig.11.2 shows the attenuation of the fundamental guided mode. Similar peaks to those seen in Fig.11.1 are observed at $t/\Lambda = 0.030$, 0.037 and 0.044; a comparison with Fig.11.1 shows that the attenuation feature has shifted towards to a lower wavelength for thinner glass struts. For example, the highest frequency peak for $t/\Lambda = 0.05$ is at $k_0\Lambda = 37.4$; for the structure with $t/\Lambda = 0.044$, it is observed at $k_0\Lambda = 40.0$.

11.4 The effect of core size on the attenuation

We now consider the variation of the size of the central defect. The frequency $k_0\Lambda$ and the thickness of glass strips t/Λ are fixed to be the standard values of 40 and 0.05 respectively. Variation of the central defect is created by moving the four glass strips nearest to the centre by different amounts.

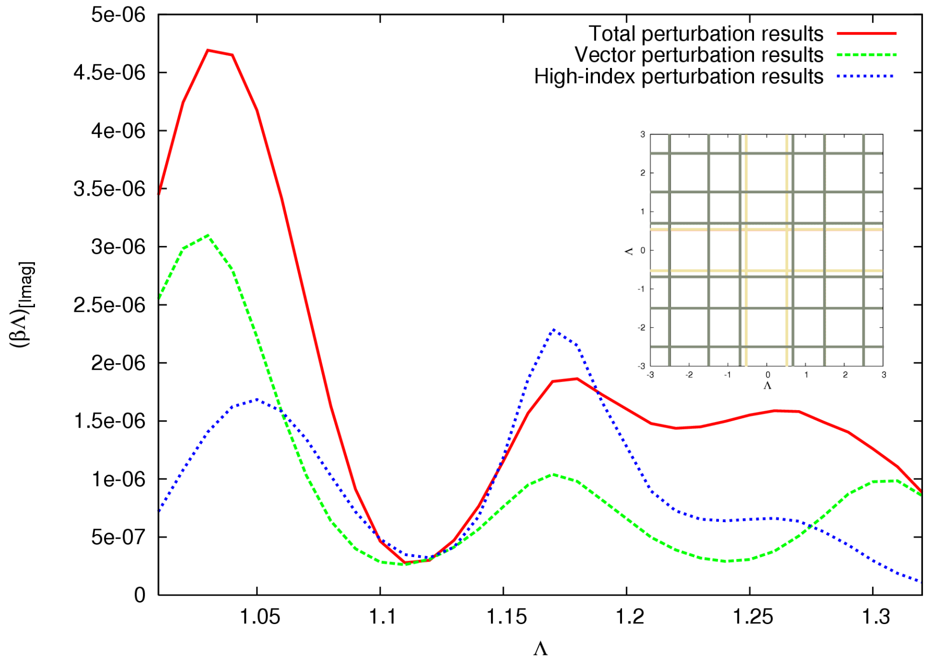

Figure 11.3: Dependence of attenuation on the size of the central defect. The results calculated by the full, vector and high-index perturbations are shown by the red, green and blue colours respectively.

Fig.11.3 displays the attenuation for different sizes of the central defect from 1.01Λ to 1.32Λ; a schematic of the fibre structure for the maximum and minimum sizes of the central defect is shown in the inset. The $(\beta\Lambda)_{[imag]}$ values vary from 2.7×10^{-7} to 4.7×10^{-6}. The plots show a lower attenuation region, from 1.1Λ to 1.15Λ, surrounded by two relatively high loss areas. The minimum value of $(\beta\Lambda)_{[imag]}$ is about 2.8×10^{-7} (i.e. a loss of $0.16dB/m$ for $\Lambda = 15\mu m$) at 1.11Λ. In this case, both the vector and the high-index perturbations are simultaneously suppressed.

In order to investigate this low-loss region in more detail, we have calculated the attenuation for a central defect size of 1.11Λ. The results in Fig.11.4 show a comparison of the attenuation with the standard central defect of 1.20Λ. They

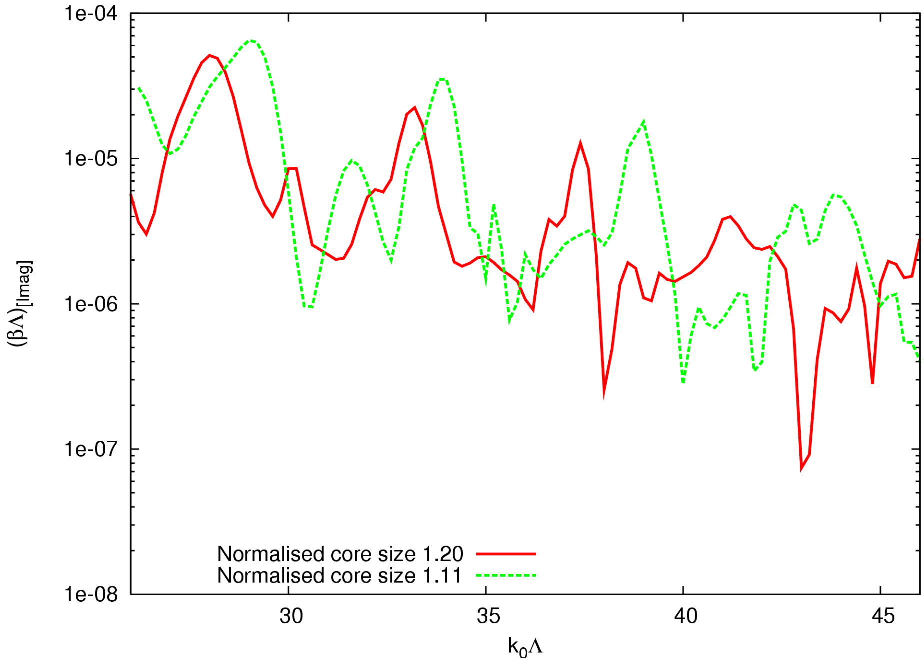

Figure 11.4: Attenuation values for different sizes of the central defect as a function of frequency. The red and green lines correspond to central defects of 1.20Λ and 1.11Λ, respectively. The normalised thickness of the glass strips in both structures is 0.05.

exhibit a very similar variation with frequency, but for the smaller core size, the attenuation characteristic is shifted towards to a lower wavelength. This is similar to what happens for the thinner glass strips. A comparison of the magnitude of the attenuation for the same peaks in Fig.11.4 shows that, for a larger central defect, the perturbation leakage is relatively lower.

11.5 Density of states

In order to understand the attenuation results presented in this chapter, it is helpful to return to Eq.(9.81). The attenuation is given by a combination of the mode interaction $\delta L'_{mm_0}\delta L'_{m_0m}$ and the density of states $\delta\left(\beta^2 - \beta'^{\,2}_{0m}\right)$ of the glass-guided modes. The latter is given by

$$\rho(\beta^2) = \sum_m \delta\left(\beta^2 - \beta'^{\,2}_{0m}\right), \tag{11.7}$$

where ${\beta'}^2_{0m}$ represents the shifted propagation constant of the glass-guided mode m. As in Section 10.5, Eq.(11.7) is written as

$$\rho\big((\beta\Lambda)^2\big) = \frac{1}{N^2}\sum_m \frac{1}{\sqrt{2\pi}\sigma} e^{-\left(\frac{(\beta\Lambda)^2-(\beta'_{0m}\Lambda)^2}{\sigma}\right)^2/2}, \tag{11.8}$$

where $1/N^2$ is a normalisation factor for a $N \times N$ supercell. As above, we use $\sigma = 10$, and we look at the value of the density of states at the propagation constant of the fundamental guided mode.

In our calculations the glass-guided modes appear in groups, where each group of N modes arises from a combination of closely spaced high-index modes with a delocalised mode. Each group has extremely close β values, and we can therefore treat each group as a whole. The matrix element term of $\delta L'_{mm_0}\delta L'_{m_0m}$ in Eq.(9.81) can be used to classify the groups, in particular, by looking for groups with a total interaction larger than a specific value.

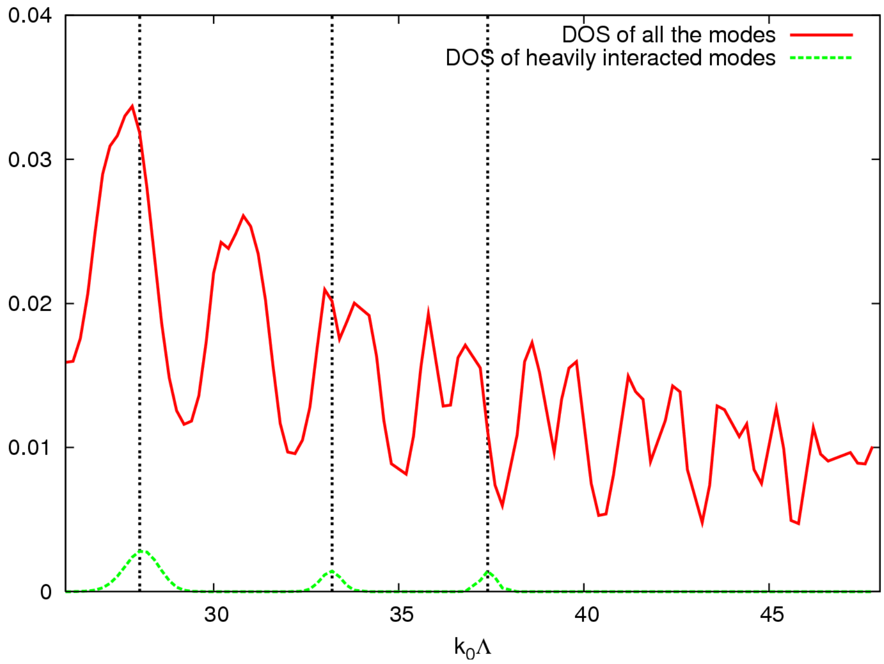

Figure 11.5: Density of states as a function of frequency for the standard fibre structure, where the central defect and normalised thickness of glass strips are 1.20Λ and 0.05, respectively. The red and green lines are for all the glass-guided modes and only strongly interacting modes, respectively. The locations of the three peaks in Fig.11.1 (a) are indicated by dashed lines.

Fig.11.5 shows the density of states for all the glass-guided modes and for only the most strongly interacting groups with a sum of $\delta L'_{mm_0}\delta L'_{m_0m}$ larger than 0.001. As in Fig.11.1, the density of states for all the glass-guided modes exhibits a decreasing trend with an increase of frequency. For the peaks that occur in Fig.11.1, we find a strong correlation with the density of states of the heavily interacting glass-guided modes. This shows that the peaks in the attenuation depend on a limited number of modes with strong interaction the fundamental guided mode, rather than a higher density of states of the cladding modes.

11.6 Conclusions

In this chapter, the attenuation of rectangular hollow-core PCFs has been discussed and the loss of the fundamental guided mode has been calculated as functions of the frequency and fibre parameters (the central defect size and glass strip thickness). The magnitude of the perturbation results for the attenuation are in good agreement with the boundary element simulations and experimental data. It has been found that the largest variations of the attenuation are caused by the effects of the vector perturbation term. We have also found that a smaller central defect or a thinner glass strut thickness plays a similar role to a larger frequency and therefore pushes the attenuation feature to a lower wavelength. Although changes in a specific fibre geometry, for example by using a larger central defect, can reduce the attenuation at a given frequency, this optimisation is not effective for other frequencies, and the order of magnitude of the attenuation is not strongly affected by details of the fibre structure. The generally low attenuation of rectangular hollow-core PCFs is due to a relatively low density of glass-guided modes and a generally weak interaction between the glass-guided modes and the fundamental mode.

Chapter 12

Conclusions

The work presented in this thesis focuses on modelling and understanding a novel guidance mechanism caused by the weak interaction of modes in PCFs. In this chapter, an overall interpretation of the light guidance and suggestions for fibre optimisation are summarised. The further development of this work is also discussed at the end of this chapter.

The main technical conclusion of the work is that the perturbation method for analysing rectangular hollow-core PCFs works well. Based on the analytic scalar ideal structure, results can be obtained quickly and the behaviour of the attenuation is in agreement with the full computational results of the boundary element method. This level of agreement gives us confidence that the perturbation method can be used to analyse and interpret the weak interaction guidance mechanism.

Due to the similar optical phenomena and guidance features, it is also possible to give an overall explanation of the guidance mechanism beyond a particular fibre structure. As illustrated in our modelling, cladding modes exist in groups in terms of their propagation constants at a specific frequency. The propagation constants for each group change as a whole with the variation of frequency. Thus in both Kagome and square-lattice hollow-core PCFs, the photonic density of states exhibits many similar features, with regard to regions with dense or sparse states.

To differentiate the states between the air-guided and glass-guided modes, two particular features can be used. The first is the difference in their distributions. The propagation constants for air-guided modes in high-transmission windows are lower than the fundamental guided mode and are located further below the air-line. In contrast, glass-guided modes have a much broader distribution, covering both the air-line and the propagation constant of the fundamental mode. In their allowed regions, the distribution of the groups of glass-guided modes is relatively even with respect to the propagation constant, giving a fairly uniform density of states. In contrast, the groups of air-guided modes are more concentrated. This point is clearly seen in the weighted density of states plots in our modelling. As a result, air-guided modes are seen as high density regions in density of states plots in a 'background' of glass-guided states. The second feature is the trend of the variation with frequency. The variation of the propagation constant with frequency for glass-guided modes is much stronger than for air-guided modes. This arises because the fields of glass-guided modes are located in the high refractive index material and their propagation constants are mainly affected by high-index modes in our modelling. Therefore, the groups with concentrated air-guided modes have a lower slope of the propagation constant as a function of frequency.

Equipped with this knowledge, and looking at the density of states of weak interaction guidance PCFs, one can find that there actually exist bandgaps for air-guided modes in the high-transmission windows. Our quantitative calculations have shown that the separation of propagation constants between the fundamental and other air-guided modes are sufficiently large so as to effectively prohibit the perturbation leakage. The glass-guided modes can coexist with the fundamental mode at the same frequency and propagation constant. However, their low density of states and high spatial frequency suppress the perturbation leakage from the fundamental guided mode. Light can therefore be guided under such a mechanism in weak interaction guidance PCFs.

There is another use of the density of states in predicting general attenuation features. In rectangular hollow-core PCFs, the general trend of the attenuation matches with the density of states at the propagation constant of the fundamental guided mode in the high-transmission windows. However, it can not determine the fine variation of the attenuation that is observed in the high-transmission windows. For example, the attenuation peaks are related only to the density of states of the mode groups with significant coupling to the fundamental mode. Because the variations of propagation constant with frequency of the fundamental guided mode and glass-guided modes are not synchronous, the attenuation of weak interaction guidance PCFs is consequently significantly varied. This is a unique feature which can be used to identify weak interaction guidance PCFs. For a specific fibre geometry, the whole attenuation feature can be shifted by changing the central defect size or glass strut thickness. However, this has only a limited effect on the overall magnitude of the confinement loss because the key factors, cladding density of states and the mode interaction, are mainly attributed to the fibre geometry.

For a generally low leakage, both the density of states of the glass-guided modes and interactions between the fundamental guided mode and glass-guided modes should be reduced. By employing an appropriate cladding structure, the density of states of glass-guided modes in the vicinity of the propagation constant of the fundamental guided mode can be generally reduced over all transmission windows. The other potential improvement regards the detailed fibre structure around the central defect area. In both rectangular and Kagome hollow-core PCFs, the field of the fundamental guided mode has a large, primary intensity in the central air hole and several residuals in some of the surrounding air holes. This can be seen in our model structure: there exist four concentrated field regions in the outer air holes. These air holes are separated from the central defect by four glass strips. Our simulations show that the glass-guided modes with fields in these four glass strips are the dominant factor in the perturbation leakage. Therefore, we can achieve a suppressed perturbation leakage by optimising the defect area for a specific cladding geometry. This is done by having a low field intensity and small field area in the outer air defect regions, and a short glass strut connecting these regions with the central air hole.

There is considerable scope for the future work applying perturbation methods to understanding PCF guidance; these can be described by: continuation, simplification and generalisation. The continuation aims to obtain a more complete guidance characteristic for rectangular hollow-core PCFs, particularly by analysing the attenuation features in more high-transmission windows and by looking in more detail at the mode interactions in the resonance regions. It is also expected that further analysis of the correlation between the interaction magnitude and the field profile will assist in explaining the finer variation of the attenuation. In the simplification, we could hope to build up a more concise perturbation model by including only the major factors, for example, by only considering the vector perturbation term or the nearest glass strips. The generalisation means a development from our model structure to a more general form satisfying a variety of fibre structures. One possibility may be to separate the transverse governing equation into three directions, which is suitable for Kagome PCFs. Another is to consider two orthogonal directions, as in the current treatment, but where each one-dimensional field is expressed as a combination to match a complicated fibre geometry.

References

[1] E. Yablonovitch, Phys. Rev. Lett., **58**, 2059 (1987).

[2] S. John, Phys. Rev. Lett., **58**, 2486 (1987).

[3] O. Painter, R. K. Lee, A. Scherer, A. Yariv, J. D. O'Brien, P. D. Dapkus and I. Kim, Science, **284**, 1819 (1999).

[4] M. Lončar, T. Yoshie, A. Scherer, P. Gogna and Y. Qiu, Appl. Phys. Lett., **81**, 2680 (2002).

[5] H. G. Park, S. H. Kim, S. H. Kwon, Y. G. Ju, J. K. Yang, J. H. Baek, S. B. Kim and Y. H. Lee, Science, **305**, 1444 (2004).

[6] S. Fan, P. R. Villeneuve and J.D. Joannopoulos, Phys. Rev. Lett., **78**, 3294 (1997).

[7] M. Boroditsky, T. F. Krauss, R. Coccioli, R. Vrijen, R. Bhat and E. Yablonovitch, Appl. Phys. Lett., **75**, 1036 (1999).

[8] Y. J. Lee, S. H. Kim, J. Huh, G. H. Kim and Y. H. Lee, Appl. Phys. Lett., **82**, 3779 (2003).

[9] Ph. Lalanne and A. Talneau, Opt. Express, **10**, 354 (2002).

[10] S. J. McNab, N. Moll and Y. A. Vlasov, Opt. Express, **11**, 2927 (2003).

[11] J. D. Joannopoulos, R. D. Meade and J. N. Winn, *Photonic Crystals: Molding the Flow of Light*, Princeton University Press (1995).

[12] J. C. Knight, T. A. Birks, P. St.J. Russell and D. M. Atkin, Opt. Lett., **21**, 1547 (1996).

[13] R. F. Cregan, B. J. Mangan, J. C. Knight, T. A. Birks, P. St.J. Russell, P. J. Roberts and D. C. Allan, Science, **285**, 1537 (1999).

[14] F. Luan, A. K. George, T. D. Hedley, G. J. Pearce, D. M. Bird, J. C. Knight and P. St.J. Russell, Opt. Lett., **29**, 2369 (2004).

[15] J. C. Knight, Nature, **424**, 847 (2003).

[16] A. R. Bhagwat and A. L. Gaeta, Opt. Express, **16**, 5035 (2008).

[17] D. G. Ouzounov, F. R. Ahmad, D. M*ü*ller, N. Venkataraman, M. T. Gallagher, M. G. Thomas, J. Silcox, K. W. Koch and A. L. Gaeta, Science, **301**, 1702 (2003).

[18] J. D. Shephard, J. D. C. Jones, D. P. Hand, G. Bouwmans, J. C. Knight, P. St.J. Russell and B. J. Mangan, Opt. Express, **12**, 717 (2004).

[19] J. D. Shephard, F. Couny, P. St.J. Russell, J. D. C. Jones, J. C. Knight and D. P. Hand, Appl. Opt., **44**, 4582 (2005).

[20] F. Benabid, J. C. Knight, G. Antonopoulos and P. St.J. Russell, Science, **298**, 399 (2002).

[21] A. W. Snyder and J. D. Love, *Optical Waveguide Theory*, Chapman and Hall (1983).

[22] T. A. Birks, J. C. Knight and P. St.J. Russell, Opt. Lett., **22**, 961 (1997).

[23] J. C. Knight, T. A. Birks, R. F. Cregan, P. St.J. Russell and P. D. de Sandro, Electron. Lett., **34**, 1347 (1998).

[24] M. D. Nielsen, J. R. Folkenberg and N. A. Mortensen, Electron. Lett., **39**, 1802 (2003).

[25] J. Limpert, T. Schreiber, S. Nolte, H. Zellmer, T. Tunnermann, R. Iliew, F. Lederer, J. Broeng, G. Vienne, A. Petersson and C. Jakobsen, Opt. Express, **11**, 818 (2003).

[26] W. J. Wadsworth, R. M. Percival, G. Bouwmans, J. C. Knight and P. St.J. Russell, Opt. Express, **11**, 48 (2003).

[27] W. J. Wadsworth, R. M. Percival, G. Bouwmans, J. C. Knight, T. A. Birks, T. D. Hedley and P. St.J. Russell, IEEE Photon. Technol. Lett., **16**, 843 (2004).

[28] A. Ortigosa-Blanch, J. C. Knight, W. J. Wadsworth, J. Arriaga, B. J. Mangan, T. A. Birks and P. St.J. Russell, Opt. Lett., **25**, 1325 (2000).

[29] T. P. Hansen, J. Broeng, S. E. B. Libori, E. Knudsen, A. Bjarklev, J. R. Jensen and H. Simonsen, IEEE Photon. Technol. Lett., **13**, 588 (2001).

[30] K. Suzuki, H. Kubota, S. Kawanishi, M. Tanaka and M. Fujita, Electron. Lett., **37**, 1399 (2001).

[31] K. Saitoh and M. Koshiba, IEEE Photon. Technol. Lett., **14**, 1291 (2002).

[32] K. Saitoh and M. Koshiba, J. Lightw. Technol., **23**, 3580 (2005).

[33] J. Broeng, D. Mogilevtsev, S. E. Barkou and A. Bjarklev, Opt. Fib. Tech., **5**, 305 (1999).

[34] T. A. Birks, D. M. Bird, T. D. Hedley, J. M. Pottage and P. St.J Russell, Opt. Express, **12**, 69 (2004).

[35] G. J. Pearce, T. D. Hedley and D. M. Bird, Phys. Rev. B, **71**, 195108 (2005).

[36] G. J. Pearce, J. M. Pottage, D. M. Bird, P. J. Roberts, J. C. Knight and P. St.J Russell, Opt. Express, **13**, 6937 (2005).

[37] S. G. Johnson and J. D. Joannopoulos, Opt. Express, **8**, 173 (2001).

[38] D. Mogilevtsev, T. A. Birks and P. St.J. Russell, Opt. Lett., **23**, 1662 (1998).

[39] D. Mogilevtsev, T. A. Birks and P. St.J. Russell, J. Lightw. Technol., **17**, 2078 (1999).

[40] T. M. Monro, D. J. Richardson, N. G. R. Broderick and P. J. Bennett, J. Lightw. Technol., **17**, 1093 (1999).

[41] T. M. Monro, D. J. Richardson, N. G. R. Broderick and P. J. Bennett, J. Lightw. Technol., **18**, 50 (2000).

[42] T. P. White, B. T. Kuhlmey, R. C. McPhedran, D. Maystre, G. Renversez, C. M. de Sterke and L. C. Botten, J. Opt. Soc. Am. B, **19**, 2322 (2002).

[43] T. P. White, R. C. McPhedran, L. C. Botten, G. H. Smith and C. M. de Sterke, Opt. Express, **9**, 721 (2001).

[44] B. T. Kuhlmey, T. P. White, G. Renversez, D. Maystre, L. C. Botten, C. M. de Sterke and R. C. McPhedran, J. Opt. Soc. Am. B, **19**, 2331 (2002).

[45] B. T. Kuhlemy, K. Pathmanandavel and R. C. McPhedran, Opt. Express, **14**, 10851 (2006).

[46] A. Bjarklev, J. Broeng and A. S. Bjarklev, *Photonic Crystal Fibres*, Kluwer Academic (2003).

[47] S. Selleri and M. Zoboli, J. Opt. Soc. Am. A, **14**, 1460 (1997).

[48] F. Brechet, J. Marcou, D. Pagnoux and P. Roy, Opt. Fiber Tech., **6**, 181 (2000).

[49] A. Peyrilloux, S. Février, J. Marcou, L. Berthelot, D. Pagnoux and P. Sansonetti, J. Opt. A: Pure Appl. Opt., **4**, 257 (2002).

[50] D. Ferrarini, L. Vincetti, M. Zoboli, A. Cucinotta and S. Selleri, Opt. Express, **10**, 1314 (2002).

[51] M. H. Cho, W. Cai and T. H. Her, J. Sci. Comput., **28**, 263 (2006).

[52] N. Guan, S. Habu, K. Takenaga, K. Himeno and A. Wada, J. Lightw. Technol., **21**, 1787 (2003).

[53] T. L. Wu and C. H. Chao, IEEE Photo. Tech. Lett., **16**, 126 (2004).

[54] X. Wang, J. Lou, C. Lu, C. L. Zhao and W. T. Ang, Opt. Express, **12**, 961 (2004).

[55] P. St.J Russell, Science, **299**, 358 (2003).

[56] A. Argyros, T. A. Birks, S. G. Leon-Saval, C. M. B. Cordeiro, F. Luan and P. St.J. Russell, Opt. Express, **13**, 309 (2005).

[57] M. Koshiba and K. Saitoh, Opt. Express, **11**, 1746 (2003).

[58] K. Saitoh and M. Koshiba, Opt. Express, **11**, 3100 (2003).

[59] J. M. Pottage, D. M. Bird, T. D. Hedley, J. C. Knight, T. A. Birks, P. St.J. Russell and P. J. Roberts, Opt. Express, **11**, 2854 (2002).

[60] T. A. Birks, G. J. Pearce and D. M. Bird, Opt. Express, **14**, 9483 (2006).

[61] J. M. Stone, G. J. Pearce, F. Luan, T. A. Birks, J. C. Knight, A. K. George and D. M. Bird, Opt. Express, **14**, 6291 (2006).

[62] A. Wang, G. J. Pearce, F. Luan, D. M. Bird, T. A. Birks and J. C. Knight, Opt. Express, **14**, 10844 (2006).

[63] M. Qiu and S. He, Phys. Rev. B, **60**, 10610 (1999).

[64] E. C. Mägi, P. Steinvurzel and B. J. Eggleton, J. Appl. Phys., **96**, 3976 (2004).

[65] F. Couny, F. Benabid, P. J. Roberts, P. S. Light and M. G. Raymer, Science, **318**, 1118 (2007).

[66] F. Couny, F. Benabid and P. S. Light, Opt. Lett., **31**, 3574 (2006).

[67] J. C. Knight, F. Gérôme and W. J. Wadsworth, Opt. Quant. Electron, **39**, 1047 (2007).

[68] F. Benabid, Phil. Trans. R. Soc. A, **364**, 3439 (2006).

[69] N. A. Mortensen and M. D. Nielsen, Opt. Lett., **29**, 349 (2004).

[70] R. Amezcua-Correa, N. G. R. Broderick, M. N. Petrovich, F. Poletti and D. J. Richardson, Opt. Express, **14**, 7974 (2006).

[71] J. Hu and C. R. Menyuk, Opt. Express, **15**, 339 (2007).

[72] C. M. Smith, N. Venkataraman, M. T. Gallagher, D. Müller, J. A. West, N. F. Borrelli, D. C. Allan and K. W. Koch, Nature, **424**, 657 (2003).

[73] J. A. West, C. M. Smith, N. F. Borrelli, D. C. Allan and K. W. Koch, Opt. Express, **12**, 1485 (2004).

[74] H. K. Kim, J. Shin, S. Fan, M. J. F. Digonnet and G. S. Kino, IEEE J. Quantum Electron., **40**, 551 (2004).

[75] M. J. F. Digonnet, H. K. Kim, J. Shin, S. Fan and G. S. Kino, Opt. Express, **12**, 1864 (2004).

[76] G. Humbert, J. C. Knight, G. Bouwmans, P. St.J. Russell, D. P. Williams, P. J. Roberts and B. J. Mangan, Opt. Express, **12**, 1477 (2004).

[77] N. M. Litchinitser, A. K. Abeeluck, C. Headley and B. J. Eggleton, Opt. Lett., **27**, 1592 (2002).

[78] H. K. Kim, M. J. F. Digonnet, G. S. Kino, J. Shin and S. Fan, Opt. Express, **12**, 3436 (2004).

[79] R. Amezcua-Correa, N. G. R. Broderick, M. N. Petrovich, F. Poletti and D. J. Richardson, Opt. Express, **15**, 17577 (2007).

[80] P. J. Roberts, D. P. Williams, B. J. Mangan, H. Sabert, F. Couny, W. J. Wadsworth, T. A. Birks, J. C. Knight and P. St.J. Russell, Opt. Express, **13**, 8277 (2005).

[81] P. J. Roberts, D. P. Williams, H. Sabert, B. J. Mangan, D. M. Bird, T. A. Birks, J. C. Knight and P. St.J. Russell, Opt. Express, **14**, 7329 (2006).

[82] T. Murao, K. Saitoh, N. J. Florous and M. Koshiba, Opt. Express, **15**, 4268 (2007).

[83] R. Amezcua-Correa, F. Gèrôme, S. G. Leon-Saval, N. G. R. Broderick, T. A. Birks and J. C. Knight, Opt. Express, **16**, 1142 (2008).

[84] F. Benabid, F. Couny, P. S. Light and P. J. Roberts, Laser Focus World, **44**, 61 (2008).

[85] A. R. Bhagwat and A. L. Gaeta, Opt. Express, **16**, 5035 (2008).

[86] R. W. Boyd, *Nonlinear Optics*, CRC Press, 2nd edn. (2003).

[87] G. P. Agrawal, *Nonlinear Fiber Optics*, Academic Press (2001).

[88] F. Benabid, G. Bouwmans, J. C. Knight, P. St.J. Russell and F. Couny, Phys. Rev. Lett., **93**, 123903 (2004).

[89] A. Argyros and J. Pla, Opt. Express, **15**, 7713 (2007).

[90] G. J. Pearce, G. S. Wiederhecker, C. G. Poulton, S. Burger and P. St.J. Russell, Opt. Express, **15**, 12680 (2007).

[91] F. Couny, P. J. Roberts, T. A. Birks and F. Benabid, Opt. Express, **16**, 20626 (2008).

[92] A. Argyros, S. G. Leon-Saval, J. Pla, and A. Docherty, Opt. Express, **16**, 5642 (2008).

[93] P. K. Kythe, *An Introduction to Boundary Element Methods*, CRC Press (1995).

[94] Y. C. Luo, S. J. Wang, Y. G. Chiou, J. C. Lin and C. Y. Cheng , Jpn. J. Appl. Phys., **34**, 5556 (1995).

[95] C. M. Linton, J. Eng. Math, **33**, 377 (1998).

[96] A. Dienstfrey, F. Hang and J. Huang, Proc. R. Soc. Lond. A, **457**, 67 (2001).

[97] D. G. Duffy, *Green's Functions with Applications*, Chapman & Hall/CRC. (2001).

[98] V. N. Monakhov, *Boundary-Value Problems with Free Boundaries for Elliptic Systems of Equations*, American Mathematical Society (1983).

[99] S. K. Cho, *Electromagnetic Scattering*, Springer-Verlag (1990).

[100] E. Butkov, *Mathematical Physics*, Addison-Wesley (1973).

[101] P. St.J. Russell, T. A. Birks and F. D. Lloyd-Lucas, *Confined Electrons and Photons*, Plenum Press, 585 (1995).

[102] H. Y. Ryu, J. K. Hwang and Y. H. Lee, Phys. Rev. B, **59**, 5463 (1999).

[103] J. Broeng, T. Søndergaard, S. E. Barkou, P. M. Barbeito and A. Bjarklev, J. Opt. A: Pure Appl. Opt., **1**, 477 (1999).

[104] F. Benabid, P. J. Roberts, F. Couny and P. S. Light, J. Europ. Opt. Soc. Rap. Public., **4**, 09004 (2009).

[105] A. W. Snyder and W. R. Young, J. Opt. Soc. Am., **68**, 297 (1978).

[106] R. Haydock, Phys. Rev. B, **61**, 7953 (2000).

[107] E. N. Economou, *Green's Functions in Quantum Physics*, Springer-Verlag, 2nd edn. (1990).

[108] P. W. Anderson, Phys. Rev. **124**, 41 (1961).